

Effects of Transient Loading on Wind Turbine Drivetrains

By Kenneth Scott

Supervisor: Professor David Infield

For the award of Ph.D

Wind Energy CDT

Department of Electrical and Electronic Engineering

2014

Declaration of Authenticity and Author's Rights

This thesis is the result of the author's original research. It has been composed by the author and has not been previously submitted for examination which has led to the award of a degree.

The copyright of this thesis belongs to the author under the terms of the United Kingdom Copyright Acts as qualified by the University of Strathclyde Regulation 3.50. Due acknowledgement must always be made of the use of any material contained in, or derived from, this thesis.

Signed:

Date:

Previously Published Work

“Effects of Extreme and Transient Loads on the Wind Turbine Drivetrain”, 30th
ASME Wind Energy Symposium, Nashville, USA, 2012

“Bearing Damage Model for Different Drivetrain Designs”, European Wind Energy
Association Conference 2013, Vienna Austria, 2013

Acknowledgements

I would like Romax Technology for their assistance with software and engineering expertise during the project.

NREL for allowing me to collaborate with the Gearbox Reliability Collaborative (GRC) and giving access to test data.

EPSRC for funding the project. Project reference number EP/G037728/1.

Professor Nigel Barltrop for his assistance and guidance at key moments through the project work.

Professor David Infield for his work supervising me and guiding me through the years to achieve my PhD.

Abstract

This project aims to tackle some of the fundamental issues with modelling the drivetrain of the wind turbine. Reliability data shows that gearboxes and generators have higher failure rates than expected, in particular the high speed bearings which are shown to be most problematic. Models of gearboxes are generally isolated from the rest of the structure and loading applied at boundaries to the model. This may not adequately represent conditions that bearings encounter and in certain cases bearings fail due to under prediction of loads.

A full drivetrain model is created showing how flexibility of certain subcomponents affects loading on other parts of the drivetrain. Stiffness of the gearbox mounts, the bedplate and the coupling is revealed to have a large effect on the loading that high speed bearings experience.

Transient loading is also examined to discover if this has a significant effect on high speed bearing loading. Static models have been used to analyse drivetrains using predicted inputs applied at the boundaries but this cannot include any contributions from the structural modes. Transient events such as a grid loss emergency stop are performed on a model of a 2 MW wind turbine and sensitivities of the control strategies are found in relation to LSS torque and rotor speed. Findings show that static models are able to predict general motion of the drivetrain structure so long as the response follows the input conditions; transient models of the drivetrain showed significant differences in the response between loading predicted by static models and transient models.

Finally, medium speed drivetrains are analysed showing how design of the drivetrain can reduce the susceptibility of the drivetrain bearings to vibrational modes of the structure. Findings show problematic bearings are removed and drivetrain bearings become insensitive to loading concluding that medium speed drivetrains could improve reliability.

Contents

Chapter 1 – Project Motivation and Background	1
1.1. Kyoto Protocol	3
1.2. Renewable Energy Targets	3
1.3. Cost of Energy	6
1.4. The Wind Turbine	7
1.4.1. The Modern Wind Turbine	9
1.4.2. Rotor	11
1.4.3. Drivetrain	11
i) <i>Gearing</i>	12
ii) <i>Bearings</i>	13
iii) <i>Mechanical Brake</i>	15
iv) <i>Flexible Coupling</i>	15
1.4.4. Gearbox Mounts	16
1.4.5. High Speed Drivetrains	16
1.4.6. Direct Drive	17
1.4.7. Medium Speed	18
1.4.8. Drivetrain Concept	19
1.4.9. Generator	22
i) <i>Doubly Fed Induction Generator (DFIG)</i>	22
ii) <i>Permanent Magnet Generator (PMG) and Fully Rated Converter</i>	23
1.4.10. Structure	24
1.5. Wind Turbine Reliability	25
1.6. Failure Methods of Gears and Bearings	34
1.6.1. Macropitting	34
1.6.2. Micropitting	36

1.6.3.	Root Bending Moment Cracks	37
1.7.	Drivetrain Modelling.....	38
1.7.1.	Multibody Models.....	38
1.7.2.	Mathematical Models	42
1.7.3.	Finite Element Models.....	43
1.7.4.	Drivetrain Test Rigs.....	43
1.8.	Alternative Drivetrain Technologies.....	43
1.9.	Fatigue Predictions.....	44
1.9.1.	Energy Methods	46
1.9.2.	Bearing Damage	47
1.9.3.	Rainflow Counting.....	47
1.10.	Project Plan.....	48
	Chapter 1 References	49
	Chapter 2 - Static Modelling of the Wind Turbine Drivetrain	60
2.1.	Misalignments.....	62
2.2.	Methodology	64
2.3.	RomaxWIND	65
2.3.1.	Timoshenko Beam Elements	65
2.3.2.	Hertzian Contact	66
2.3.3.	Finite Element.....	67
2.3.4.	Model Reduction.....	68
i)	<i>Guyan Method</i>	68
ii)	<i>Craig-Bampton Method</i>	70
2.4.	Drivetrain Model.....	71
2.4.1.	Low Speed Shaft (LSS)	71
2.4.2.	Stage 1.....	72

2.4.3.	Stage 2.....	73
2.4.4.	Stage 3.....	74
2.4.5.	Coupling.....	75
2.4.6.	Generator	76
2.4.7.	Gearbox Housing	76
2.4.8.	Bedplate	77
2.4.9.	Drivetrain Assembly	78
2.5.	Damage Model	80
2.6.	Coordinate System	81
2.7.	Gearbox Mount Stiffness	81
2.8.	Coupling Stiffness.....	85
2.9.	Summary	88
	Chapter 2 References	90
	Chapter 3 - Transient Loading of the Wind Turbine	92
3.1.	Energy in the Wind	94
3.2.	Aerodynamic Models	94
3.2.1.	Disc Actuator Model.....	95
3.2.2.	Rotor Disc Theory	97
3.2.3.	Blade Element Momentum Theory.....	98
3.2.4.	Computational Fluid Dynamics	101
3.2.5.	Discrete Vortex Method Aerodynamics	102
3.2.6.	Wind Shear	102
3.2.7.	Tower Shadow	104
3.2.8.	Gravity Loading.....	105
3.3.	Structural Loading.....	105
3.4.	GH Bladed.....	106

3.4.1.	Wind Conditions	106
3.4.2.	Aerodynamic Model	107
3.4.3.	Drivetrain Model.....	107
3.4.4.	Control and Generator Model	107
3.5.	Wind Turbine Model.....	108
3.6.	Modal Analysis	112
3.7.	Power Production Loading.....	112
3.8.	Normal Stops.....	115
3.9.	Emergency Stops.....	118
3.9.1.	Effect of Pitch Rate.....	124
3.9.2.	Effects of Brake Loading	127
	<i>i) Maximum Brake Load</i>	127
	<i>ii) Ramp Time</i>	129
3.9.3.	Effects of Wind Speed	131
3.10.	Summary	133
	Chapter 3 References	133
	Chapter 4 - Transient Modelling of the Wind Turbine Drivetrain	163
4.1.	Problems with Static Modelling.....	138
4.2.	Pseudo Transient Modelling	139
4.3.	Comparison with Measured NREL GRC data	139
4.3.1.	Test Rig.....	140
4.3.2.	Model.....	142
4.4.	Transient Start	143
4.5.	Torque Sweep.....	147
4.6.	Discussion of Results	148
4.6.1.	Summary.....	149

4.7.	Transient Modelling of Grid Loss Emergency Stop Simulation.....	149
4.7.1.	Transient Modelling Software	150
4.7.2.	Connection Joints.....	151
4.7.3.	Full Drivetrain Model	152
4.7.4.	Model Natural Frequencies.....	155
4.7.5.	Applied Loads.....	158
4.7.6.	Pseudo-Transient vs. Transient Deflections	160
4.7.7.	Bearing Stress	170
4.8.	Truncation	170
4.8.1.	High Speed Bearing Stresses	172
4.9.	Skidding	176
4.10.	Summary	181
	Chapter 4 References	182
	Chapter 5 - Medium Speed Drivetrains	184
5.1.	Improved Reliability?.....	185
5.2.	Drivetrain Structure Sensitivity.....	186
5.3.	Medium Speed Drivetrain Loads	193
5.3.1.	Response to Transient Events	196
5.3.2.	Resizing Medium Speed Brake.....	200
5.3.3.	Wind Turbine Response to Turbulent Wind.....	202
5.4.	Transient Drivetrain Structural Response	203
5.5.	Summary	211
	Chapter 5 References	212
	Chapter 6 - Summary	214
6.1.	Summary of Project.....	215
6.1.1.	Chapter 1	215

6.1.2.	Chapter 2.....	215
6.1.3.	Chapter 3.....	215
6.1.4.	Chapter 4.....	216
6.1.5.	Chapter 5.....	216
6.2.	Recommendations for Future Work.....	217
	Appendix A.....	220
	Appendix B.....	226

1.

Project Motivation and Background

Nomenclature

Symbol	Explanation	Unit
b	Fatigue Strength Coefficient	
C_D	Dynamic Capacity of Bearing	N
c	Fatigue Ductility Coefficient	
E	Young's Modulus	Nm^{-1}
L_{10}	L_{10} Lifetime Prediction	hrs
K	Cyclic Strength Coefficient	
$2N_f$	Number of Cycles to Failure	cycles
n'	Cyclic Strain Hardening Exponent	
P_{eq}	Equivalent Load	N
p	Load-Life Exponent	
σ	Stress	Nm^{-1}
ϵ_e	Plastic Strain	
ϵ_p	Elastic Strain	
ϵ'_f	Fatigue Ductility Exponent	
σ'_f	Fatigue Strength Exponent	

1.1. Kyoto Protocol

Climate change has been a hotly debated topic over the past decade. In 1997 the Kyoto Protocol was introduced to reduce greenhouse gas emissions and curb effects of these gases on the world's climate. The target was to introduce legally binding obligations to reduce global emissions of these gases by 5.2% from the 1990 level, coming into effect in February 2012. The UK was one of the countries that participated in ratifying this protocol with targets set to reduce emissions by 12.5% of the 1990 level [1.1].

1.2. Renewable Energy Targets

The aim of the European Union renewable energy targets is that by 2020, 20% of energy will be come from renewable resources. Renewable resources may include wind, solar, tidal or hydro and also including geothermal and biomass. In 2010 each member state was given a target to achieve by 2020 [1.2-1.3]. Since some countries were better placed to meet the 20% renewable energy than others, individual targets were set according to their perceived ability to achieve these targets. Table 1.1 shows the targets for each member country along with the EU's estimate whether the country will meet the target in 2020. The UK has a target of 15% renewable energy by 2020 and although there is a predicted deficit until 2017 the UK is expected to meet the 15% target. Other countries such as Denmark are not predicted to be on course to meet targets despite having a high target of 30% renewable energy. Spain has the highest surplus at 2.7% equating to 2700ktoe (tonne of oil equivalent).

The UK's target of producing 15% of its energy from renewable resources is a challenging target since very little renewable infrastructure was already in place. Figure 1.1 highlights the magnitude of the task that is required to achieve the target.

Chapter 1 – Project Motivation and Background

Table 1.1 - EU Renewable Energy Targets showing Predicted Energy against 2020 Targets (Green shows a surplus predicted and blue a deficit compared to their plan to achieve 2020 targets) [1.2]

ktoe (tonnes of oil equivalent)	2011-2012	2013-2014	2015-2016	2017-2018	2020	2020 target
Austria	0	0	0	0	0	34%
Belgium	675	857	812	521	-279	deficit (12.3% vs 13%)
Bulgaria	1-144	186-346	231-481	53-375	-140 to 289	surplus (18.7% vs 16%)
Cyprus	0	0	0	0	0	13%
Czech Rep.	0	0	0	0	0	13%
Denmark	613-809	769-784	473-657	333-366	-337	deficit (28% vs 30%)
Finland	0	0	0	0	0	38%
France	0	0	0	0	0	23%
Estonia	47-69	78-96	79-88	52-67	3	surplus (25.1% vs 25%)
Germany	5930-7058	5866-6997	4657-5917	3842-5088	1387	surplus (18.7% vs 18%)
Greece			70.9	239	488	surplus (20% vs 18%)
Hungary	0	0	0	0	0	13%
Ireland	251-259	255-272	403-430	138-148	0	16%
Italy		-86	-860	-1170	-1170	deficit (16% vs 17%)
Latvia	0	0	0	0	0	40%
Lithuania	96.3	93.9	79.7	52.9	18.3	23.% vs 23%
Luxembourg					-43 to -300	deficit (5-10% vs 11%)
Malta	2.8	6.2	7.1	14.1	-43.5	deficit (9,2% vs 10%)
Netherlands	0	0	0	0	0	14%
Poland	519-866	705-1032	647-1162	613-1129	333	surplus (15.5% vs 15%)
Portugal	0	0	0	0	>0%	surplus (result still 31%)
Romania	0	0	0	0	0	24%
Slovenia	0	0	0	0	0	25%
Slovakia	56	112	134	167	143	surplus (15.2% vs 14%)
Spain	4200		4791		2700	surplus (22.7% vs 20%)
Sweden	1074	1273	1286	1105	486	surplus (50.2% vs 49%)
UK	-119	-210	-254	40		15%

The UK's strategy separates energy usage into three main sectors: electricity, heat and transport. Figure 1.2 shows the breakdown of how renewable energy will be split amongst the groups. Electricity is identified as the sector where most of renewable energy development shall occur. 30% of the total UK's electricity generated will come from renewable resources making up 49% of new renewable energy. Wind power, both onshore and offshore, make up a vast portion of the renewable electricity generation. Heating will account for 30% of the total installed renewable energy with the majority coming from biomass and biogas. Ground source and air source heat pumps will also provide a substantial amount of energy to the heat sector. The final

Chapter 1 – Project Motivation and Background

sector is transport where a required 10% of energy will come from renewable transport.

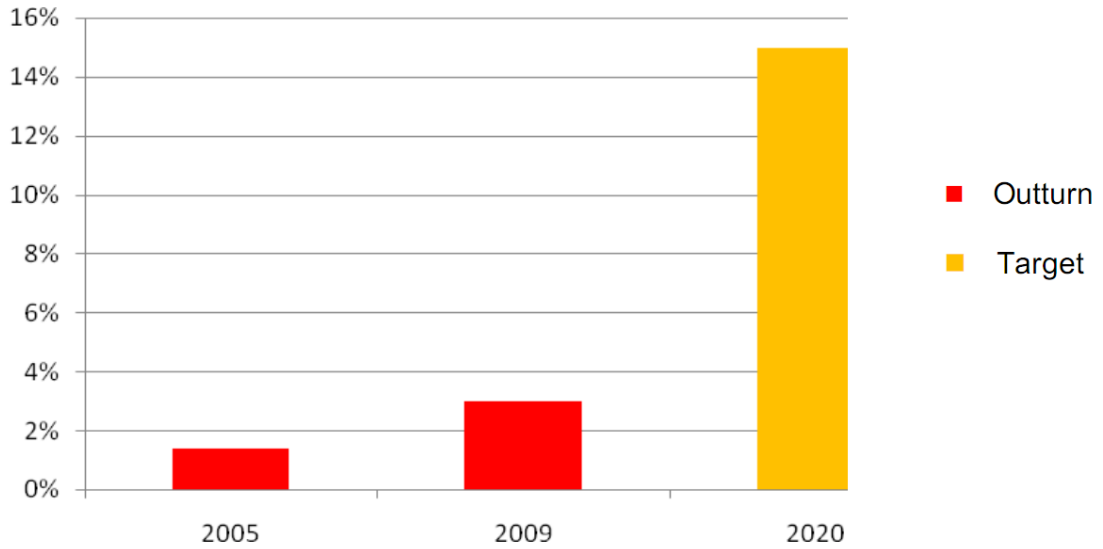


Figure 1.1 - UK's Share of Renewable Energy in Power Mix [1.2]

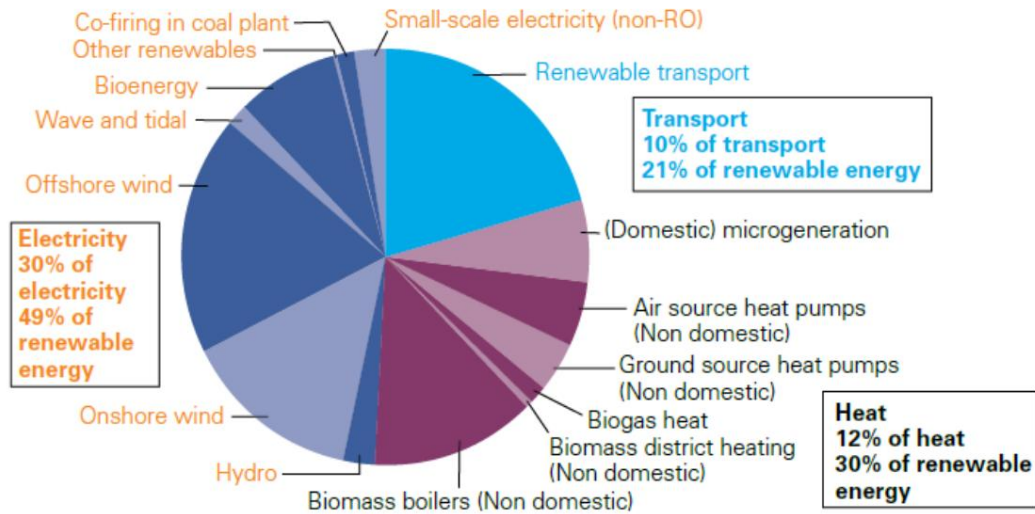


Figure 1.2 - UK Strategy to Achieve EU Renewable Energy Targets [1.2]

Energy generation is not the only way by which improvements can be made: reduction in demand through more energy efficient use and increasing the proportion of renewable energy can also contribute.

Scotland in particular has very ambitious targets of reaching 100% electricity generated from renewable resources. Along with the required 10% transport and 11% heat targets Scotland will contribute 30% of energy produced from renewable resources, far surpassing EU targets. Wind energy is seen as one of the most achievable ways of generating vast amount of electricity required and Scotland has some of the best wind resources in the world, claiming to have 25% of Europe's offshore wind resource. Offshore wind power therefore has massive potential in Scotland.

1.3. Cost of Energy

The goal of improving the wind turbines is to reduce the cost of energy (CoE). CoE is a measure of the total amount of energy produced to the cost that has been spent on installing and operating the turbine. As more research is undertaken and turbines are further developed, CoE has decreased. Minimum CoE for onshore wind turbines has been found for 1MW machines, although siting factors can make turbines up to 3 MW attractive. As turbines move offshore, higher rated machine are expected to have a lower CoE than smaller machines. Higher installation and maintenance costs as well as increased downtime per failure can result in larger turbines having a far less favourable cost of energy offshore when compared to onshore. To reduce CoE, especially for the large offshore turbines, minimising the frequency of failures will be critical.

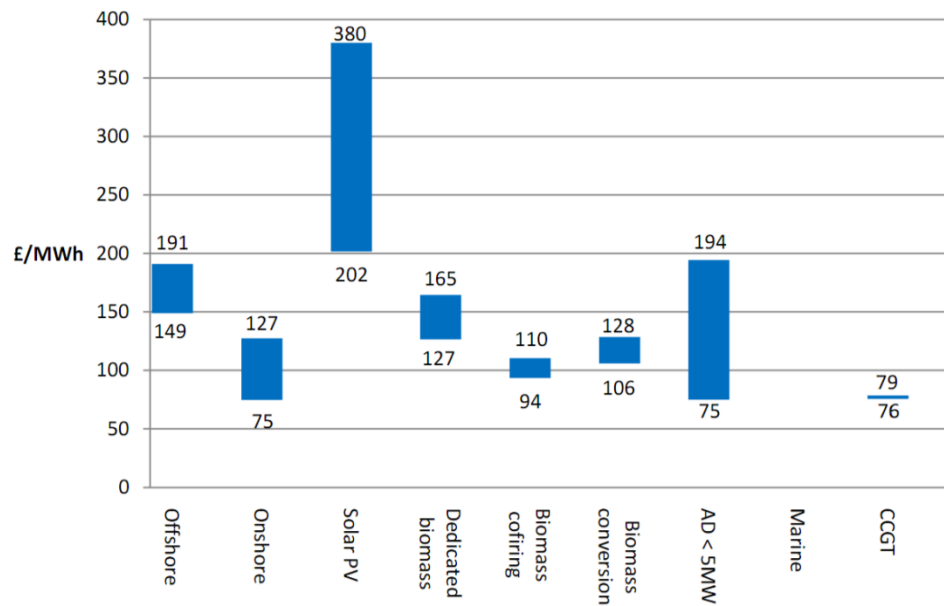


Figure 1.3 - Cost of Energy of Generation Types [1.3]

Figure 1.3 shows the CoE in 2011 for each renewable resource in the UK [1.4]. At the moment onshore wind energy is very competitive when compared to other forms of renewable energy and against Combined Cycle Gas Turbines: CCGTs. When infrastructure for mass manufacture of wind turbines becomes realised in the UK then cost per MWh will drop wind energy will become competitive with fossil fuels such as coal and oil.

1.4. The Wind Turbine

Wind has been harnessed for thousands of years to be used for many different purposes. Historically wind mills were a commonly used to grind corn for flour or used to pump water. The first modern wind turbine was created in July 1887 by Scottish engineer James Blyth at his holiday home in Marykirk, Scotland [1.5]. Although wind power had been used for many centuries before for mechanical work such as milling or water pumping, James Blyth was the first to connect the rotor to an electric generator. He used to the generated electricity to charge accumulators that could then be used to light his home. Blyth offered to give surplus energy to the town of Marykirk but locals refused as it was believed electricity was “the work of the devil”. Later, Blyth constructed a wind turbine which was used to power the local Lunatic Asylum, Infirmary and Dispensary of Montrose.

Chapter 1 – Project Motivation and Background

Blyth's machine was a vertical axis design that used differences in drag forces that the wind creates on the buckets to turn the machine. The central shaft was connected directly to the generator to generate electricity when the rotor spun.

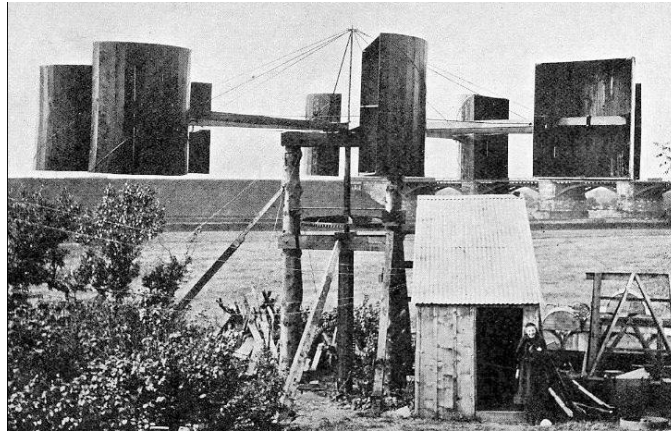


Figure 1.4 - James Blyth's Wind Turbine at Marykirk, Scotland (Note woman in front for scale) [1.5]

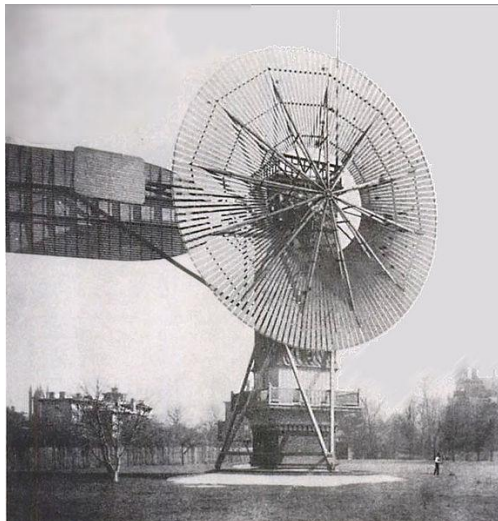


Figure 1.5 - Charles F. Brush's 12kW Wind Turbine at Ohio, USA

Chapter 1 – Project Motivation and Background

The same year in Cleveland, Ohio, USA, Charles F. Brush created a 12kW horizontal axis turbine. This was used to power 100 incandescent light bulbs, 3 arc lamps and various motors in Brush's laboratory or could be connected to a bank of batteries when the laboratory did not require power. The rotor was 17m in diameter with 144 blades and because of the high number of blades turned extremely slowly.

The next stage of development occurred in Denmark where the Danish concept was created. Helped by the decentralisation of the electrical grid, development of wind turbines was allowed to flourish. Johannes Juul in 1957 installed a three bladed upwind stall regulated turbine signifying the beginnings of modern wind turbines. 1975 saw development of the first multi-MW turbine that used specially design blades, tubular towers and pitching blades. Tvindkraft was created by the students and teachers at Tvind, Ulburg and is still in operation today [1.6].

Steady development of wind turbines has led to the refined horizontal axis three bladed upwind Danish concept now seen today.

1.4.1. The Modern Wind Turbine

In the immediate future wind turbine size will grow at an incredible rate, especially with initial developments in the offshore environment. Diameter of the rotor is especially noticeable since the greater the swept area of the rotor, the greater the power available to the wind turbine.



Figure 1.6 - Tvindkraft Wind Turbine, courtesy of Anders Kjeldsen [1.6]

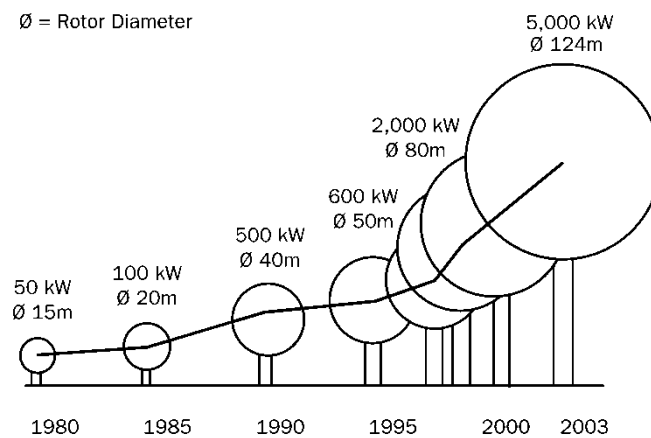


Figure 1.7 - Wind Turbine Rotor Size Growth

Current onshore technology is beginning to reach maturity with limits on the size of turbine. Most manufacturers sell 3MW wind turbines as their onshore turbines: Siemens [1.7] have a 3.6MW geared, Vestas [1.8] 3MW V90 machine, Enercon [1.9] 3MW E-84. The push to offshore sites coupled with minimal height restrictions has

encouraged greater wind turbine sizes. Larger wind turbines are thought to be most cost effective offshore with Siemens designing a 6MW direct drive machine with a 120m or 154m diameter rotor, Enercon a 7.5MW direct drive machine with 127m rotor diameter, and Vestas an 8MW geared machine with a 164m diameter.

1.4.2. Rotor

The rotor is arguably the most important component on a wind turbine. Energy is extracted from the air through the blades and the rotational kinetic energy is passed onto the drivetrain. The rotor is a very complex part of the wind turbine reflected by the significant cost: the blades are predicted to cost 22% of an onshore turbine [1.10]. Blades commonly consist of glass reinforced plastic (GRP) with wooden supports specially made in single sections to minimise flaws occurring between sections. GRP is moulded and cured to ensure quality. Optimised aerofoil sections and twist is used to extract a large amount of energy from the wind. The Danish concept uses three blades attached to a cast iron hub that all combine to produce the torque pass through to the drivetrain. In variable pitch machines the hub also houses pitch bearings and mechanisms or motors which allow the blades to pitch in operation.

1.4.3. Drivetrain

The drivetrain transfers torque and rotational speed from rotor to generator. A few different layout options exist with each one having advantages and disadvantages. Drivetrains can include a gearbox which steps up rotational speed by the gearbox ratio and also steps down torque by the same ratio since power remains constant. The advantages of using gearboxes are that smaller robust induction generators can be used which are relatively cheap and light. The disadvantages are a significantly increase in the number of moving components and therefore failures are expected to be more frequent. Direct drive machines use a simpler drivetrain where the hub is connected directly to the generator with no gearbox in between. In order to achieve the same power rating larger, heavier generators are required though with simpler operation direct drive machines are expected to be more reliable. An overview and background of the drivetrain can be found in [1.11].

i) Gearing

Two types of gearing are used in wind turbine drivetrains: spurs gears and planetary gears. Parallel gear arrangements are used to transmit power between two parallel shafts. Power in and out of the system is constant, minus contact losses, though rotational speed can be changed through the number of teeth on each gear. Since power is related to rotational speed through $Power = Torque \times Rotational\ Speed$, if an increase in rotational speed occurs torque must decrease so power remains constant. Interlocking gear teeth allow transfer of load between two gears so long as the module of the gears is compatible. Module is defined as the number of teeth per mm of circumference and must be equal for both gears to interlock,

$$Module = \frac{Number\ of\ Teeth}{Circumference\ of\ Gear}$$

where teeth form part of helix. Load sharing between teeth can occur since several teeth can be in contact at the same time. This allows a smoother transmission of load since load can be distributed over numerous gears reducing stress and reducing noise.

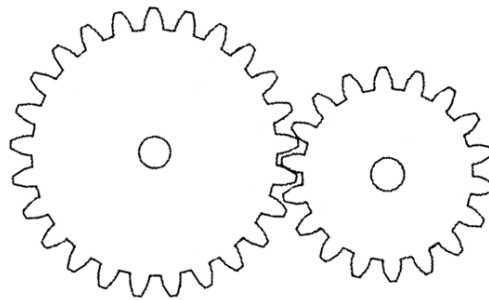


Figure 1.8 - Parallel Gear Pair

Planetary gearing is a more complex system where three types of gear are used: ring (annulus) gear, sun gear and planets. The ring gear is fixed to the casing of the gearbox and does not rotate, the sun gear is at the centre surrounded by planet gears which are free to rotate about their own axis and planet gears are interconnected through a planet carrier meaning planet gears move around the annulus when rotation is applied to the planetary stage. In wind turbines the input is rotation of the planet carrier; output of the gear stage is rotation of the sun shaft. A big advantage of using planetary gears is that more power can be transferred through a smaller volume than for parallel gears since power is split into three paths. Theoretically the same power

density can be achieved for $\frac{1}{3}$ of the size of parallel gears. The downside of shrinking gearing to this size is heat dissipation becomes a problem and overheating can occur. A compromise between the two types of gearing is commonly used with planetary gears used in the first stages where most benefit is seen.

Each gearing stage typically has a gear ratio of between 4:1 and 5:1 but generally not larger than 6:1. Multi stage gearboxes make use of compounded gear stages; if a 3 stage gearbox with each stage having a gear ratio of 5:1, the total output ratio for the gearbox would be 125:1 ($5 \times 5 \times 5$). This allows the wind turbines rotational speed to be increased from around 17rpm at rated power to 1500 rpm required for use with induction generators.

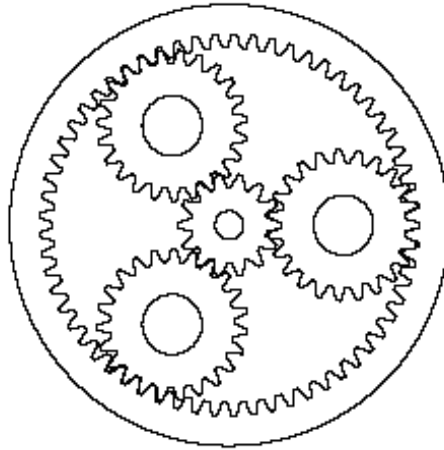


Figure 1.9 - Planetary Gear Stage

ii) Bearings

Bearings are used in rotating machinery to locate shafts in structures whilst minimising losses through friction. Bearings contain an outer raceway, inner raceway and rolling elements, normally balls or rollers.

Ball bearings have ball rolling elements in grooved raceways that allow the bearing to locate the shaft both radially and axially. An oil film between ball and raceway prevents the ball and raceway coming into contact with each other preventing surface wear. The oil film also allows traction between the two surfaces allowing the rolling element to rotate and not slide along the raceway.

Chapter 1 – Project Motivation and Background

Some other types of bearing include cylindrical rollers and tapered rollers. Cylindrical roller bearings replace ball bearing elements with cylindrical rollers which are only able to resist radial loading. The advantage is load is more spread across the contact between the rolling element and raceway. Tapered rollers use cylindrical rollers though tapered at an angle to allow for axial loads to be taken as well as radial loads. Figure 1.12 shows a double tapered bearing with tapered section in opposite directions allowing for axial resistance in both directions. X and O type double tapered bearing exist, relating to the direction of the rolling element. Though the O type bearing is more stable, it is more difficult to install therefore the X type is more common.

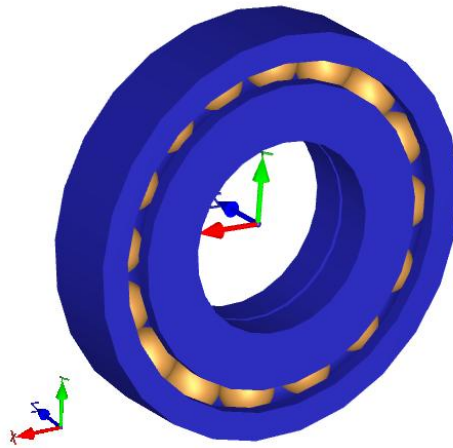


Figure 1.10 - Ball Bearing

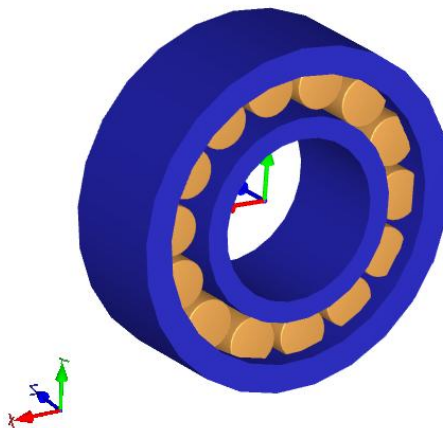


Figure 1.11 - Cylindrical Roller Bearing

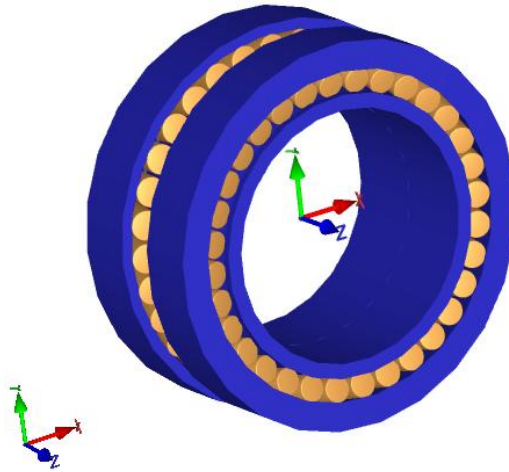


Figure 1.12 - Double Tapers Cylindrical Roller Bearing

iii) Mechanical Brake

A mechanical brake is normally situated on the high speed shaft. It is used to bring the turbine to rest when required as aerodynamic pitching of the blades is ineffective at low rotor speeds. The mechanical brake uses friction between a disc and calliper to bring the turbine to rest when required. By being on the high speed shaft the effective torque applied to braking is stepped up through the gearbox and therefore has a greater effect on the rotor speed and torque.

iv) Flexible Coupling

Flexible couplings are used to minimise effects of misalignments between gearbox and generator in modular designs. Since the gearbox and generator are modular components, individually attached to the bedplate, independent movements relative to each other can occur. Misalignments between the two components can cause high stresses to occur on gearbox and generator bearings if some compliance was not introduced into the system. By introducing compliance as a flexible coupling, tolerances are designed for.

Flexible coupling can be fabricated of flexible material allowing off axis loads to be present whilst not transmitting the increased loading to the bearings. Other designs can include plastic torque tubes with flexible connectors at each end to introduce flexibility. Saavedra [1.12-1.13] modelled and tested the vibration of couplings in the drivetrain, showing effects of different types of coupling on dynamic performance.

1.4.4. Gearbox Mounts

Gearbox mounts are the connections between the gearbox and bedplate. Normally the gearbox sits on two mounts either side with flexible properties to minimise transmitted vibrations from the rest of the turbine. Different mounts can be used from simple trunnion mounts to more elaborate hydraulic mountings. Modelling gearbox mounts has been studied by Haastrup [1.14] using multibody analysis to model effects of mounts and how this affects system dynamics.

1.4.5. High Speed Drivetrains

High speed drivetrain are the most common type for onshore turbines. It combines a 3 stage gearbox with an induction generator and is the most mature drivetrain configuration, having been used successfully for many years. Figure 1.13 is an example of a high speed drivetrain. The gearbox (blue) and generator (red) can be seen clearly. The mechanical brake calliper (green) on the high speed shaft is also clearly visible as well as the flexible coupling between the gearbox and generator (black).



Figure 1.13 - High Speed Drivetrain, Gearbox (Blue), Generator (Red), Brake Calliper (Green)

1.4.6. Direct Drive

Since the gearbox is observed as the most unreliable component, an alternative drivetrain is proposed to improve reliability, the direct drive drivetrain. In this design the gearbox is completely removed and the hub is directly connected to the generator. Since the rotor speed of the wind turbine is low the generator is large since electrical machines have upper torque density limits. Direct drive generators are defined by large torque ratings, therefore volume and consequentially weight is large. Since the aim of the direct drive drivetrain is to improve reliability, complexity is reduced by using permanent magnet synchronous generators avoiding the high failure rates of wound rotors. Siemens and Enercon have championed this technology with their large offshore wind turbines being direct drive. The downside of direct drive wind turbines is that tower top weight is significantly heavier due to the large increase in mass of the generator. Larger foundations and stronger towers are

therefore required for direct drive machines. In addition, the capital cost of direct drive machine is greater than high speed, gearbox driven machines meaning that to have a lower cost of energy the wind turbine must have lower operating costs or increased energy capture. Interestingly, failure statistics do not show direct drive arrangements to be more reliable than conventional drive trains with gearboxes [1.15-1.16].



Figure 1.14 - Direct Drive drivetrain from Enercon E-48

1.4.7. Medium Speed

Medium speed drivetrains are a new hybrid between high speed and direct drive drivetrains. First proposed by Gamesa, the medium speed drivetrain removes the high speed stage of the gearbox, shown to be the most problematic, and replaces the high speed generator with a medium speed permanent magnet generator. The aim is to try and reduce the capital costs by using a lighter generator to reduce tower top mass in comparison with the direct drive whilst improving reliability compared to the high speed drivetrain. It has been suggested that the medium speed design has the lowest cost of energy [1.17-1.18].

In addition to removing a gearing stage, the generator is also bolted onto the back of the medium speed gearbox with the whole drivetrain cantilevered on the gearbox mounts. By cantilevering the drivetrain the need for a flexible coupling is eliminated

since the two components cannot move independently though for repairs to any component the whole drivetrain must be removed.



Figure 1.15 - Romax Technology Medium Speed "Butterfly" Drivetrain

1.4.8. Drivetrain Concept

Polinder [1.19], McMillan [1.16] and Poore [1.20] compared the high speed drivetrain against other drivetrain types, in particular the direct drive. Polinder discovered the 3 stage gearbox with DFIG to be the lightest and cheapest solution with the direct drive with synchronous generator the most expensive. A more attractive direct drive solution is using Permanent Magnet Generators PMGs which could become competitive if costs decrease.

McMillan [1.16] compared techno-economic aspects of high speed gearbox driven wind turbines with direct drive wind turbines. Using Markov chains for availability analysis coupled with economic analysis, including initial costs and lost revenue whilst unavailable, overall revenue for both drivetrains was found. Figure 1.16 shows availability of direct drive machine is slightly better than gearbox driven machine but, because of increased capital cost and repair cost the gearbox driven wind turbine generates more revenue, shown in Figure 1.17.

Chapter 1 – Project Motivation and Background

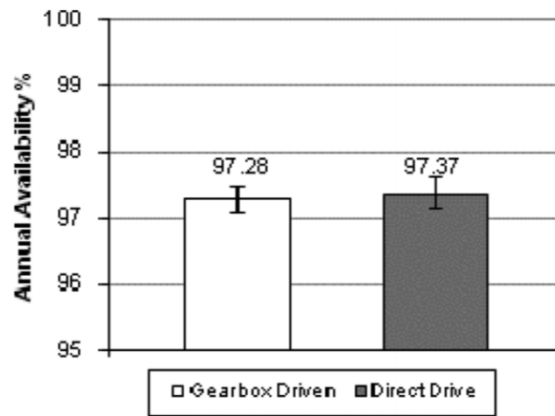


Figure 1.16 - Wind Turbine Availability [1.16]

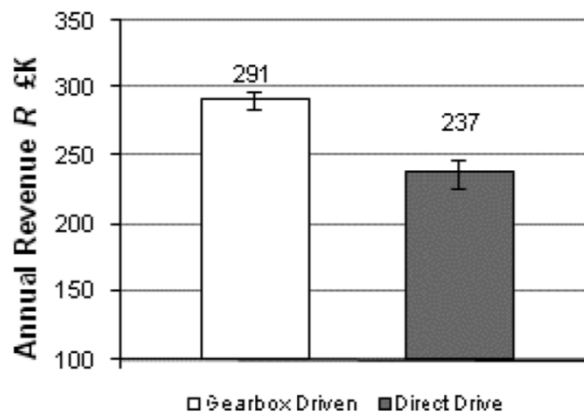


Figure 1.17 - Wind Turbine Annual Revenue [1.16]

Poore [1.20] compared the cost energy of the 3 stage driven drivetrain with direct drive and other drivetrains such as multi-PMGs and induction drivetrains. Direct drive machines show a large increase in cost of energy as the turbine size increases, though with PMGs a cost reduction is predicted.

Chapter 1 – Project Motivation and Background

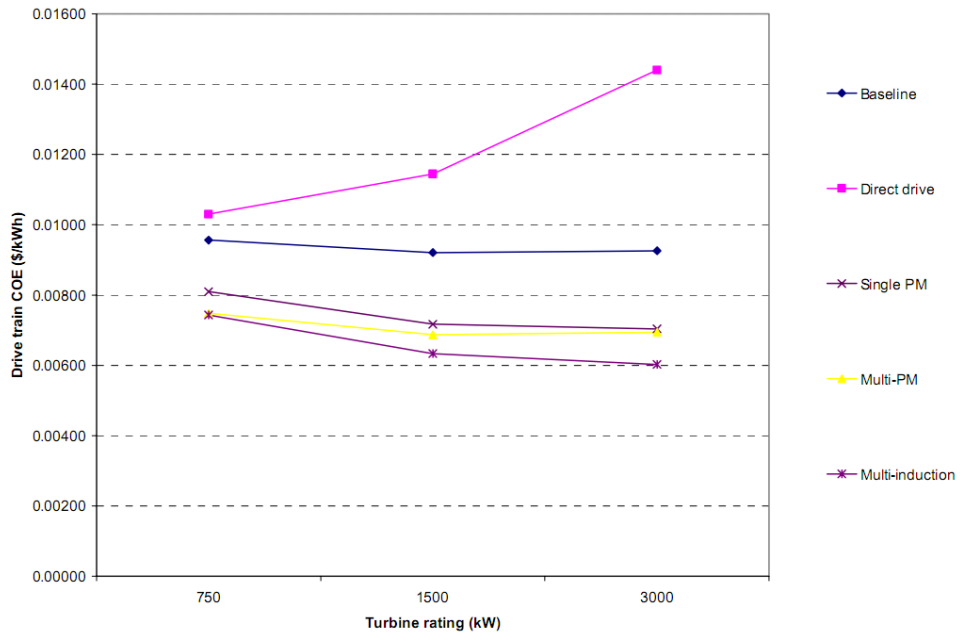


Figure 1.18 - Cost of Energy for Different Drivetrain Configurations [1.20]

Schmidt [1.17] and Halse [1.21] compare the medium speed drivetrain to high speed and direct drive drivetrains. In both analyses the medium speed drivetrain has the lower cost of energy. Figure 1.19 highlights that medium speed drivetrains are predicted to have the lowest cost of energy.

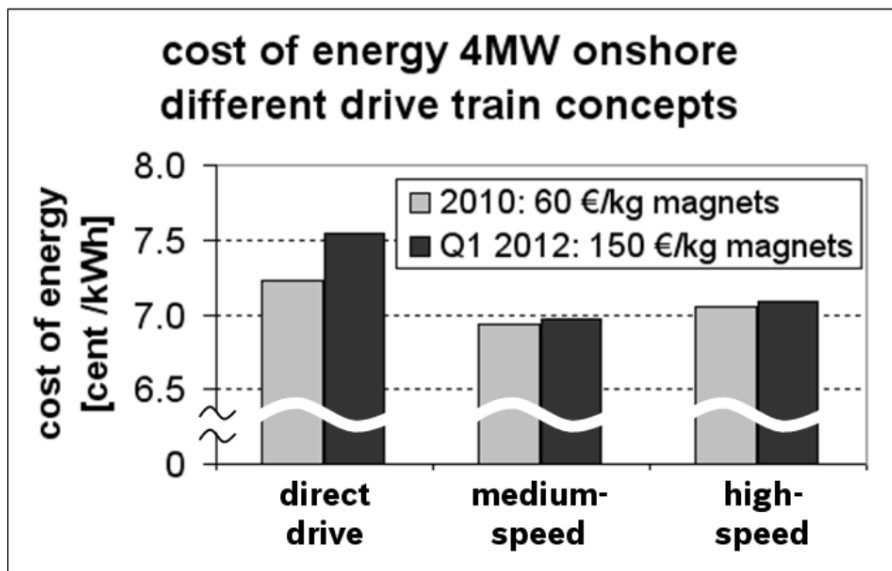


Figure 1.19 - Drivetrain Cost of Energy [1.17]

1.4.9. Generator

Producing the maximum amount of energy from available resources is vitally important for a wind turbine. The generator is the component that converts kinetic energy from the rotor into electrical energy. The most common place for the generator is inside the nacelle at the top of the tower.

Electrical power is created from motion of the generator's rotor causing a potential difference to be induced on the stator causing current to flow. This power can be exported to the grid.

Most wind turbines now are variable speed but power exported to the grid must be at grid frequency, therefore different configurations of generator and power electronics allow control of stator output power so grid frequency can be achieved. Two main types of configuration used are doubly fed induction generator and permanent magnet or induction generator with fully rated converter.

i) Doubly Fed Induction Generator (DFIG)

DFIG's are common in high speed machines where cheap and robust induction generators can be used. The stator is connected directly to the grid, therefore the output from the stator must be at grid frequency. To achieve this, the windings in the rotor are controlled so grid frequency is generated on the stator. As shown in Figure 1.20 a second branch loops round to the rotor of the generator. On this branch Pulse Width Modulation (PWM) converters decouple the frequency either side of the converters and control the input frequency to the rotor. By measuring rotational speed of the wind turbine, the controller can decide what frequency the PWM converters should output to achieve grid frequency on the stator, $\omega_{rotor} + \omega_{PWM\ Converters} = \omega_{Grid}$. The major advantage of using the DFIG design is approximately 1/3 of the power of the machine goes through this branch so the PWM converters can be rated for a reduced power, saving capital expenditure on electronics.

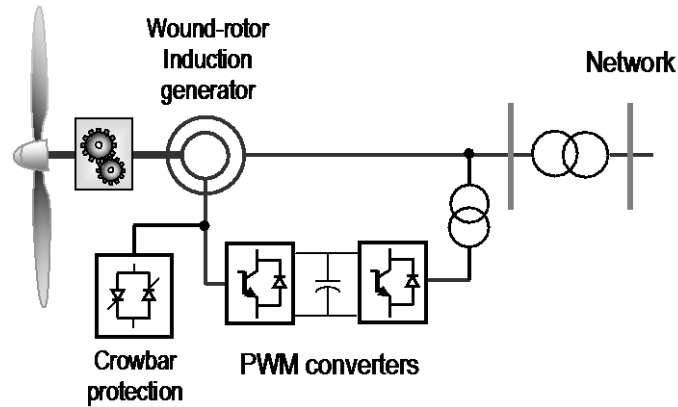


Figure 1.20 – Doubly Fed Induction Generator [1.22]

ii) Permanent Magnet Generator (PMG) and Fully Rated Converter

High failure rates of electrical components along with tightening of grid codes has seen DFIG's become more unpopular with wind turbine designers. To reduce complexity of the generator, permanent magnet machines are being used in place of wound rotor generators. It is thought that reducing complexity of the generator should improve reliability.

Fully rated converters are now being used with induction generators and PMGs decoupling the wind turbine from the rest of the grid. All of the power exported from the wind turbine travels through the power electronics meaning that electronic components are required to be fully rated for the wind turbine adding cost. By decoupling the wind turbine from the grid, the generator side converters handle wind turbine dynamics while the grid side converters ensure compliance with grid code conditions [1.23]. This is attractive to grid operators as more wind turbine are becoming present on the grid and with fully rated converters they are more likely to comply with grid code regulations.

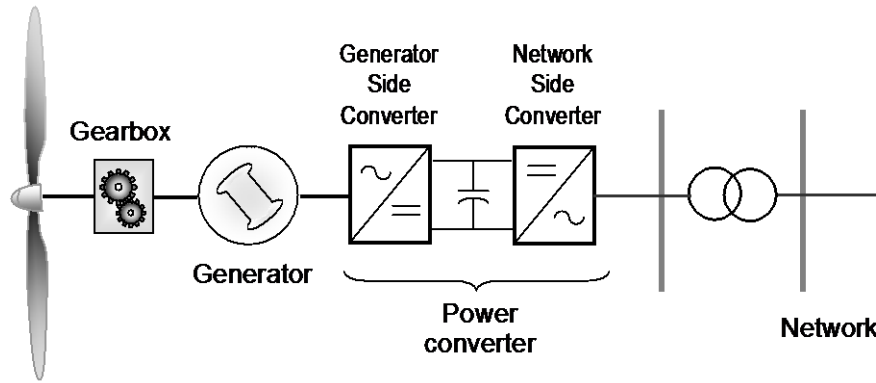


Figure 1.21 - PMG with Fully Rated Converter [1.22]

1.4.10. Structure

The tower of the wind turbine holds the hub and nacelle at the require hub height above the ground. Since wind speed exhibits significant wind shear with the no slip condition at ground level, increasing hub height rapidly improves energy capture. The downside is that increasing hub height means stronger and more expensive towers. Turbine hub height is therefore a trade off between cost and energy capture.

There are generally two types of tower design: steel tubular tower and steel lattice tower. Tubular towers have changed substantially over years: manufacturing capabilities have now allowed smooth tapering of tower sections so a sweeping tower can be created [1.24]. Before, tower sections of different diameters were welded together to create the general effect of a tapered tower. Main design parameters taken into consideration when designing towers are buckling under compression, resilience to fatigue loads and tower stiffness so not to excite natural frequencies. Other design issues such as road transportation of tower sections are a limiting factor on tower diameter and section length [1.25]. The tower first natural frequency is likely to be excited if careful design is not considered. Effects such as blade-passing frequency and rotor thrust fluctuations can cause natural frequencies to be excited with disastrous consequences.

Steel lattice towers are an assembly of steel beams in a tower structure. Advantages of this method are substantial material savings through tower design with legs widely spread at the base aiding stability. Width of the tower gives stability though this is not possible higher up where rotor effects such as tower shadow and blade tip

clearances become important. Transportation of lattice towers does not cause as many problems as tubular towers since towers can be assembled on site.

Foundations of onshore wind turbines are typically concrete, gravity based designs. These can be separated into slab, multi-piled and mono-piled foundations. Slab foundations are wide foundations used when ground material is suitable. Slabs are wide and shallow to resist overturning moment of the wind turbine when in operation. Ground properties require bedrock close to the surface in order to bear load.

Multi-pile and mono-piles are used in weaker grounds where material is needed to be used more effectively. Piles are put deep into the ground meaning vertical and lateral loads resist wind turbine overturning moments. Mono-pile foundations are generally cylindrical since material in the middle of the foundation does not play much of a structural role [1.24].

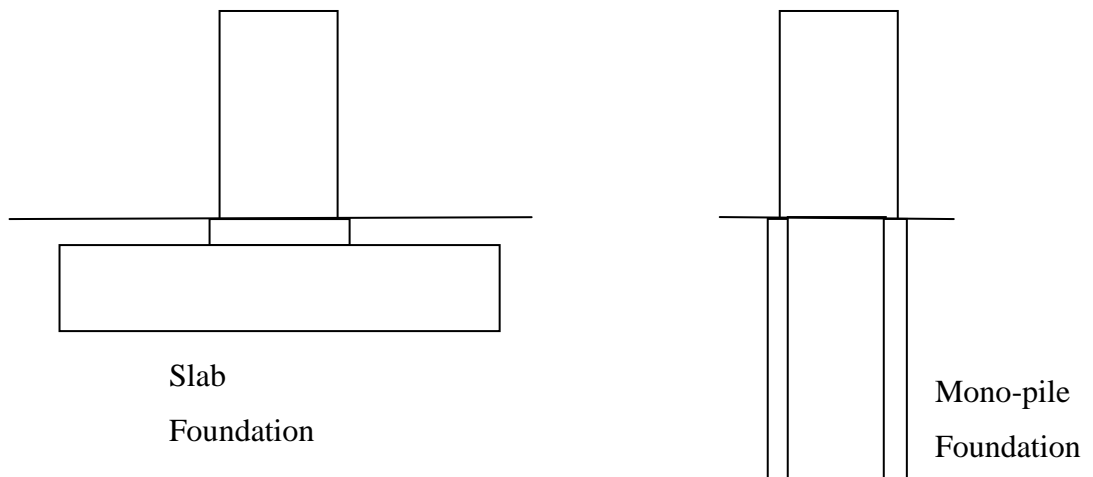


Figure 1.22 - Foundation Types

1.5. Wind Turbine Reliability

Motivation for the project originated from studies into reliability data from wind farms. Many failure studies into reliability of wind turbines show a lot of the similar trends with gearbox and generator contributing most to overall downtime. Main studies undertaken in this field are by Ribrant and Berting [1.26-1.27], Faulstich [1.28-1.29] and Tavner [1.30-1.32].

Chapter 1 – Project Motivation and Background

Faulstich [1.33] modelled failure statistics of over 1500 German onshore wind turbines. Downtimes and annual failure rates of components were calculated to identify which components were the most troublesome. Figure 1.23 was the result of these studies.

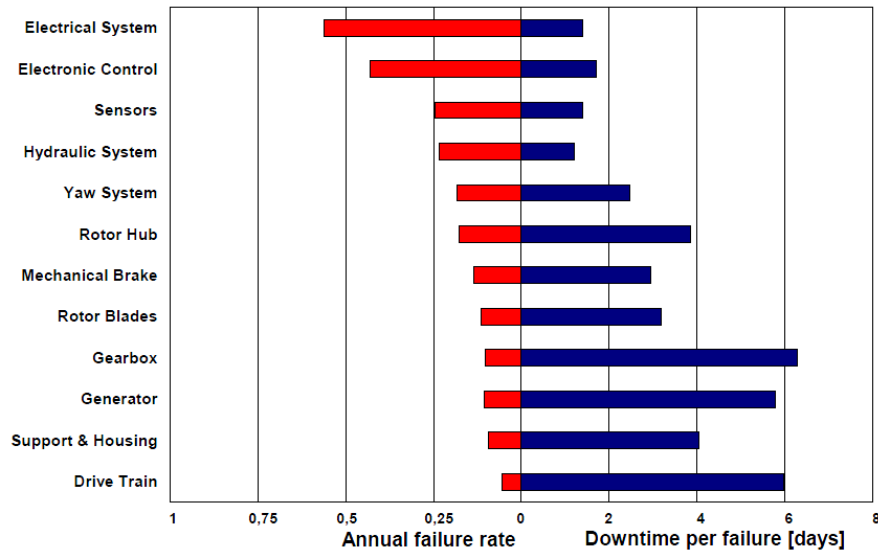


Figure 1.23 - Comparison of Different Turbine Concepts [1.33]

A large spread a results for both annual failure rates and downtime per failure was discovered. The electrical system and electronic control was found to have the highest annual failure rate but a relatively short downtime per failure. In comparison, components such as the gearbox, generator and drivetrain have relatively low numbers of failures (~ 0.1 failure per year) but downtime per failure is massively higher. The gearbox and generator were the components that contributed most to the total downtime of the wind turbines.

Ribrant and Berting [1.27] published data on Swedish, Finnish and German wind farms. Figure 1.24 and Figure 1.25 show reliability data for wind turbines in Sweden from 2000 – 2004.

Chapter 1 – Project Motivation and Background

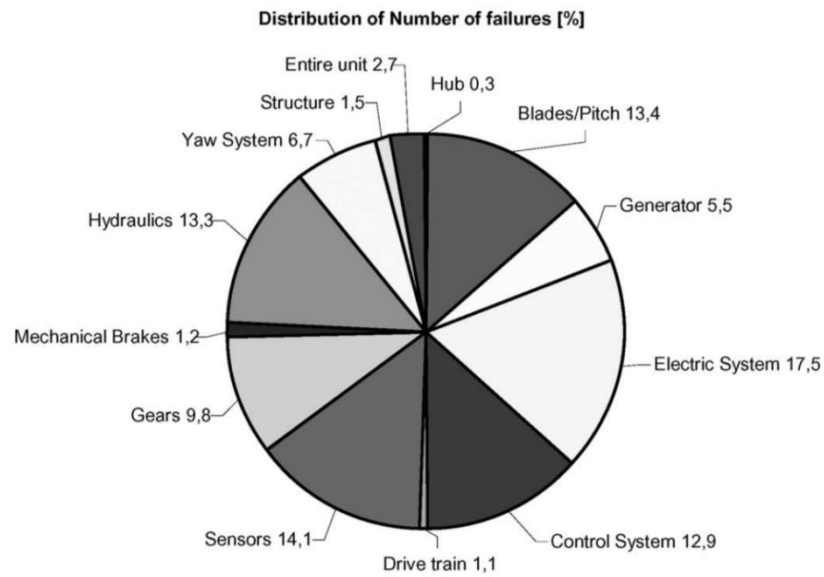


Figure 1.24 - Swedish Wind Farm Failure Rates [1.27]

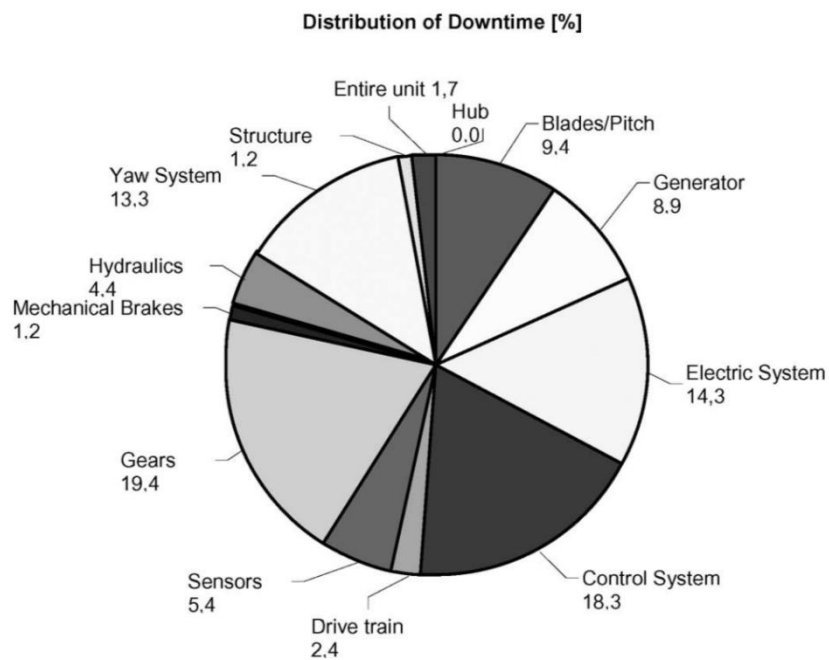


Figure 1.25 - Swedish Wind Farms Downtime Distribution [1.27]

Swedish reliability data displays generally similar findings to Faulstich. The electrical system has high frequencies of failure whereas downtime per failure is not as great, only 14.3% of overall downtime. The gearbox has a lower failure rate but due to high downtime per failure contributes the greatest overall downtime in the wind turbine (19.4%).

Chapter 1 – Project Motivation and Background

Table 1.2 shows Swedish gearbox subcomponent failure rate from the same study. More in-depth analysis of gearbox failures found that bearings are overwhelmingly the greatest cause of downtime. Failure caused by wear, B1, when separated from other failures makes up the majority of failures. The last column also reveals that wear failures are likely to cause substantially longer downtimes than average.

Table 1.2 - Swedish Gearbox Failures [1.27]

Component	Number of Failures	Average Downtime (hrs)	Number of Failures: Cause B1	Average Downtime: Cause B1
Bearings	41	562	36	601
Gear Wheels	3	272	2	379
Shaft	0	0	0	0
Sealing	8	52	4	30
Oil System	13	26	5	36
Not Specified	44	230	19	299

These reliability studies highlight the need to discover the root causes of gearbox and generator failure in order for appropriate measures to be taken in the wind turbine design phases.

Tavner [1.34] also found gearbox failures to contribute the greatest downtime of component in the wind turbine, followed by electrical systems and generators.

Failure data can be sparse when detailing exactly subcomponents that failed. For this investigation, a more in-depth study to find root causes of gearbox failures was carried out. Several wind farms across the UK were analyzed to find if previously published data correlated with data previously found. Figures 1.26 to 1.28 were taken from anonymous failure rates of wind farms across the UK, both onshore and offshore, to find correlations existed with data found in German and Scandinavian failure statistics.

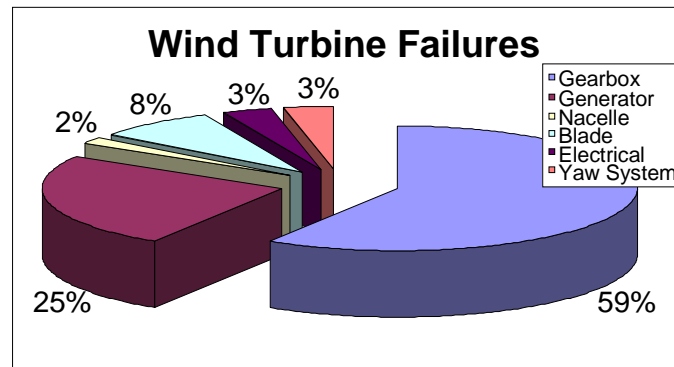


Figure 1.26 - Failure Statistics for 26 UK Wind Farms

Figure 1.26 shows the gearbox is the main contributor to the number of failures occurring in the turbine with 59% of all the turbine failures occurring. The generator accounts for 25% of failures in the turbine and is the next highest number of failures. The electrical system accounts for only a small proportion of all failures in the wind turbine. This is contrary to the German and Scandinavian failure statistics where the electrical system was by far the most frequent component to fail. In the UK statistics only 3% of all failures are attributed to electrical system faults. There may be a few reasons for the differences in failure statistics: discrepancies in reporting failures occur with electrical problems since downtimes are very short and may not be reported. Failure statistics therefore may be skewed towards faults with larger downtimes, such as gearboxes and generators. Secondly the environment the turbine experiences may cause more gearbox and generator faults whilst not particularly affecting failures of the electrical system. Overall the gearbox seems to experience a vastly greater failure rate than predicted by other studies.

Further in-depth failure statistics for gearboxes were analyzed to find if trends in subcomponents were occurring. Data available from one specific wind farm was used to find if any subcomponents are failing substantially more than other subcomponents. The gearbox used was a three stage gearbox, consisting of an initial planetary stage followed by two parallel stages.

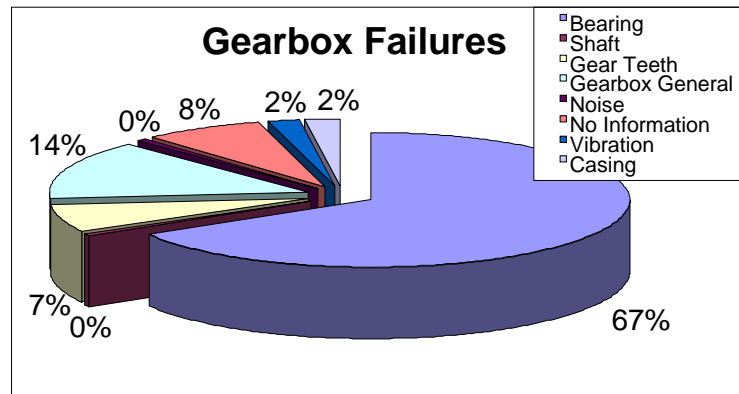


Figure 1.27 - Failures of Gearbox Subcomponents

Two thirds of gearbox failures came from bearings with the remaining failures split between gear teeth and general gearbox failures. The general gearbox failure criterion was unclear on what subcomponent had failed. It is therefore likely that these failures are a mixture of the other types of failure that have continued on to cause greater destructive damage to the rest of the gearbox with the root cause undetermined.

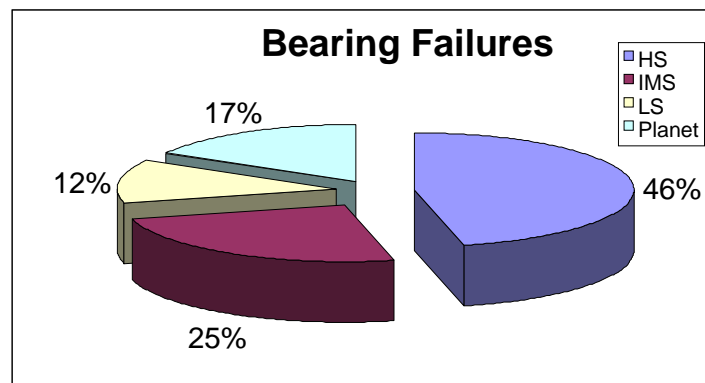


Figure 1.28 - Bearing Failures in Gearbox

Since bearings were the most common failure in the gearbox, failure data was analysed to find out which individual bearings had failed. Figure 1.28 shows high speed bearings are most problematic, accounting for 46% of all bearing failures. Intermediate bearings have the next highest failure rate followed by planetary gear bearings and low speed shaft bearings. This outcome is counter intuitive since low speed shaft and planetary gears are where higher load is transferred and therefore where most failures would be expected. A possible explanation for why high speed

shaft bearings fail so frequently is that misalignments of bearings are likely between the high speed output shaft and the input shaft of the generator. This misalignment would cause large radial forces to be applied onto the bearing, possibly in a cyclic manner, which can result in increased bearing wear. Initial studies on effects of misalignment have been presented in [1.35].

Relative downtimes of each component can be compared to find out which require the most amount of time to repair or replace. High speed bearings are the only component with an average time to repair greater than the gearbox overall average repair time, almost twice the time to repair intermediate speed bearings. The results again show interesting outcomes which may have not necessarily been expected: the high speed shaft is the output of the gearbox and therefore easier access is expected whereas intermediate speed shaft bearings are further inside the gearbox meaning access is more difficult. It would be expected that intermediate speed shaft bearings would therefore take longer to change than high speed bearings yet results show the opposite. One reason could be the output shaft is connected to the generator through a coupling which needs to be disconnected for access to high speed shaft, increasing the time required to replace the bearing.

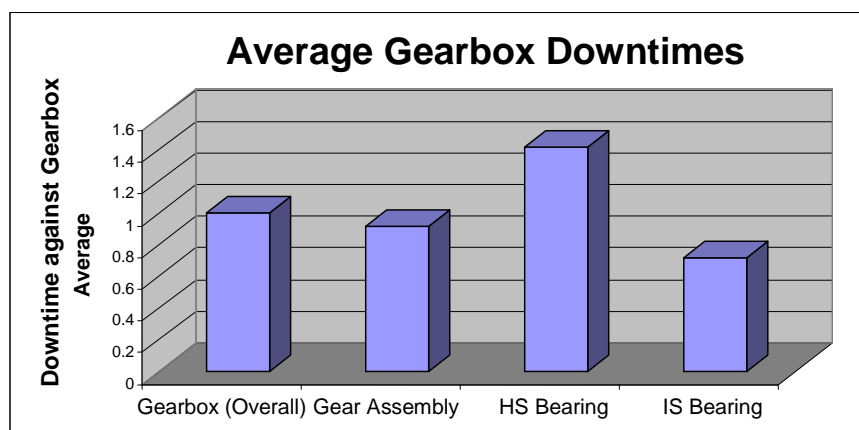


Figure 1.29 - Average Downtimes for Gearbox Repairs

Position of bearings faults can be found as well as inflicted damage on the bearing. All bearings on the low speed shaft were found to have indentations but these were not serious as none of the low speed shaft bearings were recommended for replacement by maintenance reports. High speed and intermediate speed bearings, on

Chapter 1 – Project Motivation and Background

the other hand, are where severe damage appears to occur. High speed, intermediate speed and planet bearings all show strong dependency on position of the bearing on the shaft. The output side of the shaft shows more damage highlighted in Figure 1.30 with significant number of high speed bearings experiencing spalling. Although more low speed shaft bearings have some degree of damage, it is damage to high speed shaft bearings that cause most concern.

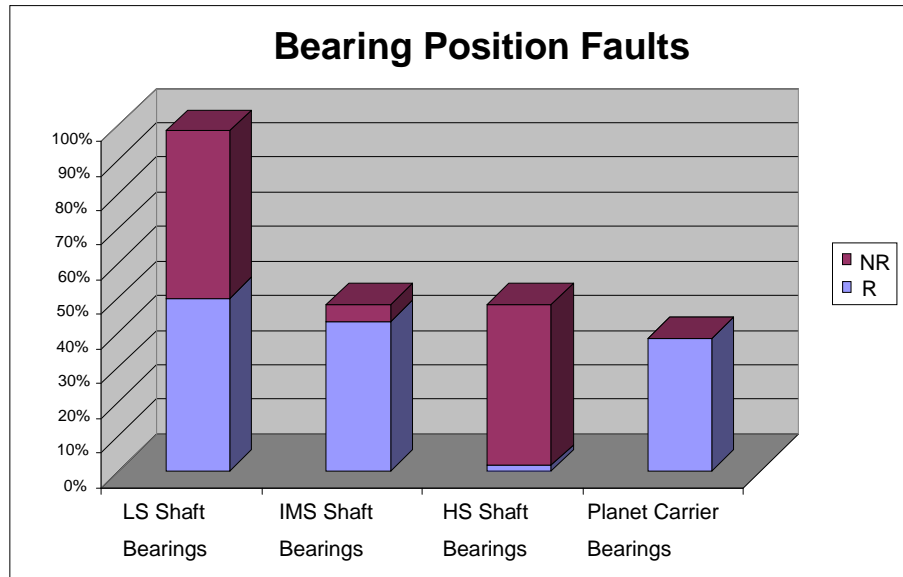


Figure 1.30 - Position of Bearing with Faults (R = Rotor Side, NR = Non Rotor Side)

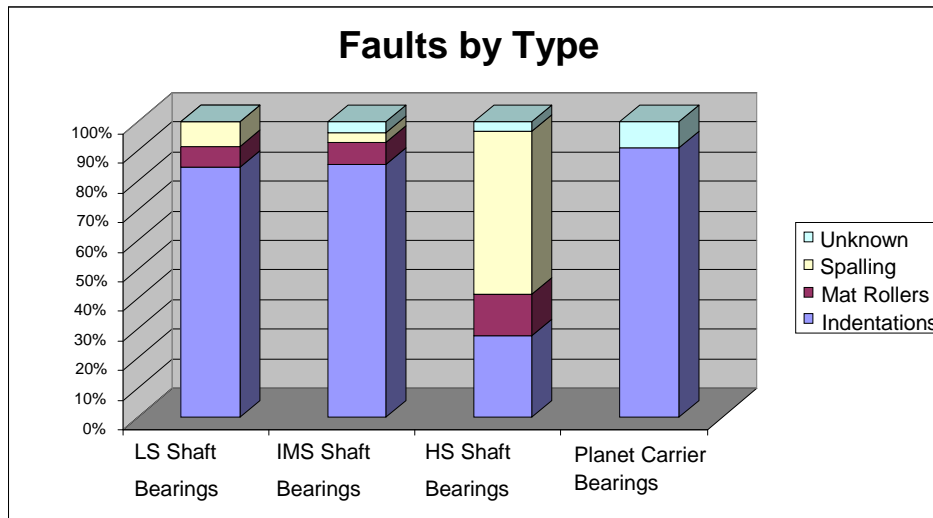


Figure 1.31 - Types of Faults on Bearings

As stated earlier, modern wind turbines are becoming increasingly large in size. With increasing size there is a trend for increasing failure rates. Tavner [1.34] showed the

Chapter 1 – Project Motivation and Background

distribution of failure rate dependent on rated power of wind turbine in Figure 1.32. If trends for turbine size are to continue to increase then the number of failures per turbine per year is also likely to increase.

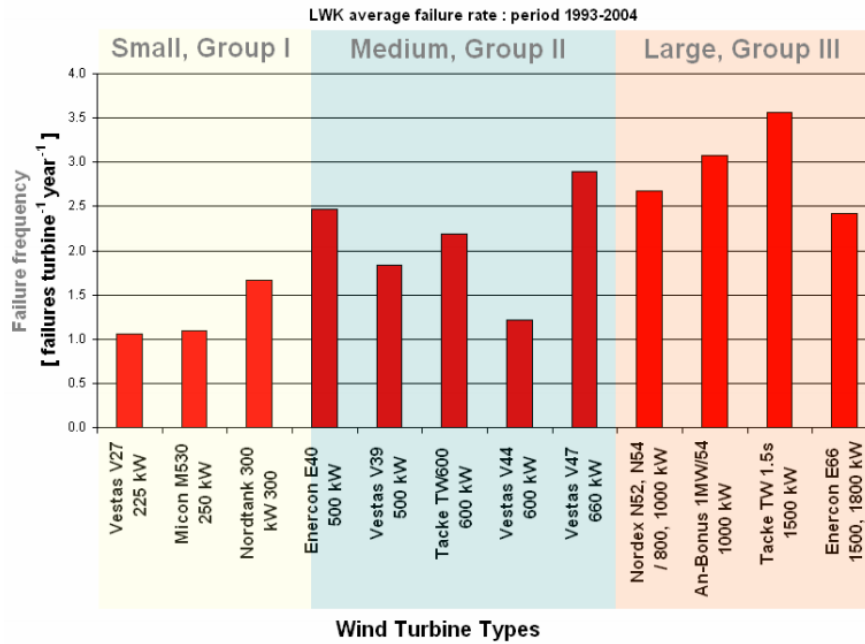


Figure 1.32 – German Wind Turbine Failure Rate against Rated Power [1.34]

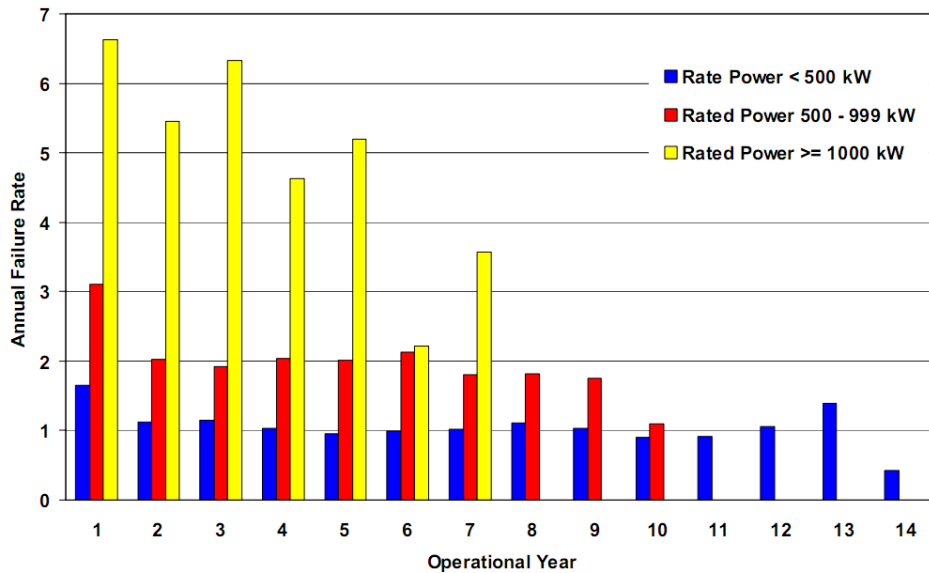


Figure 1.33 - Annual Failure for German Turbines [1.34]

Hahn, Durstewitz and Rohig [1.36] also found substantially greater failure rates for large multi-MW machines. Since new large turbines are most likely to be built

offshore, high failure rates could become a problem as it is more difficult to maintain turbines due to lack of access [1.37]. Therefore a better understanding of loads during operation is vital to reduce the frequency of failure of major components, increasing availability of the turbine. Coupled with improved design of crucial components the CoE of wind turbines should be reduced.

1.6. Failure Methods of Gears and Bearings

Gears and bearings fail in many different ways [1.38-1.39]. Understanding the mechanisms by which these components fail is important when trying to design for greater reliability. Some of the most prevalent wear mechanisms are explained in this section.

1.6.1. Macropitting

Macropitting is a contact fatigue phenomenon that occurs when a crack has formed either on or just under the surface. Under cyclical loading, the crack grows for a distance parallel to the surface each cycle before branching back to the surface. A sizeable pit on the surface remains when the dislodged material falls away.

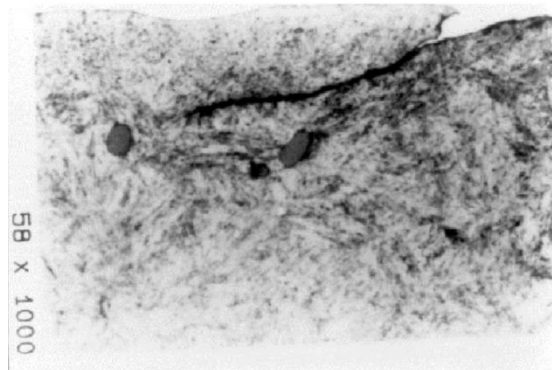


Figure 1.34 - Macropitting Crack originating from the Surface [1.38]

As macropitting covers a wide range of damage severity, subcategories are used to better describe the severity level. The four categories are non-progressive, progressive, flake and spall. Non-progressive is the mildest form and tends to remove the roughness of the surface, usually stopping when the roughness element has been worn down or removed. Pits are normally less than one mm in diameter and commonly do not grow further once created.

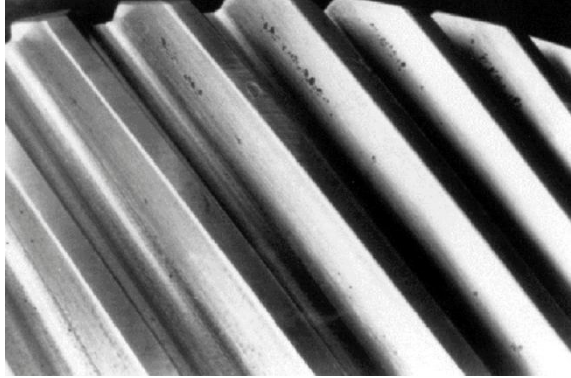


Figure 1.35 - Non-Progressive Macropitting [1.38]

Progressive pitting is the next level of severity. Here, pits have grown to a size larger than one mm and may continue to grow at an increasing rate covering the majority of the surface if cyclic loads remain.

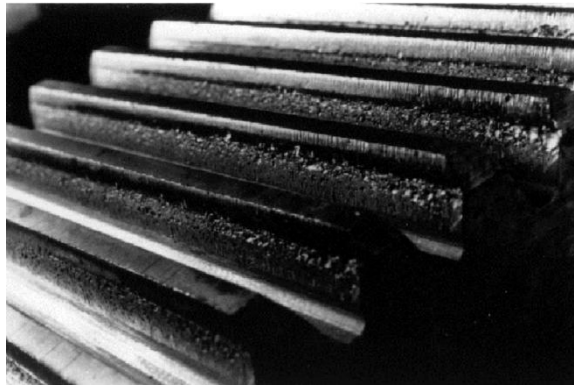


Figure 1.36 - Progressive Macropitting [1.38]

Flake pitting occurs when large shallow pits are formed. The crack initiates at the surface and spreads out in a wide triangular manner which, when it branches to the surface, causes the remaining pit to be triangular in shape.

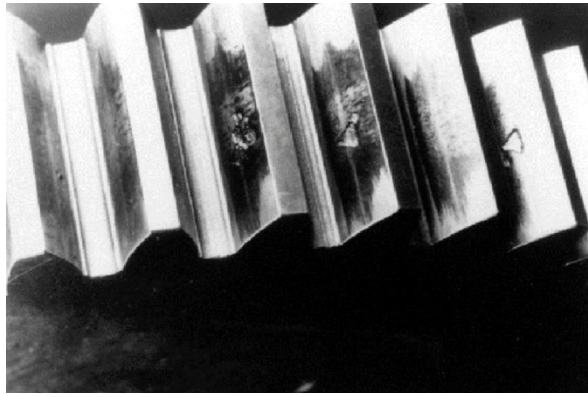


Figure 1.37 - Flake Pitting [1.38]

The most severe stage is spalling. At this stage progressive pitting has become so bad that pits combine creating a very irregular surface affecting contact between gear teeth. Material wear is significantly accelerated and this very progressive form of macropitting can cover large areas of the surface.

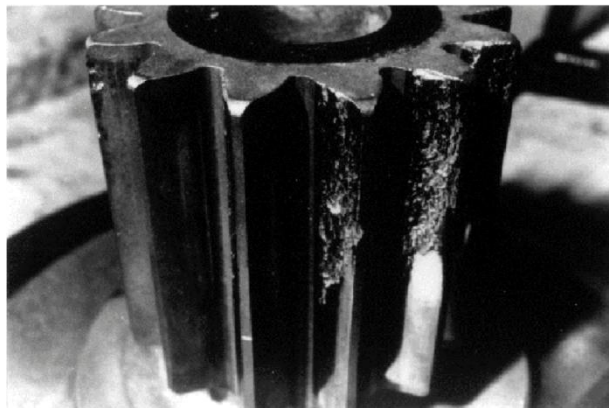


Figure 1.38 - Spalling [1.38]

1.6.2. Micropitting

Micropitting occurs when extremely small pits form on the surface giving a frosted, matt or grey stained appearance. The difference between micropitting and macropitting is the size of the pits created. Generally micropitting is not severe and often improves contact by removing surface asperities, but if pits join together to form macro scale pits, it may become a problem. This most commonly occurs when the gear or bearing has been surface hardened and can occur across any part of the gear profile or bearing.

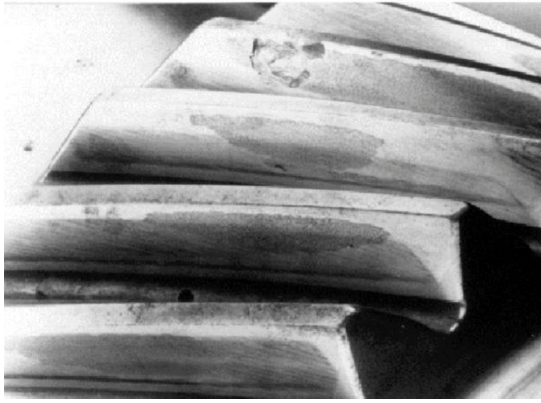


Figure 1.39- Micropitting [1.38]

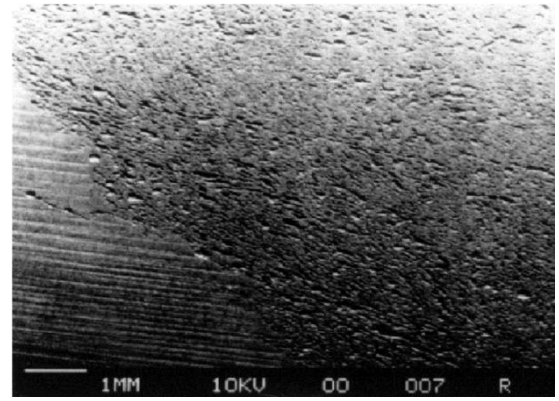


Figure 1.40 - Gear Tooth Surface undergoing Micropitting [1.38]

1.6.3. Root Bending Moment Cracks



Figure 1.41 - Crack at Root of Tooth Due to Bending Moments [1.38]

Fatigue cracks are almost always at the root of the tooth where bending moments are greatest. The crack originates from this point acting as a stress raiser at the join between the tooth and the rim further increasing nominal stress.

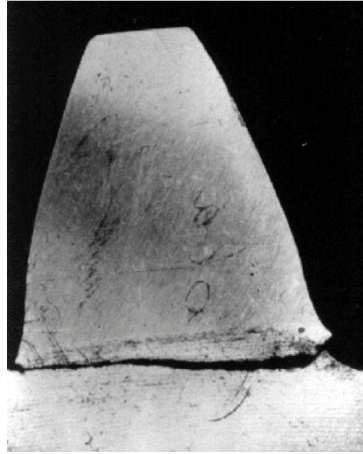


Figure 1.42 - Sheared Gear Tooth [1.38]

In some cases a large shear force can cause the tooth to shear completely away. Cases like this are almost always caused by a single severe overload rather than crack growth through fatigue loading.

1.7. Drivetrain Modelling

Drivetrain modelling is crucial if root causes of drivetrain and gearbox failure are to be found. The difficulty with modelling drivetrains is a wide range of load frequencies are applied. Since rotating machinery components are present, large rotations relative to other components occur. Drivetrain modelling packages must be able to cope with movements of multiple masses along with flexibility in shafts and support structures. Mathematical models and multibody analysis can be used to find natural frequencies of the drivetrain and therefore transient response. Finite element representations of the structures can be created for individual components to show responses to applied loads.

1.7.1. Multibody Models

Multibody analysis is a useful method for analysing dynamic problems. Origins of this method are from Newton and d'Alembert as explained in [1.40].

Most drivetrain and gearbox dynamic modelling has been done using the multibody technique. Shabana [1.41] has created a review of past and recent developments occurring in the field of flexible multibody dynamics. Multibody analysis is an

Chapter 1 – Project Motivation and Background

effective way to model transmitted forces through the drivetrain. In a purely torsional model, stiffness is assigned between each body and when an external force is applied system dynamics can be observed. This could be a useful method as it is able to represent dynamic forces occurring between the gears as well as hub outputs and generator inputs.

Shabana [1.42] describes multibody systems as rigid or deformable bodies that can undergo large deformations. Wang [1.43] describes how this method can be used to describe nonlinear systems for flexible bodies showing how objects such as beams can be described using the flexible multibody approach.

Peeters [1.44-1.47] used three different models for evaluation: a purely torsional model, a rigid multibody model with discrete flexible elements and a fully flexible model (finite element model). The purely torsional models only takes into account the torsional degree of freedom (DOF) neglecting all other DOF's. In this case flexible elements are placed between mating gear teeth as shown in Figure 1.43 to represent the contact flexibility between gear teeth. At the other end of the spectrum the full finite element model includes distortions of gears but it is extremely computationally heavy and still may not calculate accurate results. Rigid multibody with discrete flexible elements is midway between the two other techniques. Gears are not modelled as finite elements but rigid elements connected through linear springs. Each gear has 6 DOF therefore is able to translate and rotate in any direction with appropriate stiffness constraining motion.

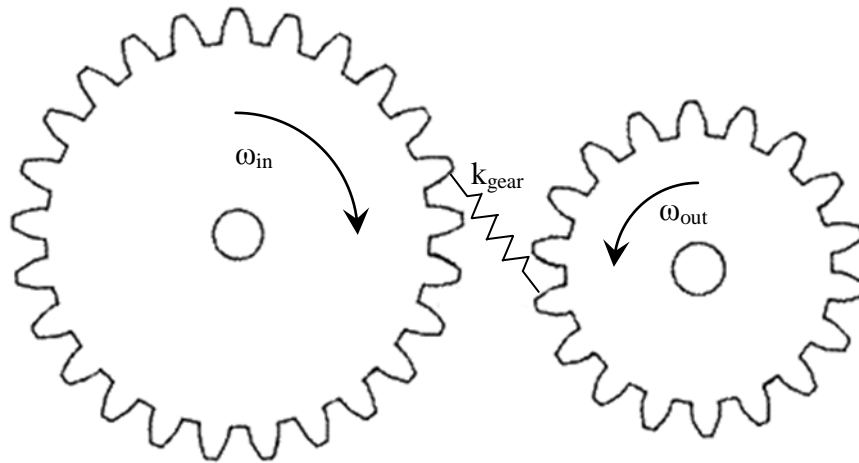


Figure 1.43 - Torsional DOF Mating Gear Teeth

What Peeters does not take into account is misalignment of gears and shafts when a torque is applied. Bearing stiffness plays a vital role in alignment of shafts and fatiguing of the drivetrain components. Multibody analysis is suitable for finding natural frequencies of the drivetrain.

Schlecht [1.48] used the multibody simulation package SIMPACK to model forces, find eigenvalues and study fatigue of the drivetrain. Input loads to the system are simulated using wind turbine dynamics package Flex4. SIMPACK models the drivetrain as a series of linear springs connected by masses. This model has 2 DOF: in the torsional direction of the rotating shafts and in the axial direction. The axial force allows internal reactions to be calculated within the gearbox from the applied wind loads.

Natural frequencies in the axial and rotational directions can be calculated but all other DOFs are neglected. Applying transient loads from Flex4 to the drivetrain model allows transient loading on bearings to be found in the axial direction. The drawbacks of a simplified model are that other DOFs are ignored and fundamental loading on the drivetrain during transient events are therefore likely to be missed. Effects from other parts of the turbine such as tower motion and drivetrain flexibility will not be captured which may contribute to increased loading on drivetrain bearings. Schlecht also suggests fatigue methods that could be used to discover how different loads affect fatigue life of the drivetrain.

Chapter 1 – Project Motivation and Background

Heege [1.49-1.51] models a complete wind turbine using a mixture of finite elements and multibody analysis. The gearbox is a 3 stage high speed, two planetary and one parallel, represented using the multibody analysis method. Blades are modelled using finite elements reduced to super elements¹ with blade loading calculated using blade element momentum theory [1.24]. Computational time is reduced by modelling all the shafts as nonlinear beam elements, the gearbox housing and planet carriers as solid elements reduced to super elements. Heege also ties these models to fatigue life calculations using Wohler curves to characterise the fatigue life. It is unclear how complex the gearbox model is and with no suggestion of bearing loading in the drivetrain. Effects of drivetrain components flexibility on loading of bearings and gear contacts is not dealt with. In addition it is unclear what wind loading is applied to the turbine and whether this is realistic. Heege also attempts to estimate the damage of rotor and gearbox bearings using Wohler curves and Miner's Rule. Although these can be used to estimate high cycle fatigue life, with such short cycle numbers during transient events these models are unlikely to adequately represent what is occurring. Wohler curves are well known not to represent low cycle fatigue well [1.52]; curves such as Manson-Coffin are better suited for this methodology. L10 bearing lifetime curves are also available for better representations of bearing lifetimes although these are suited to high cycle fatigue prediction.

Helsen [1.53-1.55] created a multibody representation of a 13.2MW drivetrain and was able to compare it to a test rig. Although larger than any current wind turbine this is useful for testing drivetrains at much higher power ratings and finding how these models scale. Multibody analysis coupled with finite element modelling of certain components is used find natural frequencies of the drivetrain. Focus on flexibility and transient behaviour of the first stage planet carrier show this might have an impact of loading within the gearbox. Despite analysis of flexibility in these components the effects of flexibility on modes were studied but not how alignments of other components were affected in the gearbox and whole drivetrain.

¹ See page 67 for definition of superelements

Lacava [1.56] compared multibody models to experimental results of the NREL test rig studying the loading on the first stage planetary stage for varying degrees of model fidelity.

1.7.2. Mathematical Models

Oh [1.57] derived equations of motion for gears using the assumption that gears conserve energy, which in the case of heavily loaded gears is true. Contact between gears is modelled as stiffness elements with changing properties. As gears mesh, one or two gear teeth pairs can be in contact meaning a cyclic stiffness property. The harmonic that this cyclic stiffness introduces is captured in the torsional models.

Todorov [1.58-1.59] combines aerodynamic rotor loading, dynamic gearbox modelling and generator reaction torque. Aerodynamic loads are produced from look up tables using calculated wind flows across the aerofoil. Induction machine equations are used to represent generator loading. The drivetrain model is a series of stiffness connections between masses therefore dynamics are found through stiffness and mass matrices. Varying stiffness in contact between gears is also used to show effects on the whole system dynamics.

Wang [1.60] created a model similar to Todorov with lumped masses connected through flexible elements. A simplified model of the rotor and generator are used to apply external loads to the drivetrain model though an extra DOF is included for stiffness of bearings meaning vertical alignments of shafts are taken into consideration. Shafts are modelled as simply supported beams on stiffness elements. The shafts themselves are rigid and do not deform so trigonometry can be used to find positions of shafts. Movement of the shafts causes changes in contact force between gears and therefore affects transmitted power. Lagrangian dynamics is used to find the equations of motion for the drivetrain resulting in a 61x61 matrix for a 3 stage gearbox. The outputs from the model showed natural frequencies of off axis loading of gears and shafts that would have been missed otherwise. Despite movement of shafts being modelled, alignment issues such as skewing of gears are not taken into consideration.

1.7.3. Finite Element Models

Xing [1.61], using the NREL test rig, performed analysis on the flexibility of the first stage planet carrier showing effects of the model sophistication and showing effects on the importance of including components such as planet pins when analysing the dynamics.

Coultate [1.62] using a coupled finite element model with a multibody drivetrain model. Gearbox housings and planet carriers were modelled as finite elements so that the effects of distortion can be modelled. The model was created in RomaxWIND, in-house software used by Romax Technology. Loading on bearings and gear contact was seen to change as the intricacy of the models was improved. Predicted lifetime of the gear also changed dramatically as model flexibility was introduced, highlighting the importance of accurately predicting flexibility within the gearbox.

1.7.4. Drivetrain Test Rigs

NREL Gearbox Reliability Collaborative (GRC) has achieved very interesting work with a 750kW wind turbine drivetrain that has been implemented in a wind turbine and now mounted on a test rig [1.63]. Highly instrumented tests on the gearbox have been carried out along side modelling analysis for several group members for comparison.

1.8. Alternative Drivetrain Technologies

Poore [1.20] compared different drivetrain configurations in a cost of energy analysis, shown earlier in the reliability section. Multiple generator drivetrains (both induction and PMG's), the Henderson drivetrain, the Klatt drivetrain and the Heller-DeJulio drivetrain were compared. Multiple generator drivetrains have gearboxes with multiple outputs, in this case six, connected to individual generators. The advantages are lower component cost and higher energy production. The other three drivetrains all turned out to have higher cost of energy than the original three stage gearbox with induction generator. A cost comparison between the designs is shown in Figure 1.18.

Magnetic gearing is a proposed alternative method to step up rotational speed of the rotor for use in high speed generators [1.64-1.66]. The idea of using a magnetic gearbox in wind turbines has been explored in [1.67-1.68]. The rotational speed is stepped up using a ratio of pole pairs between the two sides of the gearing. Expected advantages of magnetic gears is less acoustic noise, reduced maintenance with improved reliability, physical isolation between input and output.

Hydraulic gearboxes have also been researched and prototypes created by Artemis [1.69]. Instead of a mechanical gearbox connecting the rotor to the generator a hydraulic system connects the two. A specialised pump pressurises the fluid using input power from the rotor; a digital displacement motor [1.70] converts back to kinetic energy to use in the generator.

Voith have created WinDrive [1.71] a novel concept using hydraulics to produce a constant output power thus removing the need for power conversion electronics. A hydraulic circuit filled with oil takes some of the power from the output shaft and uses it to rotate the ring gears so that the power output is constant. The claimed advantages of this system are that it reduces wear on the drive system and therefore extends lifetime by up to 12% [1.72]. Since power electronics are not required, failure rate of the turbine improves by a predicted 19%.

1.9. Fatigue Predictions

Fatigue prediction of components in the drivetrain is an extremely difficult task. With many different flexible components all in motion, accurately being able to predict fatigue or failure when load and stress predictions are uncertain is difficult and unreliable.

Palmgren [1.73] and Miner [1.74] proposed the initial idea of a relationship between the number of cycles a component experiences to its overall damage. This allows prediction of remaining life of a component after it has undergone a known amount of previous loading.

Shigley [1.52] describes general fatigue prediction methods. The most commonly used fatigue prediction is Wöhler or S-N curves coupled with Miner's Rule [1.74].

Measured stress ranges and numbers of cycles (m) are compared with S-N curves (n) to estimate expended lifetime. The number of cycles experienced can be divided with the number of cycles to failure giving a percentage of damage. For numerous stress ranges, the damage is added to find the total damage on the material. This method is the least accurate method and especially poor when applied to low cycle fatigue situations.

These ideas have been further taken to include other linear theories and also non linear theories developed by Fatemi [1.75] and Hweng [1.76].

Strain life methods are more suited to low cycle fatigue problems. Manson [1.77] and Coffin [1.78] produced an equation to describe how low cycle fatigue is related to number of cycles. This relates total strain of the material to number of cycles at a strain range. The Manson-Coffin equation includes elastic deformations of the material but also takes into account plastic deformations of the material and how this affects design life. The Manson-Coffin equation can then be used with Miner's Rule to find damage to the material. The Basquin equation [1.79] refined to give a simple relation between total strain and number of cycles giving rise to the Manson-Coffin-Basquin equation.

$$\frac{\Delta\epsilon_t}{2} = \frac{\Delta\epsilon_e}{2} + \frac{\Delta\epsilon_p}{2} = \frac{\sigma'_f}{E} (2N_f)^b + \epsilon'_f (2N_f)^c \quad (1.1)$$

Ramberg and Osgood [1.80] created equations relating stress and strain to constant amplitude loading. Combined with the Manson-Coffin-Basquin equation it is possible to relate stress, strain and number of cycles of a material.

$$\epsilon = \frac{\sigma}{E} + \left(\frac{\sigma}{K}\right)^{\frac{1}{n'}} \quad (1.2)$$

A problem with strain life equations is that strain data is difficult to measure whereas stress life data is simpler to attain. Niesłony [1.81] combined the Manson-Coffin-Basquin equation with the Ramberg-Osgood equation. Combining the two equations allows use of the Manson-Coffin-Basquin when stress data is available.

Plumtree [1.82], Berrego [1.83] and Skelton [1.84] all used the Ramberg-Osgood equation for low cycle fatigue of material when a cyclic loading is applied to them.

Further clarifications of the methods can be found in the ESDU standards along with experimental results for the constants in the equations [1.85-1.87].

Szusta [1.88] and Seweryn [1.89] have published papers relating to the damage accumulation of low cycle fatigue. The papers describe how materials fail in the low cycle fatigue where the failures are due to the initiation of a single crack that grows to cause failure. This differs from high cycle fatigue as multiple cracks join to cause failure.

Murakami [1.90] studies whether or not previous fatigue damage to the component will be a factor. The results showed that in the low cycle regime if the component is likely to fail it is due to the growth of a single surface crack and not the combination of multiple cracks. Prior history has no effect on the damage history of the component and the surface ductility changes as the component is subject to varying stresses.

1.9.1. Energy Methods

Strain energy dissipated in each stress cycle can be compared to the total energy before failure occurs. Neuber's Rule was the first to use strain energy to calculate the fatigue of a material but this model tends to underestimate the energy lost due to strain energy. Molski and Glinka [1.91] proposed an alternative method of calculating the fatigue properties.

Li [1.92] tests the compatibility of the strain energy equations for use in low cycle fatigue problems based on the work of Morrow [1.93] and Halford [1.94]. The work confirms, with experimental data, the effectiveness of using this method as a valid method of fatigue analysis.

Raji [1.95] tackles the problem of low cycle fatigue in floating production storage and offloading units. Three methods for calculating the local stresses and strains are the elasto-plastic finite element method, Neuber's Rule and Glinka's strain energy density method.

1.9.2. Bearing Damage

The basis for bearing stress and fatigue was researched by Palmgren [1.73, 1.96] where the idea of the L10 lifetime was proposed. The service life of bearings for a prescribed load was predicted where 10% of bearings are expected to fail. The Lundberg-Palmgren theory [1.97] predicted the subsurface stresses in the bearing assuming Hertzian contact.

$$L_{10} = \left(\frac{C_D}{P_{eq}} \right)^p \quad (1.3)$$

The L10 lifetime is a relationship between the dynamic capacity of the bearing, C_D , and the equivalent radial load. P is the load-life exponent, for ball bearings this is 3.

Further work on the L10 life prediction was done by Zaretsky [1.98-1.100]. This work showed that Palmgren's equations were too conservative and suggested bearing manufacturers used their own constants in the lifetime relationships. These equations were again for high cycle fatigue problems and struggle to accurately predict failure at lower numbers of stress cycles.

1.9.3. Rainflow Counting

When data for measured components is viewed, stress and strain outputs contain a great deal of harmonic information. If fatigue processing of this information is to be done, the information needs to be suitably split into stress ranges with numbers of cycles experienced. In addition simple counting of peaks does not identify all present frequencies since underlying frequencies cannot be picked up. Rainflow counting is a method used to identify frequencies present in a time series.

Matsuishi and Endo [1.101] were first to propose the concept of rainflow counting for analyzing complex variable loading stress time histories. This cycle counting method gave a simple output that could be used with fatigue analysis techniques. The technique was then taken further by Downing and Socie [1.102] and applied by Niesłony [1.103].

Polak [1.104] describes how rainflow analysis can be used effectively for low cycle fatigue with variable loading. The paper also suggests that the fatigue life of a

specimen is subject to variable amplitude loading can be predicted from constant amplitude data as the two responses approximately each other very well. Both of these data sets also have very good agreement with experimental data.

1.10. Project Plan

From the studies shown in this chapter, the gearbox has been identified as the highest contributor to total downtime highlighting the unusually high failure rates of the high speed bearings. Current modelling techniques do not show that these bearings are of importance and should easily last the required lifetime [1.105]. This project will study how the modelling techniques and show they may not be adequate when attempting to capture loading on high speed bearings.

Chapter 2 uses current state of the art modelling software package, RomaxWIND, to extend an example 2MW gearbox model, provided by Romax Technology, out to include a model of the whole drivetrain. A drivetrain was designed and modelled using the example 2MW gearbox to show how the alignments between the gearbox and generator can be examined and how the stiffness of certain key components affect bearing loading that would otherwise have been missed. Results show the stiffness of the bedplate, the gearbox mounts and the flexible coupling affect alignment between the gearbox and generator and therefore loading on high speed bearings. These results suggest that if the gearbox and generator move, high speed bearing loading sensitivity is seen which could be especially noticeable during extreme transient events. RomaxWIND models the drivetrain statically which does not take into account effects of transient loading. The added knowledge this chapter brings is how the whole drivetrain responds to input conditions and how certain parameters affect loading on high speed bearings.

Chapter 3 goes onto explore what loads are created during extreme transient events using GH Bladed and how certain parameters affect loads created on the drivetrain. Knowledge of how parameters affect loading on wind turbines during grid loss emergency stop is gained and transient loading on the wind turbine is obtained for use in the next chapters.

Chapter 1 – Project Motivation and Background

Chapter 4 then uses these transient loads created on the wind turbine and compares the deflections from a static RomaxWIND drivetrain model to a transient structural model in ANSYS Transient of the drivetrain. Results from Chapter 2 show that internal gearbox bearings are not affected by misalignments between gearbox and generator so internal complexity of the gearbox does not need to be included in the model. Deflections at key points on the drivetrain are compared, showing how the effects of the mode shapes of the bedplate cause increased drivetrain distortion with the resultant bearings loads highlighting this difference. Knowledge gained here shows that for high speed bearings, transient effects of the whole drivetrain structure are required to be modelled if the most damaging loads on these high speed bearings are to be found.

Chapter 5 explores the relatively new concept of the medium speed drivetrain and compares to the high speed drivetrain. Comparisons between these two drivetrains for transient cases show the medium speed drivetrains has lower inertia and therefore faster responses to loading. A similar comparison studying the structural deflections is also done comparing the cantilevered design of the medium speed drivetrain to the traditional design. Knowledge added here was the initial work in the response of the medium speed to transient conditions. The structural response also shows that the cantilevered design removes all loading sensitivity problems previously associated with high speed bearings.

Chapter 1 References

- [1.1] UNFCCC. (2013, *Kyoto Protocol*. Available:
http://unfccc.int/kyoto_protocol/items/2830.php
- [1.2] "National Renewable Energy Action Plans," European Commission 2013.
- [1.3] "Forecast by Member States," European Commission 2013.
- [1.4] DECC, "UK Renewable Energy Roadmap," ed, 2011.

Chapter 1 – Project Motivation and Background

- [1.5] T. J. Price, "James Blyth - Britain's first modern wind power pioneer," *Wind Engineering*, vol. 29, pp. 190 -200, 2005.
- [1.6] Tvindkraft. 2013, *Tvindkraft- pioneer and veteran*. Available: <http://www.tvindkraft.dk/>
- [1.7] Siemens. 2013. Available: <http://www.energy.siemens.com/hq/en/renewable-energy/wind-power/>
- [1.8] Vestas. 2013. Available: <http://www.vestas.com/>
- [1.9] Enercon. 2013. Available: <http://www.enercon.de/de-de/>
- [1.10] M. I. Blanco, "The economics of wind energy," *Renewable and Sustainable Energy Reviews*, vol. 13, pp. 1372-1382, 2009.
- [1.11] E. Hau, "Mechanical Drive Train and Nacelle," in *Wind Turbines*, ed: Springer, 2013, pp. 305-383.
- [1.12] P. N. Saavedra and D. E. Ramirez, "Vibration Analysis of Rotors for the Identification of Shaft Misalignments Part 1: Theoretical Analysis," *Proceedings of the Institute of Mechanical Engineers Part C - Journal Of Mechanical Engineering Science*, vol. 218, pp. 971-985, 2004.
- [1.13] P. N. Saavedra and D. E. Ramirez, "Vibration Analysis of Rotors for the Identification of Shaft Misalignments Part 2: Experimental Validation," *Proceedings of the Institute of Mechanical Engineers Part C - Journal Of Mechanical Engineering Science*, vol. 218, pp. 987 - 999, 2004.
- [1.14] M. Haastrup, *et al.*, "Modeling of Wind Turbine Gearbox Mounting," *Modeling, Identification and Control*, vol. 32, pp. 141-149, 2011.
- [1.15] E. Echavarria, *et al.*, "Reliability of wind turbine technology through time," *Journal of solar energy engineering*, vol. 130, p. 31005, 2008.
- [1.16] D. McMillan and G. Ault, "Techo-Economic Comparison of Operational Aspects for Direct Drive and Gearbox-Driven Wind Turbines," *IEEE Transactions of Energy Conversion*, vol. 25, March 2010 2010.

Chapter 1 – Project Motivation and Background

- [1.17] S. Schmidt, *et al.*, "Comparison of Existing Medium-speed Drive Train Concepts with a Differential Gearbox Approach," in *EWEA*, Copenhagen, Denmark, 2012.
- [1.18] A. Crowther, *et al.*, "Technology Trends and Design Approaches for Wind Turbine Drivetrains," presented at the 8th IFToMM International Conference on Rotordynamics, Seoul, South Korea, 2010.
- [1.19] H. Polinder, *et al.*, "Comparison of Direct Drive and Geared Generator Concepts for Wind Turbines," *IEEE Transactions of Energy Conversion*, vol. 21, September 2006 2006.
- [1.20] R. Poore and T. Lettenmaier, "Alternative Design Study Report: WindPACT Advanced Wind Turbine Drive Train Designs Study; November 1, 2000--February 28, 2002," National Renewable Energy Laboratory (NREL), Golden, CO.2003.
- [1.21] C. Halse, "Wind Turbine Drivetrain Development," 2012.
- [1.22] O. Anaya-Lara, *et al.*, *Wind Energy Generation Modelling and Control*: Wiley, 2009.
- [1.23] N. D. Caliao, "Dynamic modelling and control of fully rated converter wind turbines," *Renewable Energy*, vol. 36, pp. 2287-2297, 2011.
- [1.24] S. Burton, Jenkins, Bossanyi, *Wind Energy Handbook*, 2001.
- [1.25] I. Lavassas, *et al.*, "Analysis and design of the prototype of a steel 1-MW wind turbine tower," *Engineering Structure*, vol. 25, pp. 1097-1106, 2003.
- [1.26] J. Ribrant, "Reliability performance and maintenace - A survey of failures in wind power systems," KTH School of Electrical Engineering, 2006.
- [1.27] J. Ribrant and L. M. Berting, "Survey of Failures in Wind Power Systems With Focus on Swedish Wind Power Plants During 1997-2005," *IEEE Transactions of Energy Conversion*, vol. 22, pp. 167-173, 2007.

Chapter 1 – Project Motivation and Background

- [1.28] S. Faulstich and B. Hahn, "Comparison of different wind turbine concepts due to their effects on reliability," *UpWind Deliverable*, vol. 7, 2009.
- [1.29] S. Faulstich, *et al.*, "Component Reliability Ranking with Respect to WT Concept and External Environmental Conditions," 2010.
- [1.30] P. Tavner, *et al.*, "Reliability Analysis for Wind Turbines," *Wind Energy*, vol. 10, pp. 1 - 18, July 2002 2007.
- [1.31] F. Spinato, *et al.*, "Reliability of Wind Turbine Assemblies," *IET Renewable Power Generation*, vol. 3, pp. 387-401, 2009.
- [1.32] K. Smolders, *et al.*, "Reliability Analysis and Prediction of Wind Turbines," presented at the European Wind Energy Conference (EWEC 2010), Warsaw, Poland, 2010.
- [1.33] A. Faulstich and B. Hahn, "Comparison of different wind turbine concepts due to their effects on reliability," 2009.
- [1.34] P. Tavner, *et al.*, "Reliability of different wind turbine concepts with relevance to offshore application," in *European Wind Energy Conference & Exhibition*, 2008, pp. 166-170.
- [1.35] M. Whittle, *et al.*, "A Parametric Study of the Effect of Generator Misalignment on Bearing Fatigue Life in Wind Turbines," presented at the EWEA 2011, Brussels, 2011.
- [1.36] B. Hahn, *et al.*, "Reliability of Wind Turbines, Experience of 15 years with 1,500 WT's," Institut fur Solare Energieversorgungstechnik (ISET).
- [1.37] I. Dinwoodie and D. McMillan, "Heavy Lift Vessel Strategy for Offshore Wind," in *EWEA 2013*, Vienna, Austria, 2013.
- [1.38] AGMA, "Appearance of Gear Teeth - Terminology of Wear and Failure," vol. ANSI/AGMA1010--E95, ed. Alexandria, Virginia, USA: American Gear Manufacturers Association, 1995.

Chapter 1 – Project Motivation and Background

- [1.39] "Mechanisms of Gear Tooth Failures, AGMA 912-A04," American Gear Manufacturers Association 2004.
- [1.40] W. Schiehlen, "Multibody system dynamics: roots and perspectives," *Multibody System Dynamics*, vol. 1, pp. 149-188, 1997.
- [1.41] A. Shabana, "Flexible Multibody Dynamics: Review of Past and Recent Developments," *Multibody System Dynamics*, vol. 1, pp. 189 - 222, 1997.
- [1.42] A. A. Shabana, *Dynamics of multibody systems*: Cambridge University Press, 2005.
- [1.43] Y. Wang and R. L. Huston, "A Lumped Parameter Method in the Nonlinear Analysis of Flexible Multibody Systems," *Computers & Structures*, vol. 50, pp. 421-432, 1992.
- [1.44] J. Peeters, *et al.*, "Flexible Multibody Model of a Three-Stage Planetary Gearbox in a Wind Turbine," presented at the International Conference on Noise and Vibration Engineering, Leuven, Belgium, 2004.
- [1.45] J. Peeters, *et al.*, "Structural Analysis of a Wind Turbine and its Drive Train Using the Flexible Multibody Simulation Technique," 2006.
- [1.46] J. Peeters, "Simulation of Dynamic Drive Train Loads in a Wind Turbine," University of Leuven, 2006.
- [1.47] J. Peeters, *et al.*, "Analysis of Internal Drive Train Dynamics in a Wind Turbine," *Wind Energy*, vol. 9, pp. 141-161, 2006.
- [1.48] B. Schlecht and S. Gutt, "Multibody-System-Simulation of Drive Trains of Wind Turbines," presented at the Fifth World Congress on Computational Mechanics, Vienna, Austria, 2002.
- [1.49] A. Heege, *et al.* (2006) Fatigue Load Computation of Wind Turbine Gearboxes by Coupled Structural, Mechanism and Aerodynamic Analysis. *DEWI Magazin*.

- [1.50] A. Heege, *et al.* (2003) Computation of Dynamic Load of Wind Turbine Power Trains. *DEWI Magazin*. 59-64.
- [1.51] A. Heege, "Quantification of Wind Turbine Gearbox Loads by Coupled Structural and Mechanisim Analysis," in *7th German Wind Energy Conference DEWEK*, Germany, 2004.
- [1.52] J. Shigley, *et al.*, *Mechanical Engineering Design*, 8th ed., 2008.
- [1.53] J. Helsen, *et al.*, "The influence of flexibility within multibody modeling of multi-megawatt wind turbine gearboxes," in *ISMA international conference on noise & vibration engineering*, 2008, pp. 2045-71.
- [1.54] J. Helsen, *et al.*, "Insights in wind turbine drive train dynamics gathered by validating advanced models on a newly developed 13.2 MW dynamically controlled test-rig," *Mechatronics*, vol. 21, pp. 737-752, 2011.
- [1.55] J. Helsen, *et al.*, "Multibody modelling of varying complexity for modal behaviour analysis of wind turbine gearboxes," *Renewable Energy*, vol. 36, pp. 3098-3113, 2011.
- [1.56] W. LaCava, *et al.*, "Three-dimensional bearing load share behaviour in the planetary stage of a wind turbine gearbox," *IET Renewable Power Generation*, vol. 7, pp. 359-369, 2013.
- [1.57] S. Oh, *et al.*, "Energy Conserving Equations of Motion for Gear Systems," *Journal of Vibration and Acoustics*, vol. 127, pp. 208 - 212, 2005.
- [1.58] M. Todorov, *et al.*, "Analysis of Torsional Oscillation of the Drive Train in Horizontal-Axis Wind Turbine," presented at the Electromotion 2009 - EPE Chapter 'Electric Drive' Joint Symposium, Lille, France, 2009.
- [1.59] M. Todorov and G. Vukov, "Parametric Torsional Vibrations of a Drive Train in Horizontal Axis Wind Turbine," presented at the 1ere Conference Franco-Syrienne sur le energies renouvelables, Damascus, Syria, 2010.

- [1.60] J. Wang, *et al.*, "Dynamic Behavior of Wind Turbine by a Mixed Flexible-Rigid Multi-Body Model," *Journal of System Design and Dynamics*, vol. 3, 2009.
- [1.61] Y. Xing and T. Moan, "Multi-body modelling and analysis of a planet carrier in a wind turbine gearbox," *Wind Energy*, 2012.
- [1.62] J. Coultate, *et al.*, "The Impact of Gearbox Housing and Planet Carrier Flexibility on Wind Turbine Gearbox Durability," in *EWEA 2009*, Marseille, France, 2009.
- [1.63] NREL. (2013, *Gearbox Reliability Collaborative*.
- [1.64] L. Jian, *et al.*, "Comparison of coaxial magnetic gears with different topologies," *Magnetics, IEEE Transactions on*, vol. 45, pp. 4526-4529, 2009.
- [1.65] E. Furlani, "A two-dimensional analysis for the coupling of magnetic gears," *Magnetics, IEEE Transactions on*, vol. 33, pp. 2317-2321, 1997.
- [1.66] K. Atallah, *et al.*, "Design, analysis and realisation of a high-performance magnetic gear," in *Electric Power Applications, IEE Proceedings-*, 2004, pp. 135-143.
- [1.67] L. Jian, *et al.*, "A magnetic-gear outer-rotor permanent-magnet brushless machine for wind power generation," *Industry Applications, IEEE Transactions on*, vol. 45, pp. 954-962, 2009.
- [1.68] N. W. Frank and H. A. Toliyat, "Gearing ratios of a magnetic gear for wind turbines," in *Electric Machines and Drives Conference, 2009. IEMDC'09. IEEE International*, 2009, pp. 1224-1230.
- [1.69] (2013, *Artemis Intelligent Power*. Available: <http://www.artemisip.com/>
- [1.70] G. Payne, *et al.*, "Efficiency and dynamic performance of Digital Displacement™ hydraulic transmission in tidal current energy converters," *Proceedings of the Institution of Mechanical Engineers, Part A: Journal of Power and Energy*, vol. 221, pp. 207-218, 2007.

Chapter 1 – Project Motivation and Background

- [1.71] D. Koenemann. (2009, Voith Turbo: WinDrive. *Sun & Wind Energy*.
- [1.72] Voith. (2013, *WinDrive*. Available: www.voith.com
- [1.73] A. Palmgren, "The Service Life of ball bearings," *ZVDI*, vol. 68, pp. 339-341, 1924.
- [1.74] M. A. Miner, "Cumulative Damage in Fatigue," *Journal of Applied Mechanics*, pp. 159-164, 1945.
- [1.75] A. Fatemi and L. Yang, "Cumulative fatigue damage and life prediction theories: a survey of the state of the art for homogenous materials," *International Journal of Fatigue*, vol. 20, pp. 9-34, 1998.
- [1.76] W. Hweng and K. S. Han, "Cumulative Damage Models and Multi-Stress Fatigue Life Prediction," *Journal of Composite Materials*, vol. 20, 1986.
- [1.77] S. S. Manson, "Fatigue: A Complex Subject - Some Simple Approximations," *Experimental Mechanics*, vol. 5, pp. 193-226, 1965.
- [1.78] L. F. Coffin, "A Study of the Effect of Cyclic Thermal Stresses on a Ductile Metal," *ASME Transactions*, vol. 76, pp. 931-950, 1954.
- [1.79] O. H. Basquin, "The Exponential Law of Endurance Tests," *American Society for the Testing of Material Procedures*, vol. 10, pp. 625-630, 1910.
- [1.80] W. Ramberg and W. R. Osgood, "Description of Stress-Strain Curves by Three Parameters," *National Advisory Committee for Aeronautics*, vol. 902, pp. 1-28, 1943.
- [1.81] A. Nieslony, *et al.*, "New method for evaluation of the Manson-Coffin-Basquin and Ramberg-Osgood equations with respect to compatibility," *International Journal of Fatigue*, vol. 30, pp. 1967-1977, 2008.
- [1.82] A. Plumtree and H. A. Abdel-Raouf, "Cyclic stress-strain response and substructure," *International Journal of Fatigue*, vol. 23, pp. 799 - 805, 2001.

Chapter 1 – Project Motivation and Background

- [1.83] L. P. Borrego, *et al.*, "Analysis of low cycle fatigue in AlMgSi aluminium alloys," *Engineering Failure Analysis*, vol. 11, pp. 715-725, 2004.
- [1.84] R. P. Skelton, *et al.*, "The Bauschinger effect, Masing model and the Ramberg-Osgood relation for cyclic deformation in metals," *Materials Science & Engineering A*, pp. 377-390, 1997.
- [1.85] ESDU, "An introduction to low-cycle fatigue phenomena," vol. 04022, ed, 2005.
- [1.86] ESDU, "Strain-life data for type 316 austenitic stainless steels at temperatures between -269 and 816°C," vol. 05007, ed, 2007.
- [1.87] ESDU, "Cyclic stress-strain response to type 316 austenitic stainless steels during low-cycle fatigue at temperatures between -269 and 800°C," vol. 05008, ed, 2007.
- [1.88] J. Szusta and A. Seweryn, "Low-cycle fatigue model of damage accumulation - The strain approach," *Engineering Fracture Mechanics*, vol. 77, 2010.
- [1.89] A. Seweryn, *et al.*, "Damage accumulation model for low cycle fatigue," *International Journal of Fatigue*, vol. 30, 2007.
- [1.90] Y. Murakami and M. K.J., "What is fatigue damage? A view point from the observation of low cycle fatigue process," *International Journal of Fatigue*, vol. 27, 2004.
- [1.91] K. Molski and G. Glinka, "A Method of Elastic-Plastic Stress and Strain Calculation at a Notch Root," *Material Science and Engineering*, vol. 50, pp. 93-100, 1981.
- [1.92] D. M. Li, *et al.*, "A Strain Energy-Based Approach to the Low-Cycle Fatigue Damage Mechanism in a High-Strength Spring Steel," *Metallurgical and Material Transactions A*, vol. 29A, pp. 1431 - 1439, 1998.
- [1.93] J. Morrow, "Cyclic Plastic Strain Energy and Fatigue of Metals," *Internal Friction, Damping and Cyclic Plasticity ASTM*, vol. 378, pp. 45 - 87, 1965.

Chapter 1 – Project Motivation and Background

- [1.94] G. R. Halford, "The Energy Required for Fatigue," *Journal of Material Science*, vol. 1, 1966.
- [1.95] H. Raji, "Low Cycle Fatigue in floating production storage and offloading units," Naval Architecture and Marine Engineering, University of Strathclyde, Glasgow, 2010.
- [1.96] A. Palmgren, "Ball and Roller Bearing Engineering, Translation by G. Palmgren and B. Ruley, SKF Industries," *Inc., Philadelphia, PA*, 1945.
- [1.97] G. Lundberg and A. Palmgren, "Dynamic Capacity of Roller Bearings," in *Acta Polytechnica Mechanical Engineering Series* vol. 1, ed. Stockholm, Sweden, 1947.
- [1.98] E. V. Zaretsky, *A. Palmgren Revisited--a Basis for Bearing Life Prediction*: Citeseer, 1997.
- [1.99] E. V. Zaretsky, *et al.*, "Effect of silicon nitride balls and rollers on rolling bearing life," *Tribology Transactions*, vol. 48, pp. 425-435, 2005.
- [1.100] E. V. Zaretsky, *et al.*, "Reexamination of ball-race conformity effects on ball bearing life," *Tribology Transactions*, vol. 50, pp. 336-349, 2007.
- [1.101] M. Matsuishi and T. Endo, "Fatigue of Metals subjected to varying Stress-Fatigue Lives under Random Loading," Japan Society of Mechanical Engineers, Fukuoka 1968.
- [1.102] S. D. Downing and D. F. Socie, "Simple rainflow counting algorithms," *International Journal of Fatigue*, vol. 4, pp. 31-40, 1982.
- [1.103] A. Nieslony, "Rainflow Counting Algorithm," ed: MATLAB, 2003, p. Very fast rainflow cycle counting for MATLAB.
- [1.104] J. Polak and M. Klesnil, "Cyclic Plasticity and Low Cycle Fatigue Life in Variable Amplitude Loading," *Fatigue of Engineering Materials and Structures*, vol. 1, pp. 123-133, 1979.

Chapter 1 – Project Motivation and Background

[1.105]K. Scott and D. Infield, “Effects of Extreme and Transient Loading on the Wind Turbine Drivetrain,” *30th ASME Wind Energy Symposium*, Nashville, USA, 2012

2.

**Static Modelling
of the Wind
Turbine
Drivetrain**

Nomenclature

Symbol	Explanation	Unit
A	Cross Sectional Area	m
a	Semi-Major Axis	m
b	Semi-Minor Axis	m
C_D	Dynamic Capacity	N
E	Young's Modulus	Nm^{-2}
F	Forcing Matrix	N
G	Shear Modulus	Nm^{-2}
I	Moment of Inertia	Nm^2
K	Stiffness Matrix	Nm^{-1}
L_{10}	L10 lifetime probability of survival	rev
l	Stressed Length	m
M	Mass Matrix	kg
m	Number of Cycles Experienced	cycles
N	Number of Stress Cycles	cycles
n	Number of Cycle to Failure	cycles
P	Applied Force	N
P_{eq}	Equivalent Radial Load	N
q	Distributed Load (Force per unit length)	Nm^{-1}
R_1	Radius of Elastic Body 1	m
R_2	Radius of Elastic Body 2	m
S	Probability of Survival	
V	Volume	m^3
w	Displacement of beam	m
X	Degree of Freedom	
x	Distance along beam	m
z	Distance to Sub-Surface Max Stress	m
θ_x	Deflection of Beam	rad
ν	Poisson's Ratio	
τ	Shear Stress	Nm^{-2}
ω	Natural Frequencies	$rads^{-1}$

Subscripts

Symbol	Explanation
t	Counter for Number of Loading Regimes
f	Total Number of Loading Regimes

2.1. Misalignments

Reliability studies into wind turbine gearboxes have discovered that bearings are overwhelmingly the main cause of failure. Although bearings have been shown to fail at all stages in the gearbox, bearings on the high speed stage have the most frequent failure rate. Bearings are chosen for their particular application by expected loading and rating therefore since higher than expected failure rates are observed on high speed shaft bearings, they must be subject to unexpected loading.

Misalignments are known to increase fatigue on bearings by increasing off axis loading. When an off axis load is applied to a bearing, the rolling elements and outer raceway react the applied forces to keep the shaft located. Figure 2.44 is a diagram of a bearing with an off axis load applied to the left side of the inner raceway. The off axis load causes one half of the bearing to be loaded whilst the other half is unloaded. Such off axis loading will cause deformations in the material causing relative misalignments between the inner and outer raceways to occur. Relative misalignments occur when the inner and outer raceways deflect different amounts causing high stresses at the contact with the rolling element. Although off axis loading is expected, the considerable uncertainty in loads that bearings experience in a wind turbine could mean that bearings are subject to loading well above their designed capabilities.

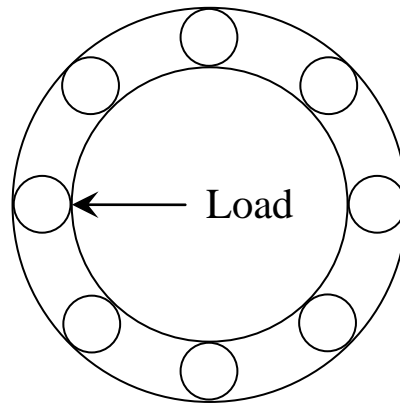


Figure 2.44 - Misalignment of Bearing

Off axis loading can occur from loading on either the inner raceway or outer raceway. Housing flexibility can cause deformation under load causing alignment to move away from normal. This can mean, that under operation, bearings can misalign in an unacceptable manner if the flexibility of the system is not properly accounted for.

Flexibility of other drivetrain components can have an important effect on alignment of shafts. Gearbox mounts affect how the gearbox can move in relation to the bedplate and therefore affects alignment of the high speed shaft with the generator. Mount compliance is important for isolating the gearbox from harsh loading that could be transmitted from the rest of the structure and for reducing transmission of gearbox noise and vibration. A flexible coupling is used to minimise the impact of misalignments between the gearbox and generator though these may not be effective enough in reducing transferred off axis loading. Bedplate distortion under load may also be a large source of misalignment not commonly analysed for its effects on bearing loading. Although the drivetrain is attached to mounts, the bedplate will still deform when loads are applied which might introduce misalignments to drivetrain bearings. The bedplate is commonly created in two parts: the upwind side of the bedplate is generally a cast section and therefore very strong; the downwind side of the bedplate is fabricated with a much higher degree of flexibility. The flexibility of the bedplate may allow it to deform potentially causing highly misaligned shafts when operational loads are applied.

2.2. Methodology

The RomaxWIND model is to be used to explore drivetrain bearing misalignment and loading. Three parameters are varied to determine the degree of misalignment and the effect on the lifetime prediction of drivetrain bearings: the gearbox mount stiffness, the flexible coupling stiffness and the structural stiffness of the bedplate itself. Table 2.3 shows the range of stiffness values that will be explored for each of these three components.

For gearbox mount stiffness and coupling stiffness, the stiffness of the connection is directly varied but for bedplate stiffness the material properties will be changed in an appropriate manner. The relative misalignments and resulting predicted damage will be compared.

Table 2.3 - Variable Range for Stiffness Sensitivity Study

Variable	Range (of Original)
Gearbox Mount Stiffness	1% – 1e5%
Coupling Stiffness	70% - 120%
Bedplate Stiffness	50% - 150%

Whittle [2.1] studied effects of how parallel misalignments of the generator can have an effect on loading of high speed shaft bearings in the gearbox and the role that coupling stiffness has in minimising this. Whittle found that both increasing misalignment and increased coupling stiffness caused increased damage on the high speed bearings, as might be expected, and quantified this, but he did not investigate how such misalignments could occur.

Bladed software has been used to calculate the aerodynamic loads on the rotor. For this study applied loading is taken at the rated wind speed of 12ms^{-1} . The applied hub torque has been calculated using GH Bladed as $1.08\text{e}6\text{Nm}$ with the rotor speed at 17.8rpm giving a system power of 2.013MW.

2.3. RomaxWIND

The computer simulation software used for this investigation is RomaxWIND. This is proprietary software from Romax Technology used for designing and analysing gearboxes. Non linear analysis of beams is used to compute beam deflections within the drivetrain, non linear contact between elastic bodies are used to describe bearings and gear contacts and finite element representations are used to predict how housings deflect under loading. RomaxWIND statically solves the drivetrain for the input loading using iteration to converge on the solution. In this model, key variable residuals had to reduce to below a threshold for acceptable convergence to occur.

2.3.1. Timoshenko Beam Elements

Shafts in RomaxWIND are modelled as nonlinear Timoshenko beam elements [2.2]. These beam elements take into account shear deformations of the beam as well as translational and rotational effects which conventional beam methods such as Euler-Bernoulli beam method ignore. In reality, deflections occur within the beam and the cross section deforms caused by shear forces. Timoshenko beam elements model effects and deformations of shear with the beam's cross section remaining planar around the neutral axis. His method has been show to agree adequately with experimental findings [2.3]. Figure 2.45 shows how shear forces deform within the beam; internal fibre gradients, $\frac{\partial w}{\partial x}$, do not match with θ_x as would be the case with no shear effects.

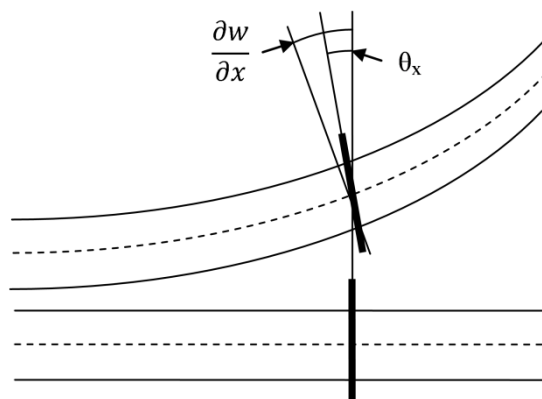


Figure 2.45 - Timoshenko Beam Theory

Timoshenko’s static beam equation includes a fourth order term to describe overall deflection, as in the Euler-Bernoulli model, but Timoshenko’s relationship also includes a second order spatial term.

$$EI \frac{d^4 w}{dx^4} = q(x) + \frac{EI}{GA} \frac{d^2 q}{dx^2} \quad (2.4)$$

2.3.2. Hertzian Contact

Hertzian contact theory [2.4] is a classical theory used to predict stresses between two elastic bodies in contact. When two bodies come into contact, elastic deformation occurs and material distortions occur. Hertzian contact theory describes how forces are transferred between the two objects and gives a model for contact stress. Deformations of the bodies at contact create an area where the material of both object are in contact with each other, called the contact patch. All transferred forces between the two bodies travel through the contact patch therefore when the deformation of the bodies is known, contact stress can be found through, *Stress, $\sigma =$*

$$\frac{\text{Force}}{\text{Contact Area}}$$

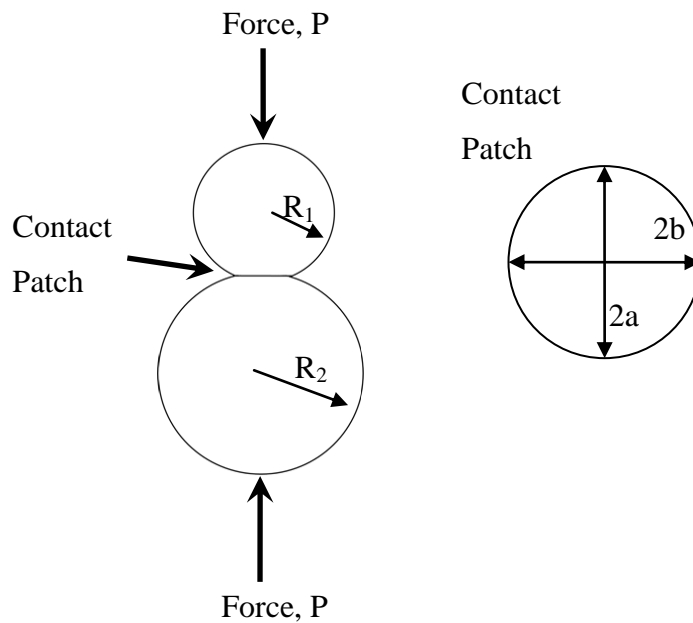


Figure 2.46 - Contact between Two Bodies

Huber [2.5] was the first to predict stresses beneath the surface of the contact area. The radius of the contact patch can be calculated from the Hertzian expression:

$$a = \left(\frac{3\pi P R_1 R_2}{4(R_1 + R_2)} \left(\frac{1 - \nu_1^2}{\pi E_1} + \frac{1 - \nu_2^2}{\pi E_2} \right) \right)^{\frac{1}{3}} \quad (2.5)$$

The size of the contact patch is therefore related to loading, body geometry and material properties: ν is Poisson’s Ratio and E is Young’s Modulus.

Reliable predictions of loading through contact are important in being able to predict when components are likely to fail. In bearings, stresses applied to bearing raceways dictate the design of the bearing. To ensure the bearing is able to withstand the applied loading, models must be able to predict what the bearing can withstand.

2.3.3. Finite Element

The finite element method is used to find static and dynamic responses to applied loading of structures. Finite elements enable complex structures to be analysed that would otherwise be incredibly difficult. Finite elements are not only used for elastic stress-strain problems but also electromagnetic fields, acoustics, heat flow, soil mechanics and fluid mechanics [2.6].

The model is discretized into an array of nodes with spatial positions interconnected through elements. The pattern of elements and nodes through the whole model is the mesh. Forces can be applied to nodes individually and the analysis will find the structures response to the loading. Forces are linked to the displacements through the stiffness matrix,

$$[nodal\ forces] = [stiffness\ matrix] \times [nodal\ displacement] \quad (2.6)$$

Element shapes are important in finding reliable solutions to input conditions. Some of the most common element types are shown in Figure 2.47.

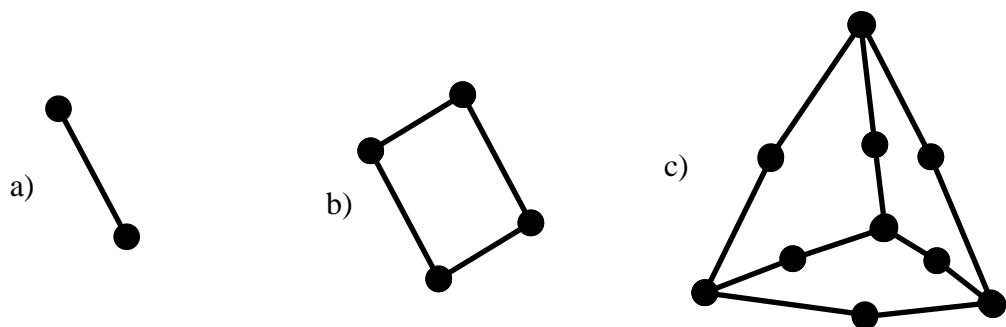


Figure 2.47 - Elements, a) single beam element, b) square element, c) 10 node tetrahedral

Beam elements, Figure 2.47a), can be used to describe simplified problems where the physical model can be accurately represented by a two node element. More complex models require more connections between nodes, b) and c) are 2 and 3 dimensional elements. Square and shell planar elements allow motion on a plane and can allow rotation and output of plane translation. The brick elements are commonly used to model 3 dimensional objects though because of restrictions of fitting regular brick to irregular structures tetrahedral element can be used. Triangular and tetrahedral elements are popular with meshing algorithms and adaptive mesh techniques. Elements can be linear or non linear. The simplest case is where elements react linearly to applied loading though with higher order elements, stress varies across the element allowing the possibility of closer approximations.

The first step in creating a finite element model is solid body modelling of the structure. 3-dimensional CAD (Computer Aided Design) drawings are used as the basis for the finite element model. The model is meshed into discrete elements and checks to ensure element size is acceptable are carried out. RomaxWIND uses finite element analysis to model deflections in housings in the gearbox. Localised deformations under load can be viewed by solving the model this way. Analysis of certain parts of the gearbox has shown that flexibility can be crucial in predicting loading on gears and bearings.

2.3.4. Model Reduction

Finite element analysis can be extremely computationally heavy and generate vast amounts of data. This can be very time consuming when numerous runs are required especially when the user is only interested in a small number of nodes. Reducing the full finite element problem to a simplified representation with only required output nodes can significantly reduce computational time and data generation. These method produce large simplified elements commonly named superelements.

i) Guyan Method

Guyan [2.7] devised a method for reducing the size of stiffness matrix for solving second order differential equations. The resultant matrix retained the structural complexity of the original matrix with the eigenvector-eigenvalues problem closely,

though not exactly, preserved. The reduced matrix should therefore retain displacement outputs with system natural frequencies close to those predicted by the full model.

Master degrees of freedom are chosen where important and significant motion occurs. Slave degrees of freedom are all the other degrees of freedom in the model and are therefore expected to move quasi-statically with respect to master degrees of freedom. The system is reduced so that the motion of the master nodes can be retained.

Equations of motion for a simplified second order system are given by

$$[F] = [M][\ddot{X}] + [K][X] \quad (2.7)$$

The potential energy of the system is given by

$$V = \frac{1}{2} X^T K X \quad (2.8)$$

The displacement vector can be rearranged into retained master nodes, X_1 , and slave nodes, X_2 ,

$$X = \begin{bmatrix} X_1 \\ X_2 \end{bmatrix} \quad (2.9)$$

The mass and stiffness matrices can be rearranged into master and slave partitions,

$$K = \begin{bmatrix} K_{11} & K_{12} \\ K_{21} & K_{22} \end{bmatrix} \quad (2.10)$$

$$M = \begin{bmatrix} M_{11} & M_{12} \\ M_{21} & M_{22} \end{bmatrix} \quad (2.11)$$

Potential energy would therefore become

$$V = \frac{1}{2} \begin{bmatrix} x_1^T & x_2^T \end{bmatrix} \begin{bmatrix} K_{11} & K_{12} \\ K_{21} & K_{22} \end{bmatrix} \begin{bmatrix} x_1 \\ x_2 \end{bmatrix} \quad (2.12)$$

Multiplying out and rearranging gives

$$V = \frac{1}{2} [X_1^T K_{11} X_1 + 2X_2^T K_{21} X_1 + X_2^T K_{22} X_2] \quad (2.13)$$

Taking partial differential with respect to slave vectors and assuming no applied forces on slaves

$$\frac{\partial V}{\partial X_2} = K_{21}X_1 + K_{22}X_2 = 0 \quad (2.14)$$

$$X_2 = -K_{22}^{-1}K_{21}X_1 \quad (2.15)$$

Since an expression for the slave degrees of freedom in terms of master degrees of freedom is found, the constraint matrix, C, can be formed (I is the identity matrix)

$$X = \begin{bmatrix} I \\ -K_{22}^{-1}K_{21} \end{bmatrix} X_1 \quad (2.16)$$

$$C = \begin{bmatrix} I \\ -K_{22}^{-1}K_{21} \end{bmatrix} \quad (2.17)$$

When the constraint matrix pre and post multiplies the mass and stiffness matrices the resultant matrices are reduced which can be used in the reduced equations of motion for the system.

$$K_C = C^T K C \quad (2.18)$$

$$M_C = C^T M C \quad (2.19)$$

$$[F_C] = [M_C][\ddot{X}] + [K_C][X] \quad (2.20)$$

ii) *Craig-Bampton Method*

The Craig-Bampton [2.8-2.9] method is similar to Guyan reduction for reducing and substructuring finite element models. It uses super-elements to reduce complex models into substructures that are connected to the rest of the structure. Interface or boundary nodes connecting super-elements to the rest of the structure remain on the model while internal nodes are restructured so that applied loading on interface nodes will produce the same output as the full finite element model.

Mass and stiffness matrices are rearranged into boundary degrees of freedom and internal degrees of freedom and partitioned as done in Guyan reduction, shown by (2.10) and (2.11). Subscript 1 is a boundary (master) degrees of freedom to be retained and subscript 2 is an internal (slave) degrees of freedom to be reduced.

As found in Guyan reduction the stiffness constraint is given by

$$\Psi_{12} = -K_{22}^{-1}K_{21} \quad (2.21)$$

The internal eigenvalues are can be found from

$$\{K - \omega^2 M\}\{\phi\} = 0 \quad (2.22)$$

ω is the natural frequencies , ϕ is the mass normalised mode shapes or eigenvectors.

The partition containing the interior degrees of freedom is Φ_{22} . q_2 is the generalised internal degrees of freedom. The size of the problem can be greatly reduced by only using the first modes of Φ_{22} . Using both constraints and internal modes the displacement vectors can be written as

$$X \equiv \begin{bmatrix} X_1 \\ X_2 \end{bmatrix} = \begin{bmatrix} I & 0 \\ \psi_{12} & \phi_{22} \end{bmatrix} \begin{bmatrix} X_1 \\ q_2 \end{bmatrix} \quad (2.23)$$

where the Craig-Bampton transform is given by

$$C = \begin{bmatrix} I & 0 \\ \psi_{12} & \phi_{22} \end{bmatrix} \quad (2.24)$$

Pre and post multiplying the full mass and stiffness matrices will give the reduced mass and stiffness matrices.

2.4. Drivetrain Model

Modelling the drivetrain structure has only relatively recently been used to find the effects components have on alignments and loading of other components. Traditionally, the gearbox and generator were analyzed and designed individually using expected load inputs. The cast section of the bedplate and the low speed shaft were analyzed using finite element to ensure the structure could withstand the expected loading. Little work on the rear part of the bedplate has been done to find its effect on drivetrain loading. For effective analysis, a model of the complete drivetrain was assembled. The drivetrain has a modular 3 stage high speed gearbox and a high speed generator connected through a flexible coupling. The initial 2 stages of the gearbox are planetary stages with a final high speed helical stage. The drivetrain has a 4-point mounting onto the bedplate: two main bearings on the low speed shaft and two gearbox mounts, one either side of the gearbox.

2.4.1. Low Speed Shaft (LSS)

The low speed shaft is a hollow shaft connecting the hub to the first stage planet carrier of the gearbox. Two main bearings are used to hold the shaft in place. The rotor end bearing is a double row taper bearing resisting most of the off axis loading in the rotor. The tapered rolling elements allow axial loading to be resisted in this

bearing. The non rotor end bearing is a cylindrical bearing that does not resist axial loading preventing issues with axial alignment. The shaft is rigidly connected to the first stage planet carrier at the non-rotor end to imitate a shrink fit. Rotor mass, inertia, rotor torque loading and off axis loading is applied at the hub connection at the input of the shaft.

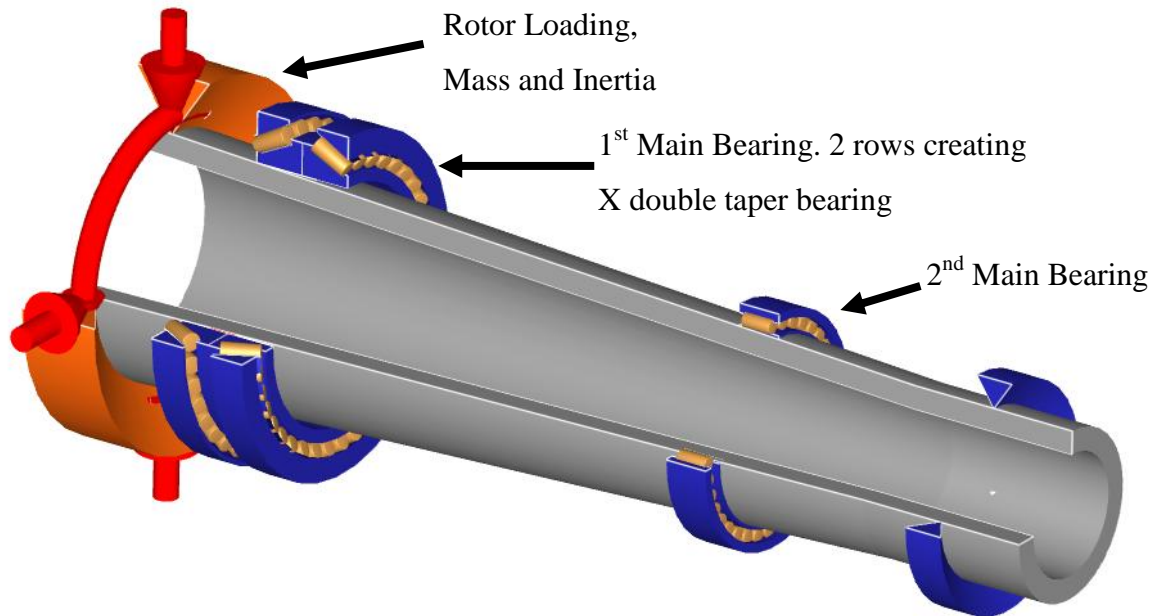


Figure 2.48 - Low Speed Shaft

2.4.2. Stage 1

The stage 1 gearing is a planetary system with 3 planet bearings separated by 120°. The sun gear, S, has 29 teeth, the planets, P, have 43 teeth and the ring gear, R, has 115 teeth. The ring gear is stationary and connected to the gearbox housing. Input to the stage is through rotation of the planet carrier and the output is rotation of the sun gear. The gear ratio, GR, for a planetary stage can be calculated by $GR = \frac{S+R}{S}$ giving a gear ratio of 4.9655 for this stage. The planet carrier is a finite element model with beam elements modelling the planet pins.

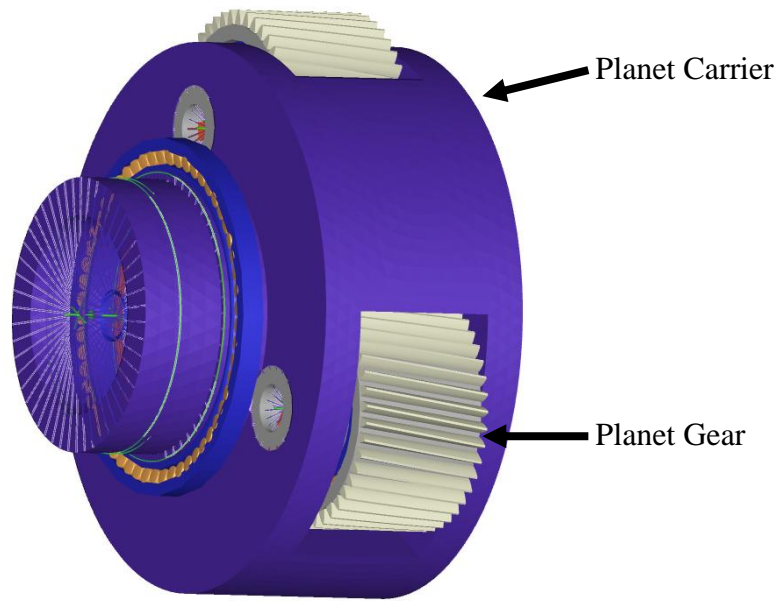


Figure 2.49 - Stage 1 Planet Carrier and Planets

2.4.3. Stage 2

Similar to the stage 1 planetary system, the stage 2 planet gearing composes of a finite element carrier with beam elements for planet pins. The sun shaft from stage 1 is rigidly attached to the carrier as an input. In this stage the sun has 33 teeth, the planets have 48 teeth and the ring has 129 giving this stage a gear ratio of 4.909.

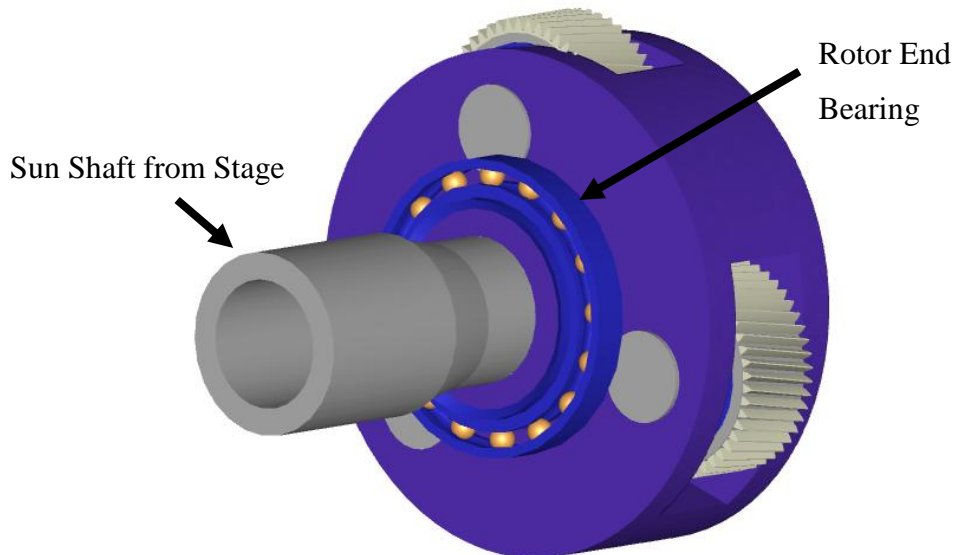


Figure 2.50 - Stage 2 Planet Carrier and Planets

2.4.4. Stage 3

The final stage is parallel with 115 teeth on the driving gear and 31 teeth on the output gear giving a gear ratio of 3.710 for this stage. Double tapered bearings are on both the input and output shafts of this stage to locate the gears and resist the axial forces created from the helical gear pair. A spline is also modelled on the input to the helical stage to allow for changes in length to the shaft.

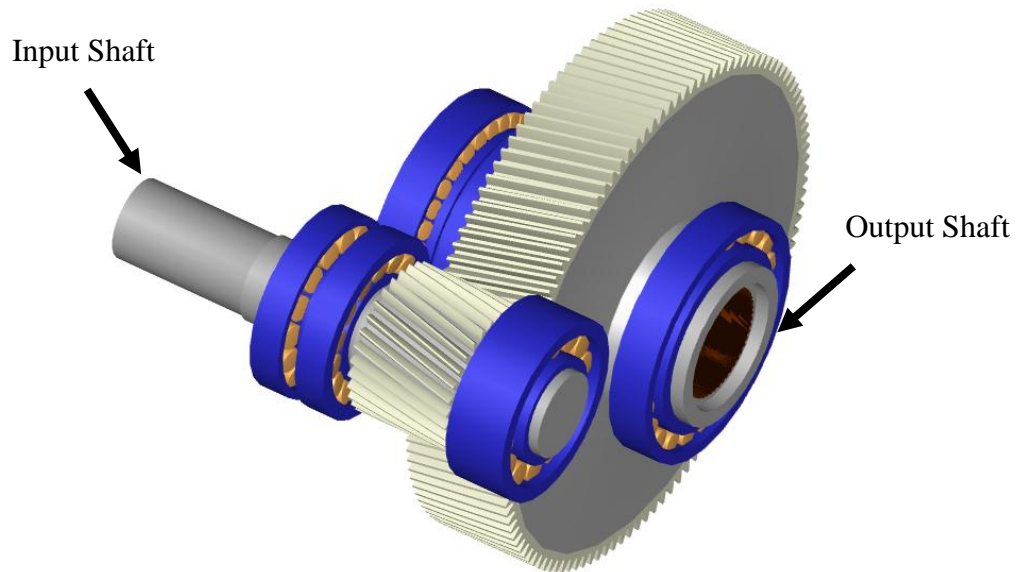


Figure 2.51 - Stage 3 Parallel Gears

2.4.5. Coupling

The flexible coupling is a difficult and complex component to model. Compliance must minimise off axis load transmission between the gearbox and generator whilst efficiently transmitting driving torque. The coupling therefore must be flexible in angular and translational misalignment but stiff in the torsional direction to maximise power transfer. The coupling was modelled as a section of flexible material, allowing flexibility for off axis loads, with the rigidity in the torsional direction keeping high power transfer efficiency.

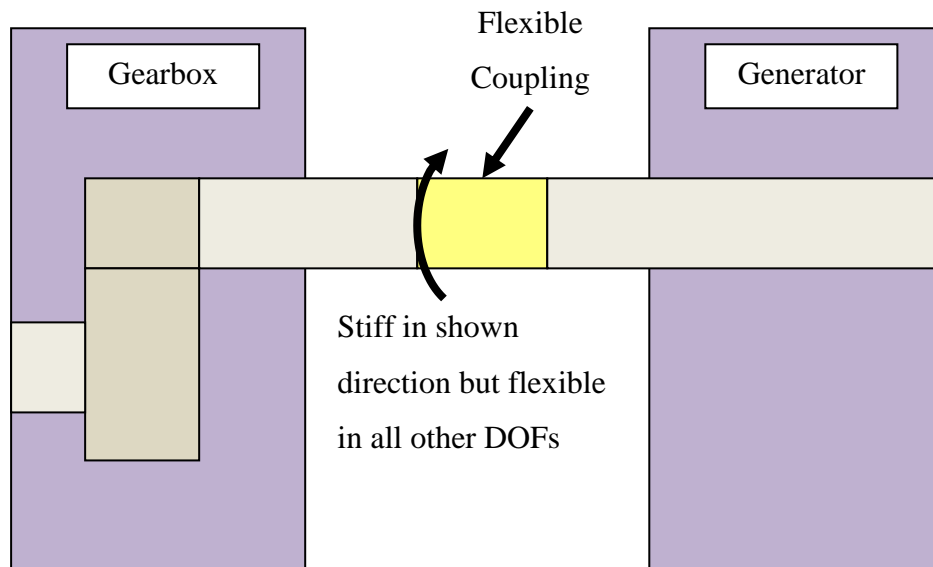


Figure 2.52 - Flexible Coupling

2.4.6. Generator

A high speed generator consists of two main subcomponents, a stator and a rotor. The rotor is connected to the input shaft and contains either windings or permanent magnets depending on design. The stator remains stationary connected to the surrounding structure, containing output windings. When the rotor turns, moving electromagnetic fields are created and a potential difference is induced on the stator windings. Two ball bearings are used to locate the rotor within the stator: a drive end (DE) and non drive end (NDE). The stator is also connected to the bedplate through generator mounts. A static torque is applied to the stator to model reaction of the generator torque allowing off axis loading to be transferred to the rest of the structure. Estimates for size and mass for the generator are taken from Polinder [2.10].

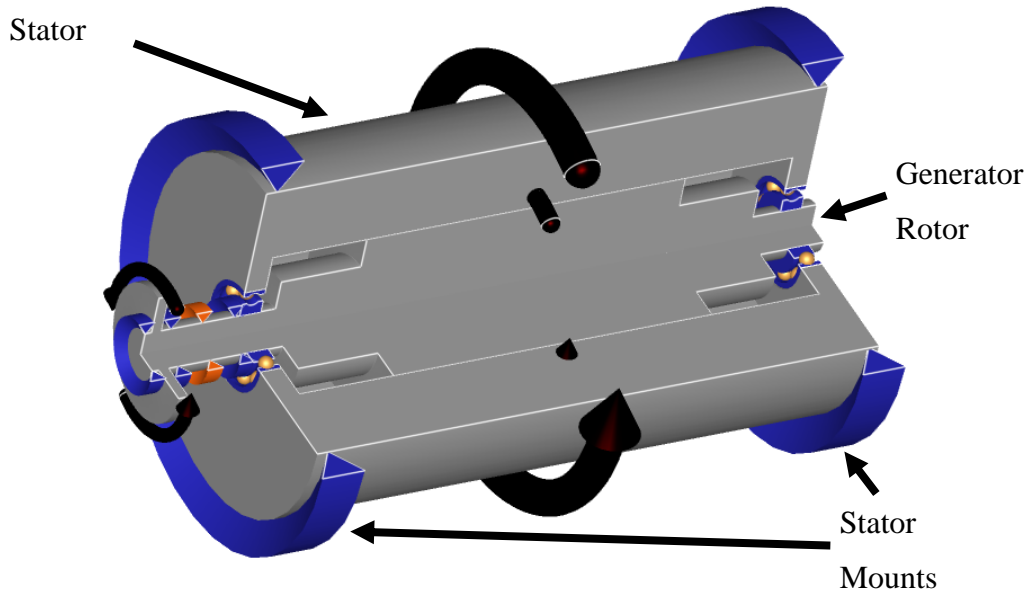


Figure 2.53 - Generator Model

2.4.7. Gearbox Housing

The gearbox housing consists of 3 distinct sections: the torque arm, the middle housing and the end housing. The torque arm is the connection of the gearbox to the bedplate and applies the gearbox reaction torque to the bedplate. The middle housing sites the two planetary systems locating the ring gears. The end housing sites the final parallel stage. Coultate [2.11] has shown that deformations of the gearbox housing have a significant impact on the prediction of loading on bearings and gears.

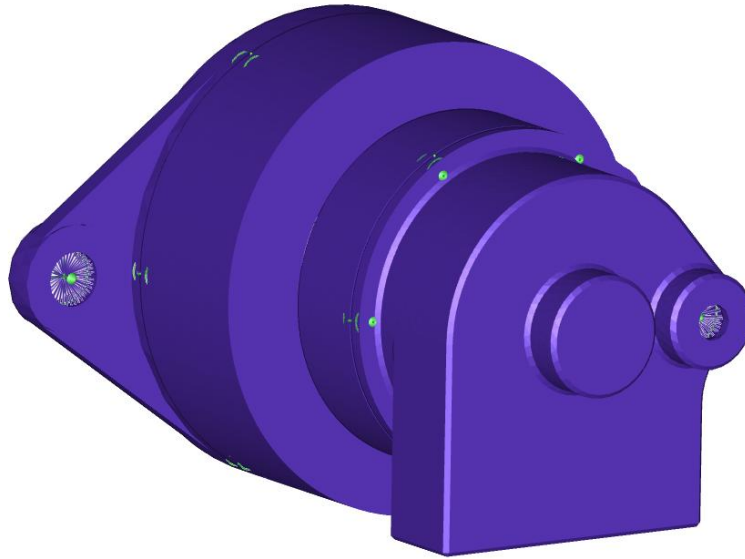


Figure 2.54 - Gearbox Housing

2.4.8. Bedplate

The bedplate positions the modular components on the complete drivetrain. The bedplate commonly consists of a cast front section with a fabricated rear section. In this model some features have had to be simplified, particularly the rear fabricated section, to allow meshing and shorter CPU solver times. Bearings and connectors attached to the bedplate are shown as green markers with RBE2 beam elements used to connect bearings and connectors to the finite element nodes. The bedplate is grounded at the yaw connection through rigid connections to ground. Structural steel is used as the bedplate's material having a Young's Modulus of $1.96e11 \text{ Nm}^{-2}$ and a density of 7800 kgm^{-3} giving a total mass of 14573.255 kg. The mesh of the bedplate consists of 368431 nodes making 187577 elements. Elements used are 10 node tetrahedral elements throughout the bedplate model.

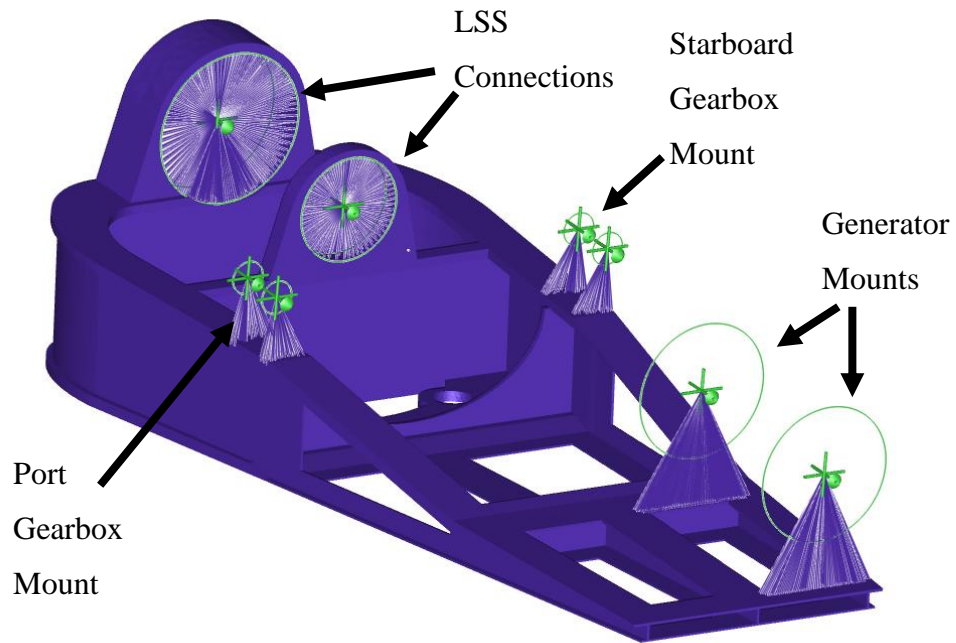


Figure 2.55 - Bedplate Model

2.4.9. Drivetrain Assembly

The complete assembled drivetrain is shown in Figure 2.56. Gearbox mounts are modelled as trunnion mounts either side of the gearbox. Mount pins are rigidly connected to the bedplate at either end through a flexible connection with appropriate stiffness connecting the centre of the mounting pin to the torque arm of the gearbox. Stiffness of this connection represents flexibility in the gearbox mounts and represents how the gearbox moves on its mounts relative to the bedplate.

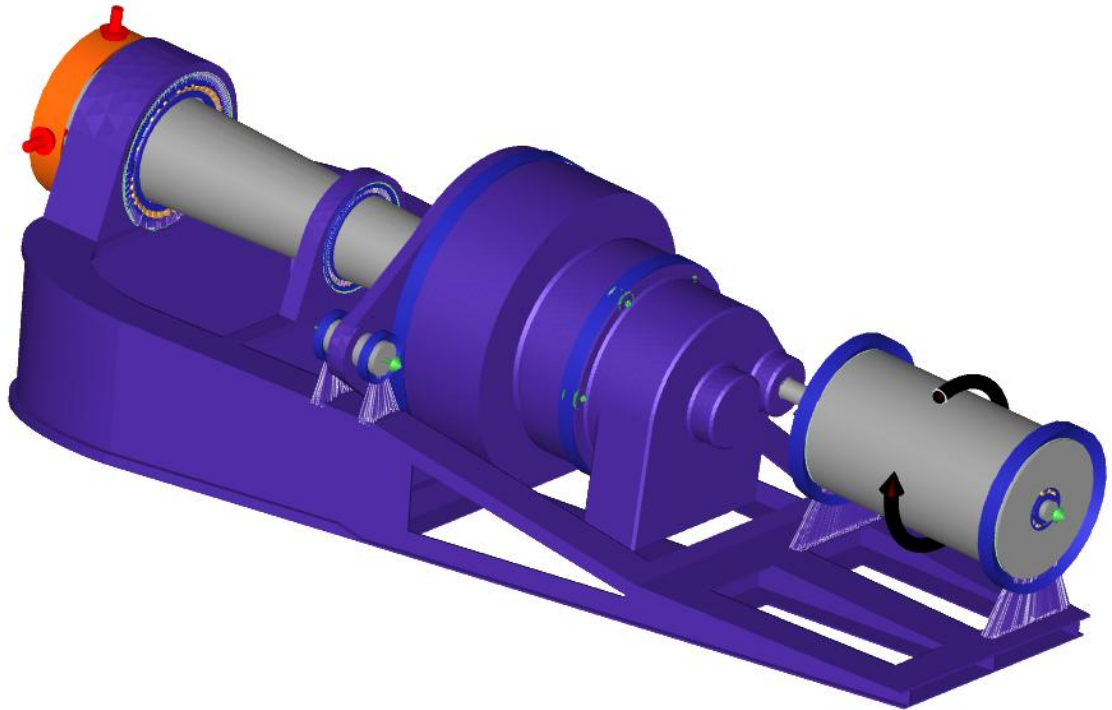


Figure 2.56 - Complete Drivetrain Model

The complete drivetrain is shown below with gearbox housing and bedplate removed. Internal gearing of the gearbox is shown in Figure 2.57 with connections onto the generator.

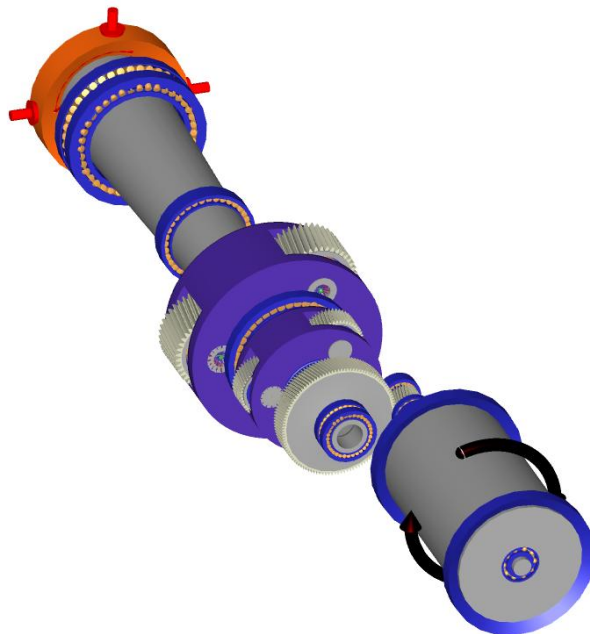


Figure 2.57 - Assembled Drivetrain Model with Housings Stripped

2.5. Damage Model

The damage model used in this work is outlined in the ISO281 standard using the L10 bearing lifetime characteristic.

Lundberg and Palmgren [2.12-2.13] continued the work of Weibull [2.14] to apply a statistical method to the fatigue of materials. Obtaining the relationship that predicts when 10% of bearings would fail,

$$L_{10} = \left(\frac{C_D}{P_{eq}} \right)^p \quad (2.25)$$

Dynamic capacity of the bearing and equivalent radial load is related to the predicted lifetime of the bearing. Exponent p is the load-life exponent related to the type of bearing being analyzed, this is 3 for ball bearings or 10/3 for cylindrical roller bearings. Dynamic capacity of the bearing is a function of the bearing geometry, such as number of rolling elements, rolling element diameter, contact angle, etc. Equivalent radial load is used since bearings are subjected to radial and axial loading. Palmgren and Lundberg used the relationship, $P_{eq} = XF_{radial} + YF_{axial}$, to find the equivalent radial load. X and Y are factors calculated by Lundberg and Palmgren, in the case of purely radial loading, $X = 1$ and $Y = 0$. L_{10} gives that predicted number of revolutions under the applied load before it is predicted to fail. When the rotational speed is known the predicted time to the L10 failure criteria can be found.

In the case where more than one loading regime is applied to the bearing a cumulative model is used to find the total damage to the bearing. Miner's Rule [2.16] uses superposition to combine all the different loading cases. The number of cycles to failure under a specific loading condition can be found using SN curves. With the number of cycle a bearing has experienced known, the two can be divided to obtain a percentage of lifetime expended. These can be summed to give the total used lifetime of the bearing.

$$Damage = \sum_{t=1}^f \frac{m_t}{n_t} \quad (2.26)$$

2.6. Coordinate System

The coordinate system used to model the wind turbine drivetrain is shown in Figure 2.58.

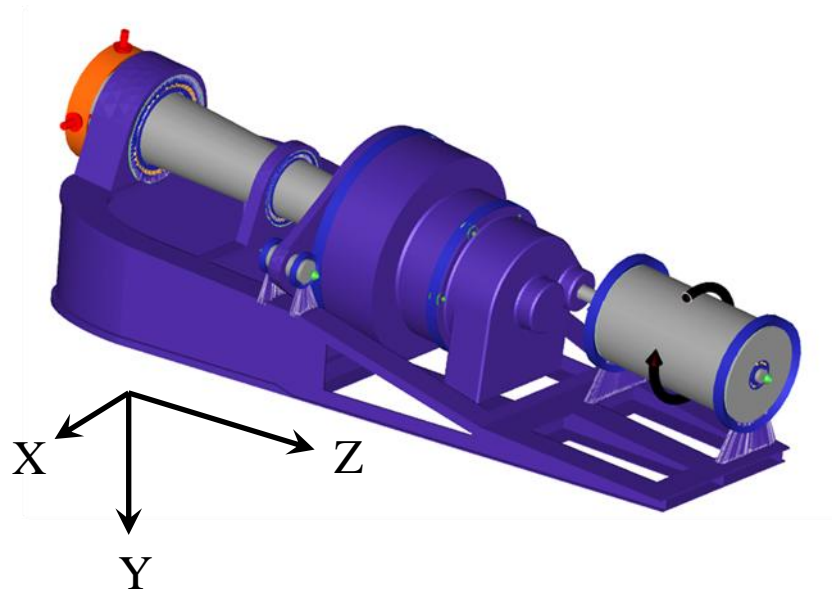


Figure 2.58 - Drivetrain Coordinate System

2.7. Gearbox Mount Stiffness

Gearbox mounts are used to introduce tolerance into the drivetrain. Mount stiffness is important for preventing harsh loading being transferred to the gearbox and also for aligning the gearbox and generator. When under load, the gearbox mounts deflect and cause misalignments to occur between components. Stiffness of the gearbox mount is consequently important for the alignment of the gearbox and generator.

Figure 2.59 shows all bearings in the drivetrain ordered from upwind to downwind. Bearing damage and mount stiffness are compared showing how bearing loading changes through the drivetrain. When gearbox mount stiffness is altered, there is little change to most of the bearings internal to the gearbox; large changes occur to generator bearings, the output bearing on the high speed shaft and stage 1 carrier bearings. The generator DE bearing appears to be the most sensitive to gearbox mount stiffness. Unfortunately, there does not appear to be a straightforward relationship between gearbox mount stiffness and bearing damage although when mount stiffness is reduced to 1% extremely large damage predictions are found: generator DE damage extends up to 180% damage at this mount stiffness.

Damage Sensitivity to Mount Stiffness

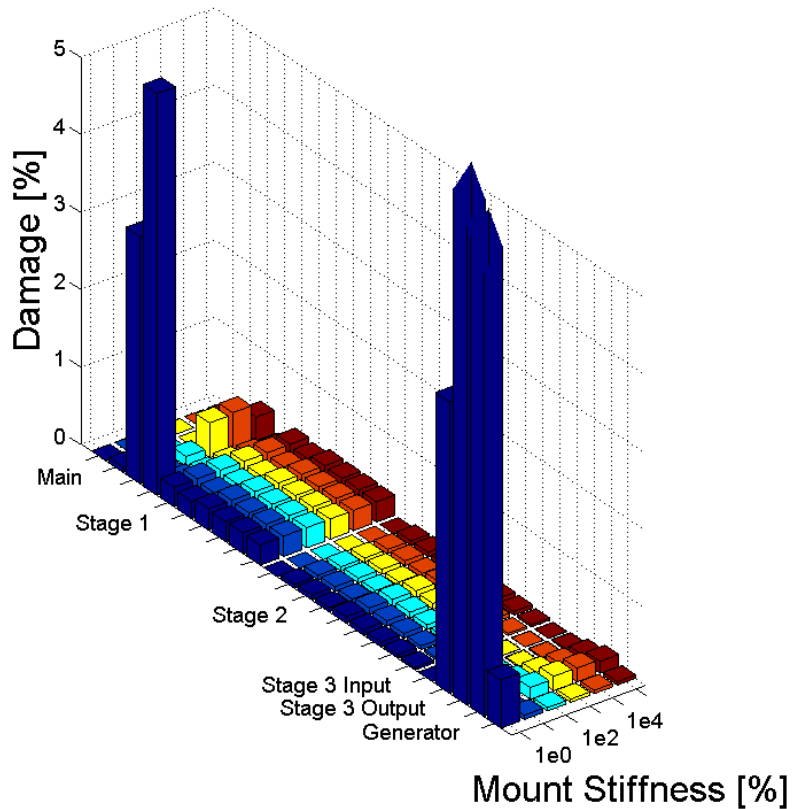


Figure 2.59 - Bearing Damage Sensitivity to Gearbox Mount Stiffness

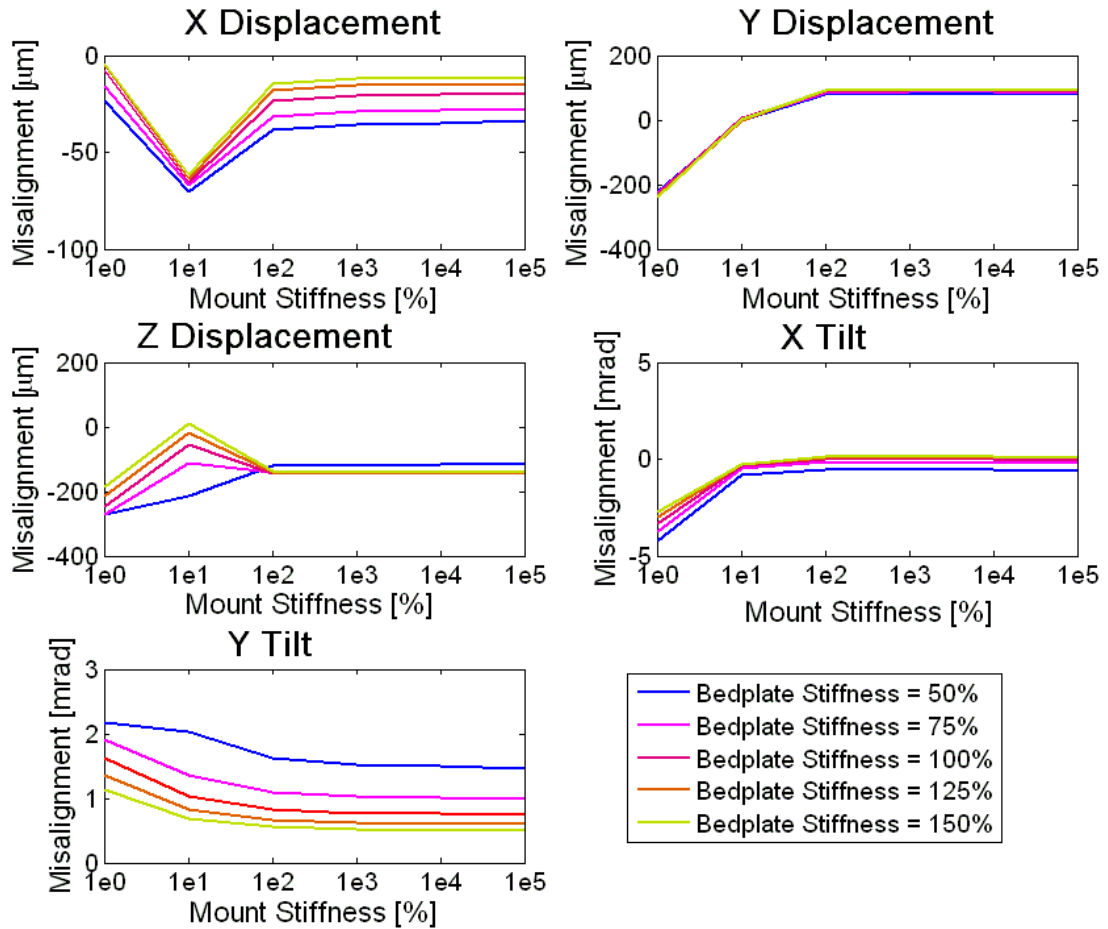


Figure 2.60 - Misalignment of Generator DE Bearing Sensitivity to Bedplate and Mount Stiffness

Relative misalignment between inner and outer raceway of the generator DE bearing are plotted in Figure 2.60, showing the 5 off axis DOF's. Relative misalignments of all drivetrain bearings are shown in Appendix A. Above 100% stiffness the effects of mount stiffness are minimal. All lines become almost horizontal signifying insensitivity of relative misalignment to mount stiffness. Below 100% however there is significant variation in relative misalignment. Y displacement (vertical) shows large changes in relative misalignment when mount stiffness is reduced further. Interestingly, misalignment changes sign showing a change in direction of the applied force to the bearing. Bedplate stiffness appears to have the impact of shifting the misalignment trend up or down. The exception is Z displacement (axial) where lines cross over below 100% mount stiffness signifying when mount stiffness is reduced far enough some dependence exists between mount stiffness and bedplate stiffness. Since relative misalignments can be difficult to perform sanity checks on,

absolute misalignments for both the inner and outer raceways are plotted in Appendix B. All cases show when mount or bedplate stiffness is reduced, more absolute displacement occurs confirming the model is behaving as expected.

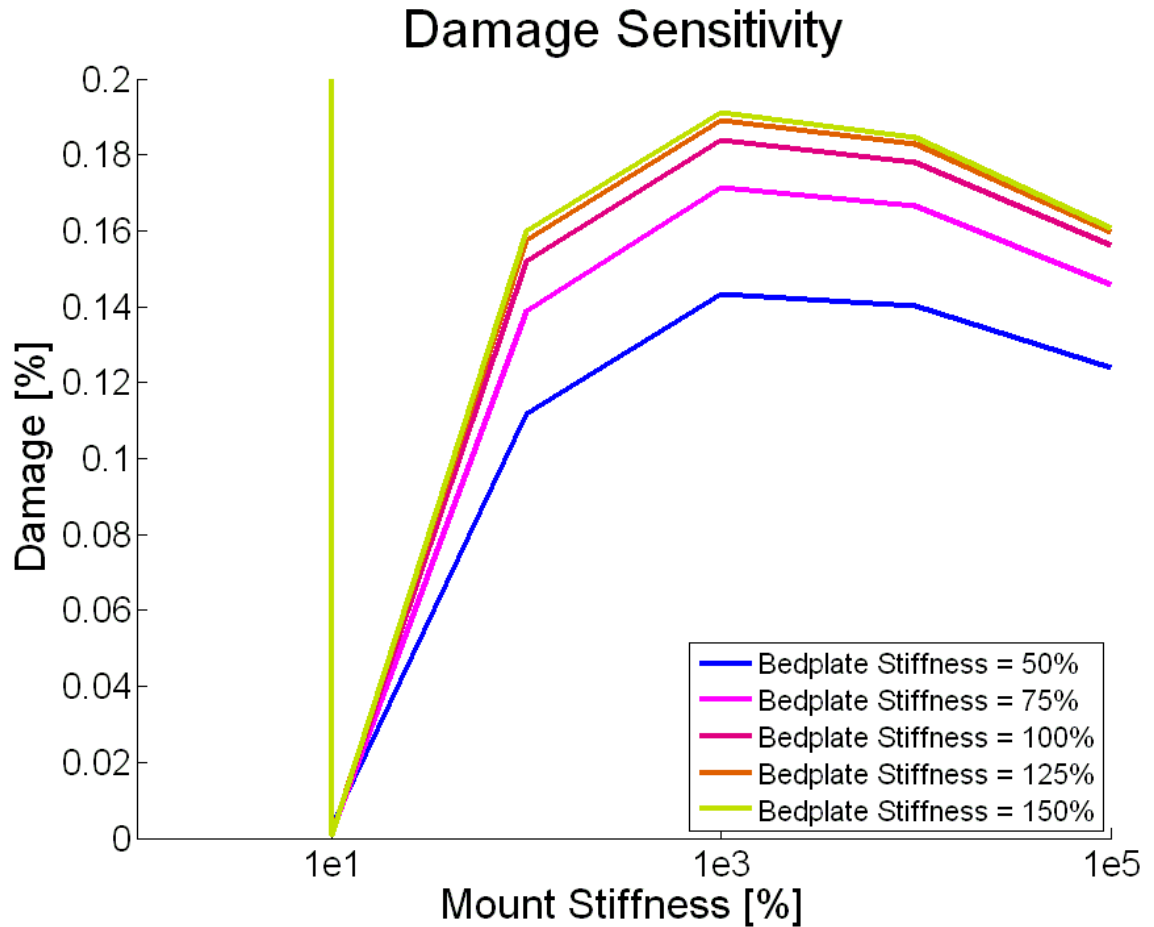


Figure 2.61 - Generator DE Bearing Damage Sensitivity to Bedplate and Mount Stiffness

Figure 2.61 shows damage to the generator DE bearing that occurs when mount stiffness and bedplate stiffness are varied. The aggregated effects of the misalignments translate into bearing loading which can be used to predict damage using the L10 lifetime criteria. Below 10% mount stiffness, damage increases massively though this has been cut off on the graph to show more useful and realistic portion of the graph. Damage ranges between 160% and 180% for the cut off section at 1% mount stiffness. With greater mount stiffness a peak in damage occurs at 1000% mount stiffness. Stiffer mounts cause a reduction in accrued damage which suggests that removing flexible mounts and rigidly attaching the gearbox to the bedplate could provide less misalignment and reduce loading on the bearing.

Similarly, reducing mount stiffness to between 10% and 100% reduces loading on the generator DE bearing, with 10% predicting damage extremely low damage. At this mount stiffness the drivetrain is able to move to minimise misalignments of high speed bearings though this has an adverse effect on the loading of other bearings, especially the NRE main bearing. Stiff mounts are not used because when mount stiffness is increased tolerances in the system are reduced and load sharing between the drivetrain bearings are not equally spread. This could lead in some cases to particular bearings being overloaded.

Unexpectedly, increasing bedplate stiffness increased damage of the generator DE bearing. Higher rigidity of the bedplate is expected to reduce misalignments and subsequently reduce loading on the bearings similar to modelling results of gearbox housing flexibility. From Figure 2.61, the model predicts the opposite with the stiffest bedplate causing the most damage to the generator DE bearing. This suggests flexibility in the bedplate allows movement of the drivetrain meaning that bearings can displace according to the applied force and reduce relative misalignments of the bearing.

2.8. Coupling Stiffness

Stiffness of the flexible coupling has been shown to be important for minimising effects of misalignments between gearbox and generator. A similar analysis to the gearbox mounts was performed using the coupling stiffness, shown in Figures 2.62 and 2.63.

Damage Sensitivity to Coupling Stiffness

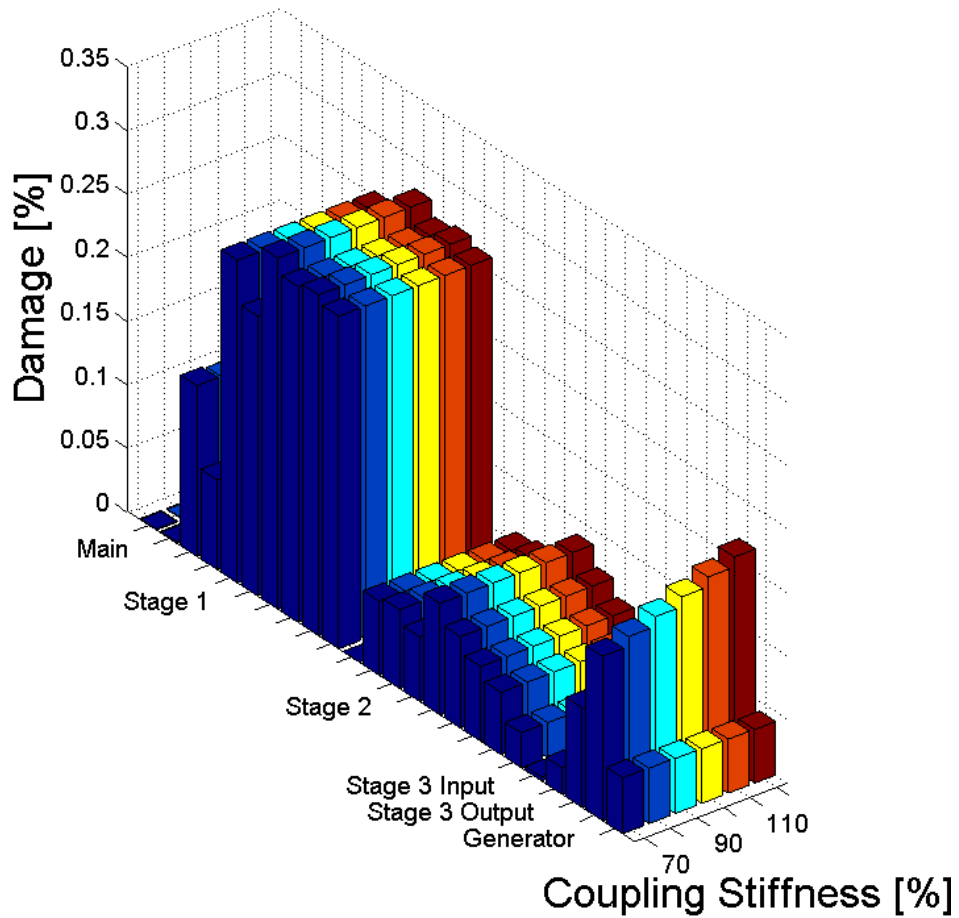


Figure 2.62 - Drivetrain Bearings Damage Sensitivity to Coupling Stiffness

Only the generator DE bearing and the output bearing on the gearbox high speed shaft are affected by the change in coupling stiffness. With a stiffer coupling damage to both the output bearing and generator DE bearing increases; the rest of the bearings are unaffected. A 50% increase in coupling stiffness causes a 0.04% increase in bearing damage, over the studied range an increase by a factor of 1.296. There is a relative lack of sensitivity as the applied loading does not cause large misalignments across the flexible coupling. This may suggest that the model does not create the appropriate misalignments under load.

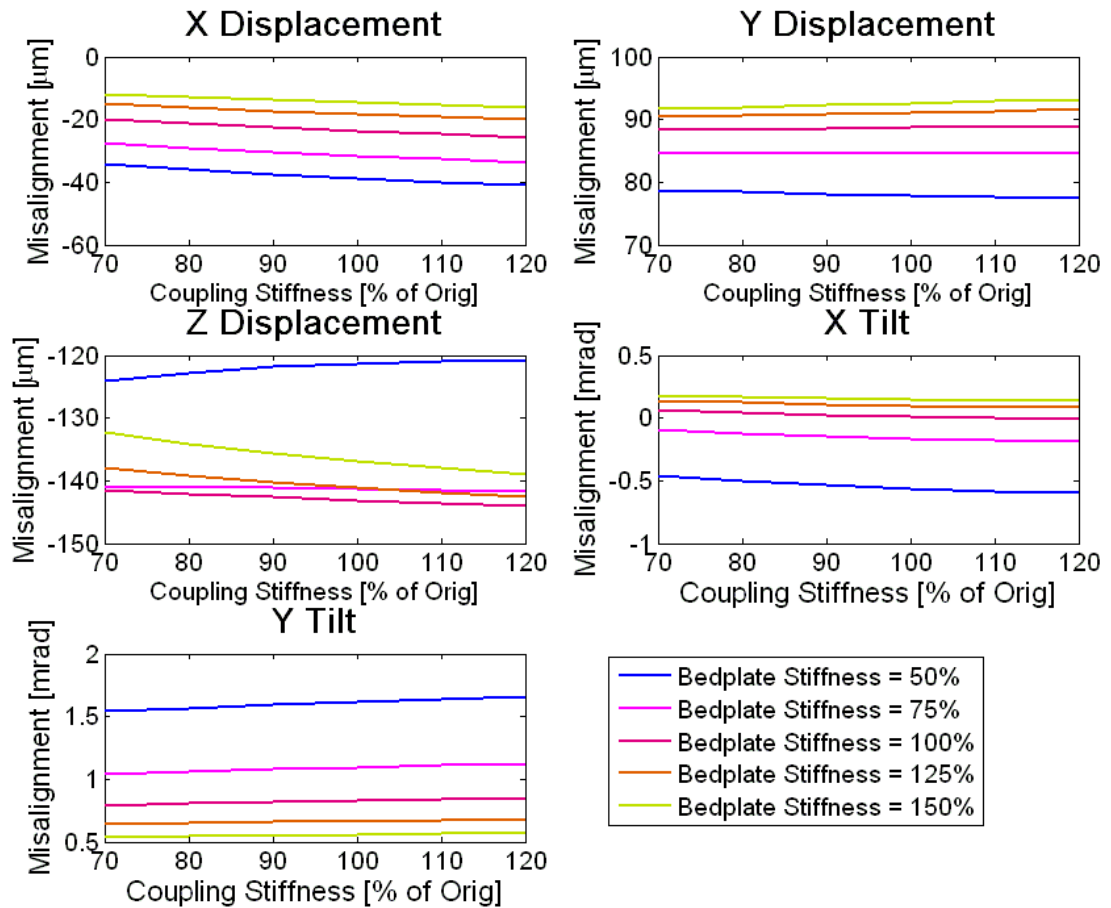


Figure 2.63 – Relative Misalignments of the Generator DE Bearing against Coupling Stiffness

Most trends vary linearly with coupling stiffness in shown in Figure 2.63. Bedplate stiffness shifts the misalignment trend up or down with more flexible bedplate stiffnesses. Bedplate stiffness increases misalignment in the Y direction but reduces in the X direction. Overall greater radial misalignments are found with increased stiffness bedplates. Z displacement (axial) shows a non linear response to both coupling stiffness and bedplate stiffness. Maximum magnitude of axial misalignment occurs when the bedplate stiffness is at 100% of original stiffness. Misalignments for both inner and outer raceway are displayed in Appendix A.

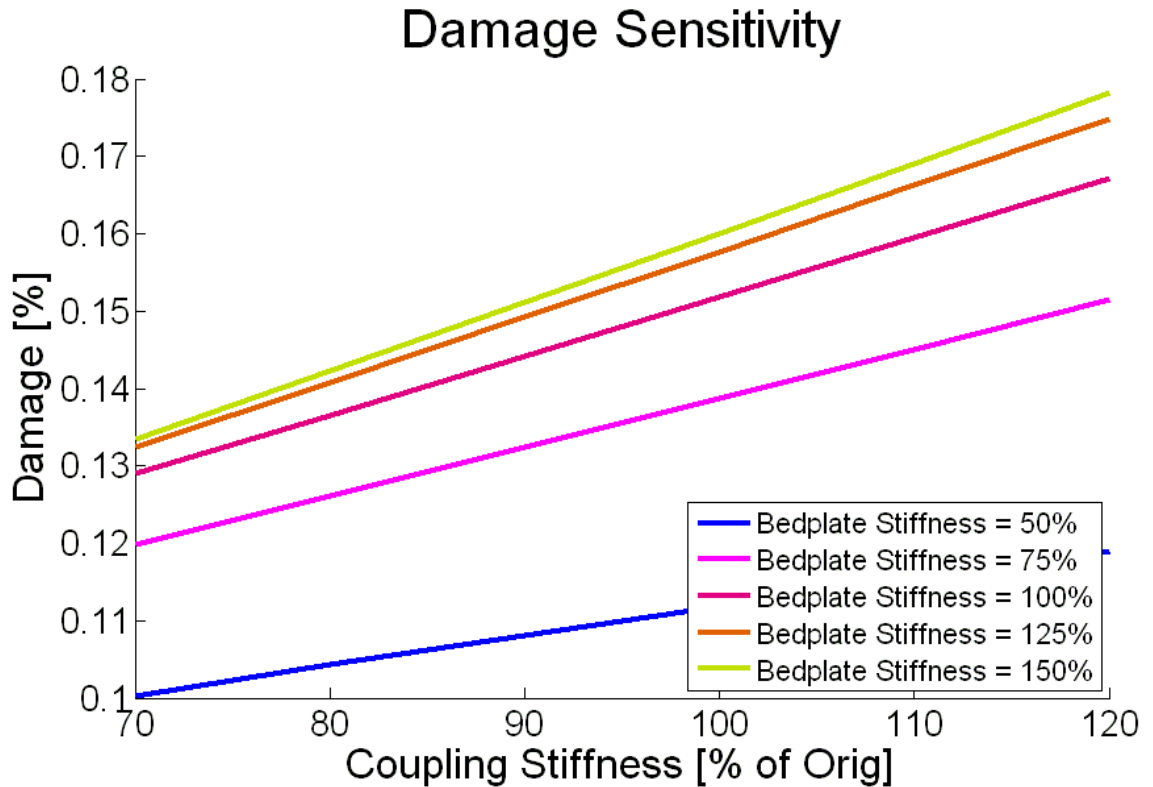


Figure 2.64 - Generator DE Bearing Sensitivity to Coupling and Bedplate Stiffness

Damage of the generator DE bearing appears to increase linearly with coupling stiffness. Although only a slight increase in damage, this could be important when simulations are stretched out to full operational lifetime.

Two main outcomes arise from analyzing bedplate stiffness. Firstly, increasing bedplate stiffness causes increased loading on the generator DE bearing. Figure 2.64 clearly shows that increasing bedplate stiffness causes greater damage for all cases. Secondly, the stiffer the bedplate becomes, lines in Figure 2.64 become closer together, showing that higher reductions in damage can be achieved with more flexible bedplates. The gearbox mount stiffness study similarly found that having a more flexible bedplate contributes greatly to reducing the loading on high speed and generator bearings.

2.9. Summary

This chapter has shown the need to model the whole drivetrain together and not just model individual components assuming they are isolated from the rest of the

Chapter 2 – Static Modelling of the Wind Turbine Drivetrain

structure. Three components have been studied in this section for their effects on the drivetrain bearings: the gearbox mounts, the flexible coupling and the bedplate. In high speed drivetrains, components are individually connected to the bedplate therefore introducing misalignments when loads are applied. Increased flexibility of all of the components reduces loading on the most sensitive bearings, though in the case of gearbox mounts too much of a reduction causes loading to wildly increase.

Chapter 2 References

- [2.1] M. Whittle, *et al.*, "A Parametric Study of the Effect of Generator Misalignment on Bearing Fatigue Life in Wind Turbines," presented at the EWEA 2011, Brussels, 2011.
- [2.2] S. P. Timoshenko, "X. On the transverse vibrations of bars of uniform cross-section," *The London, Edinburgh, and Dublin Philosophical Magazine and Journal of Science*, vol. 43, pp. 125-131, 1922.
- [2.3] Z. Kusculuoglu, *et al.*, "Finite element model of a beam with a piezoceramic patch actuator," *Journal of Sound and Vibration*, vol. 276, pp. 27-44, 2004.
- [2.4] H. Hertz, "On the contact of elastic solids," *J. reine angew. Math*, vol. 92, p. 110, 1881.
- [2.5] M. Huber, "On the theory of elastic solid contact," *Annln. Phys. Lpz*, vol. 14, pp. 153-163, 1904.
- [2.6] K. Entwistle, *Basic principles of the finite element method*: IOM Communications, 1999.
- [2.7] R. Guyan, "Reduction of stiffness and mass matrices," *AIAA Journal*, vol. 3, pp. 380-380, 1965.
- [2.8] W. C. Durham, *et al.*, "Coupling of substructures for dynamic analyses," *AIAA Journal*, vol. 6, pp. 1313-1319, 1968.
- [2.9] R. R. Craig Jr and C.-J. Chang, "On the use of attachment modes in substructure coupling for dynamic analysis," *transformation*, vol. 10, p. 3, 1977.
- [2.10] H. Polinder, *et al.*, "Comparison of Direct Drive and Geared Generator Concepts for Wind Turbines," *IEEE Transactions of Energy Conversion*, vol. 21, September 2006 2006.
- [2.11] J. Coultate, *et al.*, "The Impact of Gearbox Housing and Planet Carrier Flexibility on Wind Turbine Gearbox Durability," in *EWEA 2009*, Marseille, France, 2009.

Chapter 2 – Static Modelling of the Wind Turbine Drivetrain

- [2.12] A. Palmgren, "The Service Life of ball bearings," *ZVDI*, vol. 68, pp. 339-341, 1924.
- [2.13] G. Lundberg and A. Palmgren, "Dynamic Capacity of Roller Bearings," in *Acta Polytechnica Mechanical Engineering Series* vol. 1, ed. Stockholm, Sweden, 1947.
- [2.14] W. Weibull, *The phenomenon of rupture in solids: Generalstabens Litografiska Anst.*, 1939.
- [2.15] E. V. Zaretsky, *et al.*, "Relation between Hertz stress-life exponent, ball-race conformity, and ball bearing life," *Tribology Transactions*, vol. 51, pp. 150-159, 2008.
- [2.16] M. A. Miner, "Cumulative Damage in Fatigue," *Journal of Applied Mechanics*, pp. 159-164, 1945

3.

Transient Loading of the Wind Turbine

Nomenclature

Symbol	Explanation	Unit
A	1 dimensional flow area	m
a	Axial induction factor	
a'	Rotational induction factor	
c	Chord length of the blades	m
C_L	Lift coefficient	
C_D	Drag coefficient	
C_P	Power coefficient	
C_T	Torque coefficient	
D	Tower Diameter	m
g	Gravitational acceleration, 9.81 ms^{-1} on Earth	ms^{-1}
h	Height from a reference point	m
K	Stiffness Matrix	Nm^{-1}
k	Von Karman constant (approximately 0.4)	
M	Mass Matrix	kg
\dot{m}	Mass flow rate	kgs^{-1}
p	Pressure	Nm^{-2}
Q	Momentum of fluid around rotor	kgms^{-1}
r	Radius from centre of rotation to desired point on blade	m
U	Wind speed	ms^{-1}
U*	Friction velocity	ms^{-1}
W	Total velocity magnitude of the flow acting on the blade	ms^{-1}
z	Height above the ground	m
z_0	Surface roughness length	m
α	Angle of attack of the blade to the incoming flow	rad
β	Angle the blade is forced from the in plane line of rotation	rad
λ	Local speed ratio	
ρ	Density of the air flow	kgm^{-3}
φ	Angle from in plane line of rotation to resolved flow angle	rad
Ψ_s	A function that depends on stability of the air flow	
Ω	Blade rotational speed	rads^{-1}
ω	Natural Frequency	rads^{-1}

Subscripts

Symbol	Explanation
∞	Free Stream Position
d	Rotor Disc Position
W	Far Wake Position

3.1. Energy in the Wind

Energy in the wind is kinetic energy due to the mass of the air and its velocity. The mass flow rate, \dot{m} , through an area is given by $\dot{m} = \rho AU$

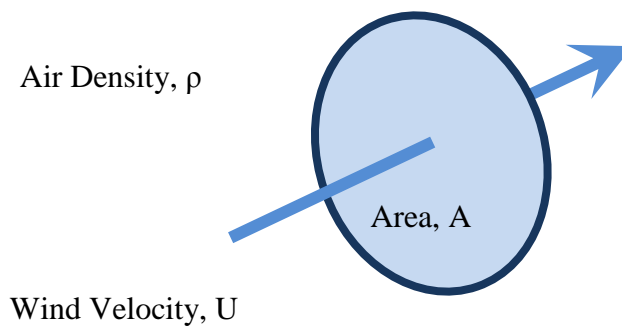


Figure 3.65 - Mass Flow Rate through a given Area

Power flowing through the area is given by $P = 1/2\dot{m}U^2$ meaning that available power in the wind is proportional to wind speed cubed, $P \propto U^3$. Energy in the wind is therefore highly dependent on wind speed [3.1].

3.2. Aerodynamic Models

Accurate aerodynamic models are important to reliably predict loading coming onto the wind turbine drivetrain. Incoming wind holds energy that is extracted through the blades of the wind turbine. The disc actuator model and blade element momentum theory can be used to find the amount of energy extracted from the wind by the wind turbine.

3.2.1. Disc Actuator Model

The disc actuator model predicts the airflow through a wind turbine. Betz [3.2] showed how the maximum energy that a wind turbine can extract from an airflow, the Betz Limit = 0.593, can be calculated. Although Betz has been credited solely for discovering this theoretical limit others achieved this result at around the same time [3.3]. Lanchester [3.4] and Joukowsky [3.5] discover similar limits; Lanchester for helicopter and screw propellers and Joukowsky derived the same limit for wind turbines.

Glauert [3.6] proposed a one dimensional representation of the airflow replacing the complex wind turbine shape and dynamics with a representative disc. This model allows a one dimensional estimation of the flow across the wind turbine rotor and therefore predicts the maximum power available to the wind turbine. This model has been successfully used for design of wind turbines [3.7] and has also been expanded to include an array of wind turbines each with its own actuator disc [3.8]. Disc Actuator theory is not solely of use to the wind turbine industry but has other uses outside this [3.9].

The actuator disc model is the most basic aerodynamic model used to describe the energy the wind turbine extracts from the wind. It is a very simple model that predicts energy available in the wind at the wind turbine by calculating kinetic energy in a stream tube before and after the wind turbine. As the flow slows in front of the wind turbine, static pressure increases to satisfy conservation of energy and the flow expands. Energy is extracted from the system across the rotor disc where a static pressure drop occurs, as displayed in Figure 3.66b. Pressure drops below ambient in the near wake and recovers to ambient in the far wake coupled with further flow expansion. An important assumption that the disc actuator model uses is that no flow crosses the stream tube so there is no mixing of air between the inside and outside of the stream tube.

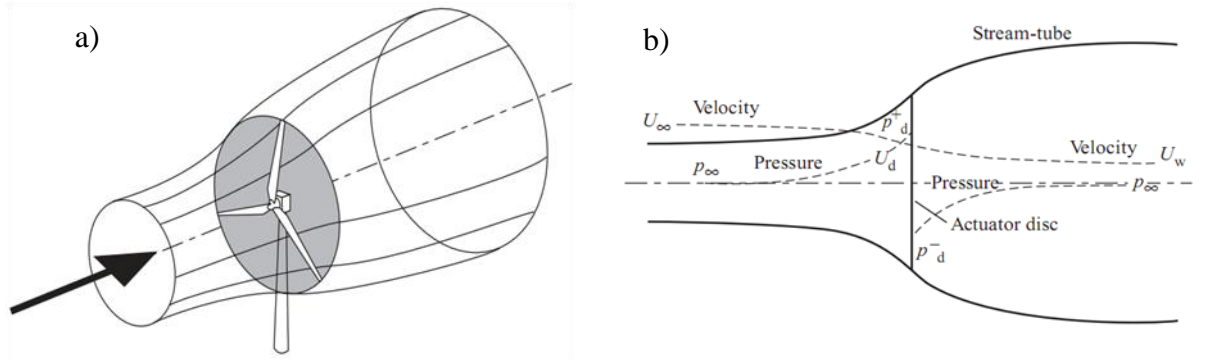


Figure 3.66 - Actuator Disc Model a) 3D representation of Stream Tube, b) 1D Actuator Disc representation

The wind turbine has a blocking effect on incoming flow causing it to slow down and the streamtube to expand. An axial induction factor, a , is introduced to describe the slowing down of the air in front of the wind turbine. The velocity of the flow at the rotor disc becomes:

$$U_d = U_\infty(1 - a) \quad (3.27)$$

The upstream velocity, U_∞ , slows to U_d at the rotor and further to U_w in the far wake. Using Bernoulli's equation and conservation of energy on upstream and downstream sides, the amount of energy extracted from the wind can be found. Conservation of mass in the stream tube is also used to find the velocities along the stream tube. Bernoulli's equation is given by:

$$p + \frac{\rho U^2}{2} + \rho gh = \text{constant} \quad (3.28)$$

Conservation of mass for the stream tube gives:

$$\rho A_\infty U_\infty = \rho A_d U_d = \rho A_w U_w \quad (3.29)$$

Momentum change is given by mass flow rate multiplied by total change in velocity from upstream flow to downstream far wake, which equates to change in pressure at the rotor disc.

$$(p_d^+ - p_d^-) = (U_\infty - U_w)\rho A_d U_\infty(1 - a) \quad (3.30)$$

Flow at all points can be calculated using Bernoulli's equation.

$$p_\infty + \frac{1}{2}\rho_\infty U_\infty^2 + \rho_\infty gh = p_d^+ + \frac{1}{2}\rho_d U_d^2 + \rho_d gh \quad (3.31)$$

Since flows are low speed the air can be treated as incompressible and the assumption can be made that $\rho_\infty = \rho_d = \rho_w$. Flow is approximately horizontal,

Chapter 3 – Transient Loading of the Wind Turbine

therefore h is constant, and ambient pressure of the flow upstream is equal to ambient pressure in the far wake. Bernoulli's equation for the upstream wind can be reduced to

$$p_{\infty} + \frac{1}{2}\rho U_{\infty}^2 = p_d^+ + \frac{1}{2}\rho U_d^2 \quad (3.32)$$

The downstream side can be calculated in a similar manner

$$p_{\infty} + \frac{1}{2}\rho U_w^2 = p_d^- + \frac{1}{2}\rho U_d^2 \quad (3.33)$$

Upstream and downstream equations can be subtracted to give the total change in pressure of the system. Combined with the change momentum equation this gives

$$\frac{1}{2}\rho(U_{\infty}^2 - U_w^2)A_d = (U_{\infty} - U_w)\rho A_d U_{\infty}(1 - a) \quad (3.34)$$

From this equation the free stream velocity can be related to the downstream wake velocity showing that half the reduction in the velocity is upstream of the turbine while the other half the reduction is downstream.

$$U_w = (1 - 2a)U_{\infty} \quad (3.35)$$

One of the outcomes from disc actuator theory is a theoretical limit for the maximum amount of power that can possibly be extracted from a wind turbine rotor, the Betz limit. The Betz limit showed that the theoretical maximum power that could be extracted from the wind was 59.3% of the power available in the free stream when an axial induction factor of $\frac{1}{3}$ is used. The power and thrust coefficient is given as

$$\frac{\text{Extracted Power}}{\text{Theoretical Power}} = C_p = 4a(1 - a)^2 \quad (3.36)$$

$$\frac{\text{Extracted Torque}}{\text{Theoretical Torque}} = C_T = 4a(1 - a) \quad (3.37)$$

3.2.2. Rotor Disc Theory

Wake rotation can also be calculated using a similar 1 dimensional model to the disc actuator method. A rotational induction factor, a' is introduced to account for the rotation of the wake. Boundary conditions for rotor disc theory are different to disc actuator as motion in the wake is rotational with no initial rotational velocity upstream of the rotor.

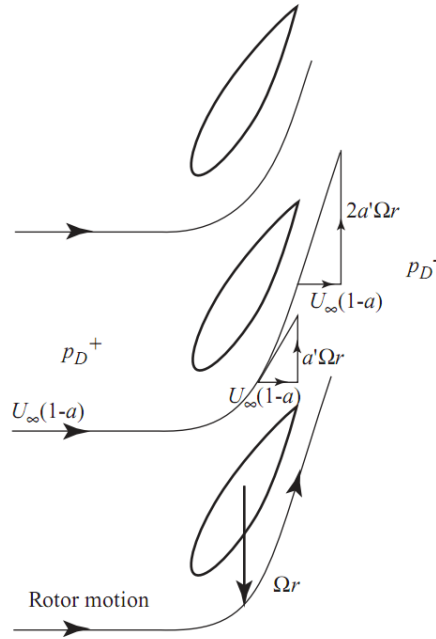


Figure 3.67 - Rotor Disc Theory

Figure 3.67 shows the total change in angular momentum of the air flow around and aerofoil given by

$$\delta Q = \rho \delta A_d U_\infty (1-a) \times 2\Omega a' r \times r \quad (3.38)$$

Through the power output equations the axial induction, a , can be related to the rotational reduction factor, a' , where λ is the local speed ratio given by $\lambda = \frac{\Omega r}{U_\infty}$,

$$a(1-a) = \lambda^2 a' \quad (3.39)$$

3.2.3. Blade Element Momentum Theory

Blade element momentum (BEM) theory uses change of momentum of air flow around the blades solely as the mechanism of force transfer onto the blades [3.1]. BEM splits blades up into independent sections with aerofoil properties therefore knowledge of the lift and drag coefficients is required for each aerofoil section used. Abbott and Von Dornhoff [3.10] describe theoretical and experimental results for the aerodynamics of the NACA aerofoils series providing lift and drag coefficient for an array of aerofoils. Glauert [3.11] was first to suggest BEM for use on aircraft propellers; since then BEM has been experimentally tested and found to adequately represent loading on the wind turbine [3.12].

Chapter 3 – Transient Loading of the Wind Turbine

BEM theory utilizes the two-dimensional characteristics of blades using angle of attack to the flow to find lift and drag forces over a swept area of the blade. As mentioned, a major assumption that BEM uses is that forces created on the blades come entirely from changes in momentum of the air flow across the blade surface. Other assumptions that BEM theory makes is that any flow in the span wise direction is ignored and three-dimensional effects on the blade are ignored.

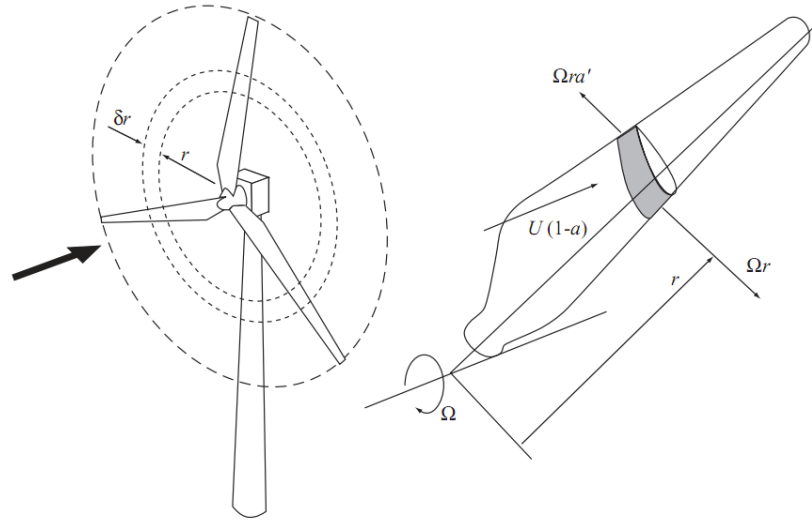


Figure 3.68 - Blade Element Theory

As torque is found from force multiplied by radius, the differential ring at a specified radius is shown in Figure 3.68. Torque developed on the blades is given by:

$$dT = \frac{1}{2} \rho W^2 c (C_L \cos \phi + C_D \sin \phi) r dr \quad (3.40)$$

As flow seen on blades is a mixture of axial wind flow and tangential velocity created by rotation of the rotor the wind speed magnitude, W , and angle, ϕ , of the incoming flow to the rotor disc is given by

$$W = \sqrt{U_\infty^2 (1-a)^2 + \Omega^2 r^2 (1+a')^2} \quad (3.41)$$

$$\phi = \tan^{-1} \left(\frac{U_\infty (1-a)}{\Omega r (1+a')} \right) \quad (3.42)$$

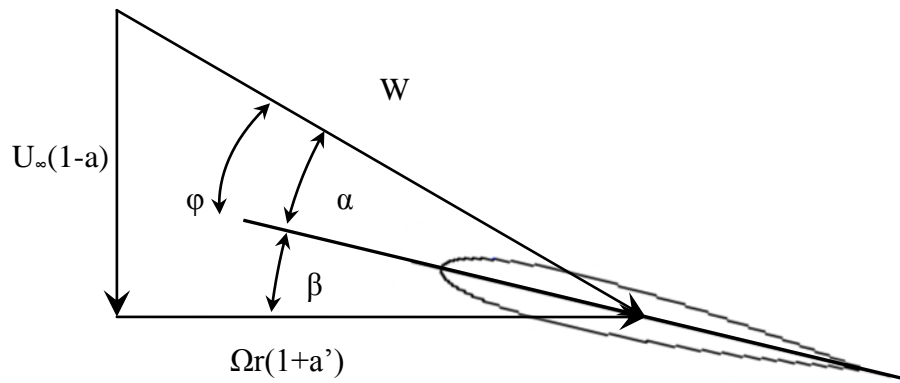


Figure 3.69 - Flow Angles on Blade

Angle of attack, α , and pitched angle, β , are shown in Figure 3.69. Lift and drag coefficients vary with angle of attack: Figure 3.70 shows the variation in C_L and C_D over a 360° change in angle of attack, α , for the prototype blade DU21 A17.

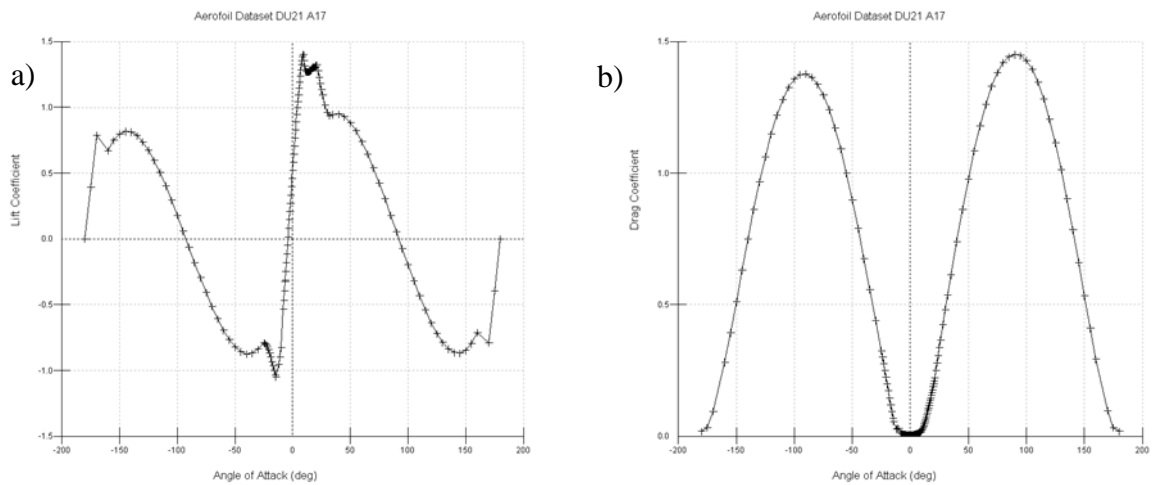


Figure 3.70 – Coefficients for Changing Angle of Attack a) Lift and b) Drag

The greatest lift force that is seen is at an angle of attack of 9.5° . Above this the blade begins to enter stall and the lift coefficient is lower but also uncertain. High angles of attack further reduce the lift coefficient of the aerofoil. The drag coefficient is different; it is very low until stall occurs but it then builds up to a peak at approximately 90° with minimums at 0° and 180° . When in operation blades function ideally at the greatest lift to drag ratio.

Chapter 3 – Transient Loading of the Wind Turbine

Using these coefficients lift and drag forces, L and D respectively, can be found:

$$L = \frac{1}{2} \rho A C_L W^2 \quad (3.43)$$

$$D = \frac{1}{2} \rho A C_D W^2 \quad (3.44)$$

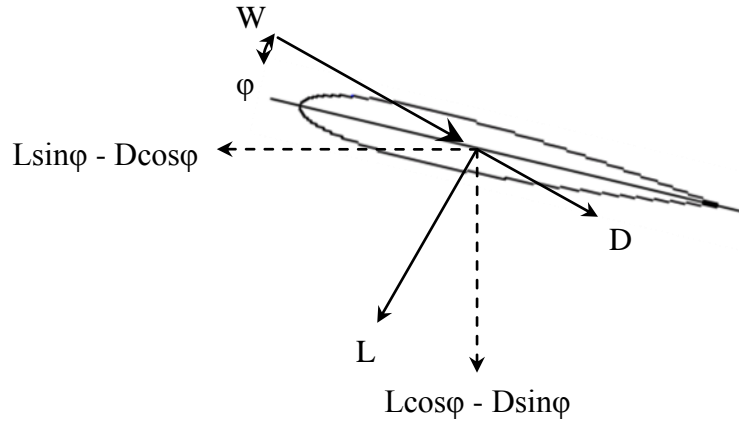


Figure 3.71 - Resolved Blade Forces

Resolving lift and drag forces into an axial force and a rotational force gives the external forces that can be used in the dynamic equations. The axial force, used in finding the structural deflections and bending moments is given by:

$$Axial\ Force = (L \cos \phi - D \sin \phi) \quad (3.45)$$

Torque developed for power production is given by:

$$\delta T = (L \cos \phi - D \sin \phi) \delta r \quad (3.46)$$

3.2.4. Computational Fluid Dynamics

Computational Fluid Dynamics (CFD) is a numerical method used to predict fluid flow around surfaces. Fluid is discretized into cells, similar to finite element, and the Navier-Stokes equations are solved iteratively to converge on a solution [3.13]. Originally CFD was only used statically to analyse wind turbine blades allowing the equations to converge on the solution, though good results were obtained when compared to experiments [3.14]. Currently CFD is being used to dynamically to predict loading on the complete wind turbine during operation [3.15]. However, CFD is too time consuming for routine application to the calculation of wind turbine rotor loads and BEM analysis predominates in commercial design analysis.

3.2.5. Discrete Vortex Method Aerodynamics

The obvious drawback that CFD has is due to the grid structure moving/rotating making it difficult to accurately capture the loading. The discrete vortex method is a gridless system that allows movement of the bluff bodies, fluctuating lift coefficients and surface pressure coefficients [3.16-3.17]. This method may provide more accurate aerodynamic load predictions for wind turbine blades than BEM but is not yet used by commercial wind turbine designers.

3.2.6. Wind Shear

Wind shear is an effect caused by the presence of a boundary layer in the earth's atmosphere. At ground level the no slip principle can be applied meaning that the wind speed is effectively zero. Wind turbine rotors are now so large that substantial differences in the wind speed can be seen at extremes of the swept area; the wind velocity experienced at the top of the cycle is different to the wind speed at the bottom of the cycle. Figure 3.72 is a diagram of what the boundary layer may look like. Above approximately 2000m there is relatively little change to the free stream velocity, below this however, where wind turbines operate, there is a substantial change in wind velocity.

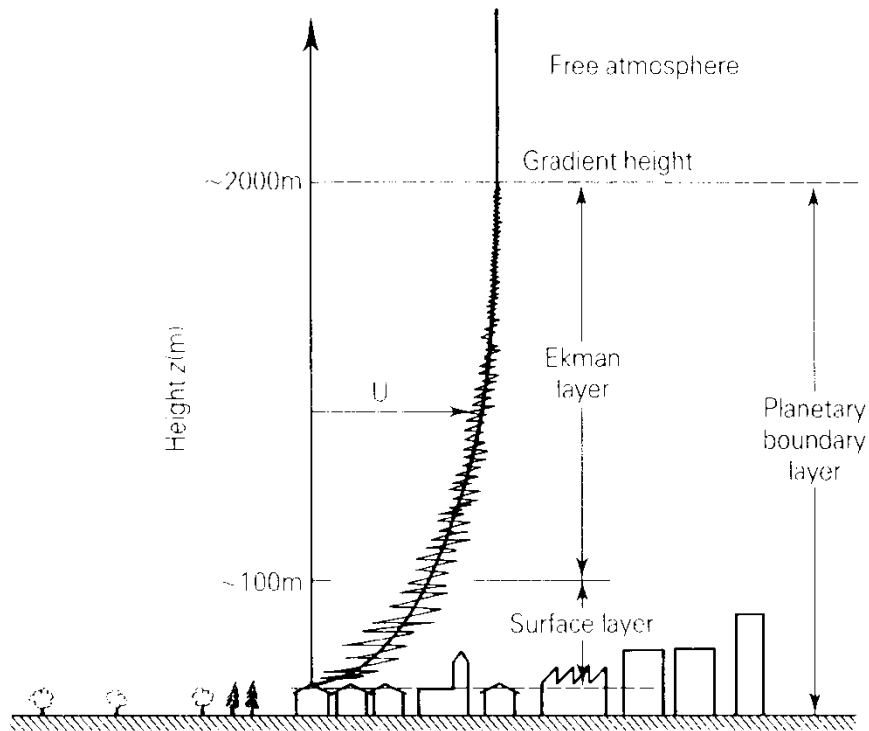


Figure 3.72 - Wind Speed Boundary Layer [3.18]

The wind speed in the boundary layer can be approximated by:

$$U(z) = \frac{U^*}{k} \left[\ln\left(\frac{z}{z_0}\right) + \psi_s\left(\frac{z}{L_s}\right) \right] \quad z \gg z_0 \quad (3.47)$$

The type of surface will obviously cause differences in the initial recovery of the boundary layer. Variable z_0 is the surface roughness length and determines the wind shear profile, i.e. the rate at which the boundary layer recovers to free stream velocity moving away from the surface. Table 3.4 shows z_0 values for some typical environments.

Table 3.4 - Surface Roughness Lengths

Type of terrain	z_0
Mud Flats, Ice	10^{-5} to 3×10^{-5}
Calm Sea	2×10^{-4} to 3×10^{-4}
Sand	2×10^{-4} to 10^{-3}
Mown Grass	0.001 to 0.01
Low Grass	0.01 to 0.04
Fallow Field	0.02 to 0.03
High Grass	0.04 to 0.1
Forest and Woodland	0.1 to 1
Built up area, Suburb	1 to 2
City	1 to 4

Since differences in wind speed occur between the top and bottom of the rotor, periodic loading is seen on the wind turbine. For a three bladed rotor, the greater loading at the top than the bottom causes a harmonic, seen by the turbine as a whole, at 3 times the rotational speed of the rotor.

3.2.7. Tower Shadow

Tower shadow is an effect that causes a reduction in wind speed and thus loading on the blades. The tower, a necessary component to hold the rotor and drivetrain at the required hub height, has a blocking effect on upstream wind and causes the wind speed to substantially reduce in front of the tower as well as in the wake, similar to that of the rotor in the disc actuator theory. Tubular towers have a greater blocking effect than lattice towers [3.1] due to the larger frontal area. Consequences of this effect are that blades encounter a lower wind speed in front of the tower causing a sharp drop in loading. The velocity deficit for an upwind turbine with a tubular tower can be approximated [3.1] by

$$U = U_{\infty} \left(1 - \frac{(D/2)^2 (x^2 - y^2)}{(x^2 + y^2)^2} \right) \quad (3.48)$$

The velocity deficit is related to the tower diameter.

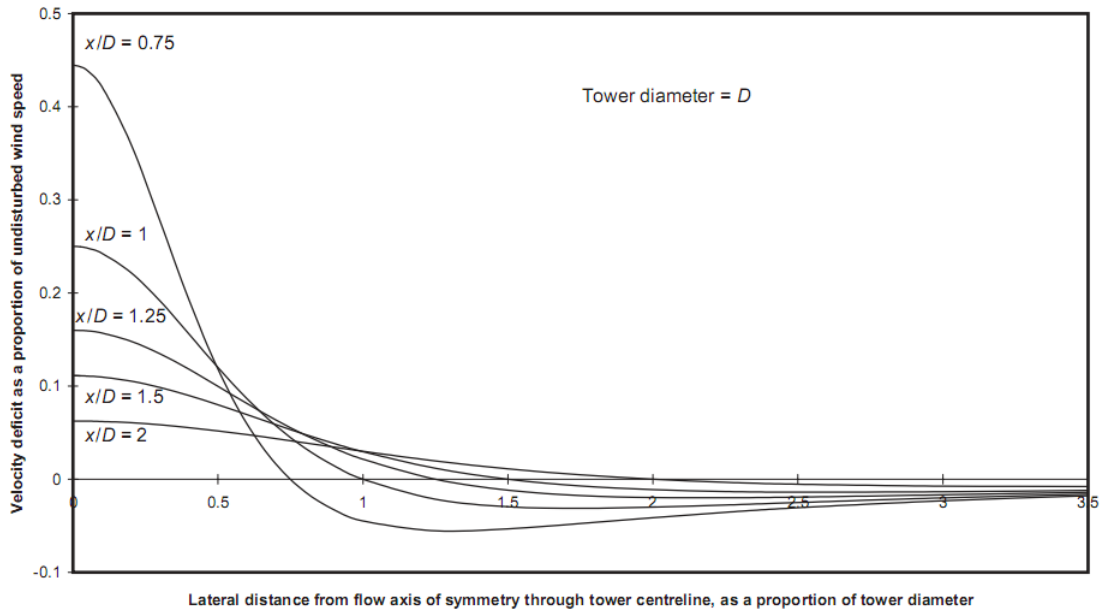


Figure 3.73 - Tower Shadow Deficit [3.1]

The sharp dip in wind speed in front of the tower is more likely to excite blade oscillations than smooth variations due to wind shear. Slight wind speed enhancements occur just around the deficit cause by the wind redistributing around the tower usually ignored though.

3.2.8. Gravity Loading

Rotation of the rotor causes sinusoidal gravity loading on blades. The weight of the blades acts in one direction for half of the rotation and the other direction for the other half of the rotation. A large sinusoidal moment at the root is experienced resisting the blade weight during operation. A large harmonic is excited which is greater than any variation cause by wind shear or tower shadow.

3.3. Structural Loading

Two methods generally used for structural load predictions are modal response and finite element. Finite element can give a fairly accurate representation of structural loads so long as the elements themselves are not overly distorted. In the case of wind turbines, modal representation of the structure is more suited as large relative deflections are involved [3.19] though if deflections become too large, nonlinear modal models will be required [3.20]. Component mode synthesis is use to reduce

complex structures to a series of boundary nodes [3.21]. The response of the model against time can be found.

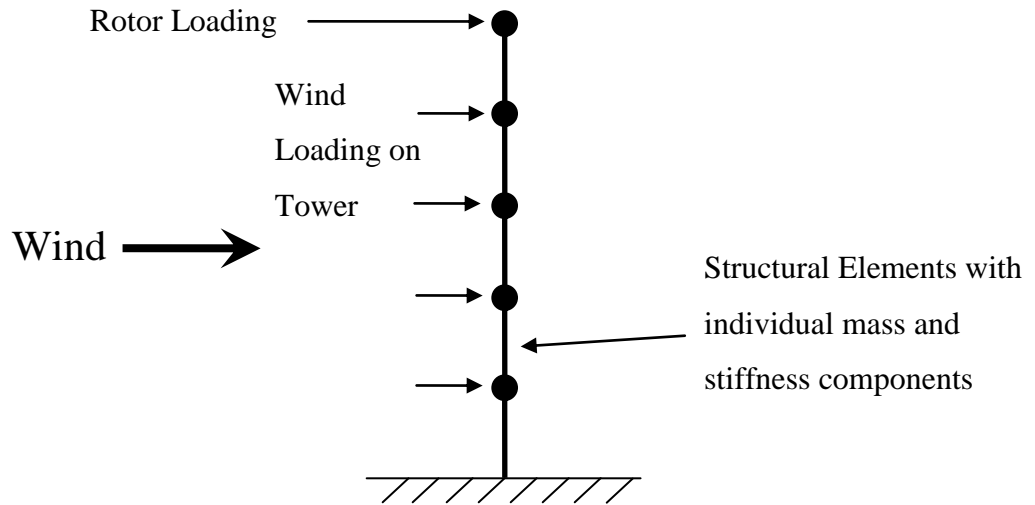


Figure 3.74 - Tower Model and Loading

He and Fu [3.22] describe how modal analysis can be used to analyse structures. Basics of modal analysis are covered with an overview of the required mathematics for analysing multi degrees of freedom systems and the application to modal systems.

Deflections of blades are found using the same method, using the lift and drag forces found for estimation of the bending of the blades.

3.4. GH Bladed

GL Garrad Hassan's Bladed is a dynamic software package that simulates the whole wind turbine system: wind resource, aerodynamics, drivetrain, structure and generation. In a wind turbine, dynamics of all these system affect how the wind turbine operates. Bossanyi [3.19, 3.23] outlines how GH Bladed creates and solves the transient response of a wind turbine.

3.4.1. Wind Conditions

Wind fields are created and used for inputs to the wind turbine. The wind input conditions available in the software package can be a steady non varying wind, a 1D

time varying wind or a 3D turbulent wind. GH Bladed has the ability to create 3D turbulent wind files covering the swept area of the rotor.

3.4.2. Aerodynamic Model

GH Bladed uses the disc actuator model with blade element momentum to calculate loading on the wind turbine. Blades are split into 19 stations each with individual aerodynamic profile and mass and stiffness properties. Loading of each section using blade element momentum is aggregated finding the total blade loading and along with other blades the total hub loading.

3.4.3. Drivetrain Model

A simplified drivetrain model is represented in GH Bladed. In the most basic case the drivetrain is represented as a black box where the rotational speed is stepped up and the torque is stepped down by the gearbox ratio. Flexible low speed shaft and high speed shafts can be used in the drivetrain model allowing for representation of some of the drivetrain modes to be included. The drivetrain model is composed of the rotor inertia, lumped gearbox inertia and generator inertia connected through the low speed and high speed shafts. Since the gearbox steps up rotational speed and steps down torque the effects, on the rotor and overall machine dynamics, of the stiffness of the high speed shaft and the inertia of the generator are substantially modified by the gearbox. GH Bladed also has the ability to use a dll files, allowing users to create their own model of the drivetrain.

3.4.4. Control and Generator Model

Modern variable speed wind turbines have the ability to pitch their blades to control torque created on the rotor and transferred through to the drivetrain. This is done through controller algorithms, the simplest being the PI controller. PI controllers use the proportional component to respond to the current difference but the integral component takes into account previous time steps to reduce steady state error. In addition to controlling the blades, the controller also monitors the generator output power to balance the input power through the blades to the output power from the generator. By controlling the output power, the generator can also be used to control the rotational speed of the wind turbine: increasing output power above input power slows the wind turbine and vice versa for increasing power.

Chapter 3 – Transient Loading of the Wind Turbine

A simple generator model is used with the wind turbine model. Wind speed and output power are measured and compared to ideal operating curves and the controller creates a demanded torque for the generator based on the differences. Demanded torque is used to control the rotational speed of the wind turbine through unbalanced forces across the drivetrain, controlling the speed and power output of the wind turbine.

3.5. Wind Turbine Model

This investigation uses a 2MW variable speed three bladed upwind Danish concept wind turbine. Some basic properties of the wind turbine are shown in Table 3.5.

Table 3.5 - Wind Turbine Properties

Property	
Gearbox Ratio	84.15
Hub Height	65 m
Blade Length	38.2 m
Rotor Diameter	78.4 m
Rotor Mass	33823 kg
Rotor Inertia	4849783 kgm ²
Nacelle Mass	65000 kg

The response of the wind turbine to a steady input at each wind speed, is shown in Figures 3.75 to 3.78.

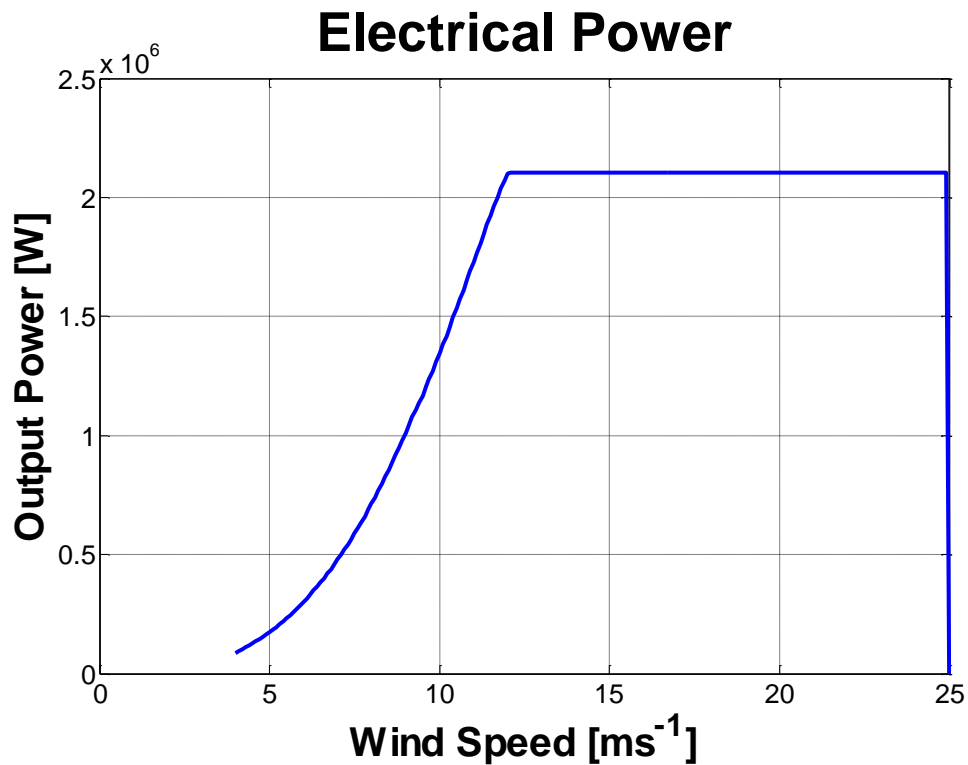


Figure 3.75 - Electrical Power Steady Power Curve

Figure 3.75 shows how output power increases as wind speed increases. When the wind speed reaches 12 ms^{-1} the control strategy limits incoming power by pitching the blades (Figure 3.77) to limits loading on components at higher wind speeds. If the turbine was to continue extracting the maximum amount of energy from the wind, the generator would need to be rated higher to cope with the increased power transfer and other components such as the gearbox and tower would also need to be able to withstand greater loads. At 25 ms^{-1} the wind turbine shuts down and pitches out of the wind to prevent overloading: at these high wind speeds the turbine would likely be damaged if still in operation.

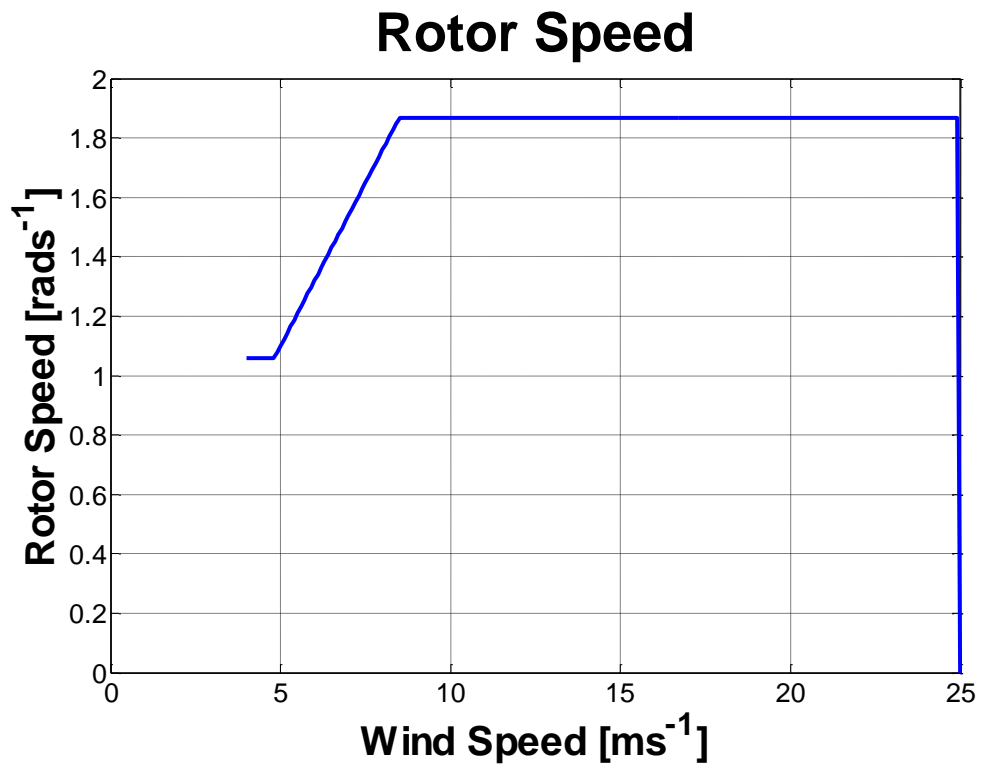


Figure 3.76 - Rotor Speed Steady Power Curve

Rotor speed for the steady power curve shows an almost linear increase as wind speed increases. Again above 12 ms⁻¹ the rotor speed remains constant reflecting the pitching strategy resulting in constant power and torque input to the wind turbine.

Pitch Angle

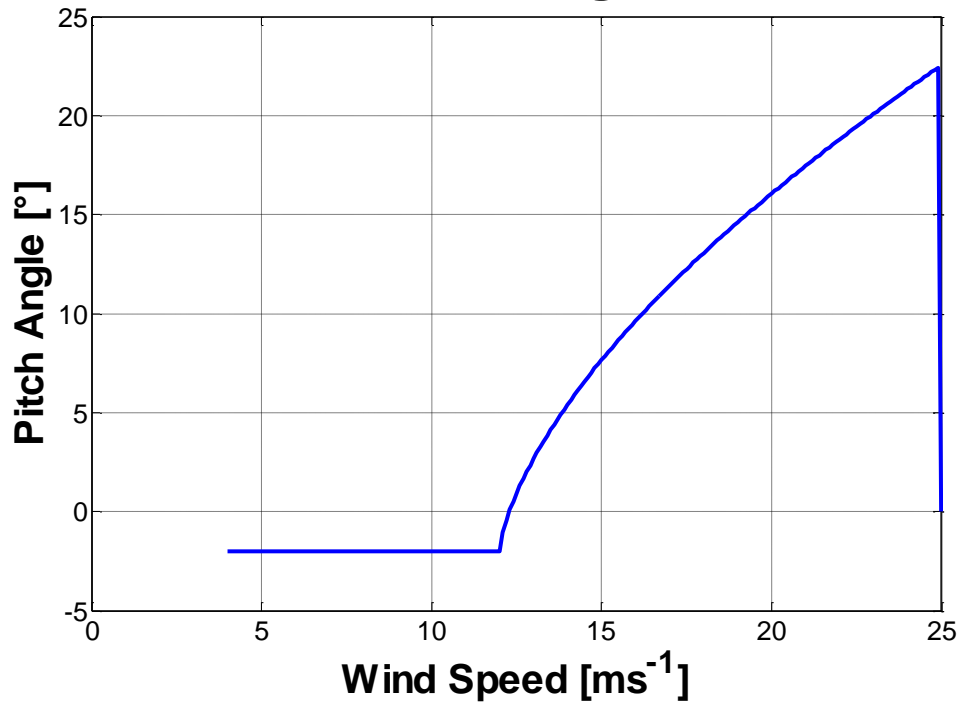


Figure 3.77 - Pitch Angle Steady Power Curve

Aerodynamic Torque

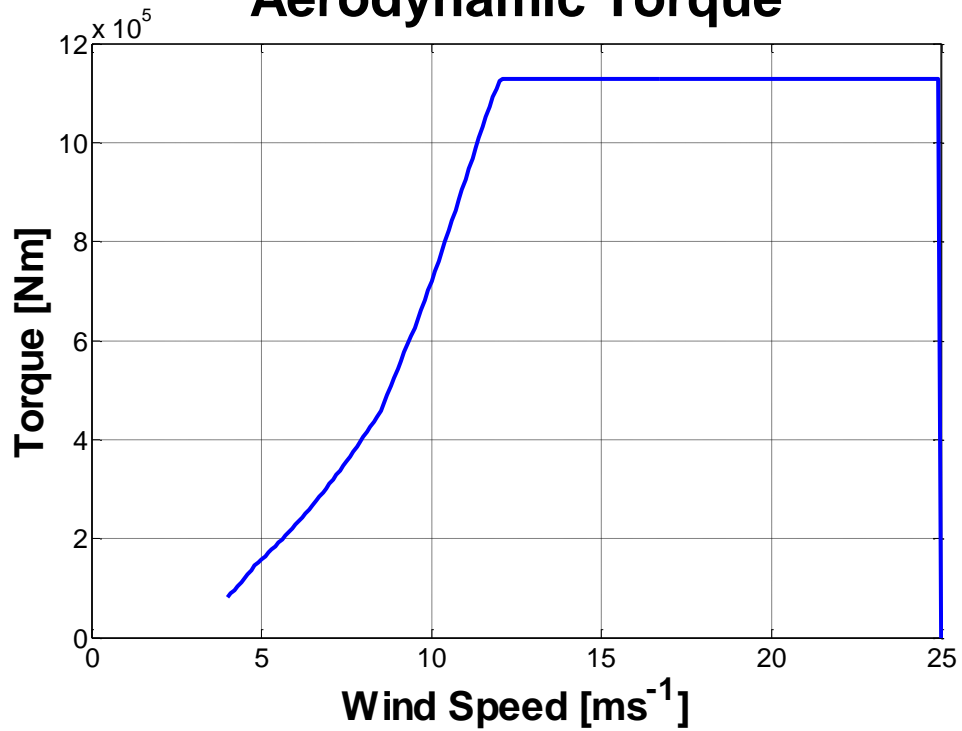


Figure 3.78 - Aerodynamic Torque Steady Power Curve

Chapter 3 – Transient Loading of the Wind Turbine

Aerodynamic torque and blade pitch angle are closely linked since pitch angle is important in determining aerodynamic loading. Below 12 ms^{-1} , blades are at the maximum power point tracking position, the optimal angle of attack to extract the most amount of energy from the wind. Above 12 ms^{-1} , torque is required to be shed to limit structural loading, so blades pitch to maintain input torque and rotor speed. Pitch angle continues to increase with wind speed of until 25 ms^{-1} where the turbine shuts down. Aerodynamic torque reflects the changing pitch angle; when wind speed increases torque remains constant reflecting the blade pitch angles.

3.6. Modal Analysis

Natural frequencies of components in the wind turbine are calculated in GH Bladed before any transient simulations are performed. Natural frequencies are found using eigenvalue analysis where $[K - \omega^2 M] = 0$.

Table 3.6 - Wind Turbine Natural Frequencies

Mode Type	Natural Frequency [Hz]
Blade Flapwise	0.874
Blade Flapwise	2.527
Blade Edgewise	1.388
Blade Edgewise	4.418
Tower Fore-Aft	0.483
Tower Side-Side	0.481
Drivetrain 1 st	3.452
Drivetrain 2 nd	10.155

3.7. Power Production Loading

Power production loading with steady wind speed is the first dynamic simulation performed. A steady wind speed of 12 ms^{-1} with no variations is used eliminating transient inputs from the wind and any response from the wind turbine caused by transient wind. Figure 3.79 shows the rotor speed of the wind turbine when the steady wind field is applied to the turbine; a 10 seconds segment of the response is

shown. Small variations in the rotor speed can be seen, caused by wind shear and tower shadow.

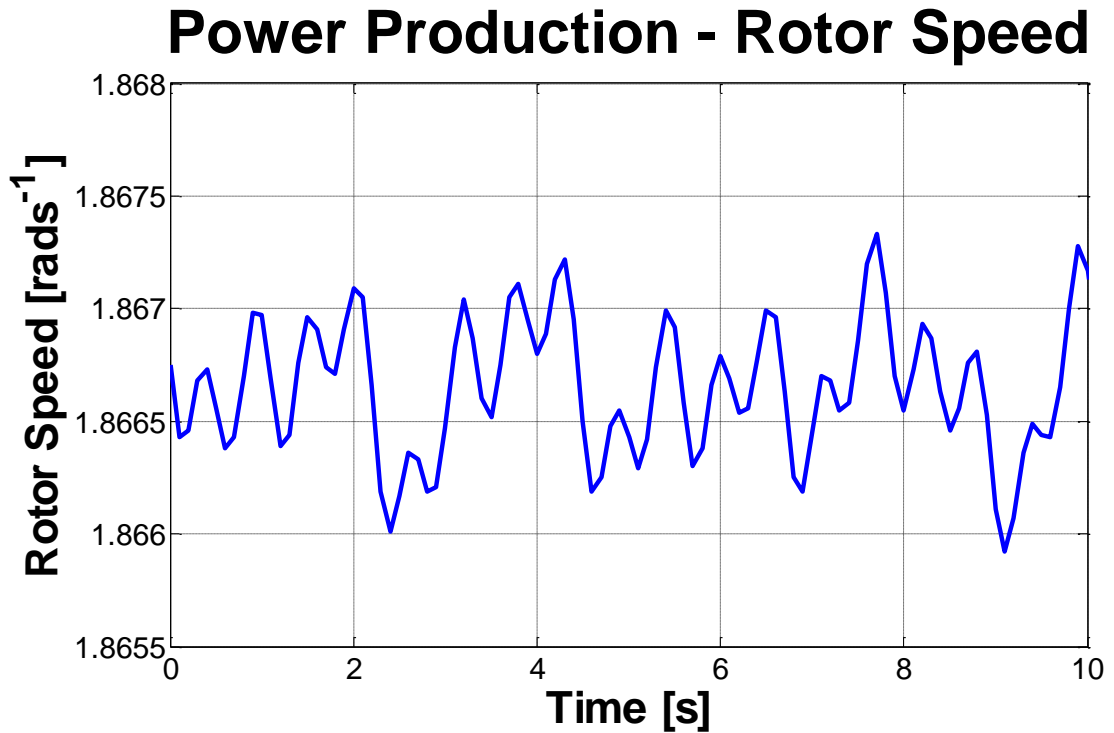


Figure 3.79 - Rotor Speed during Power Production Loading

Effects of wind shear and tower shadow are shown more clearly in the LSS torque response in Figure 3.80. Large oscillations appear at approximately 3 times the rotor speed corresponding to the frequency the blade passes in-front of the tower. A 9% drop in LSS torque occurs due to effects of both wind shear and tower shadow. The significance this has on output power of the turbine is shown in Figure 3.81. Power oscillations vary between 2.046MW and 2.073MW introducing harmonics into the output that require to be removed before export to the grid. These oscillations occur at 3 times the rotor frequency again corresponding to the blade passing frequency.

Power Production - LSS Torque

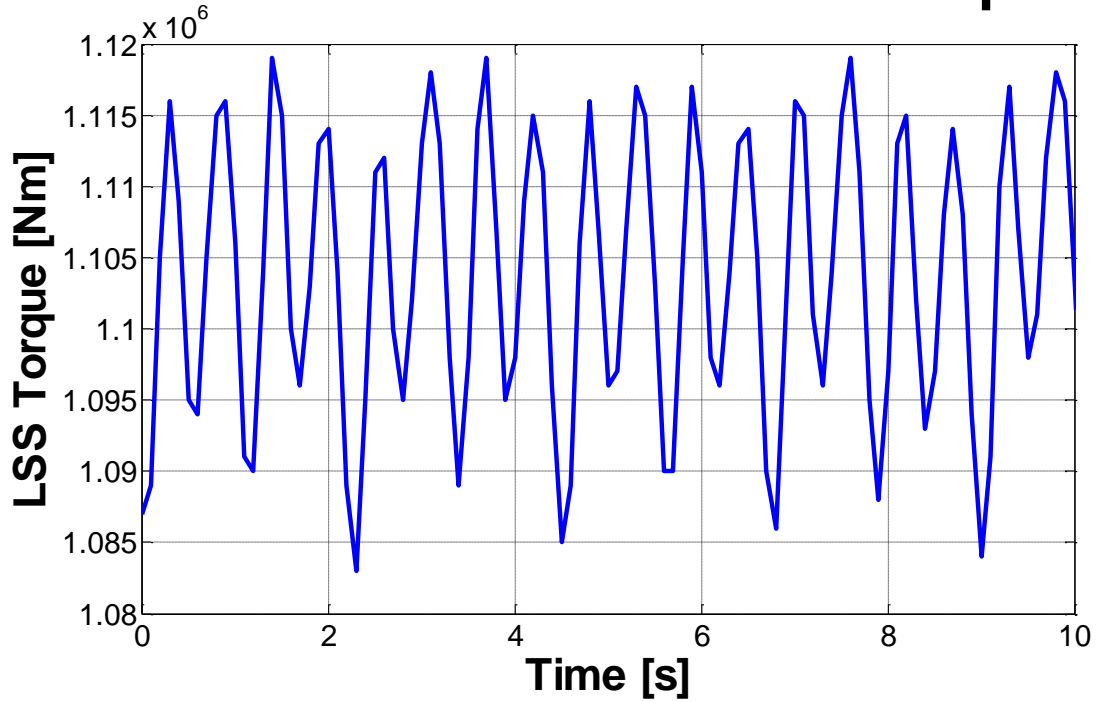


Figure 3.80 - LSS Torque during Power Production Loading

Power Production - Electrical Power

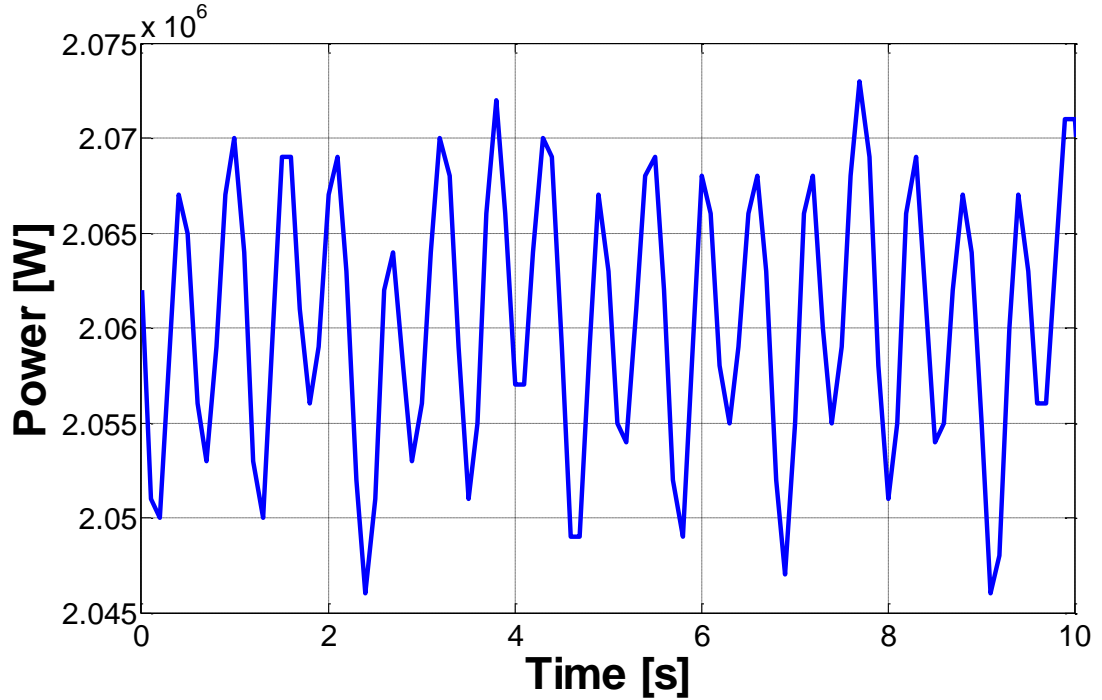


Figure 3.81 - Electrical Power during Power Production Loading

3.8. Normal Stops

On occasion, the turbine may be required to be brought to rest for maintenance purposes. In this case the turbine has to be slowed from operation to rest in a controlled manner. Since time constraints are not a particular issue in these circumstances, the turbine can perform a controlled shutdown avoiding harsh loading wherever possible.

Braking is achieved through a combination of aerodynamic braking from blades and generator reaction torque. Response of the simulated turbine is shown in Figures 3.82 to 3.87. Blades pitch at a controlled rate well within their operating range, $2^\circ/\text{s}$ in this example, until reaching the maximum pitch angle of 88° . The generator reduces demanded torque as the rotor slows down to minimise induced vibrations in the drivetrain. When the rotor has roughly slowed to rest the mechanical brake is applied to the high speed shaft bringing the rotor to a complete halt.

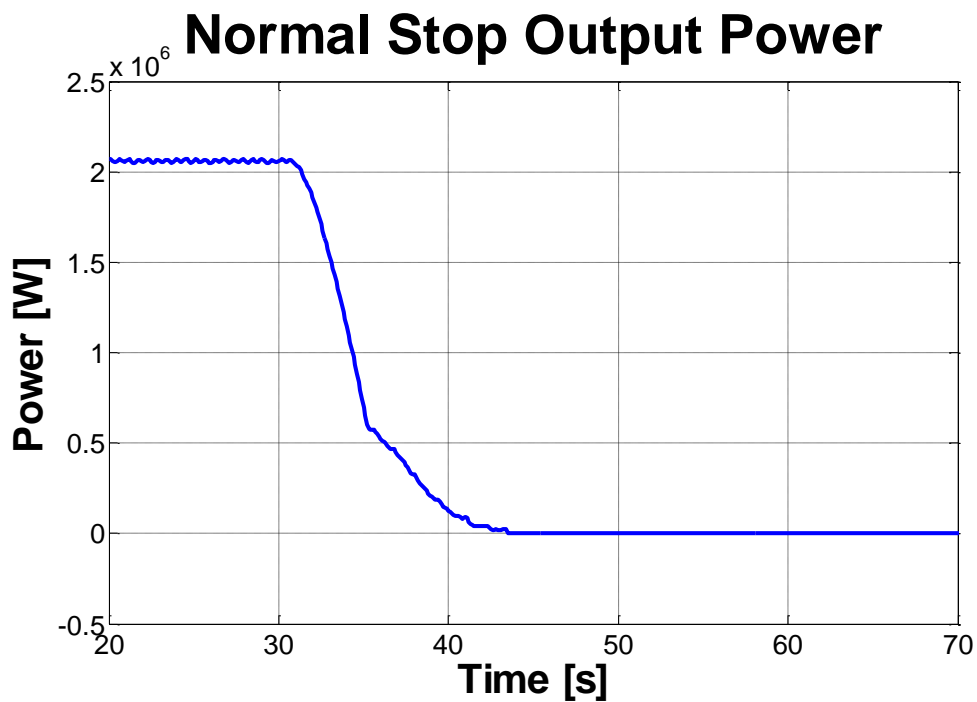


Figure 3.82 - Normal Stop Output Power

Normal Stop Generator Torque

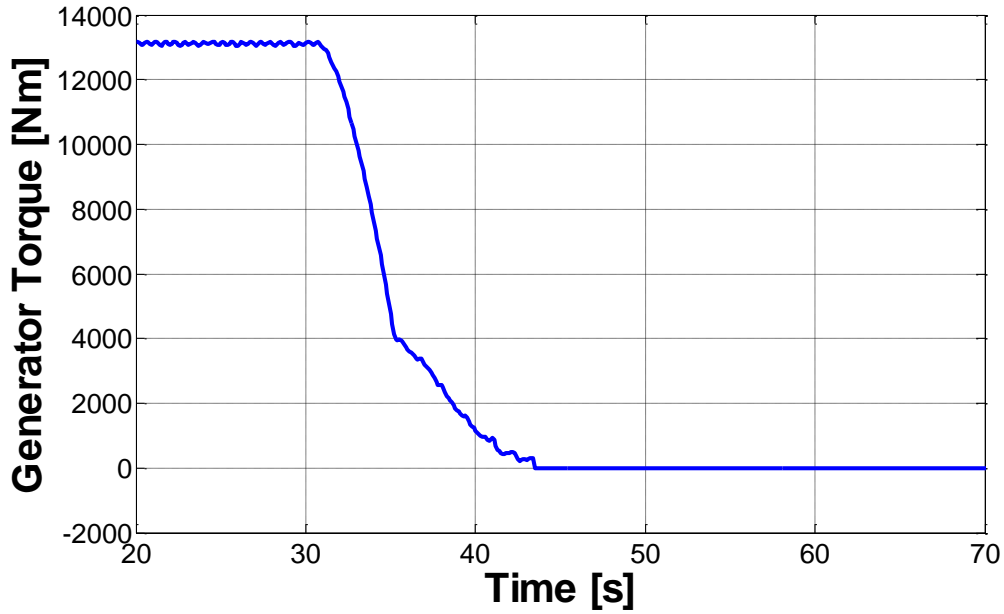


Figure 3.83 - Normal Stop Generator Torque

Normal Stop Rotor Speed

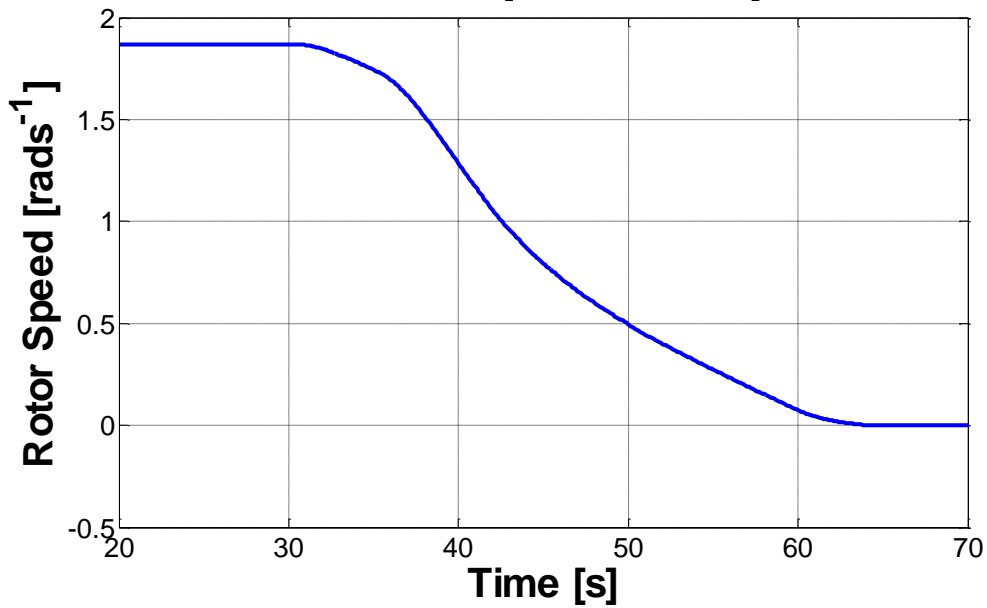


Figure 3.84 - Normal Stop Rotor Speed

A smooth deceleration in rotor speed is achieved due to the controlled manner in which the turbine is brought to rest. In Figure 3.86, harsh oscillations in the LSS torque are not seen because of the aerodynamic brakes, the generator reaction torque and mechanical brake working together. When the rotor comes to rest oscillations are

observed through the drivetrain caused by the blades flexing back and forth on the hub. Since the brake is reacting all the forces through the drivetrain oscillations are seen on the brake reaction torque.

Normal Stop Brake Torque

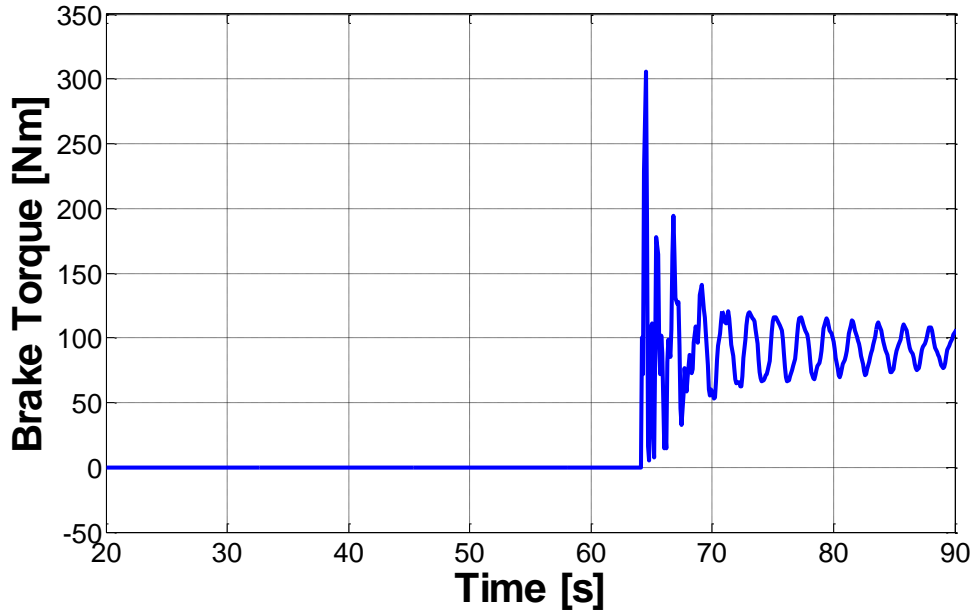


Figure 3.85 - Normal Stop Brake Torque

Normal Stop LSS Torque

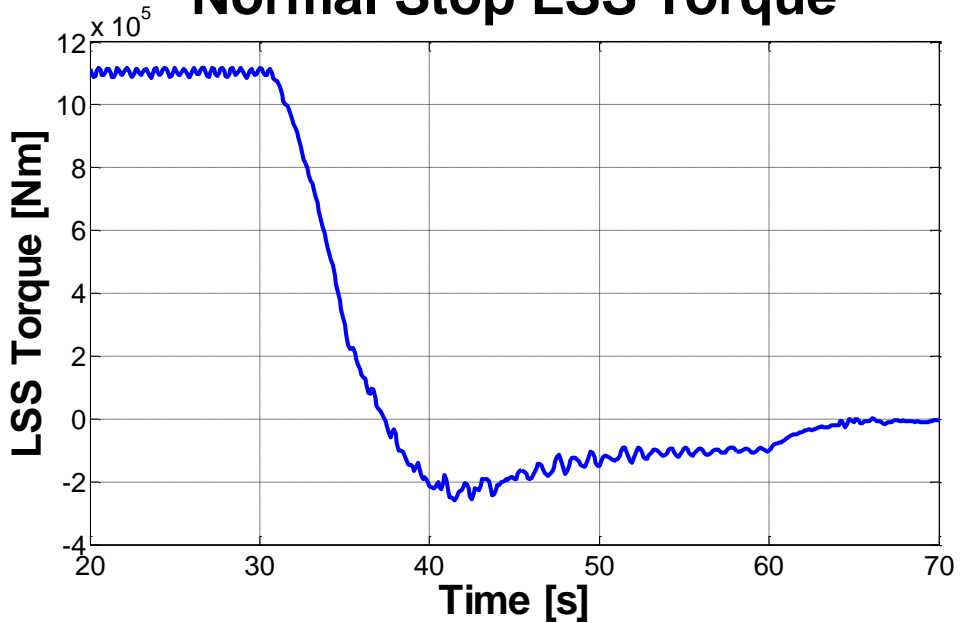


Figure 3.86 - Normal Stop LSS Torque

Normal Stop Pitch Angle

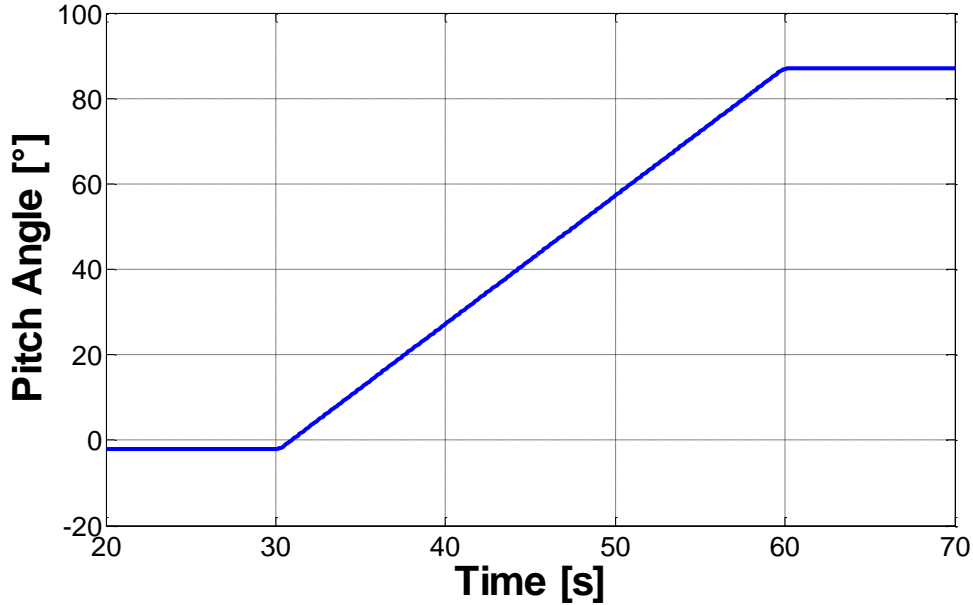


Figure 3.87 - Normal Stop Pitch Angle

3.9. Emergency Stops

The aim of the wind turbine performing an emergency stop is to regain control of the wind turbine and bring the system to rest safely in the fastest way possible in response to a fault (most commonly a loss of grid event). Emergency conditions are dangerous situations where the rotor has the ability to run away uncontrollably unless a fast and effective response occurs. If the rotor manages to run away and cannot be brought back under control disastrous consequences can occur. Tower strikes and blades failures are amongst the failures mechanisms the wind turbine is susceptible to when the rotor runs away.

The emergency stop case studied in this investigation is a grid loss event where the wind turbine loses connection to the grid. In this specific case, reaction torque from the generator immediately drops to zero, unbalancing forces on the wind turbine. The wind turbine then has to regain control of the turbine preventing it from running away and bring the rotor to rest. The grid loss event occurs at 30 seconds where the wind turbine loses electrical connection and therefore the generator reaction torque drops to zero and the power also drops to 0W, shown in Figures 3.88 and 3.89.

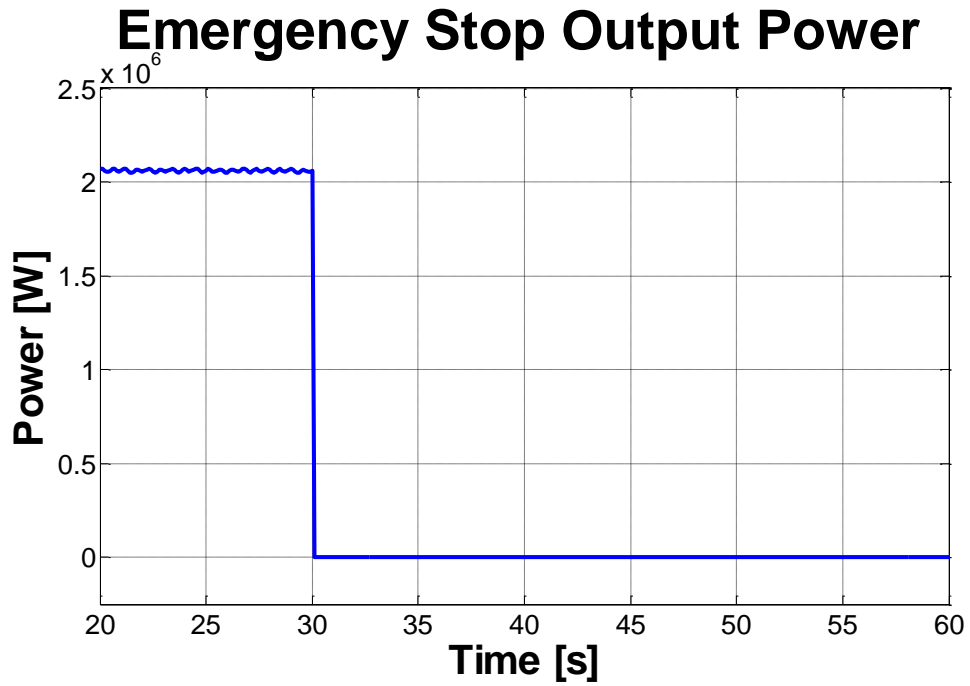


Figure 3.88 - Emergency Stop Power Output

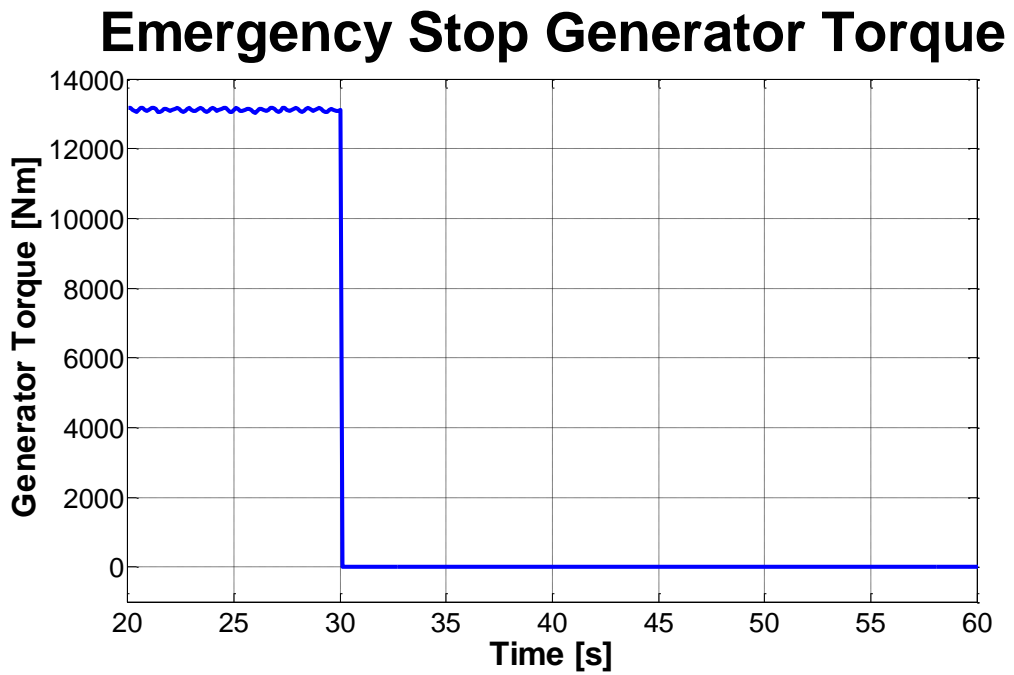


Figure 3.89 - Emergency Stop Generator Torque

Figure 3.90 shows how the rotor speed develops as the grid loss emergency stop take place. When the grid is lost the wind turbine begins the emergency stop sequence; blades pitch at the emergency pitch rate and the mechanical brake is applied to the high speed shaft. The emergency pitch rate is at the maximum permissible rate

Chapter 3 – Transient Loading of the Wind Turbine

allowed by the actuators, $9^\circ/\text{s}$ in this case, until the blades have reached the maximum pitch angle, 87° . In the initial few seconds after the grid loss event the rotor speed increases since the generator torque provides no reaction torque and the blades are still in an operating position. The unbalanced driving force causes the rotor speed to accelerate from 1.86 rads^{-1} to 1.98 rads^{-1} , a 6.4% increase, which is acceptable.

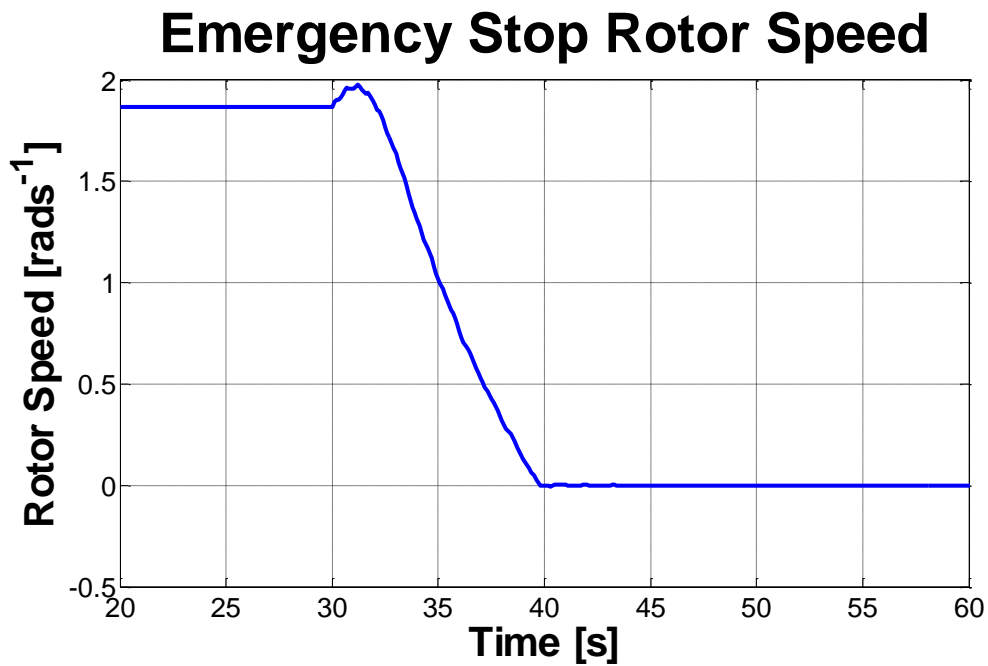


Figure 3.90 - Emergency Stop Rotor Speed

Emergency Stop Pitch Angle

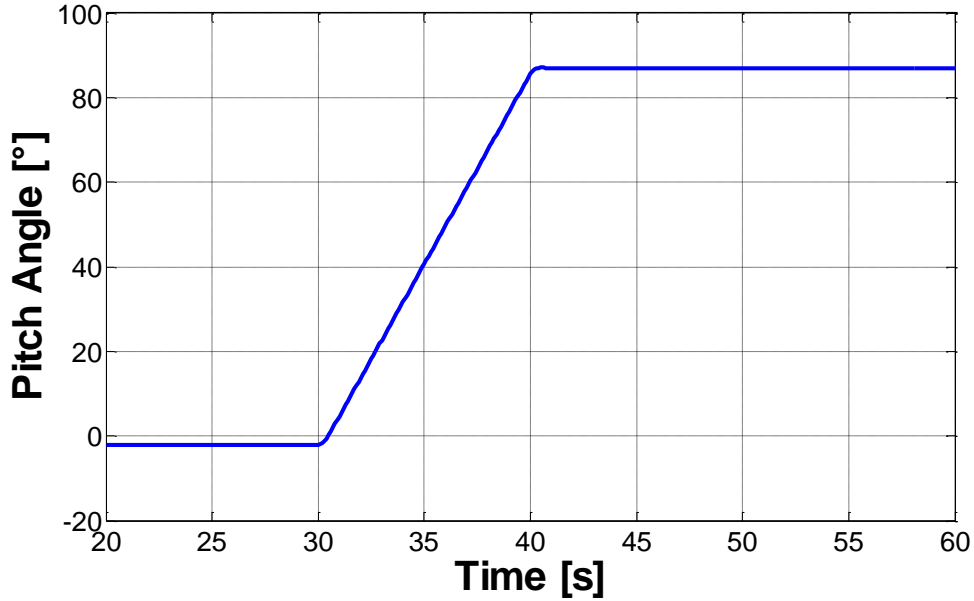


Figure 3.91 - Emergency Stop Blade Pitch Angle

The mechanical brake is not immediately fully applied when the grid is lost; instead a gradual application is used to avoid high amplitude shock loading on the system. Since the generator is unable to provide any torque all the braking effort must come from the blades and the mechanical brake. Although the mechanical brake does a small amount of braking compared to the aerodynamic brakes when the blades pitch, the mechanical brake causes torque on the LSS to remain positive minimising backlash through the drivetrain. Backlash is the phenomenon of reverse loading of the gearbox thought to cause high damage to the gears. Gears lose contact in the forward direction and then come into contact with gear teeth behind with the possibility of high shock loading and high amplitude fatigue loading. By applying the mechanical brake, LSS torque is shifted positively reducing the time, frequency and loading magnitude spent in reverse torque, as shown in Figure 3.93. LSS torque shows two distinct stages during the emergency stop: the first between 30 seconds and 39.8 seconds has a higher frequency with a mean positive torque; the second after 39.8 seconds a different lower frequency seen oscillating around 0Nm. The change in system frequency occurs when the rotor reaches rest. When the system is rotating neither end of the drivetrain is grounded and the system is free to oscillate in an unconstrained manner. When the system comes to rest the mechanical brake

effectively cuts the drivetrain in two where each is grounded at the mechanical brake displayed in Figure 3.94. The natural frequency of the system therefore changes and two distinct frequencies are seen in the LSS torque graph.

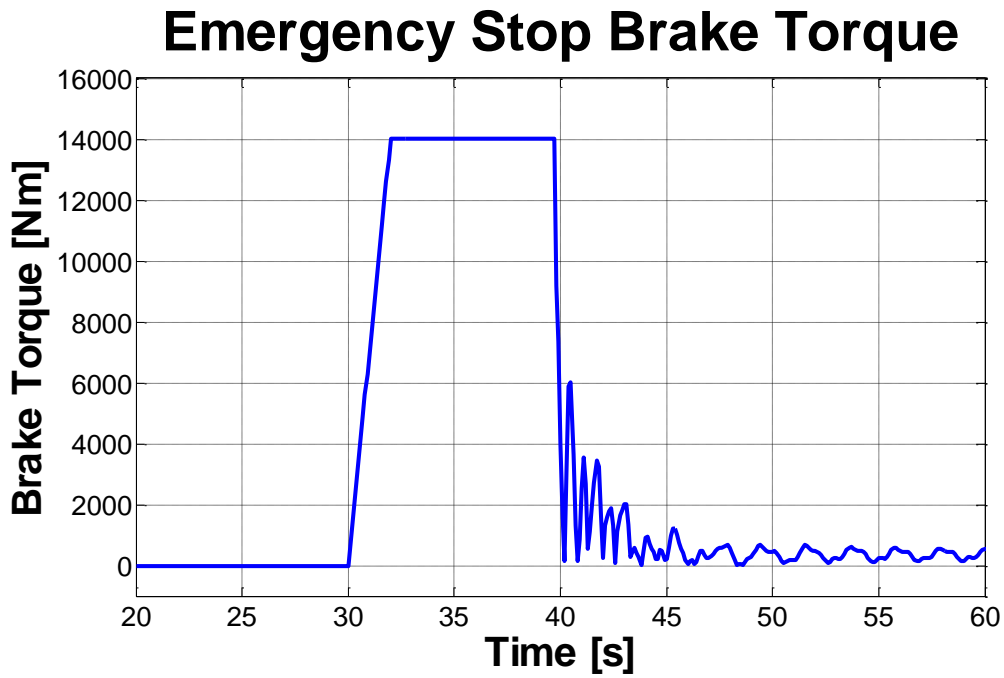


Figure 3.92 - Emergency Stop Mechanical Brake Torque

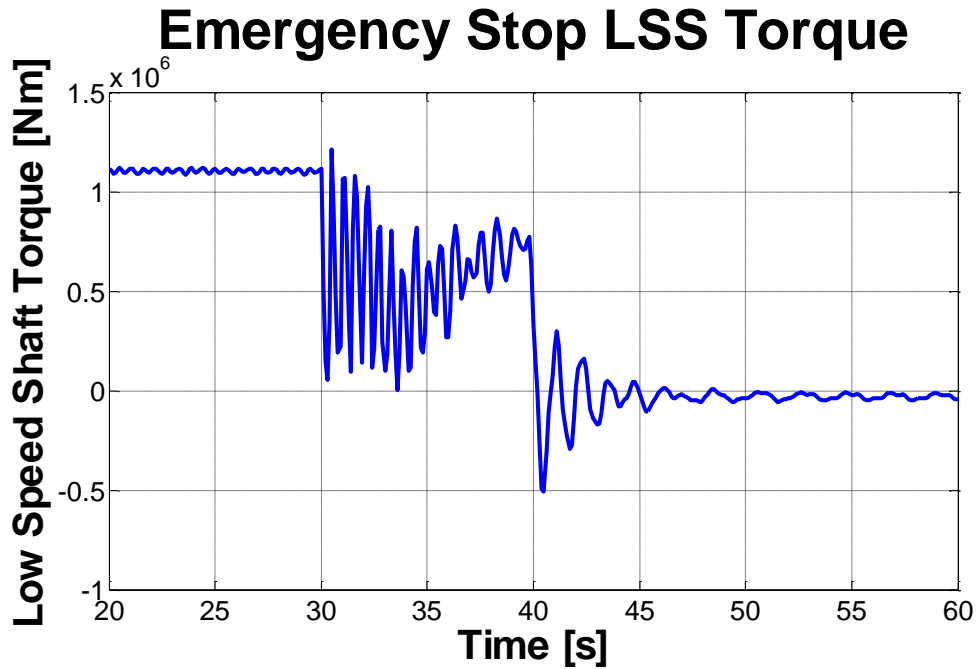
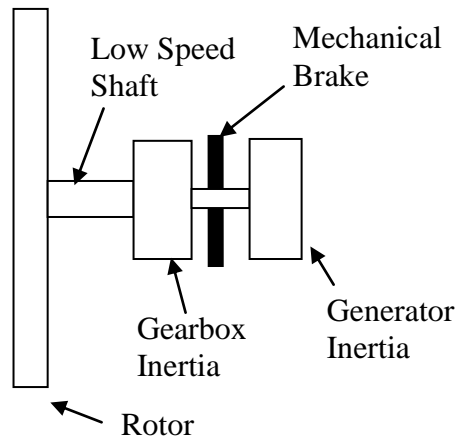


Figure 3.93 - Emergency Stop LSS Torque

Free –Free State



Fixed –Free State

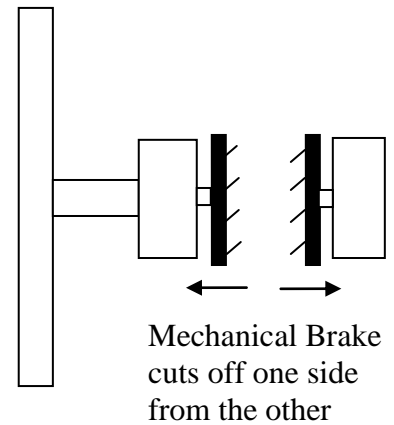


Figure 3.94 – Lumped Mass Drivetrain Systems

Fourier analysis shows three natural frequencies contained in the LSS torque are 0.78Hz, 1.78Hz and 3.96Hz. The first natural frequency is close to the fore-aft tower natural frequency, the second is close to the flapwise natural frequencies of the blade and the third is close to the first drivetrain natural frequency. Oscillations immediately after grid loss events are mainly due to oscillations of the blades, while oscillations after the rotor has come to rest are mainly due to tower effects.

Motion of the nacelle on top of the tower during the emergency stop is plotted in Figure 3.95. The Fore-Aft displacement and Nod rotation show a large response during the emergency stop where as the effect on other DOFs are not as significant. The tower and nacelle surge forward reaching a maximum caused by the blades pitching with the extreme occurring at approximately 34 seconds. There is a large loss of axial force on the rotor coupled with the blade pitching and the reaction from the tower stiffness causes the nacelle to surge forward. The tower and nacelle then oscillate until rest.

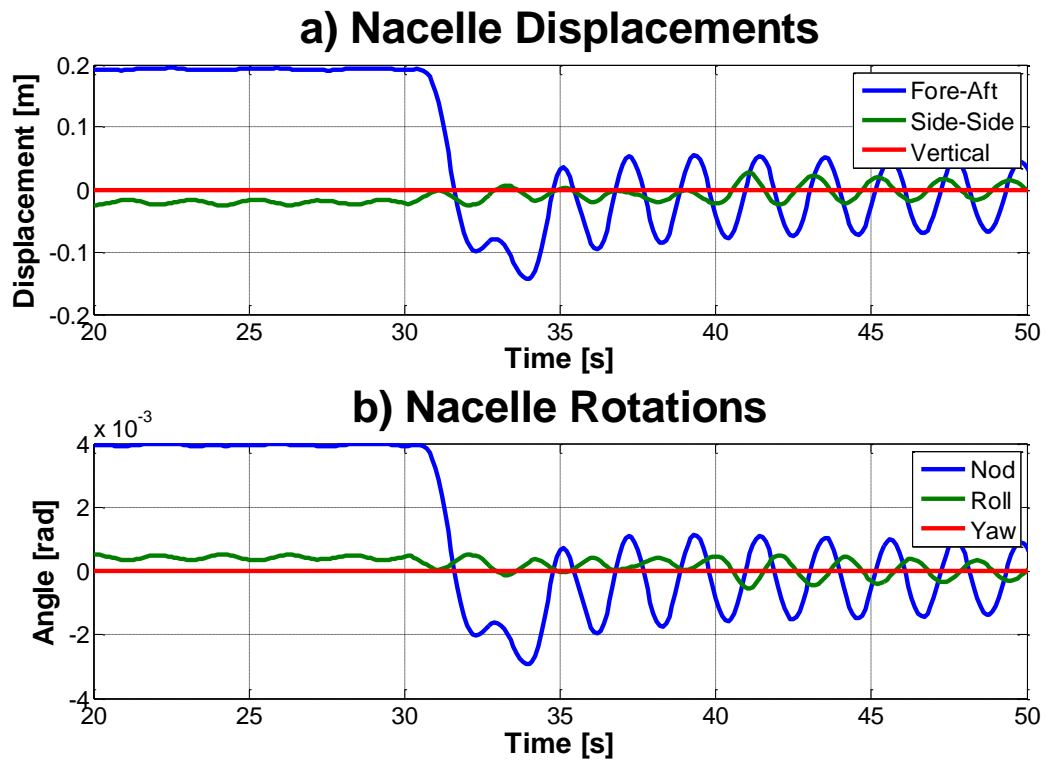


Figure 3.95 - Nacelle Motion during Emergency Stop - a) Displacements and b) Rotations

3.9.1. Effect of Pitch Rate

Loading on the wind turbine is very dependent on how the wind turbine is controlled during the emergency stop. Most braking effort is done through pitching blades. Blades pitch at the maximum pitch rate to get the rotor under control as quickly as possible though this may not be the best strategy for minimizing loading on the drivetrain. The rate at which blades pitch is varied to find its effect on loading on the turbine. Pitch rates of the blades are shown in Figure 3.96.

Pitch Rate Sensitivity - Pitch Angle

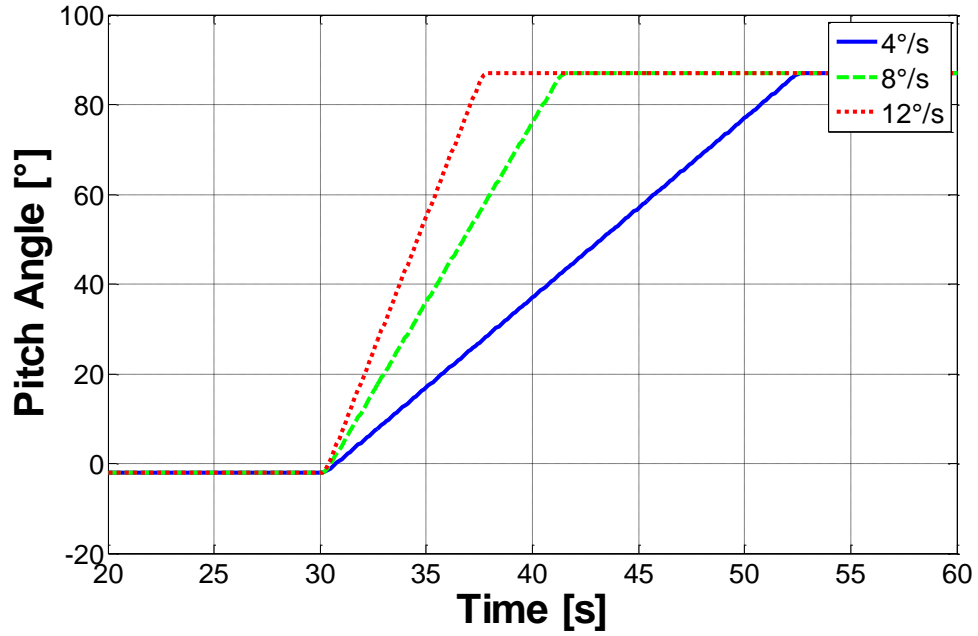


Figure 3.96 - Pitch Angle EStop Response to Pitch Rate

Rotor speed in Figure 3.97 shows that with slower pitch rates the turbine takes longer to slow but also reaches a higher overshoot after the grid loss event. This is as expected since slower pitch rates mean aerodynamic brakes are not as powerful and a greater overshoot occurs since it takes longer to reach a pitch angle to start braking the rotor.

Pitch Rate Sensitivity - Rotor Speed

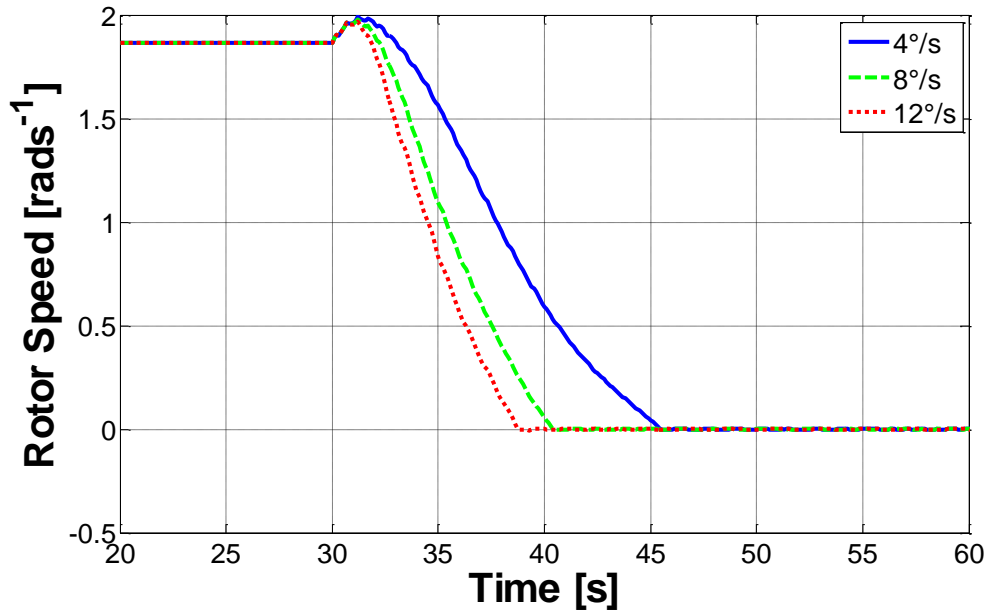


Figure 3.97 - Rotor Speed EStop Sensitivity to Pitch Rate

Pitch Rate Sensitivity - LSS Torque

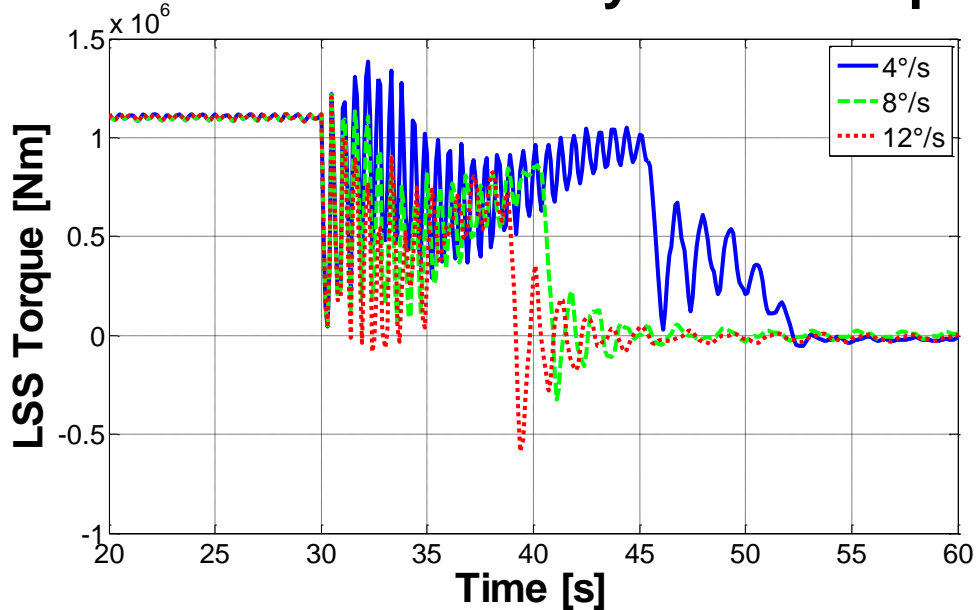


Figure 3.98 - LSS Torque EStop Sensitivity to Pitch Rate

LSS torque shows interesting outcomes: with faster pitch rates a greater reduction in torque is transferred to the drivetrain due to harsher braking and negative torques are seen more frequently. With higher pitch rates the amplitude of the loading increases which is more damaging to components.

With lower pitch rates the torque overshoot caused when the rotor comes to rest is reduced. In both the $8^\circ/s$ and $12^\circ/s$ cases the LSS torque becomes negative where as in the $4^\circ/s$ case the torque remains positive until the large oscillations are damped out and it oscillates around 0° . High pitching reduces maximum LSS torque but this is coupled with larger oscillations that may cause backlash which may cause backlash and be more damaging than a slower pitch rate.

3.9.2. Effects of Brake Loading

The HSS mechanical brake is also very important to the loading on the turbine during transient events. Two properties of the brake can be varied: the maximum load the brake can apply and the ramp time from fully disconnected to fully applied.

i) Maximum Brake Load

The maximum brake load that the wind turbine can apply to the system is varied over the range 8000Nm to 20000Nm. Figure 3.99 shows the difference in brake reaction torque when the maximum possible braking torque is changed.

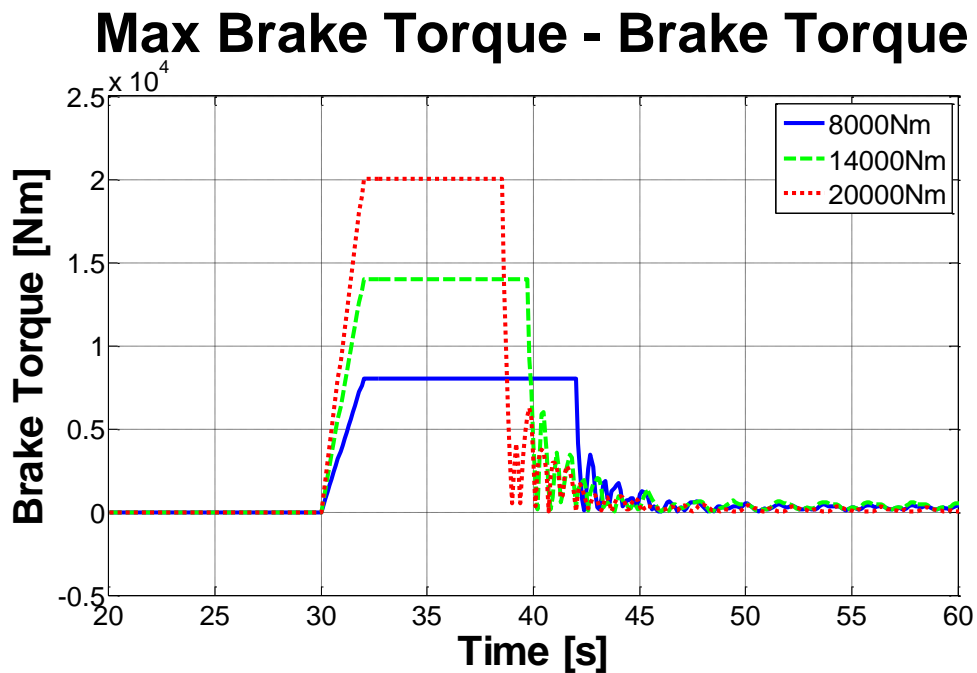


Figure 3.99 - Brake Torque EStop Sensitivity to Max Braking Torque

Effect of the maximum braking torque on the rotor speed and LSS torque during the emergency stop is shown in Figures 3.100 and 3.101. Rotor speed reaches rest

slightly faster with greater braking torque; the rotor comes to rest at 42.5s with a maximum braking torque of 8000Nm whereas with a maximum braking torque of 20000Nm the rotor reaches rest at 38.5s. The effect of braking torque on LSS torque is evident, with higher braking torque LSS torque is shifted upwards more; smaller braking torque shows LSS torque crossing from positive to negative causing backlash through the gearbox. With a larger maximum brake torque, LSS torque is in the positive direction throughout the braking preventing backlash occurring.

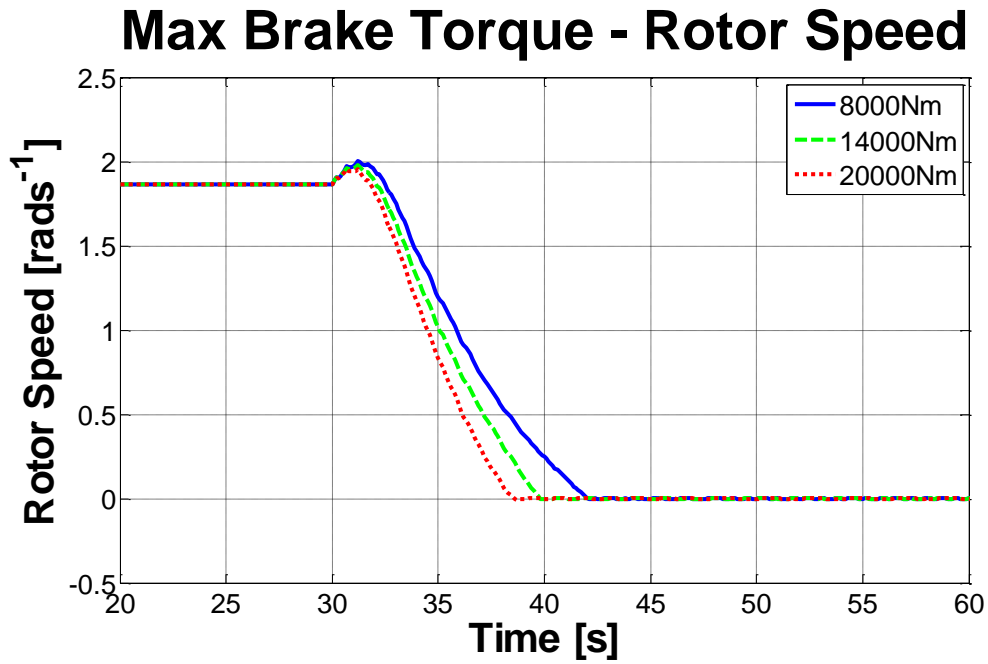


Figure 3.100 - Rotor Speed EStop Sensitivity to Max Braking Torque

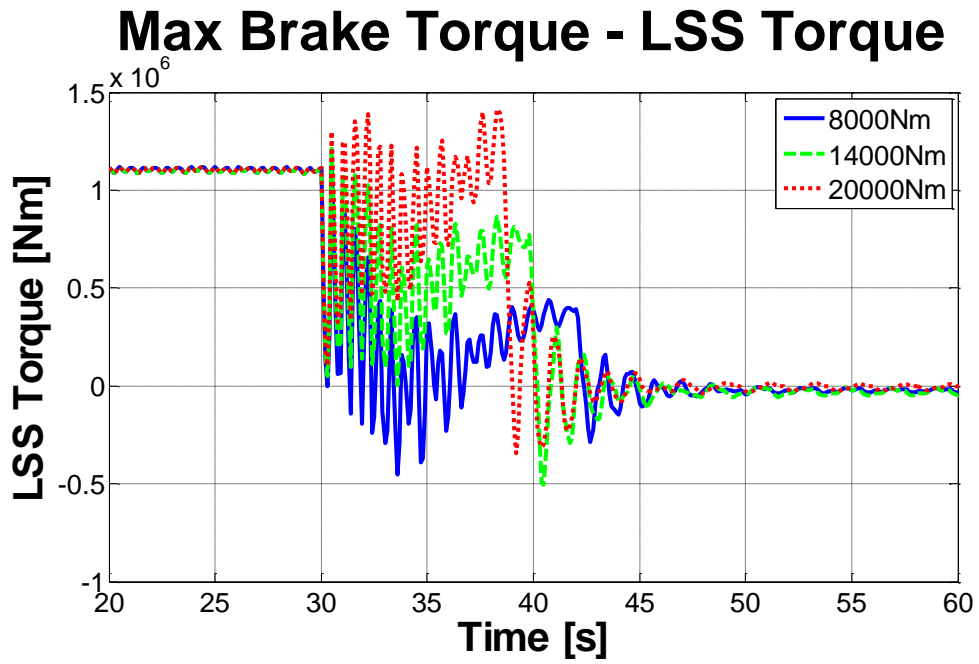


Figure 3.101 - LSS Torque EStop Sensitivity to Max Braking Torque

ii) Ramp Time

The ramp time was varied between 0.2 seconds and 2 seconds with the effect of the brake reaction torque shown in Figure 3.102.

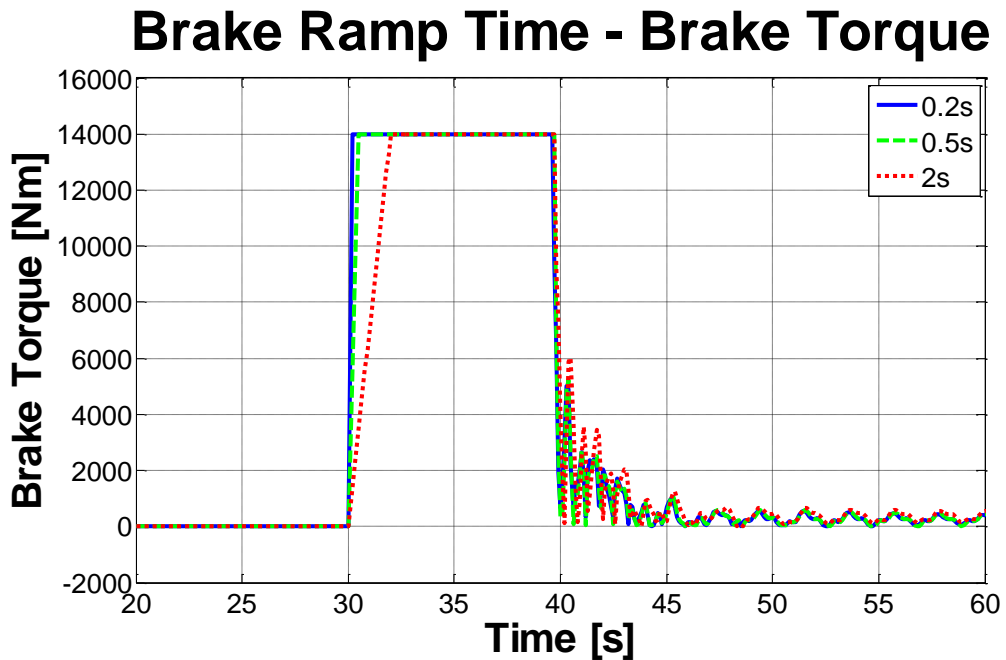


Figure 3.102 - Brake Reaction Torque EStop Sensitivity to Ramp Time

Ramp time has an effect on the overspeed initially after the grid loss event but has little effect on the overall time to bring the turbine to rest. LSS torque on the other hand shows a substantial difference in the initial torque spike after the grid loss event. Impulse of the brake loading causes high initial torque peaks but afterwards there is little difference between the torque curves. Reducing the impulse of the mechanical brake application by applying the brake over a longer period of time can lower the initial high torque spike which could minimise the most damaging loading occurring during the emergency stop.

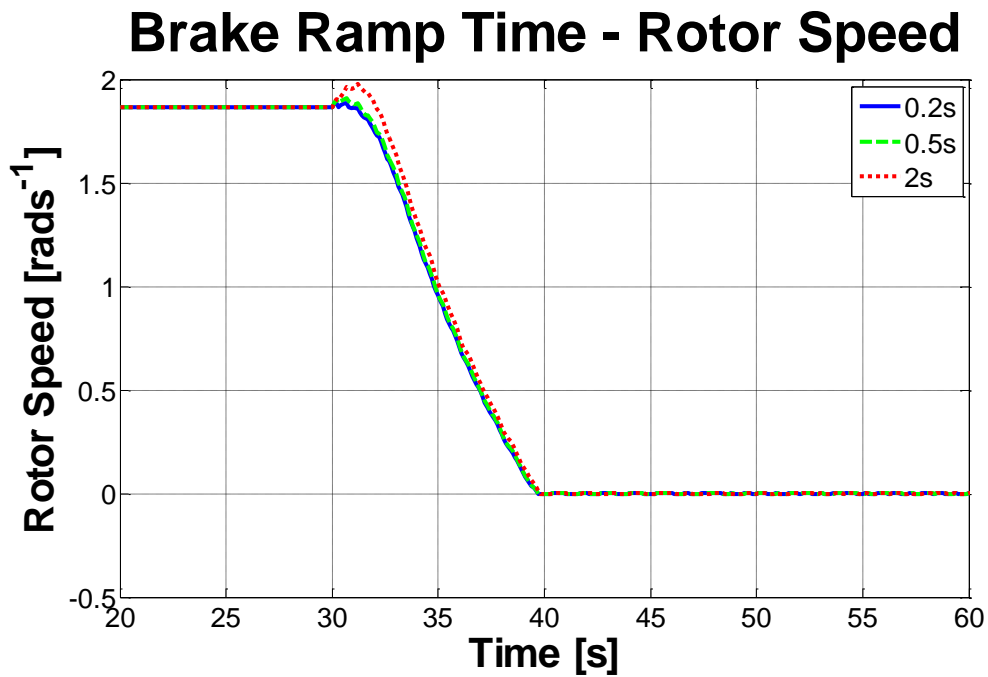


Figure 3.103 - Rotor Speed EStop Sensitivity to Ramp Time

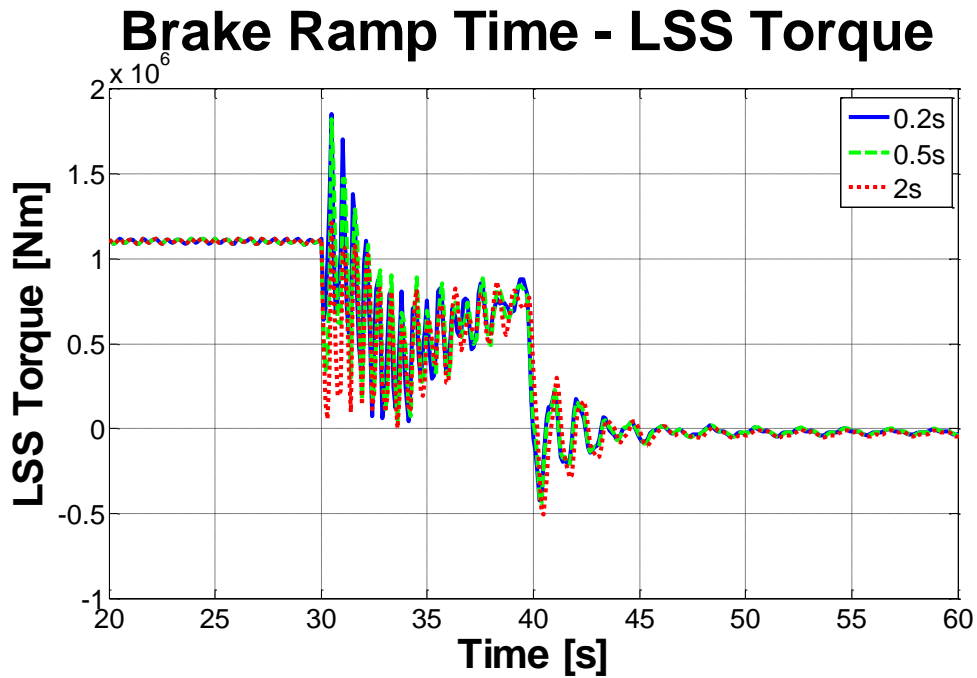


Figure 3.104 - LSS Torque EStop Sensitivity to Ramp Time

3.9.3. Effects of Wind Speed

The effects that wind speed has on response of the wind turbine to the grid loss event do not vary linearly. Since grid loss events occur unexpectedly, the wind turbine will be applying its operational control strategies when the event occurs and the wind turbine is required to perform the emergency stop from the operational point the turbine is at. Figure 3.105 shows effects that wind speed has on maximum rotor speed after the grid loss event. Below 12ms^{-1} , peak rotor speed gets higher with increasing wind speed; above 12ms^{-1} though, peak rotor speed reduces with greater wind speed. This is unexpected as increasing wind speed would expect to produce higher rotor speeds, where as the highest rotor speed is at an intermediate wind speed of 12ms^{-1} . In operation, 12ms^{-1} is the point at which rated power is achieved meaning below this wind speed, blades are at maximum power point tracking position at a pitch angle of -2° whereas above rated power, blades are pitched to shed torque with a greater pitch angle for higher wind speeds. Since the main braking effort is from the aerodynamic brakes, i.e. the pitch angle of the blades, if blades are already pitched in operation, less distance is required to be travelled to reach a braking position. Braking can then occur earlier preventing the high rotor speed peaks

explaining why there is a peak in rotor speed at 12ms^{-1} and the subsequent decline in rotor speed at higher wind speeds.

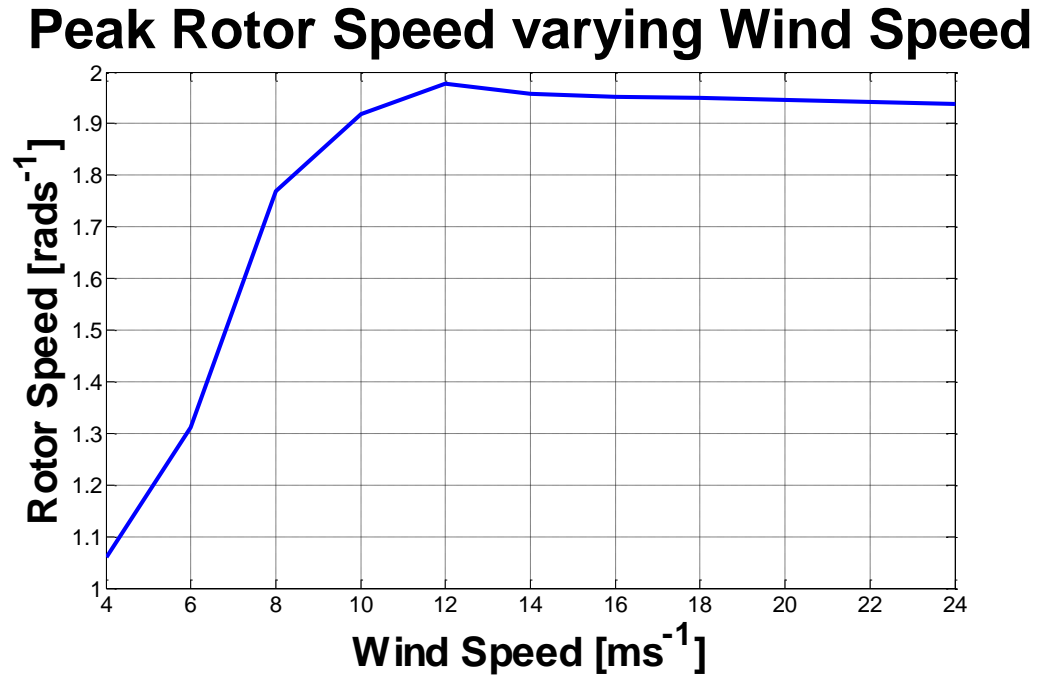


Figure 3.105 - Rotor Speed Peaks after Grid Loss Event

Similar to rotor speed, the peak of the LSS torque is seen at 12ms^{-1} . The LSS torque peak is more pronounced with a greater drop off in initial torque peak at higher wind speeds.

Peak Initial Torque varying Wind Speed

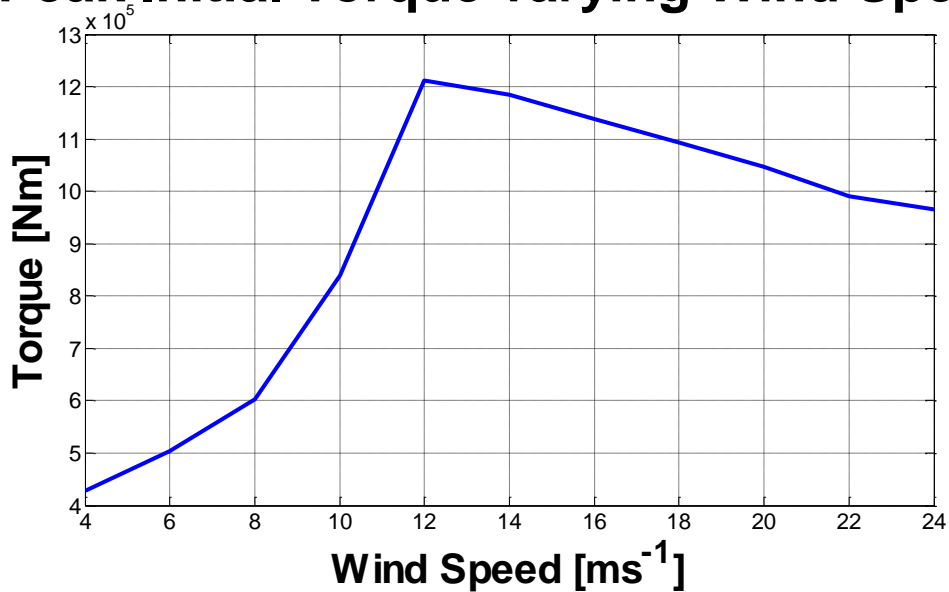


Figure 3.106 - LSS Torque Peaks after Grid Loss Event

3.10. Summary

Investigations into dynamic loading of the wind turbine during transient events have yielded some interesting results. GH Bladed allows prediction of loading combining dynamic responses of components in the wind turbine. Differences in harshness of loading on the turbine between the controlled normal stop and the emergency stop are clearly shown. The turbine is exposed to damaging loads in order for the turbine to be brought under control and prevent run away. Finding the most extreme loading on the wind turbine is likely to occur at a wind speed of 12ms^{-1} , at rated wind speed, is an unanticipated output since highest loading would have been expected to occur at high wind speeds. Sensitivity of pitch rate and mechanical brake loading is important to the transient response of the turbine in the grid loss emergency stop case. Discovering the response of the wind turbine during fault conditions allows more in-depth analysis of the drivetrain in later chapters.

Chapter 3 References

- [3.1] S. Burton, Jenkins, Bossanyi, *Wind Energy Handbook*, 2001.

Chapter 3 – Transient Loading of the Wind Turbine

- [3.2] A. Betz, "Das maximum der theoretisch möglichen ausnützung des windes durch windmotoren," *Zeitschrift für das gesamte Turbinenwesen*, vol. 26, pp. 307-309, 1920.
- [3.3] G. A. Van Kuik, "The Lanchester–Betz–Joukowsky limit," *Wind Energy*, vol. 10, pp. 289-291, 2007.
- [3.4] F. Lanchester, "A contribution to the theory of propulsion and the screw propeller," *Journal of the American Society for Naval Engineers*, vol. 27, pp. 509-510, 1915.
- [3.5] N. Joukowsky, "Windmill of the NEJ type," *Transactions of the Central Institute for Aero-hydrodynamics of Moscow*, pp. 405-409, 1920.
- [3.6] H. Glauert, *An aerodynamic theory of the airscrew*: HM Stationery Office, 1922.
- [3.7] D. Sharpe, "A general momentum theory applied to an energy-extracting actuator disc," *Wind Energy*, vol. 7, pp. 177-188, 2004.
- [3.8] B. Newman, "Multiple actuator-disc theory for wind turbines," *Journal of Wind Engineering and Industrial Aerodynamics*, vol. 24, pp. 215-225, 1986.
- [3.9] G. Gaonkar, *et al.*, "The use of actuator-disc dynamic inflow for helicopter flap-lag stability," *American Helicopter Society, Journal*, vol. 28, pp. 79-88, 1983.
- [3.10] I. H. Abbott and A. E. Von Doenhoff, *Theory of Wing Sections*: Courier Dover Publications, 1959.
- [3.11] H. Glauert, "Airplane propellers," in *Aerodynamic theory*, ed: Springer, 1935, pp. 169-360.
- [3.12] J. Schepers, *et al.*, *Verification of European wind turbine design codes, VEWTC: final report*: Netherlands Energy Research Foundation ECN, 2002.
- [3.13] R. Löhner, *Applied computational fluid dynamics techniques: an introduction based on finite element methods*: Wiley, 2008.
- [3.14] W. P. Wolfe and S. S. Ochs, "CFD calculations of S809 aerodynamic characteristics," Sandia National Labs., Albuquerque, NM (United States)1997.

Chapter 3 – Transient Loading of the Wind Turbine

- [3.15] R. Younsi, *et al.*, "Dynamic study of a wind turbine blade with horizontal axis," *European Journal of Mechanics-A/Solids*, vol. 20, pp. 241-252, 2001.
- [3.16] I. Taylor and M. Veza, "Prediction of unsteady flow around square and rectangular section cylinders using a discrete vortex method," *Journal of Wind Engineering and Industrial Aerodynamics*, vol. 82, pp. 247-269, 1999.
- [3.17] I. Taylor and M. Veza, "Calculation of the flow field around a square section cylinder undergoing forced transverse oscillations using a discrete vortex method," *Journal of Wind Engineering and Industrial Aerodynamics*, vol. 82, pp. 271-291, 1999.
- [3.18] EWEA, *Wind Energy -- The Facts*: European Wind Energy Association, 1997.
- [3.19] E. A. Bossanyi, "GH Bladed Theory Manual," Garrad Hassan2007.
- [3.20] S. Setio, *et al.*, "Modal analysis of nonlinear multi-degree-of-freedom structures," *International Journal of Analytical and Experimental Modal Analysis*, vol. 7, pp. 75-93, 1992.
- [3.21] G. Genta, *Vibration dynamics and control*: Springer, 2008.
- [3.22] J. He and Z.-F. Fu, *Modal Analysis*. Oxford: Butterworth-Heinemann, 2001.
- [3.23] E. A. Bossanyi, "GH Bladed User Manual," Garrad Hassan2007.

4. Transient Modelling of the Wind Turbine Drivetrain

Nomenclature

Symbol	Explanation	Units
a	Major Semi-Elliptical Axis	m
a*	Dimensionless parameter	
b	Minor Semi-Elliptical Axis	m
b*	Dimensionless parameter	
B	Damping Matrix	Nsm ⁻¹
c _{np}	Viscosity-Pressure Coefficient	
D	Ball diameter	m
d _m	Bearing Pitch Diameter	m
E	Young's Modulus	GPa
f _i	Inner raceway conformity	
F _C	Centrifugal Force	N
F(ρ)	Curvature Difference	
GR _{stage1}	First Stage Gear Ratio	
GR _{stage2}	Second Stage Gear Ratio	
GR _{stage3}	Third Stage Gear Ratio	
h	Film Thickness	m
K	Stiffness Matrix	Nm ⁻¹
M	Mass Matrix	kg
N	Inner Rotational Speed	rpm
Q _C	Axial Thrust Load on Rolling Element	N
R _x	Radial Force	N
r	Effective Radius of Stage	m
t	Time Step	s
T	Total Thrust on Bearing	N
T _{in}	Input Torque to Gearbox	Nm
T _{stage1}	First Stage Reaction Torque	Nm
T _{stage2}	Second Stage Reaction Torque	Nm
T _{stage3}	Third Stage Reaction Torque	Nm
u	Surface Velocity	ms ⁻¹
Z	Number of Rotating Elements	
U, G, W	Dimensional Parameters for Speed, Material and	

	Load Respectively	
α	Contact Angle	rad
η	Lubricant Absolute Viscosity	Nsm^{-2}
σ_{\max}	Maximum Contact Stress	Nm^{-2}
$\Sigma\rho$	Curvature Sum	
ω_{\max}	Maximum Frequency	rads^{-1}

4.1. Problems with Static Modelling

As observed from reliability studies in Chapter 1, the gearbox and generator contribute the most to overall downtime of the wind turbine. Static models (also known as equilibrium models) have been used extensively to predict loading on the drivetrain using sophisticated bearing and gear contact models. A disparity between lifetime predictions of models and observed lifetime during operation exists and modelling approaches have therefore been unable to predict root causes of failures. A proposed reason for this difference is that during transient events, loading is not captured properly since structural response during transient analyses comes from a combination of structural modes which are not incorporated in static models. To capture the effects of these modes, structural information is required to be passed between time steps. For static models this is not the case as each time step is independent of others since a steady state solution is determined depending only on the applied loads and material properties. In transient models, positional and velocity inputs for the upcoming time step are outputs of the previous time step and therefore time steps are linked together. This chapter investigates whether static models can adequately capture loading on the drivetrain or whether transient models are necessary to predict loads. Two modelling examples are presented, the first based on data from a gearbox test rig made by NREL, and the second an examination of the emergency stop event introduced in Chapter 3.

4.2. Pseudo Transient Modelling

To discover if static models can adequately predict drivetrain loads during transient events, two comparisons are made. To model the transient response using the static model, a pseudo-transient method is used. The methodology is shown in Figure 4.107. Input loads are created using the transient output of GH Bladed and using these input loads at each time step the drivetrain model is solved statically to obtain bearing deflections and stresses. Such pseudo-transient methods have shown to be useful for representing transient events when variables are time independent [4.1-4.2]. Time step length is very important for pseudo-transient models to ensure sufficient information is captured: too large a time step and vital information will be lost whereas too small a time step and the computational time vastly increases with no additional knowledge gained. Kant [4.3] suggested the critical time step should be $\Delta t \leq \frac{2}{\omega_{\max}}$. Two transient models are compared to the pseudo-transient drivetrain models: measured mount deflections from the NREL test rig and simulated transient loading from a combination of GH Bladed and ANSYS transient. Deflections at the mounts are compared between the models; if minimal difference is observed then static modelling is acceptable for analysing drivetrain loads and estimating component lifetimes.

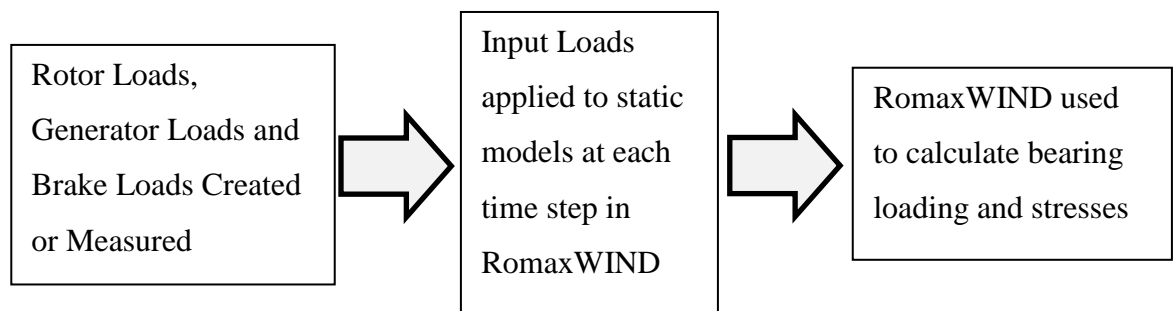


Figure 4.107 – Pseudo-transient Methodology

4.3. Comparison with Measured NREL GRC data

Pseudo-transient drivetrain modelling is compared to test data from the NREL GRC (Gearbox Reliability Collaborative). The objective of this investigation is to discover

how effectively modelling a transient event with the pseudo-transient method captures motion and loads as measured on a test rig.

4.3.1. Test Rig

The NREL test rig comprises a three-stage 750kW gearbox and generator attached to a bedplate, and is located at the NREL test centre in Boulder, Colorado, USA. The test rig is able to apply torsional loads to the low speed shaft (LSS) as well as off axis loads through two forcing arms attached to the input of the LSS, as shown in Figures 4.108 and 4.109.

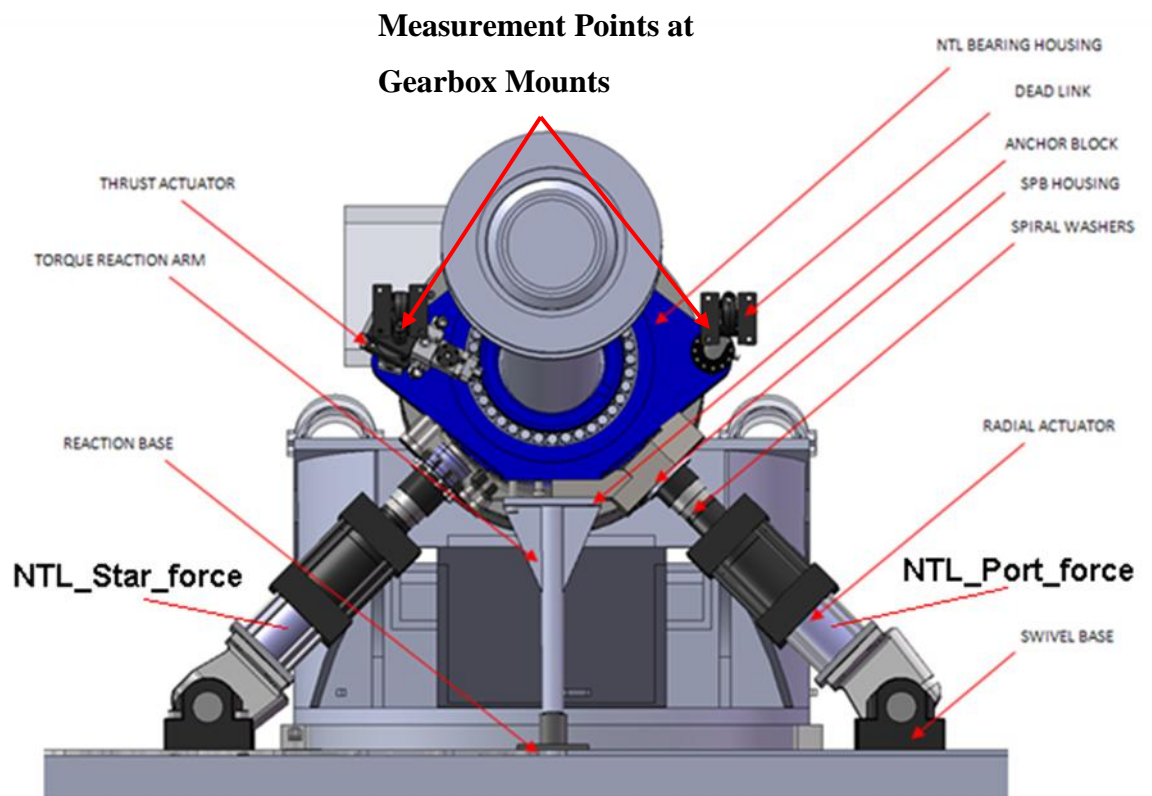


Figure 4.108 - Upwind View of the Test Rig

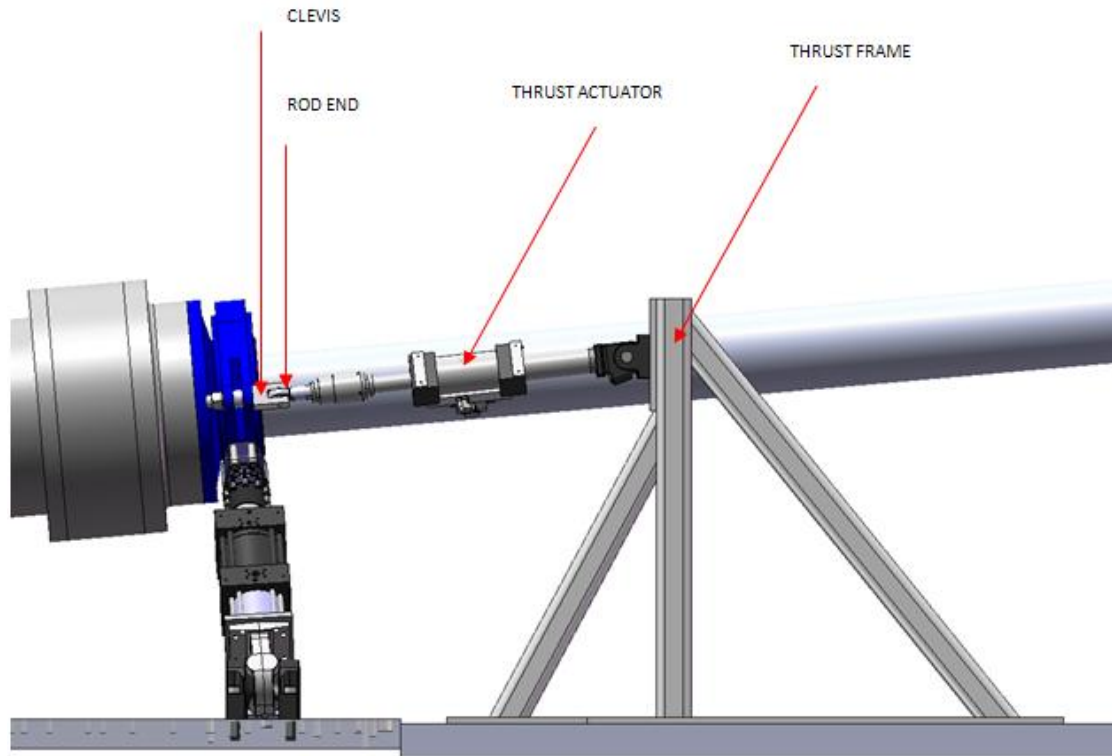


Figure 4.109 - Side View showing Thrust Components

Two dynamic tests performed on the test rig are documented. The data sets made available to those who partner with NREL by sharing results: the first test was to collect dynamic measurements of the drivetrain during transient start up from rest to rated speed, the second is a torque sweep where the drivetrain is approximately kept at constant speed but the torque is increased in stages from 0 Nm to rated torque. Measurements taken during both tests are displacements of gearbox mounts, specifically pins of the trunnion mounts. Data was collected at 100 Hz and thus the time step used for the measured displacements is 0.01 seconds. Figure 4.110 shows the position of these sensors in the mounts.

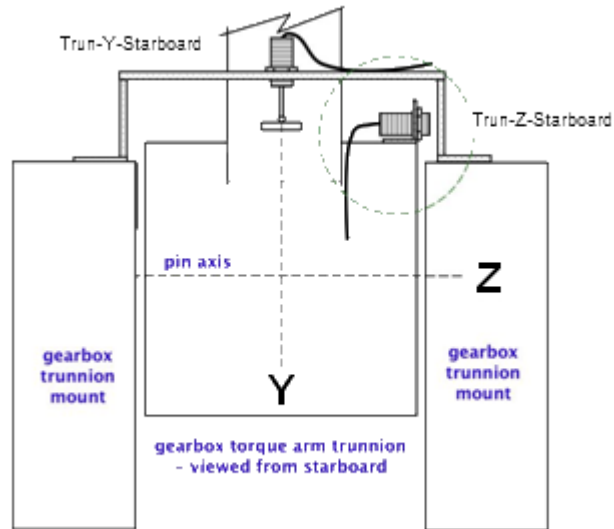


Figure 4.110 - Displacement Sensors on Starboard Trunnion Mount

In addition, main shaft bending moments were recorded but are not used in this investigation. Inputs to the test rig are LSS speed [rpm] and LSS torque [kNm].

4.3.2. Model

A model of the gearbox test rig, created by Romax Technology in RomaxWIND is shown in Figure 4.111. The model consisted of a bedplate and a three stage gearbox: an initial planetary stage and two parallel stages having a gearbox ratio of 1:81. The gearbox torque arms are connected to the bedplate through trunnion mounts modelled as a pin through the bedplate and gearbox torque arms.

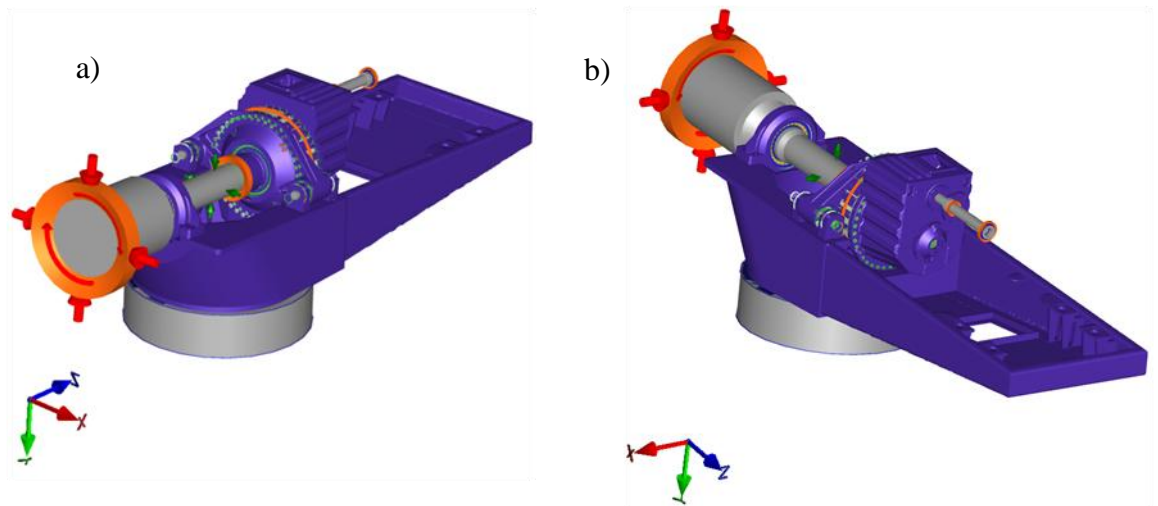


Figure 4.111 - Model of NREL Test Rig

4.4. Transient Start

The drivetrain is brought from rest to rated conditions during the transient start. Rotor speed and torque from the tests are shown in Figure 4.112a and were provided as inputs to the RomaxWIND model. Between 200 and 300 seconds, the drivetrain starts up with a sharp increase in torque to accelerate the drivetrain followed by a sharp braking torque subsequently bringing the drivetrain back to rest. After 300 seconds, the drivetrain accelerates up from rest until rated speed is reached. When rated speed is achieved generator reaction torque is introduced and increased up to rated torque. Due to the number of simulations required and the amount of storage availability the sampling frequency of the pseudo-transient model is 10Hz.

Measured vertical motion of gearbox mounts, shown in Figure 4.112c, show a great deal of movement when torque fluctuates. When the applied torque is increased, starboard mount displacement increases while port displacement decreases suggesting the gearbox rolls with applied torque. Predicted displacements of the RomaxWIND model have lower oscillation frequencies than the measured test rig although from Kant [4.3], frequencies higher than 5Hz will not be captured due to the time step of the pseudo-transient model. Generally, static modelling seems to capture vertical movements of the mounts adequately.

Axial motion in Figure 4.112b, on the other hand, shows fairly substantial differences between measured experimental data and simulated results. Measured results have been offset from the recorded values so displacements are equal at no applied load in Figure 4.112b. From experimental data, oscillations at rotor speed frequency are seen from start up and exactly match rotor speed as it increases to rated speed. This strongly relates yaw oscillations about the Y axis to input rotor speed suggesting unbalanced forces in the first stage of the gearbox. Unbalanced forces cause motion of bodies in the structure which could be observed as mount displacements and could occur if load sharing between the planets is uneven causing one planet to exert more force onto the ring gear. When input torque is increased to rated torque between 500 and 600 seconds, the mean displacement of the observed oscillations changes and separation of axial displacement between the mounts occurs suggesting loading is greater at one side of the gearbox. Port and starboard mounts are also in anti-phase with each other suggesting the gearbox is exhibiting yawing oscillation when in operation. Amplitude of these oscillations appears not to be affected by magnitude of the applied torque.

Axial displacements arise from gears having helical teeth; a component of the transferred force will be in the axial direction: gearbox mounts therefore resist axial loading as well as torsional loading. Comparing experimental data to model results in the axial direction, oscillations at the rotor speed frequency are not captured at all. Axial motion predicted by the model shows no change in mount displacement and minimal change when torque is increased. This could be important when trying to find the effect of misalignments passed through to the coupling and generator which, if not captured by modelling potentially could be very damaging to high speed bearings. The model predicts both mounts will have similar axial displacement whereas the experimental results measured a significant difference between mounts. The pseudo-transient model predicts axial displacements to be between the two measured mount displacements suggesting that the model may capture mean loading but may not capture other dynamic loading on the gearbox.

A major assumption this study makes is that both port and starboard mounts have exactly the same stiffness on the NREL test rig and therefore would displace

similarly when equal forces are applied to each mount. This may not be the case and if differences exist then static displacements will be unequal and response to dynamic excitation will be different. The RomaxWIND model however is able to use mounts with the same stiffness and therefore gearbox mounts will give similar responses.

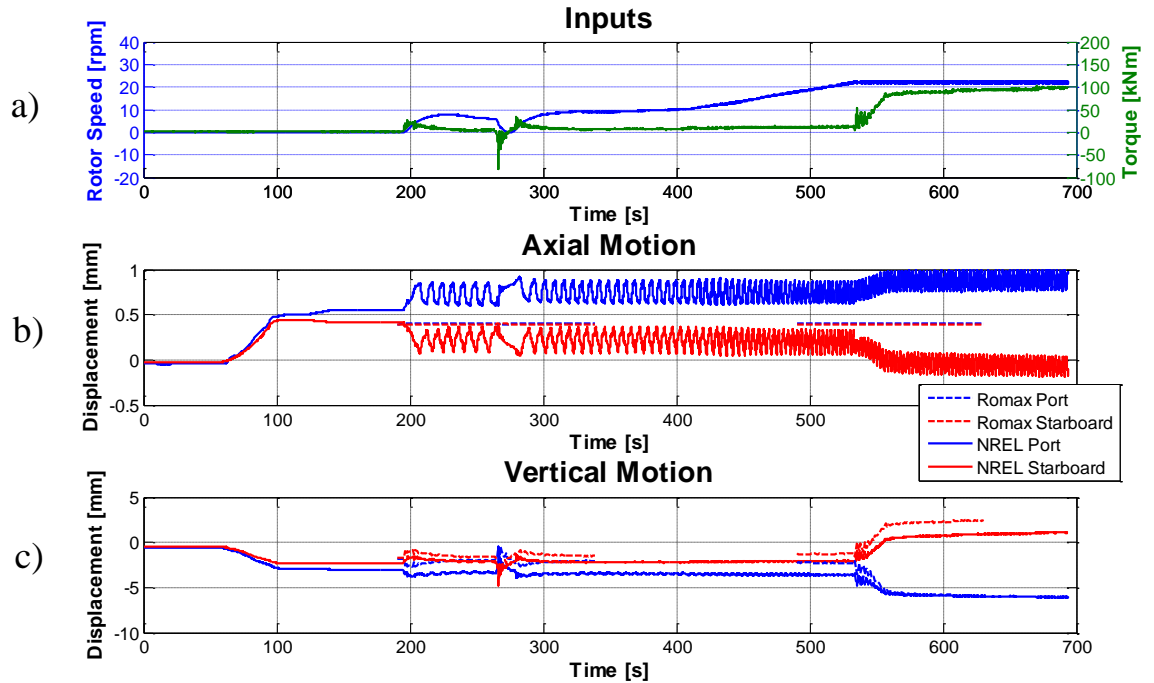


Figure 4.112 - Inputs and Response with Shifted Axial Motion²

² In the first 200 seconds mounts displace even although the rotor speed and torque are zero. This could be to do with the drivetrain being prepared such as off axis loading or brakes being removed.

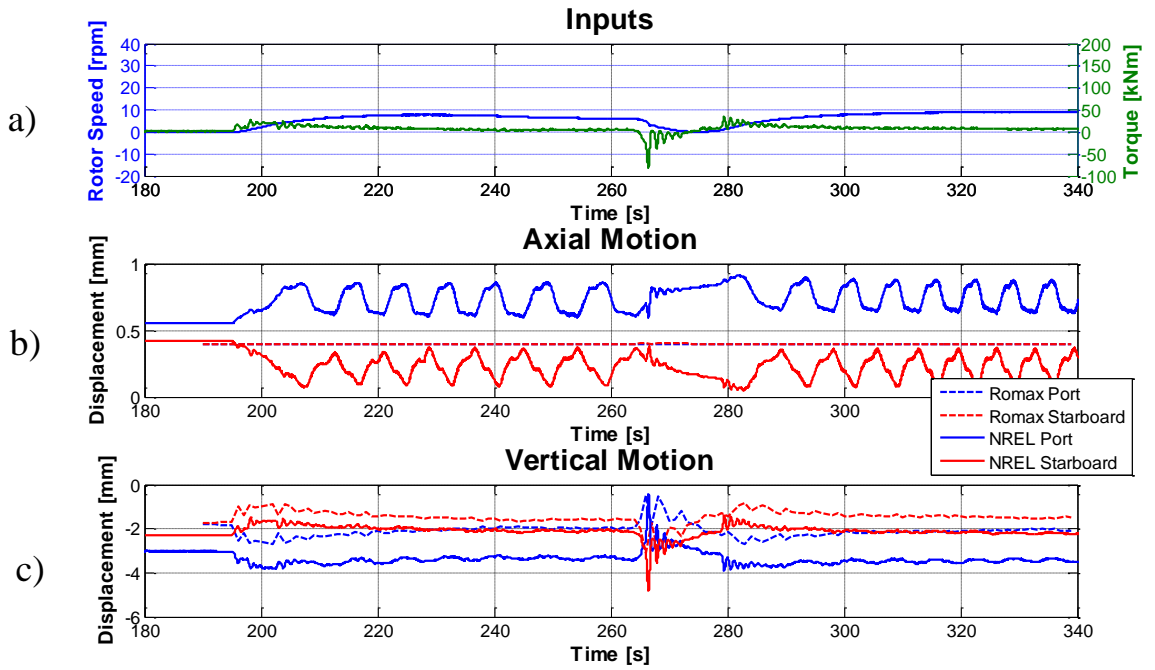


Figure 4.113 - First Transient in Start Up. This shows more clearly the transient motion between 180 to 340 seconds in Figure 4.112

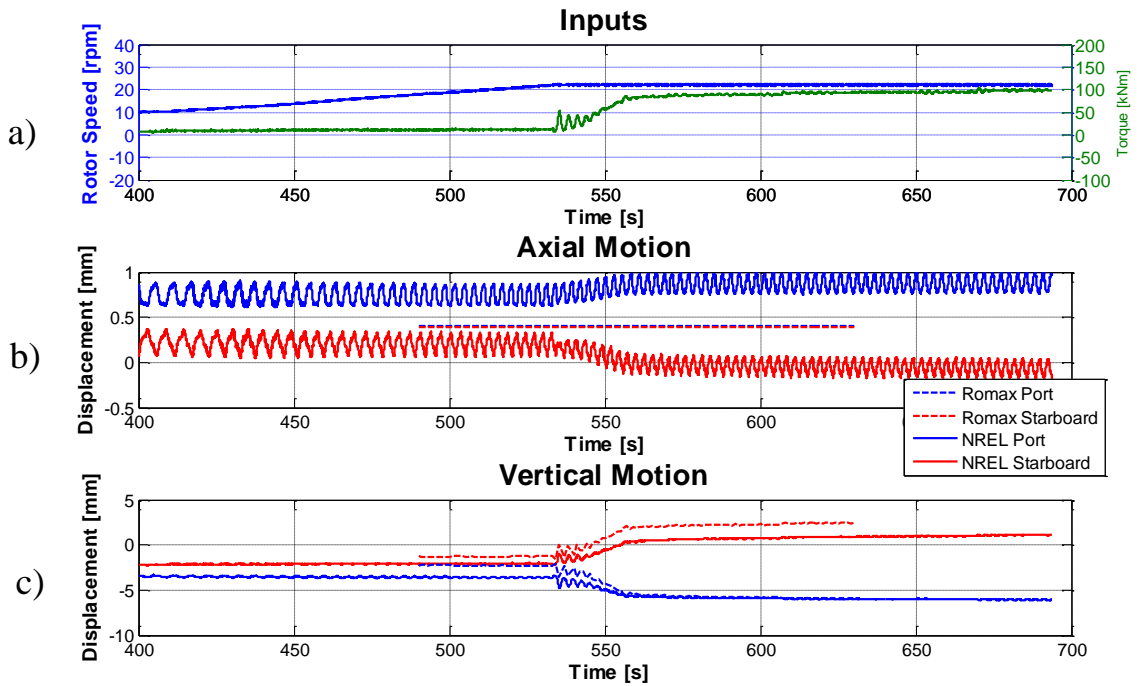


Figure 4.114 - Second Transient in Start Up. This shows more clearly the transient motion between 400 to 700 seconds in Figure 4.112

4.5. Torque Sweep

For this experiment, rotor speed remained relatively constant between 21.5 and 23 rpm and the torque was increased in 3 distinct stages: 25% - 50%, 50% - 75% and 75% - 100% of rated torque. Figure 4.115a shows the rotor speed and torque inputs to the test rig.

Vertical motion results show a difference between experimental results and static modelling. In the experimental results every time there is an increase in applied torque, a subsequent change in displacement magnitude occurs in opposite directions for the starboard and port mounts. In the model, an increase in both mounts' displacement magnitude is also observed with applied torque, though the static model predicts a much larger change than seen in the test rig.

Figure 4.115b shows axial motion in response to the transient start; experimental data shows oscillations at the mounts in anti-phase with each other at rotor speed frequency again suggesting the gearbox is yawing during operation. Relative magnitudes of the axial displacements show, at low torque inputs, starboard mounts displace 0.5mm whereas port mounts displace just greater than 0mm. When torque is increased to 50%, the gearbox straightens up with port and starboard mounts moving to a similar displacement. Second and third torque increases (50-75% and 75-100%) have minimal effect on mount displacement suggesting that mount displacements could be more sensitive to lower torque changes (<50% of rated torque) than higher torque changes (>50% of rated torque). This also suggests that gearbox mounts stiffnesses have a nonlinear response over the range of operation. Although small, the port mount shows a change in opposite direction to the first increase (25% - 50%) when the load is increased to rated torque (75% - 100%).

Comparing measured axial displacement data to modelling results, a similar discrepancy in the transient start results is noticed. No oscillations are found in the simulated axial direction from the pseudo-transient model which displays horizontal lines with very little change in axial displacement as applied torque is increased. In addition, very little change in displacement of either mounts is observed, something noticeably different when compared to experimental results.

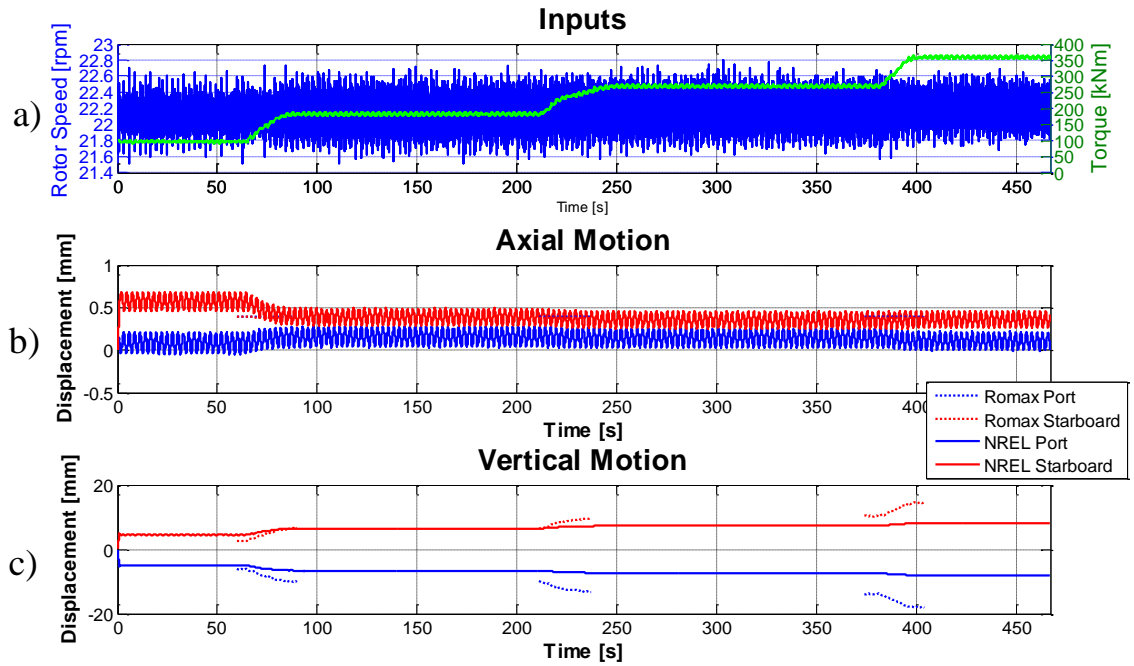


Figure 4.115 - Torque Sweep Comparison

4.6. Discussion of Results

Both tests show similar findings when experimental results are compared to static modelling. Vertical motion seems to be adequately described by static modelling with general movements of the gearbox picked up as torque and rotor speed changed although higher frequency oscillations, above 2Hz according to Kant, cannot be captured. Axial direction modelling did not pick up observed oscillations observed in the experimental runs. These oscillations at rotor speed frequency would suggest an imbalance occurring every cycle possibly due to input torque present every cycle or within in the gearbox itself, in particular the first stage planetary system, which may not be properly balanced with poor load sharing between planets gears. Imbalances in the loading of the gearbox are not represented in the pseudo-transient model where the load sharing is perfectly balanced. Oscillations such as these have been observed in other drivetrains indicating this may be a problem that requires more research. Inequality in mount stiffness between port and starboard may also cause differences between test data and rig data.

4.6.1. Summary

A pseudo-transient method using static modelling for transient events does provide some useful outputs which in some cases, such as the vertical motion, gives fairly good approximation to what is generally happening in experimental circumstances. Axial motion displacements highlight inadequacies of this method showing the need for other modelling methods and better understood input conditions. Investigations into the root cause of the oscillations could provide insight into how these anti-phase oscillations arise in axial motion and how this could be mitigated. This may also give insight into why the experimental results show differences between both mounts axial displacements that is not captured in the model.

4.7. Transient Modelling of Grid Loss Emergency Stop Simulation

This investigation compares deflections and bearing loads of a static model and a transient model of the full wind turbine drivetrain during the highly transient event explored in Chapter 3: a grid loss emergency stop. The pseudo-transient method uses a static model to represent the transient response taking input loads from GH Bladed simulations of a 2MW turbine performing a grid loss emergency stop. Response from the GH Bladed model is at time steps of 0.1 seconds which are input into the static model where the model is solved at each time step. The pseudo transient model output can be analysed to a maximum frequency of 5Hz according to Kant [4.3]. A drivetrain model using ANSYS transient structural is created and solved transiently in response to the same applied loads from GH Bladed. In the pseudo-transient model no information is passed between time steps therefore effects from drivetrain structural modes are not taken into account where-as effects from modal excitation are included in the full transient method. If differences are observed between the two models this may suggest that static models do not capture all relevant loading on the bearings. Differences in methodology are displayed in Figure 4.116.

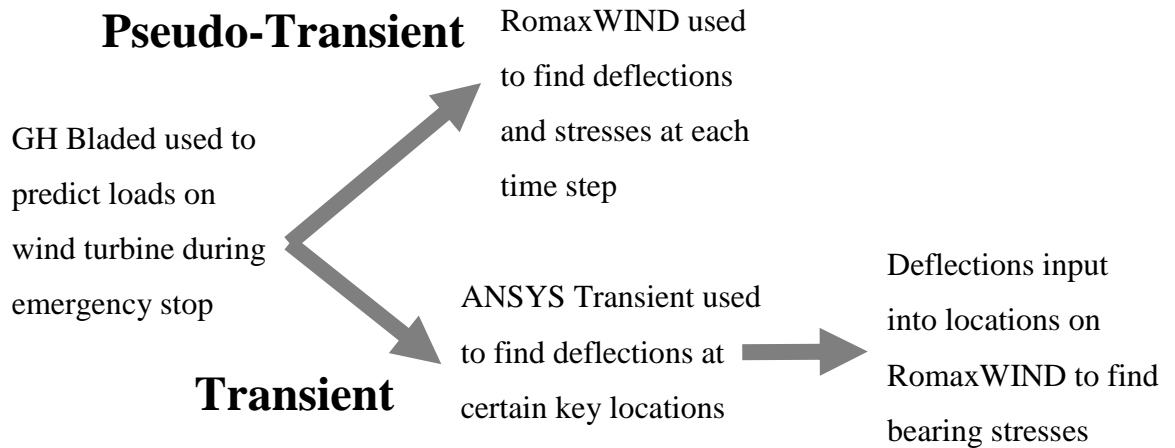


Figure 4.116 - Methodology Diagram

The advantage of using pseudo-transient modelling is that it requires much less computation, reducing the solution time and amount of data required to be stored in comparison to full transient modelling. If modes are significantly excited during the emergency stop, in a way that influences loads on key components, then full transient analysis is likely to be required to accurately model loads; if not then pseudo-transient modelling should be adequate. Analysis of high speed shaft and generator bearings will be of particular interest showing contact stresses caused by the emergency stop. If a significant difference exists between the two model deflections and contact stress predictions then this may provide an explanation of why unexpected premature failures on high speed bearings occur.

4.7.1. Transient Modelling Software

ANSYS is a commercial finite element package that uses finite element models to simulate many different analysis types, some of which can include static, transient and multibody structural responses, heat flow problems, and fluid flow. The transient model of the drivetrain was created using the ANSYS 12.1 transient structural modelling capability.

A full transient analysis gives the most accurate solution and can also include nonlinearities, the disadvantage is that it is computationally intensive and slow to run, since the full model is being analysed. Initially, 3D models of the drivetrain components are created using the solid body modelling software in ANSYS. Components are then assembled using joints to form the complete drivetrain model.

The model is then discretized into nodes and elements forming a mesh which loads are applied to at the appropriate places. The solver iterates and converges on the solution, force and displacement errors are reduced to be within specified tolerances at each time step. The solver uses a variable time step though the output is calculated at fixed steps of 0.1 second time steps. The variable time step change chosen by ANSYS depends on the response of the model to applied loading. This method is broken into two distinct areas: next time step prediction and time step bisection [4.4]. Time step prediction using knowledge of previous and present time steps to predict the next time step. The solver aims to have 20 points per cycle. Time step bisection analyzes the current time step and decides whether to reanalyze the time step using smaller time steps. If the time step does not converge in the predicted time step the new time step is reduced by 50% and reanalyzed.

The discretized mass, damping (if included) and stiffness matrices can be solved using the equations of motion.

$$[M][\ddot{x}] + [B][\dot{x}] + [K][x] = [F] \quad (4.49)$$

4.7.2. Connection Joints

Connections between bodies are important to model properly if correct responses to the applied loading are to be found. Three types of joint are used in the drivetrain model: fixed connection, revolute connection and bushing connection. Fixed connections rigidly connect nodes on two faces in all DOFs so the faces cannot move relative to one another. This is useful for connecting two shafts together or the ground connection to the bedplate. Revolute joints connect two faces where one rotational DOF is free while all other DOFs are fixed. An example of a revolute joint in Figure 4.117 shows how the two bodies can rotate around the centre pin while constrained in the other DOFs. Simplified bearings can be modelled as revolute joints assuming high radial and tilt stiffness. Ball bearings are a good example of revolute joints where the inner shaft can rotate freely whilst it cannot translate or rotate in the remaining DOFs.

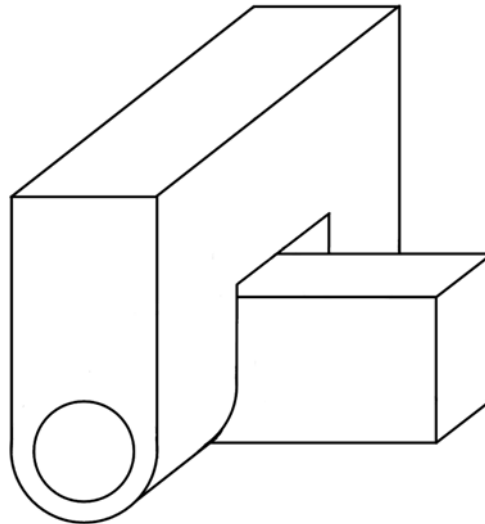


Figure 4.117 - Revolute Joint

The final joint used is a bushing joint which allows a specified stiffness in all DOFs allowing flexible joint responses. A bushing joint allows movement in all DOFs and spring stiffness can be prescribed to each DOF to resist displacement. This type of joint is useful to model flexible connections such as the mount of the gearbox where a different stiffness is required in each DOF. Gearbox mounts are modelled using bushings since trunnion mounts are free to rotate in the axial direction but are flexible in all other directions. Material of the mounts is similar to rubber with a translational stiffness of $1.5e8\text{N/m}$ and rotational stiffness of $8.4e4\text{Nm/rad}$, the same as the static model.

4.7.3. Full Drivetrain Model

A simplified drivetrain model using the same drivetrain as in Chapter 2 was created. Individual components are combined using joints to complete the model of the drivetrain shown in Figure 4.118. From Chapter 2, alignments of internal gearbox bearings are well isolated from movements in the drivetrain so the transient model can lump internal gearbox components together into a mass node, reducing model complexity but maintaining mass and inertial properties of components between the models. These nodes can be used to represent simplified mass on the drivetrain and are therefore applied at the centroid of the gearbox, the centroid of the generator and the input to the drivetrain to represent rotor mass and inertia.

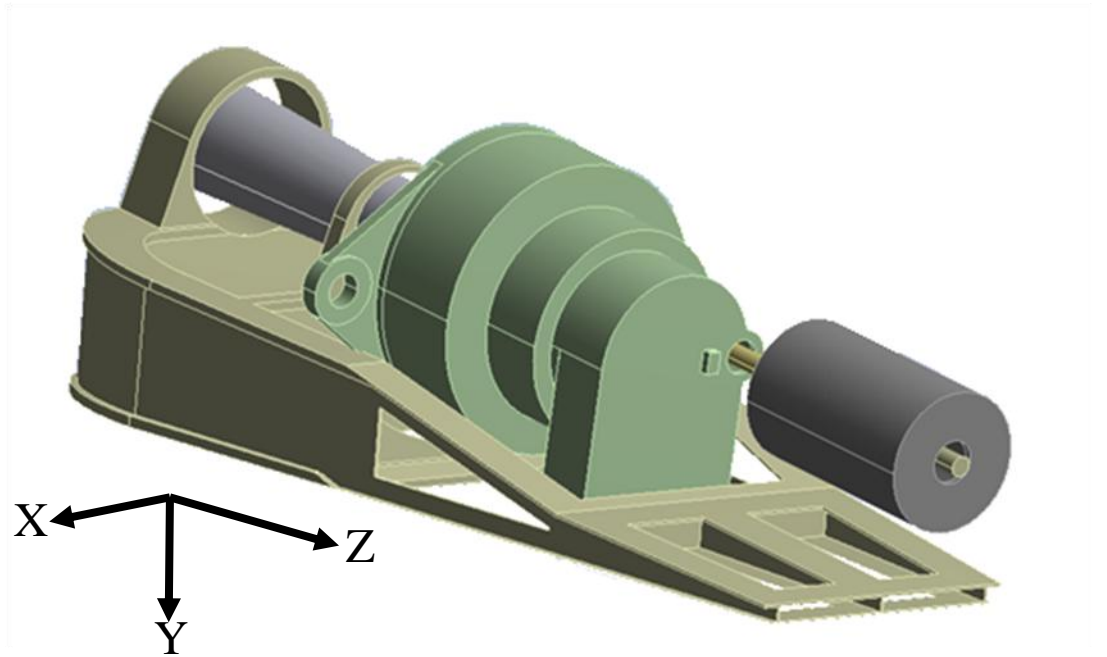


Figure 4.118 - ANSYS Model (Transient)

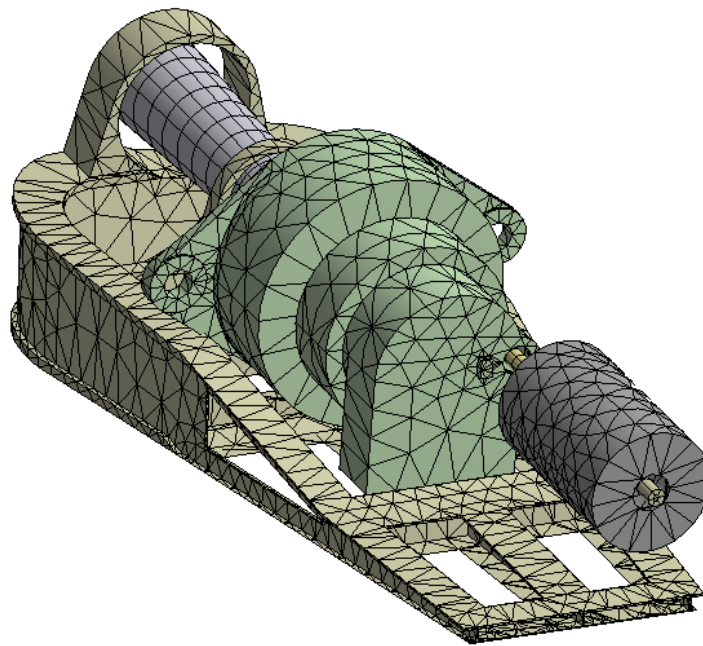


Figure 4.119 - Meshed Drivetrain

Loading is applied at the appropriate locations of the transient model to achieve a suitable response: off axis loads at the hub, torque reduction at each stage in the gearbox, axial loading created at each stage in the gearbox, brake reaction loading and generator reaction loading. With correct representation of the connection

between bodies the model should provide adequate results for the response to emergency stop loads.

Bushing mounts are used to attach the gearbox casing to the bedplate via the torque arms. Revolute joints are used to connect the LSS to the bedplate through main bearings and the HSS to the gearbox casing allowing free rotation but resisting in off axis directions. The LSS is attached to the gearbox housing through fixed connection allowing rotation about the axial direction while resisting in other directions at the appropriate locations, avoiding convergence problems from unconstrained components. The HSS, flexible coupling and generator rotor shaft are connected to each other to form the complete shaft, connecting gearbox with generator. The generator shaft uses fixed joints to connect the generator rotor to the stator to avoid convergence problems, similar to the LSS.

Loading is applied to the transient drivetrain model in the appropriate places displayed in Figure 4.120. Off axis rotor loads are applied at the hub connection with the 5 off axis DOFs taken from the transient GH Bladed simulation. Gearbox loading at each stage consists of two parts: a rotational part from the torque reduced at each stage and an axial component caused by the use of helical gears. The first two stages are planetary so loading is applied to the ring gears; on the parallel third stage loading is applied to the bearing connection of the gearbox housing. Brake loading is applied to the calliper on the housing though loading is small in comparison to other loads on the gearbox. Generator reaction torque modelled during the transient GH Bladed simulation is also applied to the stator; it is assumed that generator reaction torque is 1 dimensional therefore only torque is applied.

Key measurement areas on the transient model are at the connection points to the bedplate. Probes are used to measure displacement and rotation of the connection locations: the two main bearings, starboard and port gearbox mounts and stator DE and NDE connections at the front and rear of the generator. These measurement points can be compared to the pseudo-transient model in RomaxWIND to show similarities or differences. Gravitational loading is also included in both simulations since self weight loading of components is important for displacement calculations.

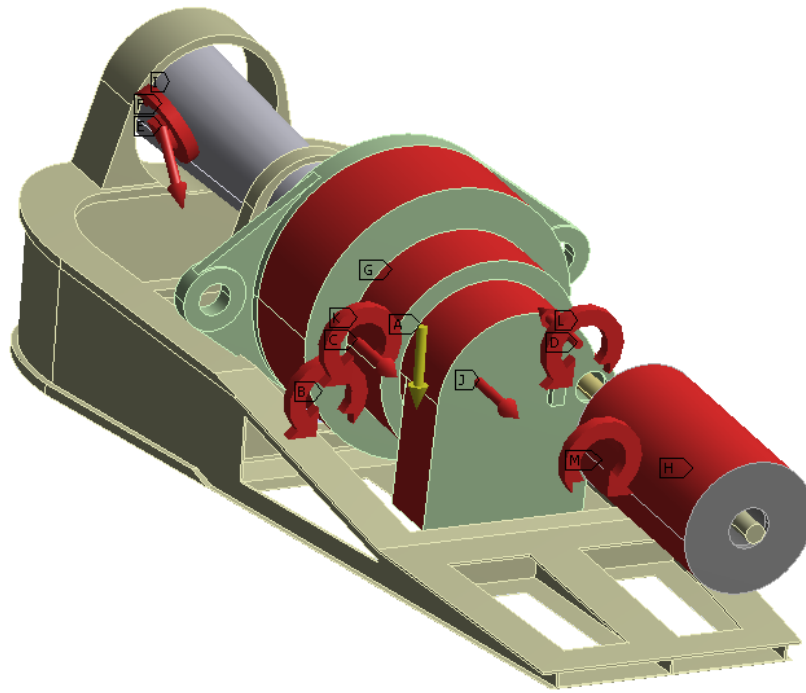


Figure 4.120 - Applied Loading Locations on the Drivetrain

4.7.4. Model Natural Frequencies

Before detailed transient analysis was undertaken, natural frequencies of the complete drivetrain model were found. This allows identification of particular modes during transient analysis and identification of the mode shapes. Natural frequency is dependent on stiffness and mass distribution of the model, related through $\omega = \sqrt{\frac{k}{m}}$.

This is a crucial parameter in determining whether transient analysis will be needed for further analysis of the wind turbine drivetrain. For transient analysis to be required, information from previous time steps, such as displacements and velocities, is needed to be passed onto the new time step. Since dynamic motions are a combination of structural modes, if any of the modes are excited then to accurately predict deflections and resulting bearing stresses will require full transient analysis. Drivetrain natural frequencies were found using the complete transient model of the drivetrain with the modal analysis software in ANSYS. Table 4.7 shows results of the modal analysis of the complete drivetrain and Table 4.8 shows the natural frequencies of the gearbox casing in RomaxWIND.

Table 4.7 - Drivetrain Natural Frequencies

Drivetrain Mode	Frequency (Hz)
1	1.01
2	5.37
3	7.05
4	8.19
5	11.40
6	14.02

Table 4.8 - Gearbox Natural Frequencies

Gearbox Casing Mode	Frequency (Hz)
1	245
2	259
3	336
4	427
5	431
6	493

If drivetrain modes are excited by transient events then they should appear prominently during output deflections of the transient model. The first drivetrain mode is displayed in Figure 4.121 showing it to be a torsional mode around the centre of the drivetrain. The first six drivetrain modes are shown in Figures 4.121 to 4.126.

Chapter 4 – Transient Modelling of the Wind Turbine Drivetrain

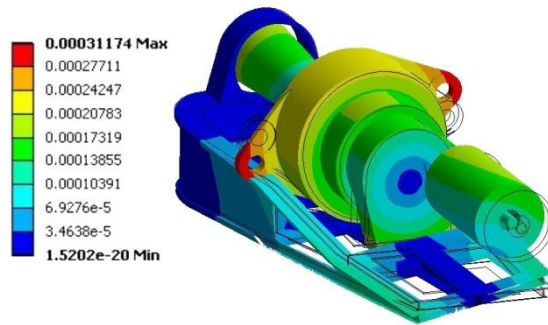


Figure 4.121 - First Drivetrain Mode showing Torsional Behaviour (1.01Hz)

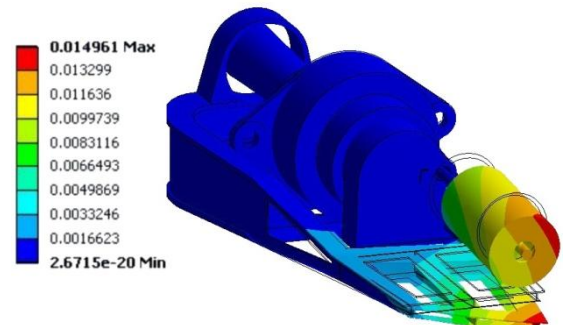


Figure 4.122 - Second Drivetrain Mode showing Bending Behaviour (5.37Hz)

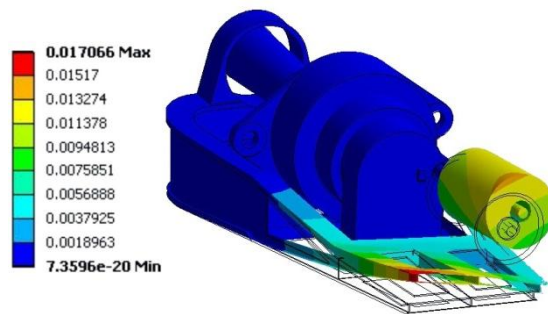


Figure 4.123 - Third Drivetrain Mode showing Bending Behaviour (7.05Hz)

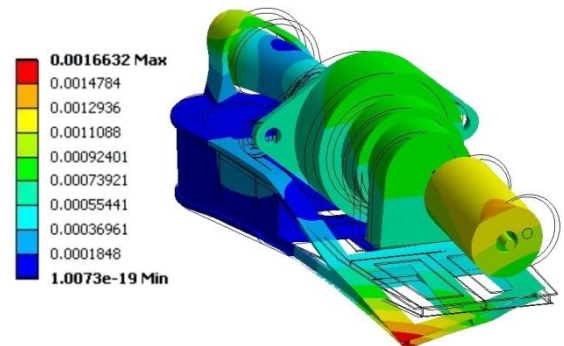


Figure 4.124 - Fourth Drivetrain Mode showing Bending Behaviour (8.19Hz)

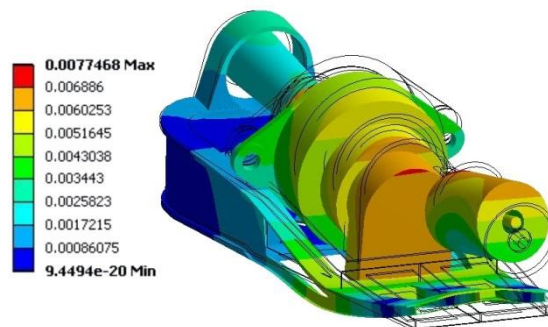


Figure 4.125 - Fifth Drivetrain Mode showing Bending Behaviour (11.40Hz)

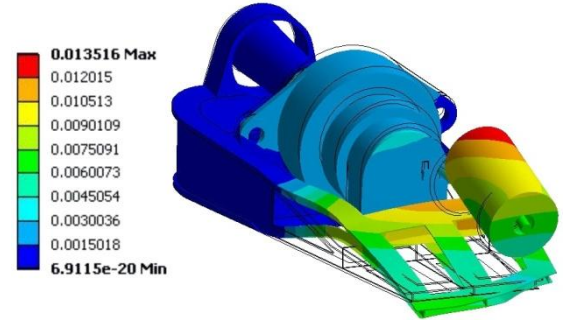


Figure 4.126 - Sixth Drivetrain Mode showing Bending Behaviour (14.02Hz)

Colours show relative deflections of mode shape with black lines displaying the original position of the edges.

4.7.5. Applied Loads

Simulated loads of a wind turbine performing a simulated grid loss emergency stop were created in GH Bladed using the same methodology examined in Chapter 3. Off axis loads applied at the hub are shown in Figure 4.127.

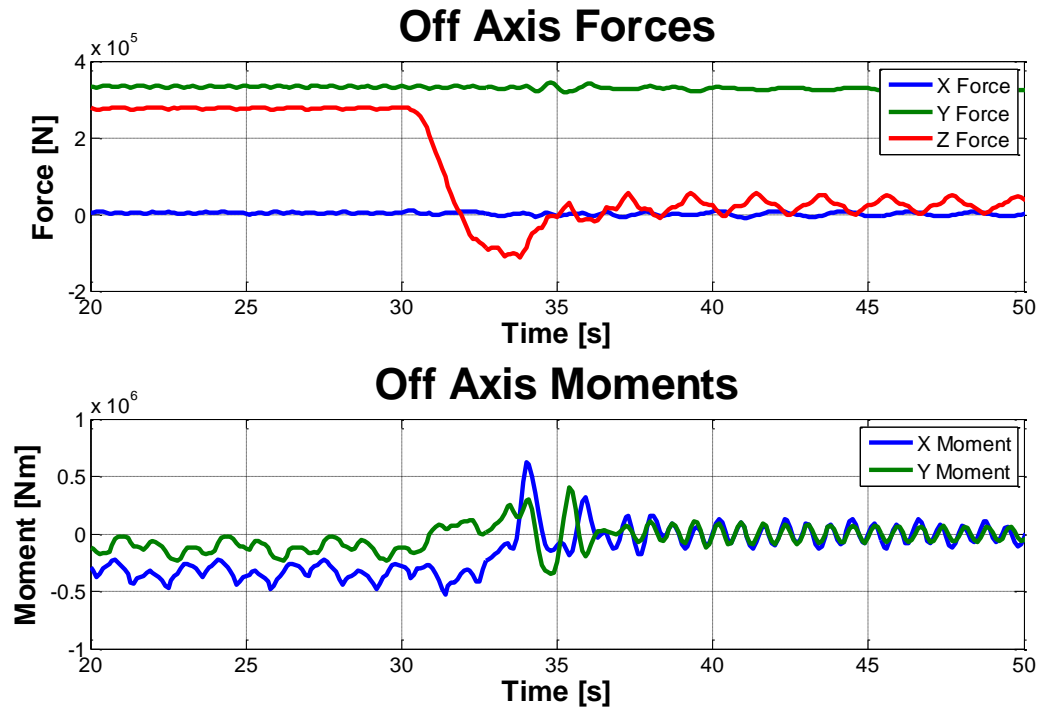


Figure 4.127 - Off Axis Loads Applied at the Hub

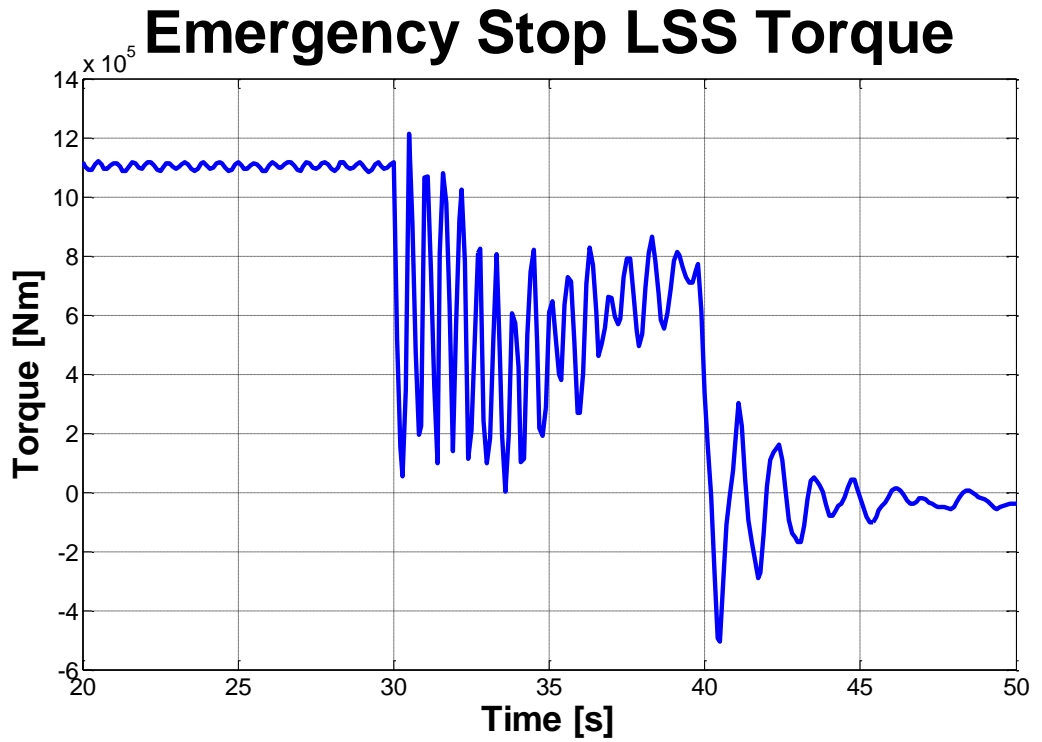


Figure 4.128 - Input Drive Torque

Torque in Figure 4.128 is simulated gearbox input torque. Although this torque enters the gearbox it is not the applied torque on the structure: torque applied at each gear stage is the difference between the input and output torque of each stage. For each time step applied torque at stage 1 is given by:

$$T_{stage1} = T_{in} - T_{in}/GR_{stage1} \quad (4.50)$$

Applied torque at stage 2 is given by:

$$T_{stage2} = T_{in}/GR_{stage1} - (T_{in}/GR_{stage1})/GR_{stage2} \quad (4.51)$$

Applied torque at stage 3 is given by:

$$T_{stage3} = T_{in}/(GR_{stage1} \times GR_{stage2}) - (T_{in}/(GR_{stage1} \times GR_{stage2}))/GR_{stage3} \quad (4.52)$$

Axial loading at each stage is also required to be applied. With knowledge of the contact angle between gears at each stage and the torque at each stage the axial loading for each time step can be calculated:

$$F_{axial} = (T_{stage}/r) \times \tan(\alpha) \quad (4.53)$$

Effective radius, r , for planetary gears is the radius of the ring gear and for parallel gears the radius of the input gear.

The reaction torque of the generator is shown in Figure 4.129.

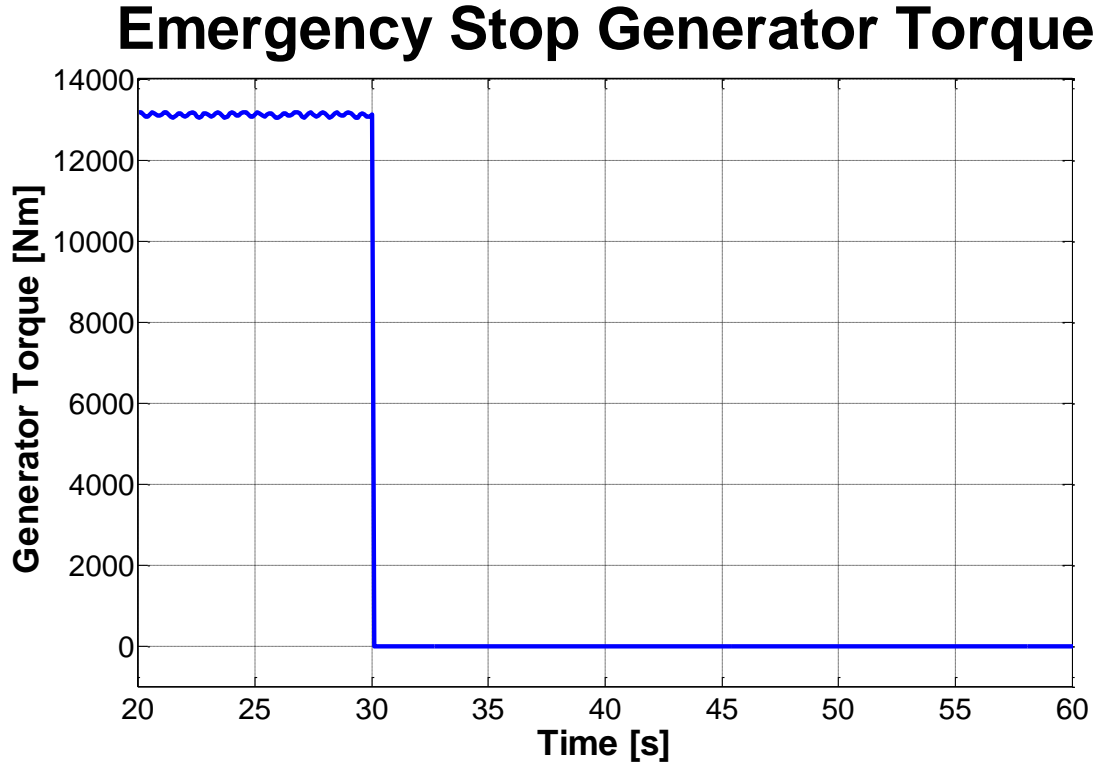


Figure 4.129 - Generator Reaction Torque

4.7.6. Pseudo-Transient vs. Transient Deflections

Comparisons at four points on the drivetrain are made: port and starboard gearbox mounts and stator drive-end (DE) and non-drive-end (NDE) mounts. Time series deflections at these mounts and spectral response of the deflection signal for the transient modelling case and the pseudo-transient case are compared.

Spectral density graphs (Figures 4.131, 4.133, 4.136 and 4.138) show three lines each representing a different section of the emergency stop sequence: before the grid loss event occurs, after the grid loss event has occurred while the wind turbine is braking and when the rotor has come to rest and the drivetrain is no longer rotating.

Deflections against time comparing pseudo-transient and transient gearbox mounts in the vertical motion are shown in Figures 4.130 to 4.133, the coordinate system shows

positive Y deflection as downwards. Gravitational loading causes a positive Y deflection to occur hence both port and starboard mounts are offset positively. The applied torque causes rotation of the gearbox and this can be observed in Figures 4.130 and 4.132: the port mount deflects in the positive Y direction whereas the starboard mount deflects in the negative Y direction.

There are obvious differences in mount deflections between the pseudo-transient and transient modelling. Input loads from the GH Bladed simulations model are clearly observed in the pseudo-transient response in Figure 4.131b with peaks at 0.78Hz, 1.78Hz and 3.96Hz. No other significant peaks on the spectral density are found since modal effects are not able to be calculated by the static model.

Figure 4.130 shows the difference in response frequency between both models. During the braking phase of the stop, magnitudes of the oscillations are not significantly different but in the final stage of the stop the transient model predicts far high magnitude oscillations than the pseudo-transient. Frequency of oscillations can clearly be seen to be different in the braking phase and in the final phase, although similar, a difference between the frequencies of oscillations is observed.

In Figure 4.131a the transient model output shows oscillatory motion not seen on the pseudo-transient output in Figure 4.131b. All peaks from input loads are present but at 1Hz another significant peak exists coinciding with the frequency of the first drivetrain mode. In Figure 4.130, the oscillatory motion in the transient models response is at 1Hz, highlighting the large difference caused by the effects from modes. This will have large impacts on alignment of shafts between gearbox and generator. Most noticeably, differences at the end of the emergency stop when the rotor has come to a standstill predict oscillations of much greater magnitude in the transient model than the pseudo-transient model which may have degrading effects on bearings. Port and starboard displacements are in anti-phase meaning the gearbox is oscillating rotationally in the axial direction (rolling) increasing the likelihood of parallel misalignments occurring between gearbox and generator. Parallel misalignments, as discussed by Whittle [4.6], can be introduced to the HSS when rotation of the gearbox on its mounts occurs as the HSS is offset from the centre of rotation. If the generator does not translate this distance then parallel misalignments

will be created. Figure 4.134 demonstrates how a parallel misalignment can be introduced by the gearbox rotating and the generator not.

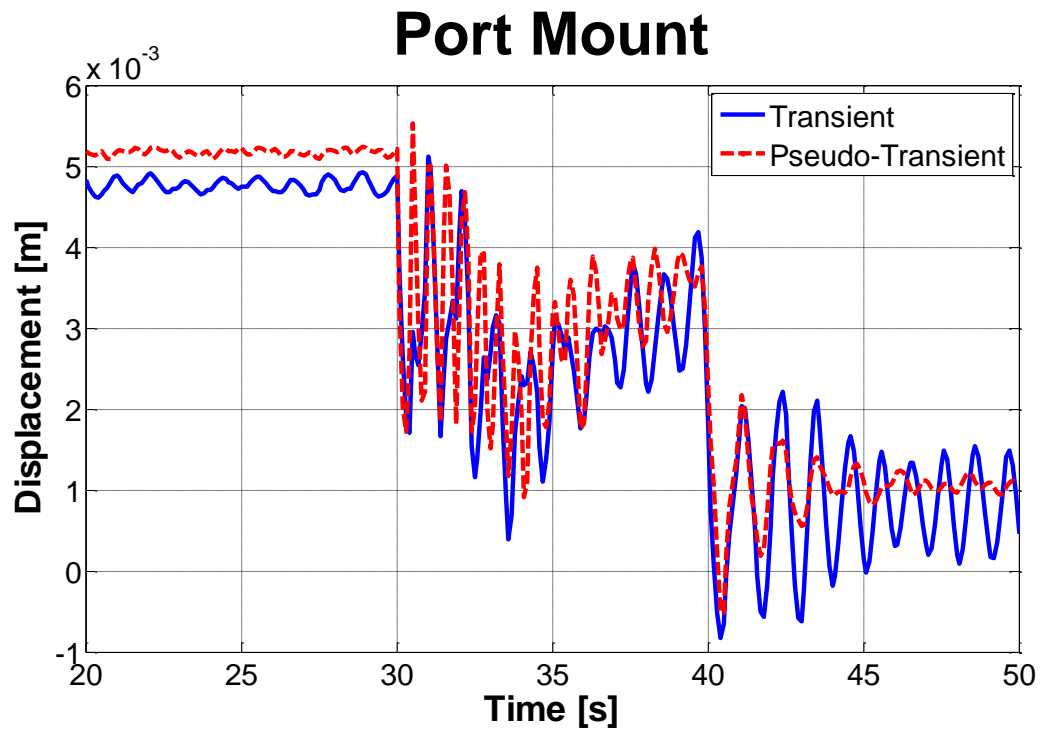


Figure 4.130 - Port Mount Deflections during Emergency Stop

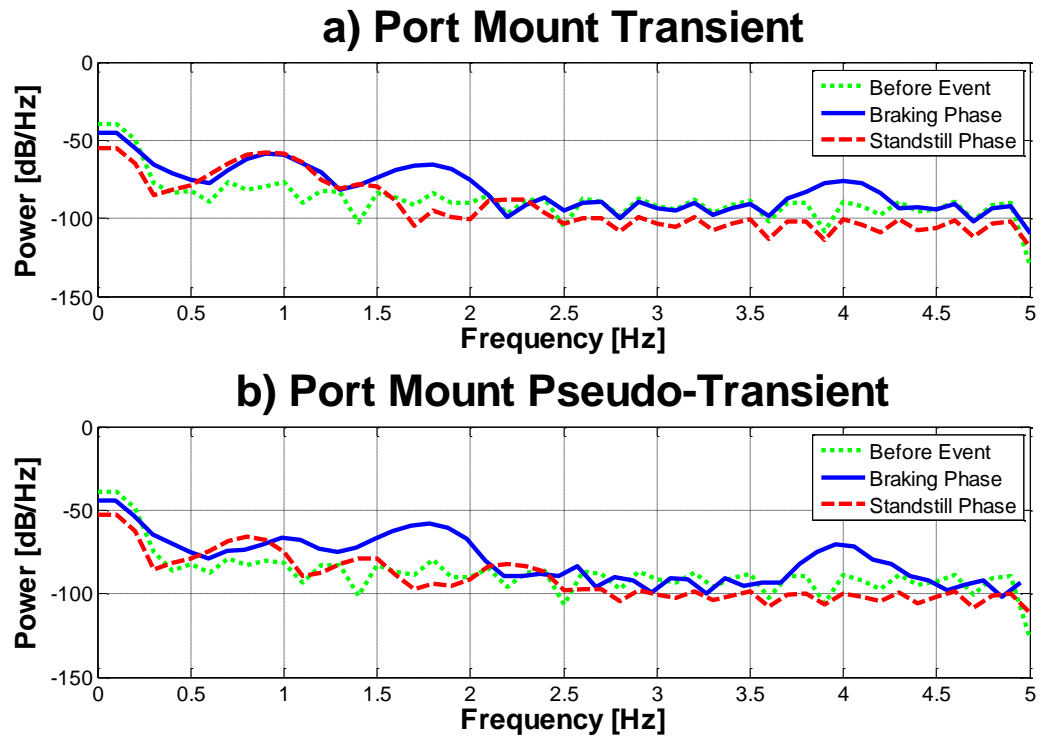


Figure 4.131 - Port Mount Spectral Analysis of Emergency Stop Deflections. Difference is the Peak seen at 1Hz in the Transient Model output showing a Significant Structural Response

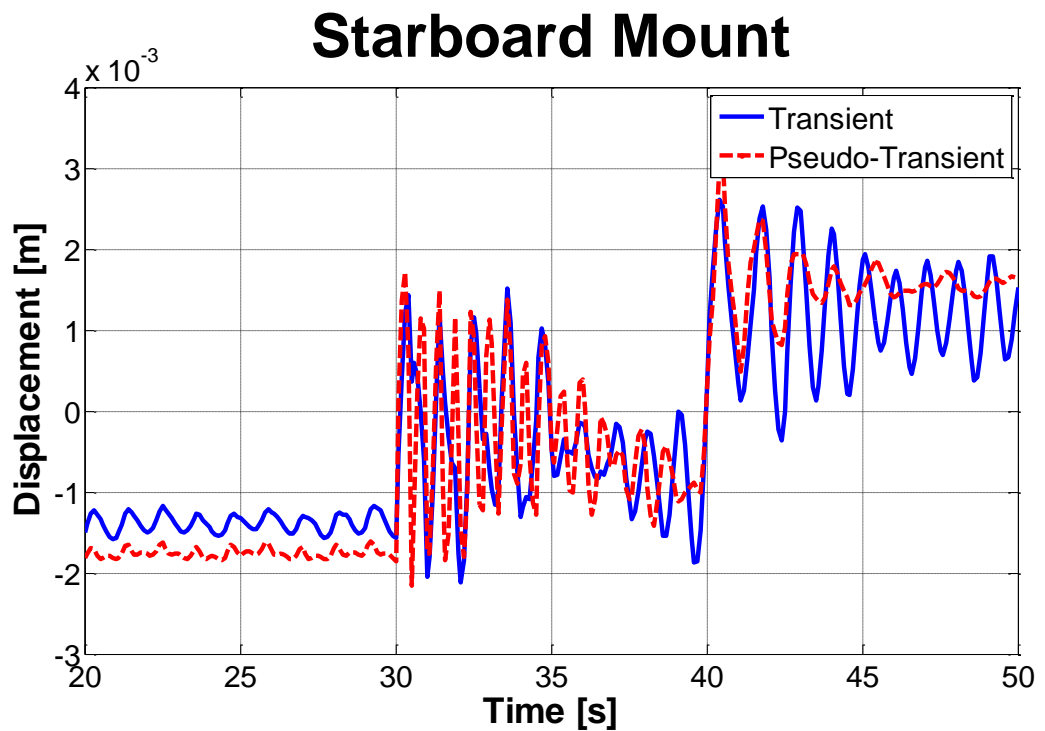


Figure 4.132 - Starboard Mount Deflections during Emergency Stop

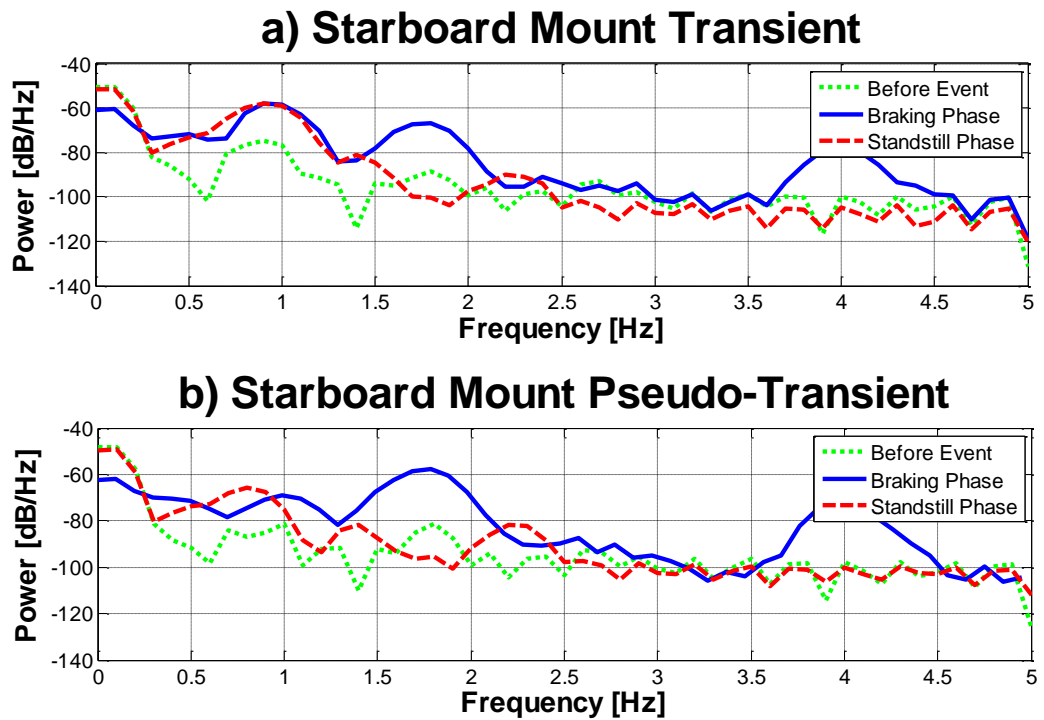


Figure 4.133 - Starboard Mount Spectral Analysis of Emergency Stop Deflection. Again Difference is the Peak seen at 1Hz in the Transient Model output showing a significant Structural Response

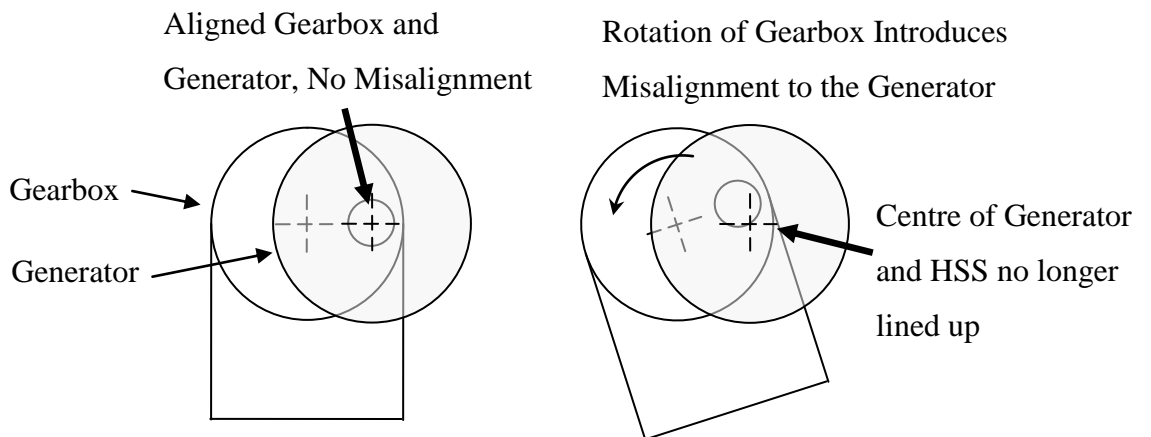


Figure 4.134 - Gearbox Rotations Introduce Parallel Misalignments between Gearbox and Generator

Figures 4.135 to 4.138 show deflections of stator mounts during the emergency stop simulation. Before the grid loss event occurs, the transient model shows higher deflections showing slightly different predictions between the models though observed oscillations are similar. After 30 seconds, the pseudo-transient model

exhibits oscillations at 1.78Hz showing loads are being transferred through the drivetrain to affect off axis loading on the generator. In contrast, deflections caused by input loads are not seen in the transient model meaning the response is dominated by the first drivetrain frequency. This could be caused by the simplicity of the transient model with drive torque not being transferred through the gearbox though could also mean that when modal responses are included this dominates the response. The structural response is especially noticeable when the rotor reaches standstill and the drivetrain bounces around as it settles. The dominant frequency for both stator mount responses in the transient model output is the first drivetrain natural frequency that is not present in the pseudo-transient model output. The drop in displacements seen on the stator mounts coincides with the movement of the nacelle and tower surging forward in response to the drop in axial rotor loading. In Figures 4.136a and 4.138a, the transient spectral responses show a slight peak at 1 Hz for both mounts, which is not seen on the pseudo-transient spectral responses and suggests effects from the first drivetrain mode are important in the response of the structure.

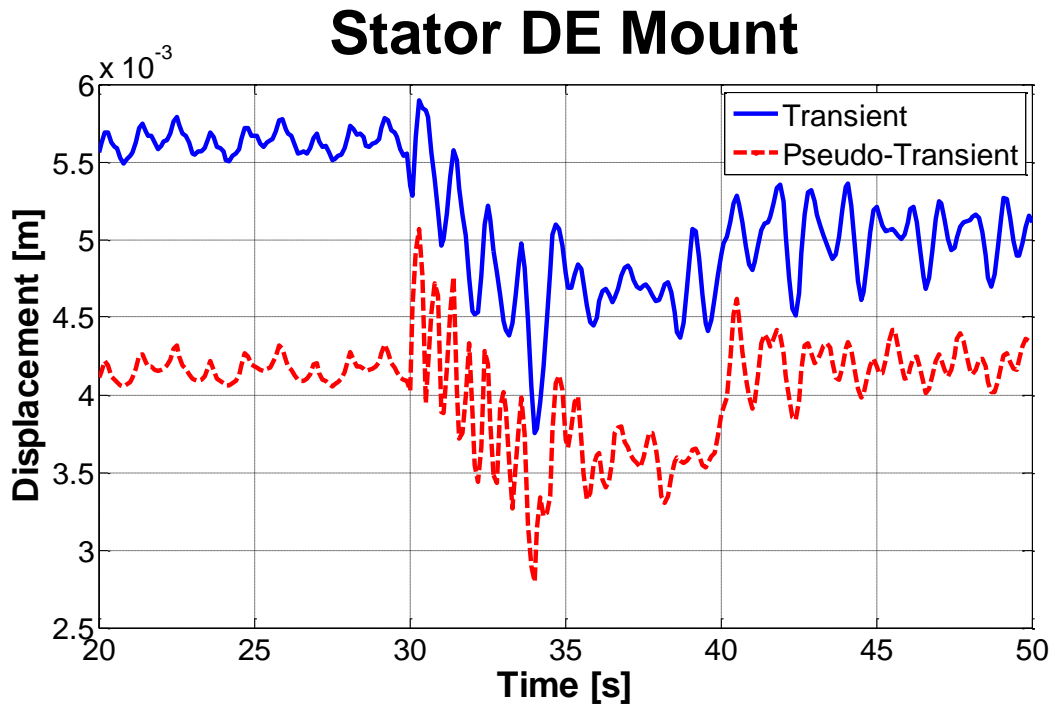


Figure 4.135 - Stator DE Mount Deflections during Emergency Stop

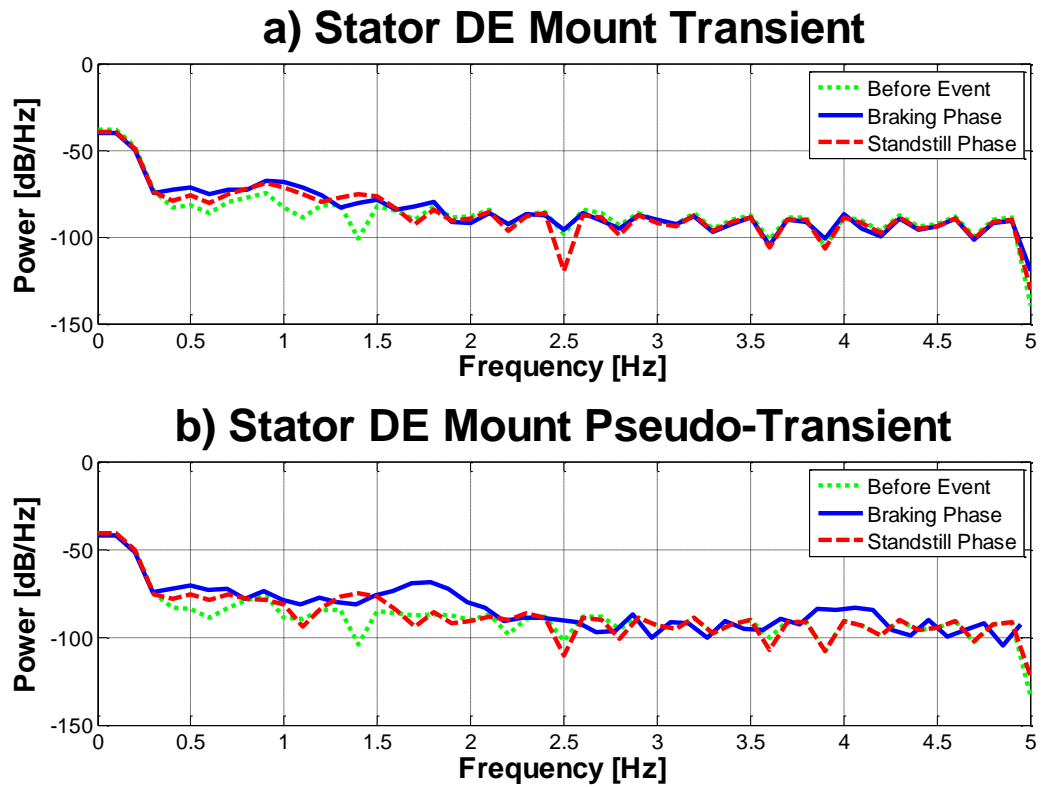


Figure 4.136 - Stator DE Mount Spectral Analysis of Emergency Stop Deflections

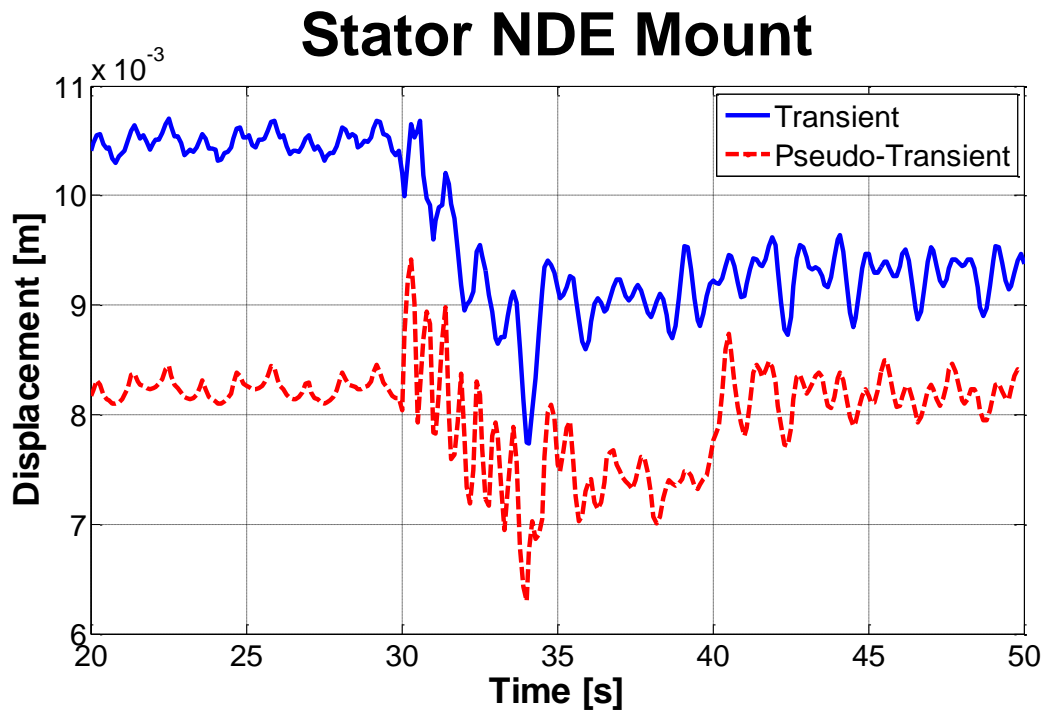


Figure 4.137 - Stator NDE Mount Deflection during Emergency Stop

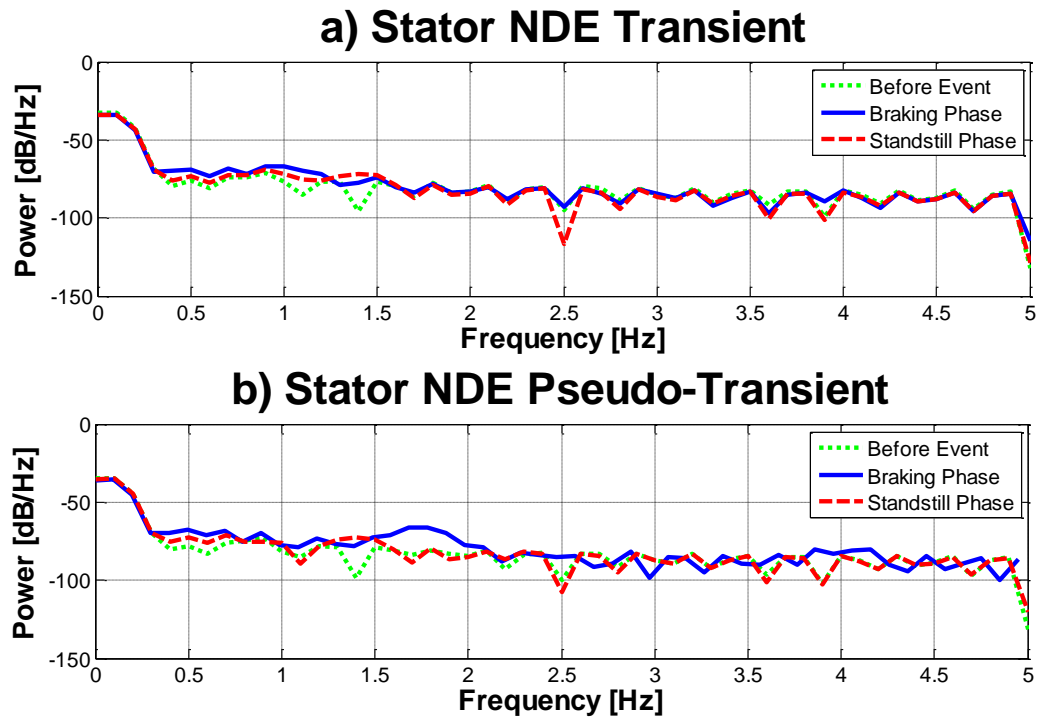


Figure 4.138 - Stator NDE Mount Spectral Analysis of Deflections during Emergency Stop

Axial motion at the mounts for both transient and pseudo-transient models are compared and shown in Figures 4.139 to 4.142. A slight difference in the operational deflections exists, before the grid loss event, though the response between the two models at the port mount is generally similar. Spectral analysis of the port mounts' response shows a slight peak at 1Hz, similar to the vertical deflections signifying that modes have a role in the stator mounts loading. The starboard mount shows similar findings to the port mount with the spectral response from the transient model having a slight peak at 1Hz. Modelling of the axial response therefore shows no response similarity to the measured response of the NREL test rig. This also suggests that the oscillations observed on the NREL test rig are not caused by a structural response and as suggested earlier are likely to be caused by other means, such as design, manufacturing and installation faults.

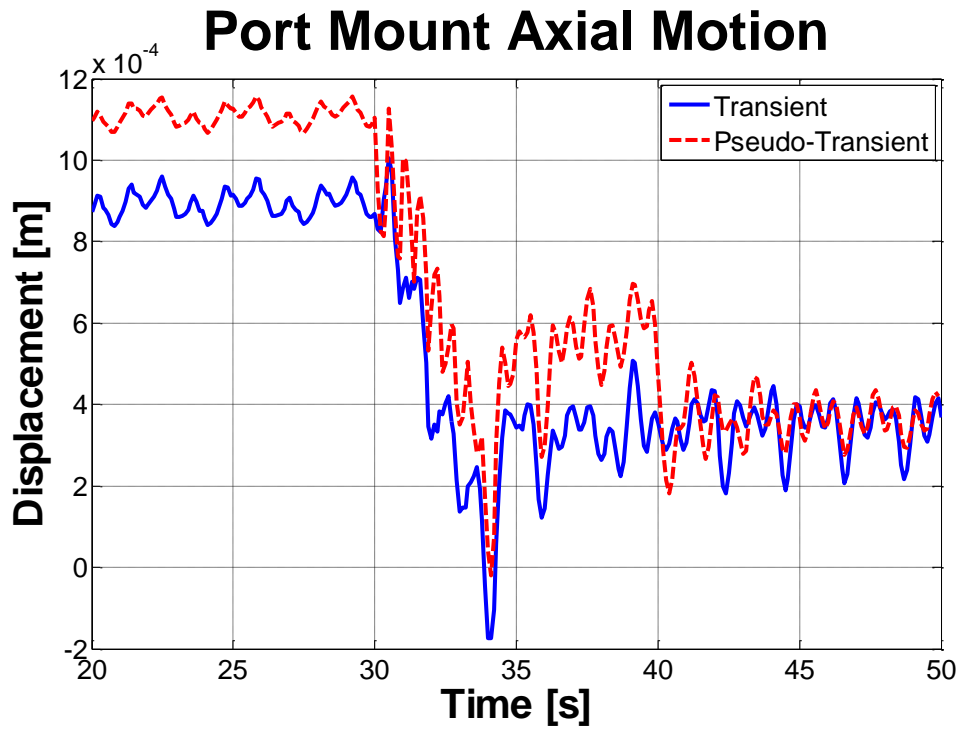


Figure 4.139 - Axial Response of Port Mount

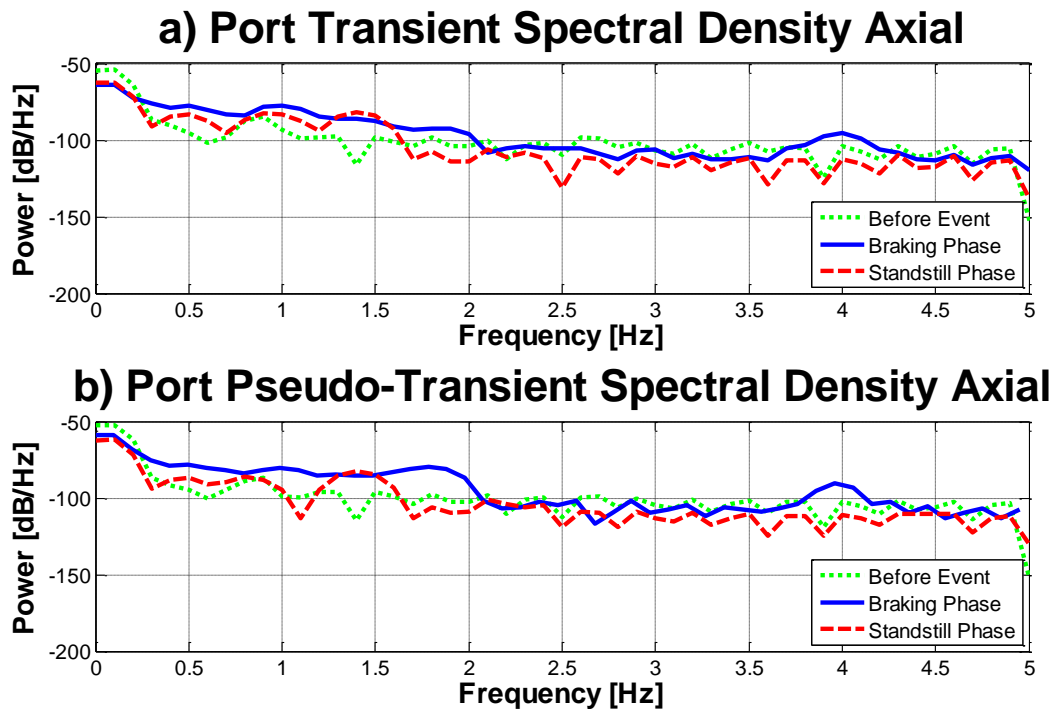


Figure 4.140 - Port Mount Spectral Response in Axial Direction

Starboard Mount Axial Motion

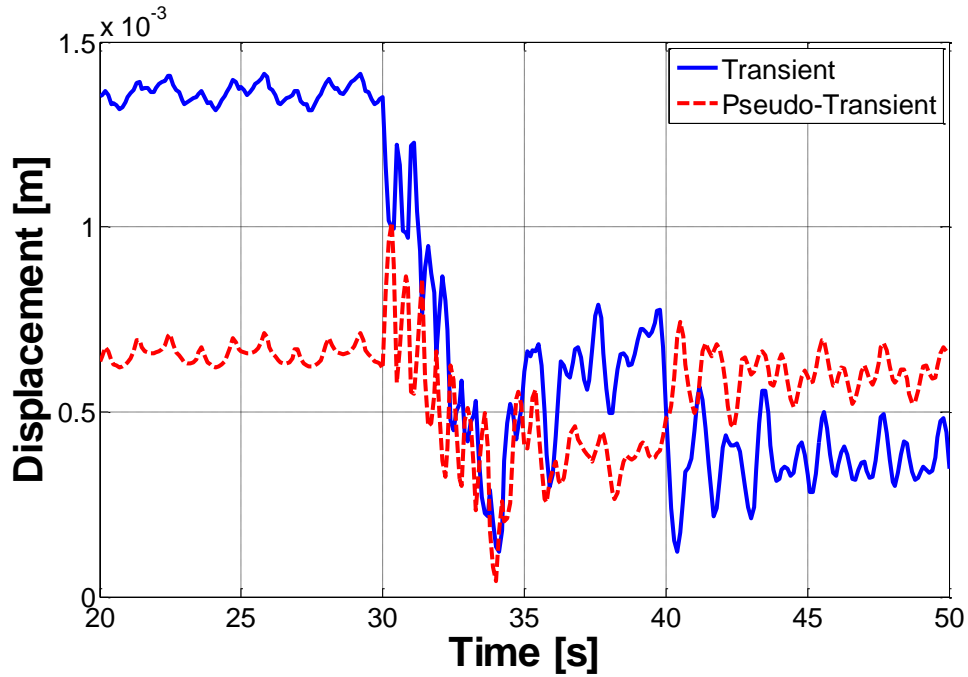
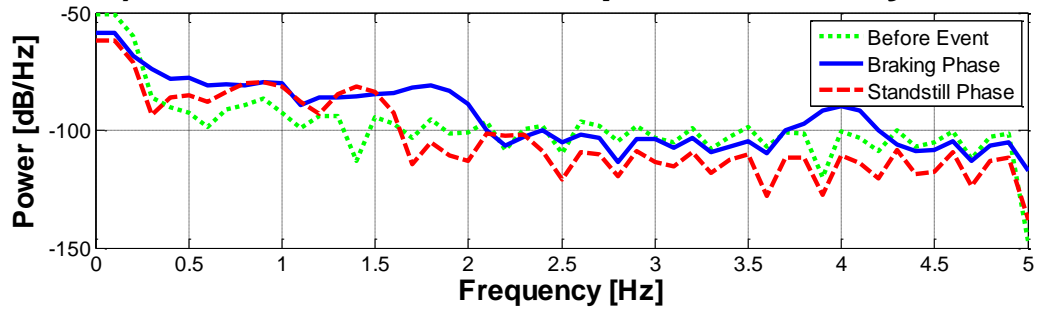


Figure 4.141 - Axial Response of Starboard Mount

a) Starboard Transient Spectral Density Axial



b) Starboard Pseudo-Transient Spectral Density Axial

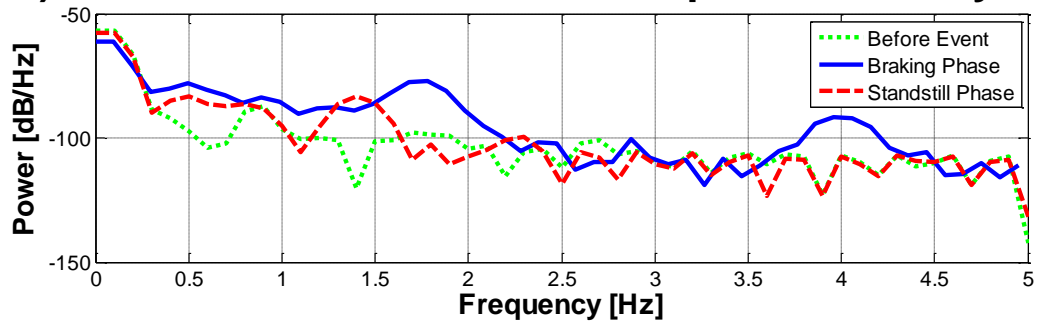


Figure 4.142 - Starboard Mount Spectral Response in Axial Direction

4.7.7. Bearing Stress

Contact stress of a ball bearing can be found by Hertzian contact analysis [4.7] between a spherical rolling element and a cylindrical element raceway. Size of the contact patch between the rolling element and raceway is determined by applied load and material of the bearing which can be used to determine contact stress since

$$Stress = \frac{Force}{Area}.$$

4.8. Truncation

Truncation occurs when the contact patch of the ball bearing is partially outside of raceway. Contact angle on the raceway can become so large that part of the rolling element overlaps the edge of the raceway causing contact area to reduce, increasing contact stress, perhaps significantly [4.8]. Figure 4.143 shows an example of a contact area that is partially outside the raceway.

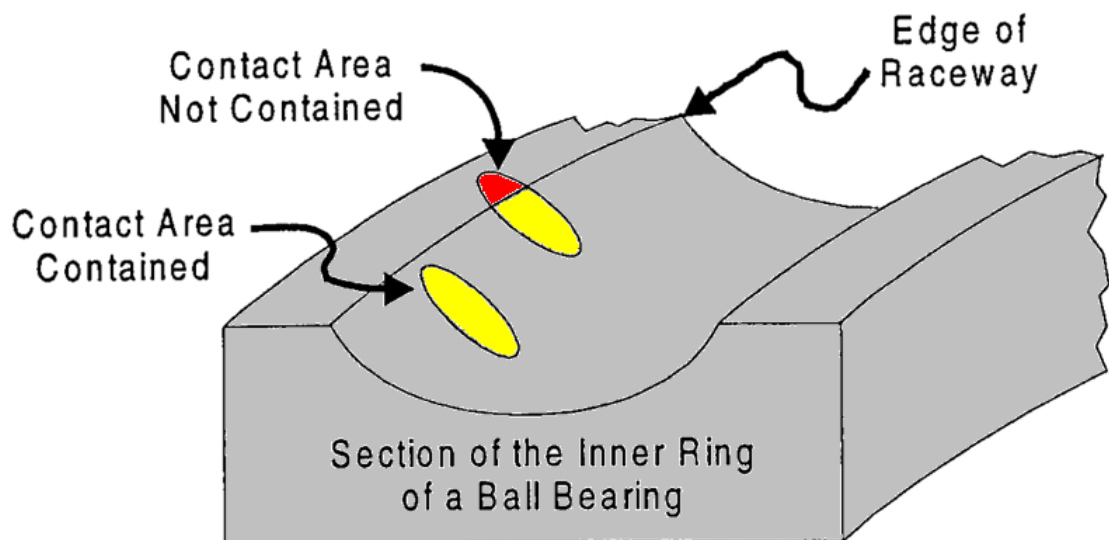


Figure 4.143 - Truncation Diagram [4.8]

Figures 4.144 and 4.145 show contact patches where the generator DE bearing has normal and excessive loads applied to it, the major axis of the contact areas are displayed. With suitable loading on the bearing, contact patches are constrained within boundaries of the raceway; with excessive loading, the contact patches may

no longer be contained and stretch outside the boundaries of the raceway. Contact stress in the latter is accompanied by a large stress peak in the transient stress calculations. Figures 4.144 and 4.145 show the major axis of the contact patches for all 10 rolling elements in the bearing. The blue lines show the limits of the raceway. In Figure 4.144 the contact patches are within the raceway limits accompanied with acceptable levels of contact stress. Figure 4.145, on the other hand, shows some of the contact patches now outside the limits of the raceway. This signifies truncation coupled with a sharp increase in contact stress.

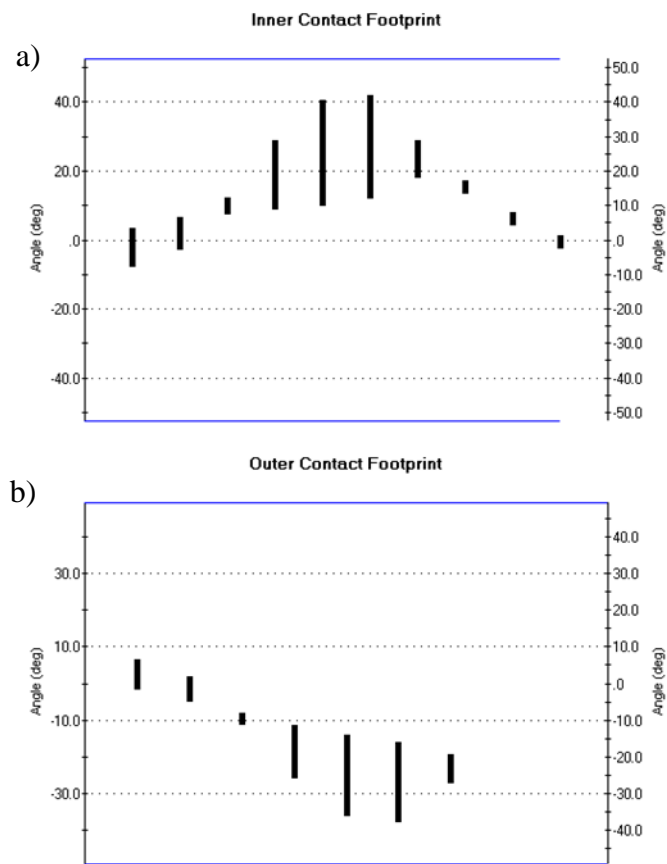


Figure 4.144 - Normal Rolling Element Contact Patch

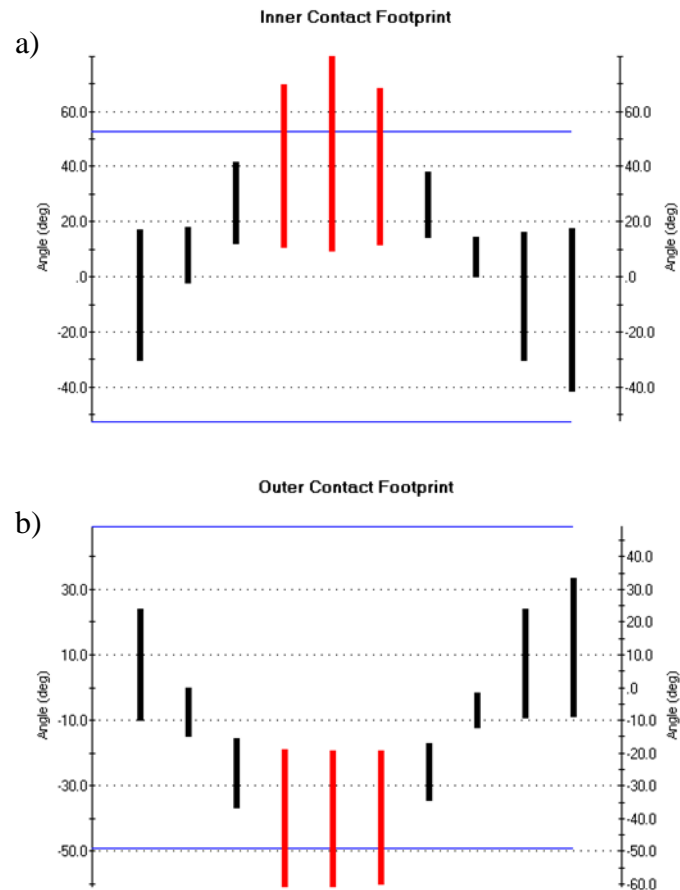


Figure 4.145 - Ball Bearing Footprint in Truncation

4.8.1. High Speed Bearing Stresses

Since high speed bearings are most prone to failing, examining contact stress during transient events may give clues as to why premature failure occurs. Differences in modelling approach between the static pseudo-transient model and transient model is likely to affect load predictions since bearing misalignments will not be the same. As highlighted in Table 4.8, natural frequencies of the gearbox and generator components are high, meaning the system is very stiff, and static models should therefore be able to predict transient loads since they are time independent for low frequency inputs. In order to find bearing stresses, a reduced static drivetrain model in RomaxWIND was created where deflections from 6 locations in the transient ANSYS model could be input, shown in Figure 4.146, and used to calculate contact stresses between rolling element and bearing raceways for each time step. 3 translational DOFs and the 2 off axis DOFs are transferred between the ANSYS

transient model and the reduced RomaxWIND static model. Deflections and contact stresses can be compared between the static model and transient model to highlight any differences in loading between them.

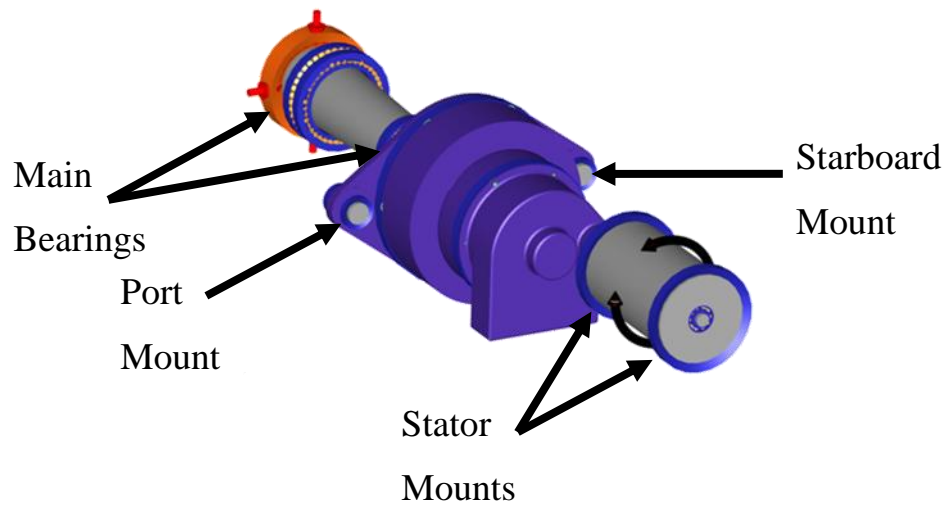


Figure 4.146 - RomaxWIND model used to find Bearing Stresses from Transient Inputs

Three high speed bearings contact stresses were analysed highlighted in Figure 4.147: the output shaft downwind bearing (double tapered roller), the generator DE (radial ball) bearing and the generator NDE (radial ball) bearing.

The output shaft downwind bearing in Figure 4.148 displayed similar loading for both transient and pseudo-transient models while the rotor is braking. When the rotor reaches standstill, large spikes are seen in the contact stress of the bearing caused by truncation of rolling elements.

Both generator bearings in Figures 4.149 and 4.150 show large stress spikes caused by truncation in the first part of the emergency stop, which are not seen on the output shaft downwind bearing. These spikes both coincide with low torque through the drivetrain after the loss of grid. Similar to the output downwind bearing, both generator bearings show contact stress spikes in the later part of the emergency stop caused by truncation. Preloading of bearings is an option that can reduce onset and severity of truncation. Interestingly, the generator DE bearing shows lower mean stresses, excluding truncation spikes, in the transient model than the pseudo-transient model though oscillations are of much greater in magnitude.

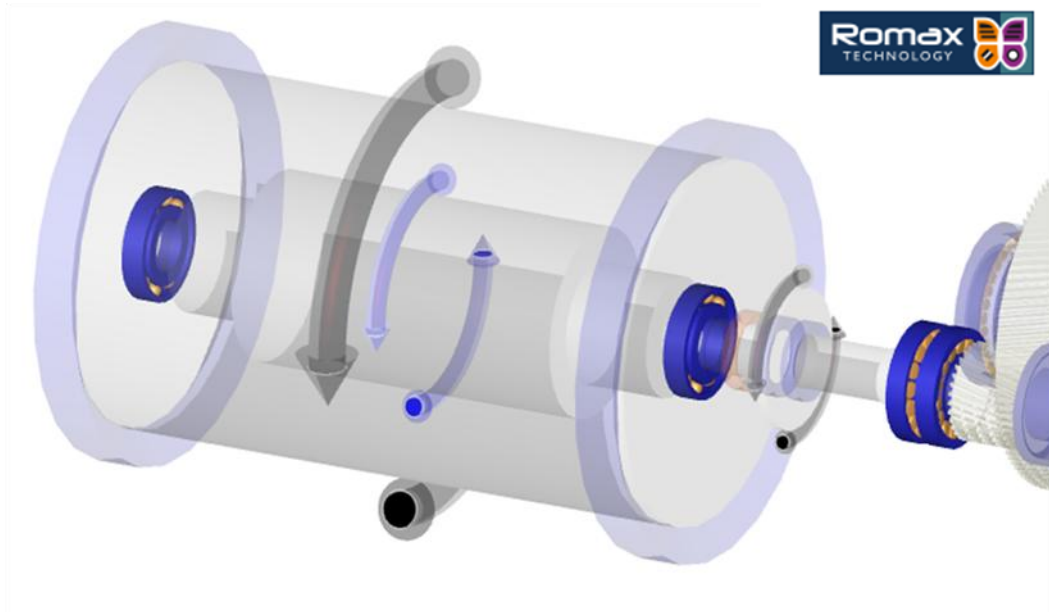


Figure 4.147 - RomaxWIND model with Output Shaft Downwind bearing, Generator DE and Generator NDE bearing highlighted

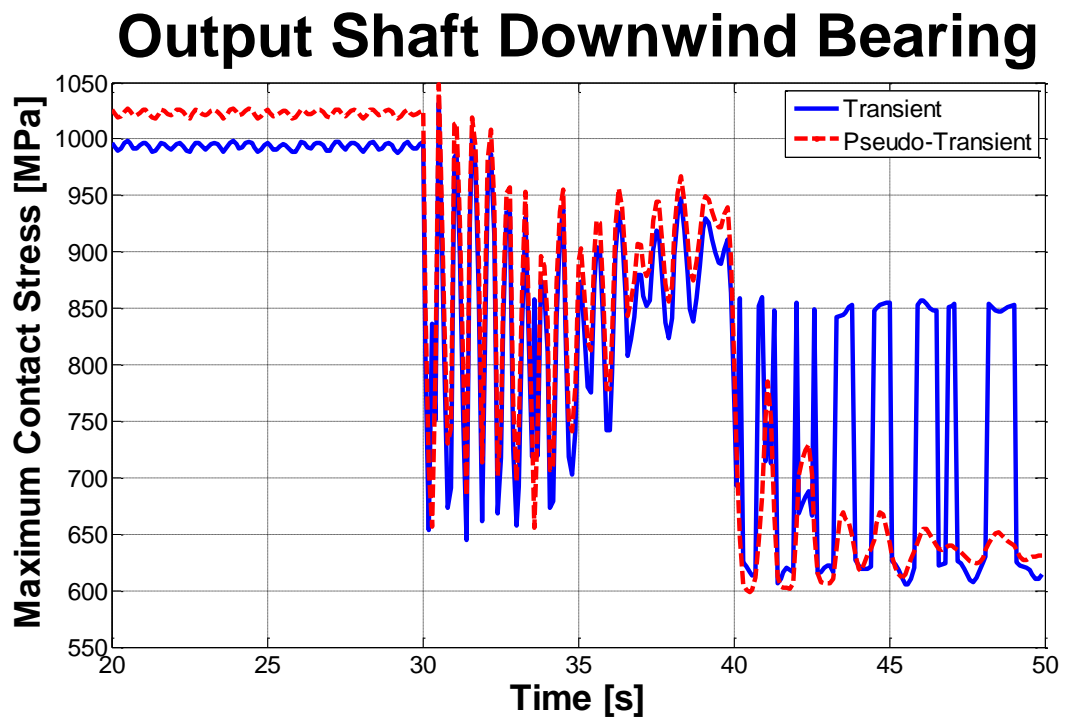


Figure 4.148 - Output Shaft Downwind Bearing Contact Stress during Emergency Stop

Generator DE Bearing

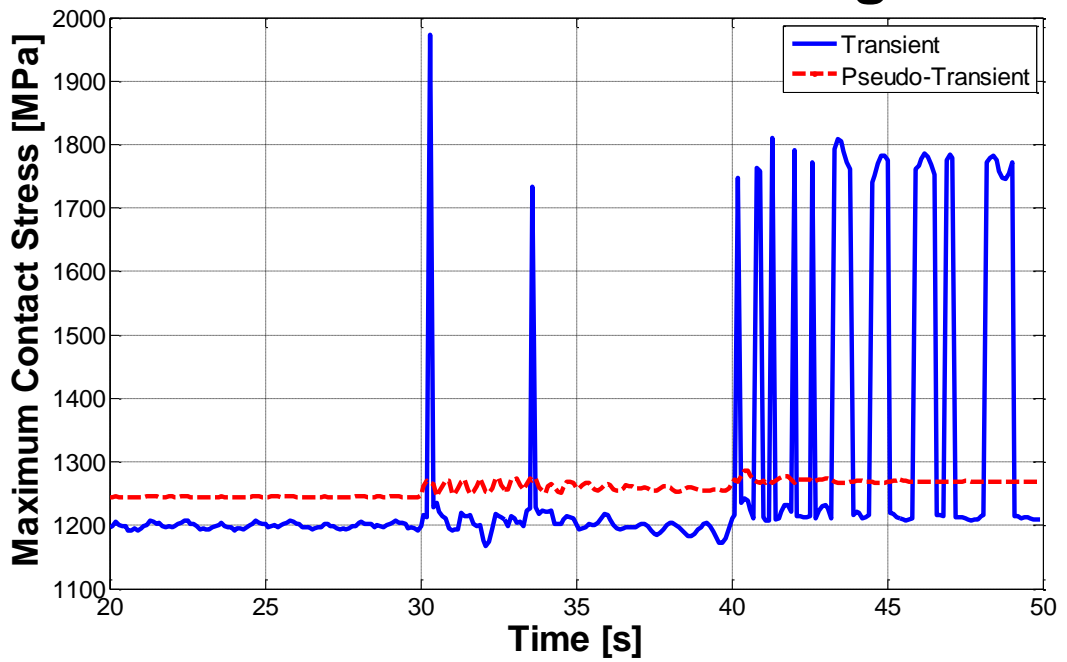


Figure 4.149 - Generator DE Bearing Contact Stress during Emergency Stop

Generator NDE Bearing

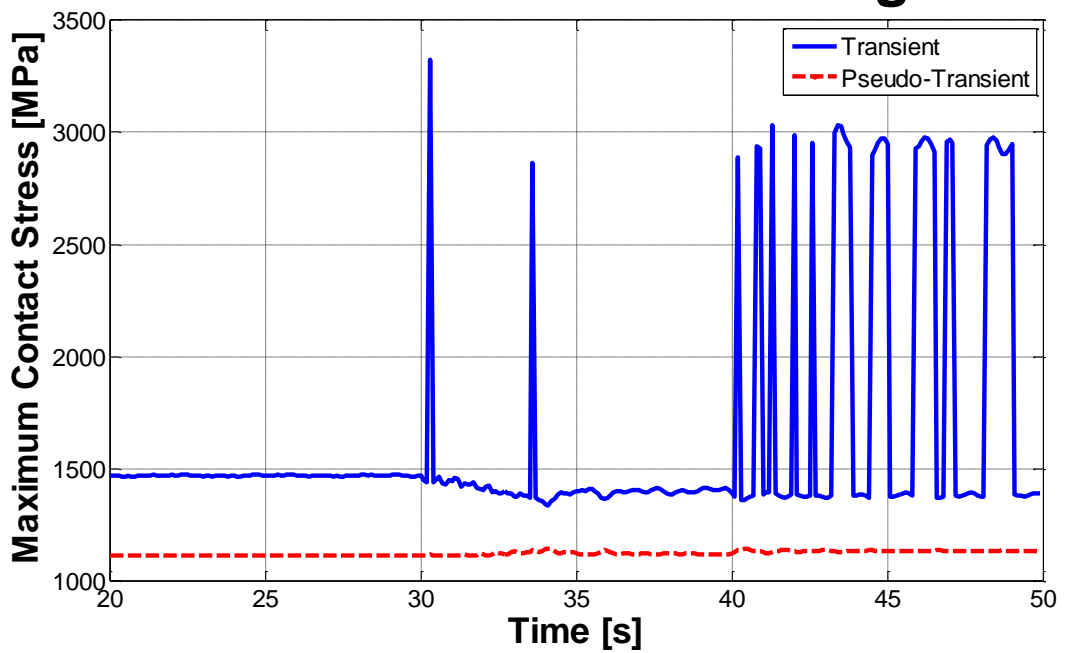


Figure 4.150 - Generator NDE Bearing Contact Stress during Emergency Stop

4.9. Skidding

Rolling contact fatigue is not necessarily the only method that can cause wear on bearings. Skidding is a phenomenon that occurs when rolling elements do not perfectly roll but slide along the raceway. This is a high wear process on surface material of both the rolling elements and raceways. First studied by Poplawski and Mauriello [4.9], several correlations were published attempting to predict the onset of skidding. Hirano [4.10] experimentally examined the motion of ball bearings and suggested that onset of skidding was a ratio of axial force, Q_C , to rolling element centrifugal force, F_C , and occurs when the following relationship becomes true.

$$\frac{Q_C}{F_C} \leq 10 \quad (4.54)$$

Kliman [4.11] proposed similar findings to Hirano for the onset of skidding though they were in disagreement over the magnitude: Kliman stating that skidding would occur at $\frac{Q_C}{F_C} \leq \cos \alpha = 1.22$ for the bearings Hirano used. Poplawski [4.9] suggested that the ratio of axial to centrifugal force was not a unique measure for the onset of skidding.

Boness and Gentle [4.12-4.14] compared computer predictions with experimental data to identify criteria that could be used to predict the onset of skidding. Elastohydrodynamic traction models were created and compared to experimental results. Maximum pressure on the inner raceway is related to rotational speed of the bearing and predicted by,

$$\sigma_{max} = 0.00733(N^2 d_m)^{0.22} (d_m Z \eta)^{-0.175} \text{ GPa} \quad (4.55)$$

The prediction of traction and load transfer is outlined in Harris [4.7] where estimation of the contact area between the rolling element and the bearing raceway is important. The curvature sum is given by:

$$\Sigma \rho_i = \frac{1}{D} \left(4 - \frac{1}{f_i} + \frac{2\gamma}{1-\gamma} \right) \quad (4.56)$$

$$\gamma = \frac{D \cos \alpha}{d_m} \quad (4.57)$$

Size of the contact area is found using empirical methods found in Harris [4.7]. The major, a, and minor, b, ellipse dimensions can be found using:

$$a_i = 0.02364a^* \left(\frac{Q_i}{\Sigma\rho_i} \right)^{\frac{1}{3}} \quad (4.58)$$

$$b_i = 0.02364b^* \left(\frac{Q_i}{\Sigma\rho_i} \right)^{\frac{1}{3}} \quad (4.59)$$

Variables a* and b* are dimensionless parameters found through the geometry of the bearing itself and can be found using the curvature difference of the bearing geometry and Figures 4.151 and 4.152.

$$F(\rho_i) = \frac{\frac{1}{f_i} + \frac{2\gamma}{1-\gamma}}{4 - \frac{1}{f_i} + \frac{2\gamma}{1-\gamma}} \quad (4.60)$$

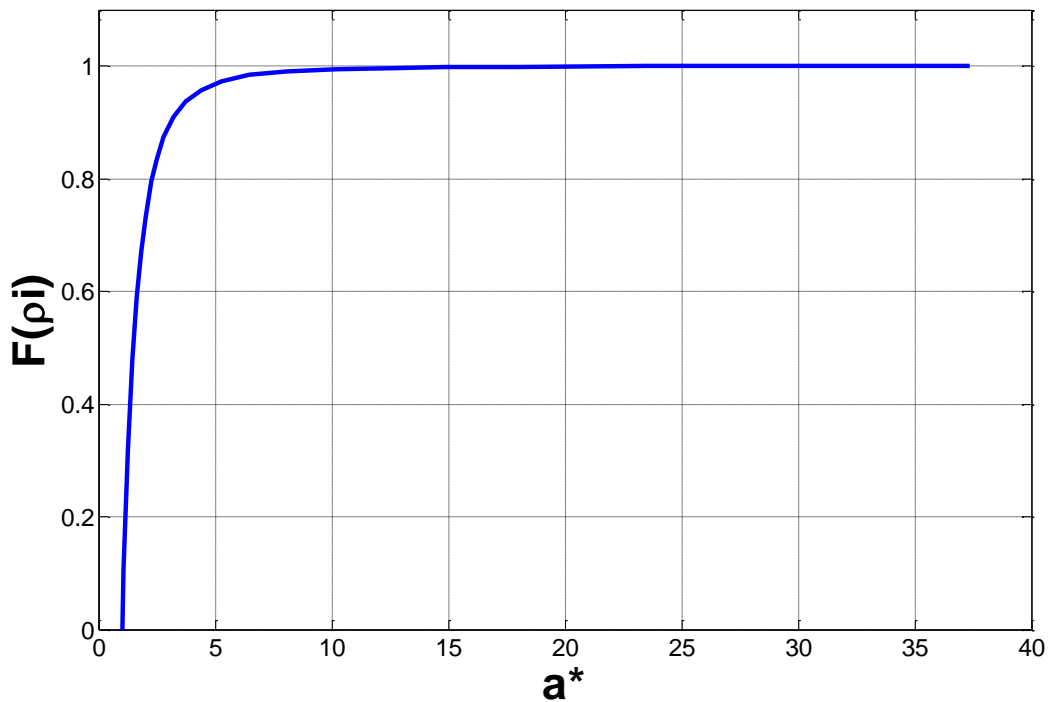


Figure 4.151 - a* dimensionless parameter

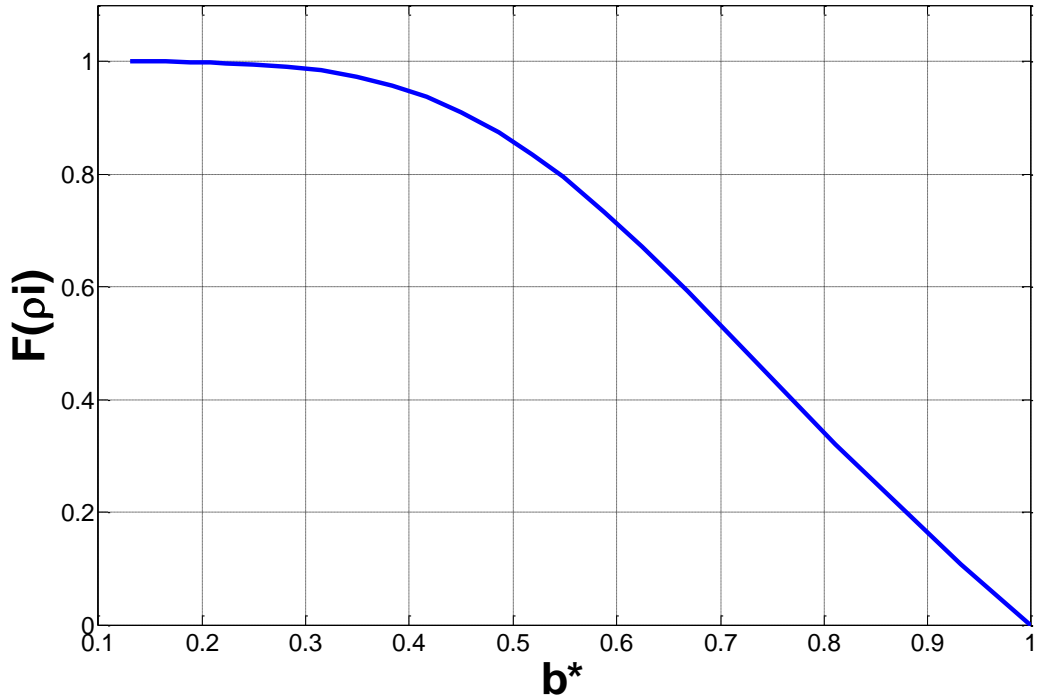


Figure 4.152 - b* dimensionless parameter

Maximum compressive stress is given by below relating compressive stress to applied load:

$$\sigma_{max} = \frac{3Q_i}{2\pi a_i b_i} \quad (4.61)$$

These equations may be combined to give the relationship relating stress to applied loading on the bearing:

$$Q_i = (0.3725\sigma_{max}\pi a^* b^*)^3 \frac{1}{\Sigma\rho^2} \quad (4.62)$$

Minimum axial loading on the bearing to avoid skidding can now be found:

$$T = ZQ_i \sin \alpha_i \quad (4.63)$$

From the transient analysis, axial loading on the generator DE bearing can be extracted. Using geometry of the bearing along with axial loading, predictions on whether skidding occurs during the grid loss emergency stop can be made. Both methods are shown in Figure 4.153 where coloured areas are regions where skidding is expected to occur. Boundary of the shaded area signifies the minimum axial force at that rotation speed to prevent skidding. Boness's Method is more conservative predicting skidding will occur at a greater axial force than Hirano's Method.

Minimum Axial Force to Prevent Skidding

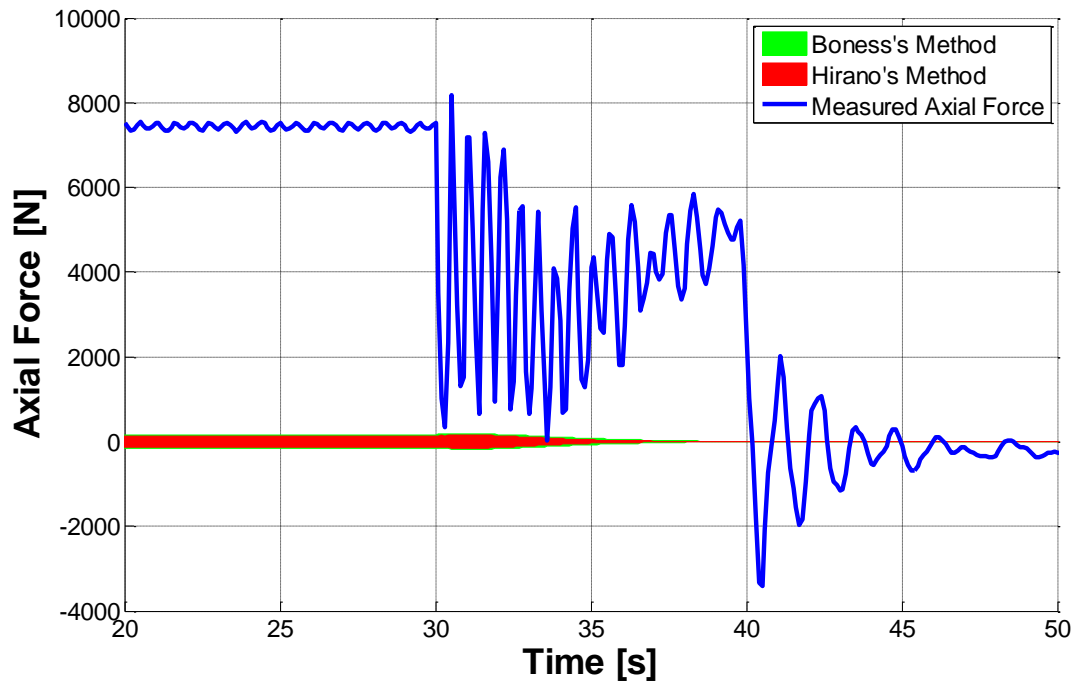


Figure 4.153 - Thrust Loading required for Skidding to Occur

Minimum Axial Force to Prevent Skidding

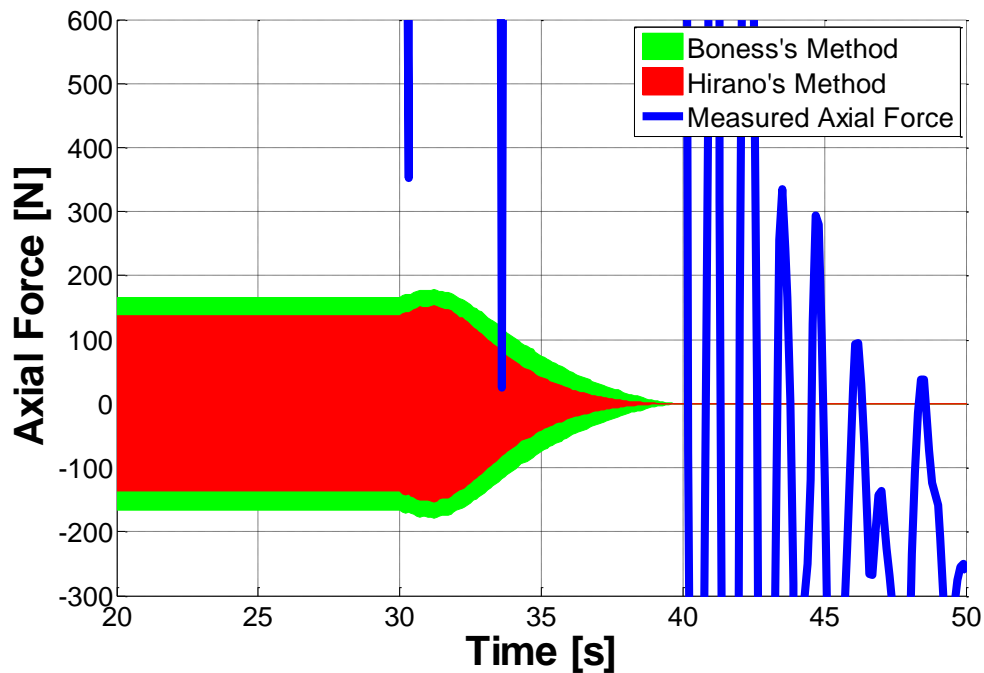


Figure 4.154 - Thrust Loading Required for Skidding (Y Axis Zoomed)

Figure 4.153 shows the loading entering the skidding region once at 33.6 seconds. Axial force required to prevent skidding increases at 30 seconds since the rotor speed accelerates subsequently increasing rotation speed on the high speed end. The applied axial loading to the bearing must also increase to prevent skidding. Similarly when the rotor slows down, minimum axial force to prevent skidding also decreases. Although Figure 4.153 suggests that skidding occurs once during the emergency stop, loading is close to the threshold on several occasions that may suggest skidding may occur to some extent during these other times. The results suggest here that skidding could be a potential issue though more work using higher fidelity models are required to provide more conclusive results.

Although these models predict skidding conditions in steady state, Gupta [4.15] suggests that shaft accelerations and decelerations cause skidding to occur at higher axial loading. Gupta created a full 6 degree of freedom model for the ball motion in a ball bearing using different lubrication traction models. Jain [4.16] similarly created a six degree of freedom model using lubricant models to predict the traction. These

traction terms were determined through oil film pressure and showed regions where skidding may occur in operation.

Jain [4.16] showed that skidding of ball bearings is likely to occur on unloaded sections of every cycle if axial loading is not sufficient. Pure rolling occurs in the loaded part of the cycle but slip occurs in the unloaded part of the cycle. When the rolling element returns to the loaded part of the cycle the rolling element has to accelerate causing sliding. This portion of the cycle is the most damaging in terms of surface wear of the raceway and rolling element.

4.10. Summary

This investigation has shown that greater magnitude deflections are predicted on gearbox mounts during the grid loss emergency stop when transient models are used instead of pseudo-transient models. This is a result of the modal excitation of the complete bedplate structure, in particular the first drivetrain mode. The pseudo-transient model cannot capture the response from the natural frequencies of the whole structure and therefore may miss some of the most damaging misalignments. Increased stress on high speed bearings could be a reason for premature failure, especially on the generator NDE bearing. Comparison between the transient and pseudo-transient highlights phenomenon such as truncation could be occurring which is not predicted by the static models. The complete drivetrain should be modelled transiently in order to achieve more accurate calculations of the loads to ensure correct loading is predicted on the bearings.

Pseudo-transient analysis, although simpler and less computationally intense, fails to capture some of the most fundamental dynamics of the drivetrain and misses effects from drivetrain modes. This would suggest that other transient events can excite these modes and contribute to additional loading on the bearings. Transient analysis would therefore be beneficial to use in cases where highly transient loading occurs.

Future work could involve more detailed analysis of the creation of loads and how they are transferred to the structure. Skidding could potentially cause problems in low loading areas where high rotational speeds in high speed bearings are coupled

with low loading. This could be especially apparent in the few seconds after the grid loss event where low loading and high rotational speed exist. More work into the onset and effects of skidding, when bearings are subjected to high accelerations or decelerations, would be useful to conclusively prove that skidding is an issue during transient events.

Chapter 4 References

- [4.1] C. Kelley and D. E. Keyes, "Convergence analysis of pseudo-transient continuation," *SIAM Journal on Numerical Analysis*, vol. 35, pp. 508-523, 1998.
- [4.2] A. Pica and E. Hinton, "Transient and pseudo-transient analysis of Mindlin plates," *International Journal for Numerical Methods in Engineering*, vol. 15, pp. 189-208, 1980.
- [4.3] T. Kant and S. Patel, "Transient/pseudo-transient finite element small/large deformation analysis of two-dimensional problems," *Computers & Structures*, vol. 36, pp. 421-427, 1990.
- [4.4] ANSYS, "ANSYS 12.1 Help Files," ed, 2009.
- [4.5] J. Coultate. (2012) Understanding Costs for Large Wind-Turbine Drivetrains. *Windpower Engineering*. Available:
<http://www.windpowerengineering.com/design/mechanical/understanding-costs-for-large-wind-turbine-drivetrains/>
- [4.6] M. Whittle, *et al.*, "A Parametric Study of the Effect of Generator Misalignment on Bearing Fatigue Life in Wind Turbines," presented at the EWEA 2011, Brussels, 2011.
- [4.7] T. Harris, *Roller Bearing Analysis*: John Wiley & Sons, 2001.
- [4.8] P. Frantz and A. Leveille, "An Approach to Predicting the Threshold of Damage to an Angular Contact Bearing during Truncation," DTIC Document2001.

- [4.9] J. V. Poplawski and J. A. Mauriello, "Skidding in Lightly Loaded High-Speed Ball Thrust Bearings," 1969.
- [4.10] F. Hirano, "Motion of a ball in angular-contact ball bearing," *ASLE TRANSACTIONS*, vol. 8, pp. 425-434, 1965.
- [4.11] P. Kliman, "High Speed Ball Bearings-Limitation and Thrust Requirements," *Lubri. Eng.*, vol. 20, pp. 151-154, 1964.
- [4.12] R. J. Boness and C. R. Gentle, "Ball motion in thrust loaded ball bearings," *Wear*, vol. 35, pp. 131-148, 1975.
- [4.13] C. Gentle and R. Boness, "Prediction of ball motion in high-speed thrust-loaded ball bearings," in *American Society of Mechanical Engineers and American Society of Lubrication Engineers, Joint Lubrication Conference, Miami Beach, Fla*, 1975.
- [4.14] R. Boness, "Minimum load requirements for the prevention of skidding in high speed thrust loaded ball bearings," *Journal of Lubrication Technology*, vol. 103, p. 35, 1981.
- [4.15] P. Gupta, "Transient ball motion and skid in ball bearings," *Journal of Lubrication Technology*, vol. 97, p. 261, 1975.
- [4.16] S. Jain and H. Hunt, "A dynamic model to predict the occurrence of skidding in wind-turbine bearings," in *Journal of Physics: Conference Series*, 2011.

5.

Medium Speed Drivetrains

5.1. Improved Reliability?

In-depth studies into gearbox failures in Chapter 1 showed high speed bearings failures were the major cause of downtime for wind turbines. Efforts in previous chapters have focused on showing that current modelling techniques may not adequately predict loading on bearings and as a result the most susceptible bearings may fail unexpectedly. In this chapter a different design of drivetrain is compared to the established three stage gearbox high speed drivetrain with a view to mitigating problems inherent to the three stage gearbox design. A medium speed design was first proposed by Gamesa with the aim of improving reliability of the drivetrain. The design, a hybrid between the high speed drivetrain and the direct drive drivetrain, uses a two stage gearbox with medium speed permanent magnet generator; the final stage of the three stage gearbox is omitted since high speed bearings are most prone to failure. Output rotational speed of the gearbox is now less than that of a high speed drivetrain so the generator must be larger in order to handle the reduced speed and increased torque. The physical size of the generator increases causing capital cost of the drivetrain to increase and more weight at the tower top may have implications for tower and foundation design, ultimately leading to higher capital costs or the whole turbine. The aim of the medium speed drivetrain is to improve overall wind turbine reliability sufficiently so that CoE of the medium speed is lower than the high speed drivetrain. By improving availability, energy capture and maintenance, costs are likely to reduce more than increased initial capital costs of new drivetrain components lowering CoE. Capital costs for the medium speed drivetrain are still substantially lower than the direct drive drivetrain which should provide an advantage in CoE analysis.

Another benefit which the medium speed drivetrain offers is a lower likelihood of skidding since the maximum rotational speeds are not as great: the removal of the final gearbox stage means rotational speeds can be 3 to 5 times lower than in the high speed drivetrain. Centrifugal force of rolling elements is therefore significantly lower reducing the minimum loading on the bearing before the onset of skidding. Since skidding is a high wear process it is likely that reducing the chance of skidding will improve bearing lifetime.

5.2. Drivetrain Structure Sensitivity

As described in 5.1 above, the final parallel stage is eliminated in the gearbox leaving the two initial stages. Both remaining gear stages are planetary meaning the gearbox and generator are in-line with each other and not offset as in the high speed drivetrain. Instead of the modular design where the gearbox and generator are separate components individually attached to the bedplate, the medium speed design attaches the generator directly to the back of the gearbox and the whole system is cantilevered on the gearbox mounts. Since the generator is bolted to the back of the gearbox, misalignments are unlikely to be introduced and therefore a flexible coupling is not required. The bedplate, LSS and first two stages in the gearbox are modelled as in the high speed drivetrain but the medium speed generator has a larger, heavier rotor. Generator bearings locate the generator rotor in the stator which in turn is connected to the drivetrain housing. A spline between the gearbox and generator allows for axial misalignments to be tolerated within the drivetrain. The cantilevered system used in this work is based on the “Butterfly Drive” design by Romax Technology [5.1]. Schmidt [5.2] estimates the weight of the medium speed drivetrain though these values seem smaller than expected.

Figure 5.155a shows the full cantilevered drivetrain. The generator is not attached directly to the bedplate rather the gearbox and generator are together in a modular drivetrain component. This does suggest that repairs in situ may be more difficult though it does allow for the whole drivetrain module to be replaced as a single unit, allowing the damaged component to be repaired elsewhere.

A similar analysis to chapter 2 was performed studying the effects of bedplate and mount stiffness on the medium speed drivetrain model.

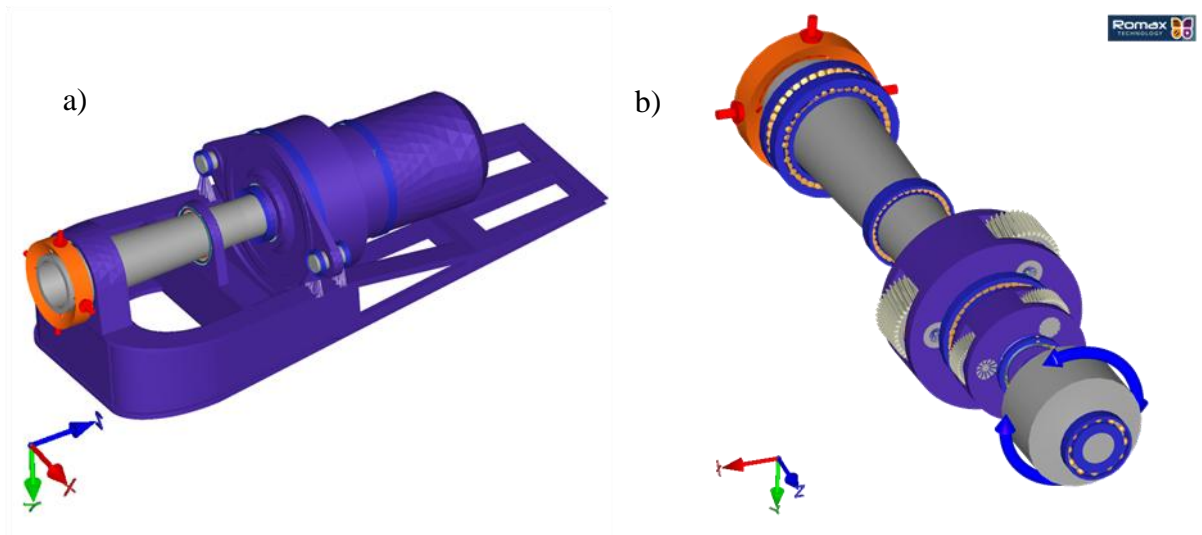


Figure 5.155 - Medium Speed Drivetrain a) Full Drivetrain b) Drivetrain with Bedplate and Gearbox Housing Stripped

Damage Sensitivity to Mount Stiffness

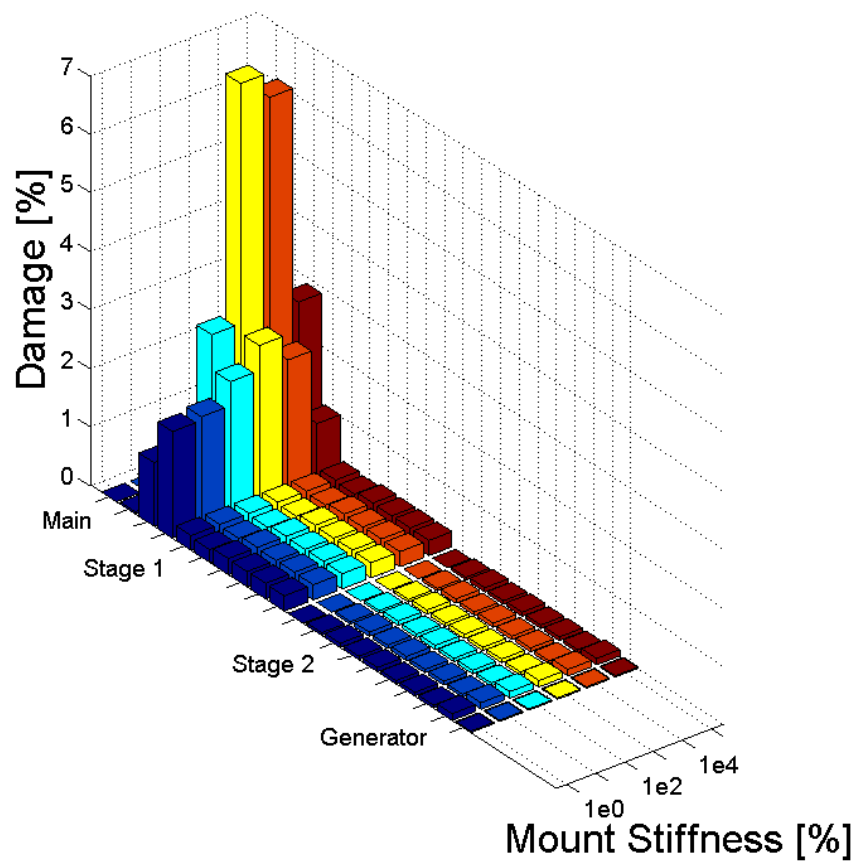


Figure 5.156 - Bearing Damage Sensitivity to Mount Stiffness

Chapter 5 – Medium Speed Drivetrains

Predicted loading on all drivetrain bearings as stiffness of the mounts was changed is displayed in Figure 5.156. Damage prediction used the L10 lifetime criteria, as before, for estimation of damage accrued. Major damage on high speed and generator bearings has been alleviated and upwind and downwind stage 1 carrier bearings now show the highest damage in the drivetrain. Reaction to the drivetrain's cantilevered weight on gearbox mounts are mostly resisted through these bearings, which are subject to higher loading and also show the most sensitivity to changes in gearbox mount stiffness. Although there is slightly increased loading on stage 1 carrier bearings, other bearing loadings are substantially lower than the high speed drivetrain case. An interesting trend is observed as mount stiffness varies: a peak occurs at 1000% of original stiffness on the planet carrier upwind bearing and reduces either side of this. Similar to findings in Chapter 2, results show that either reducing or increasing stiffness away from the peak reduces damage. All other bearings appear insensitive to the effects of mount stiffness.

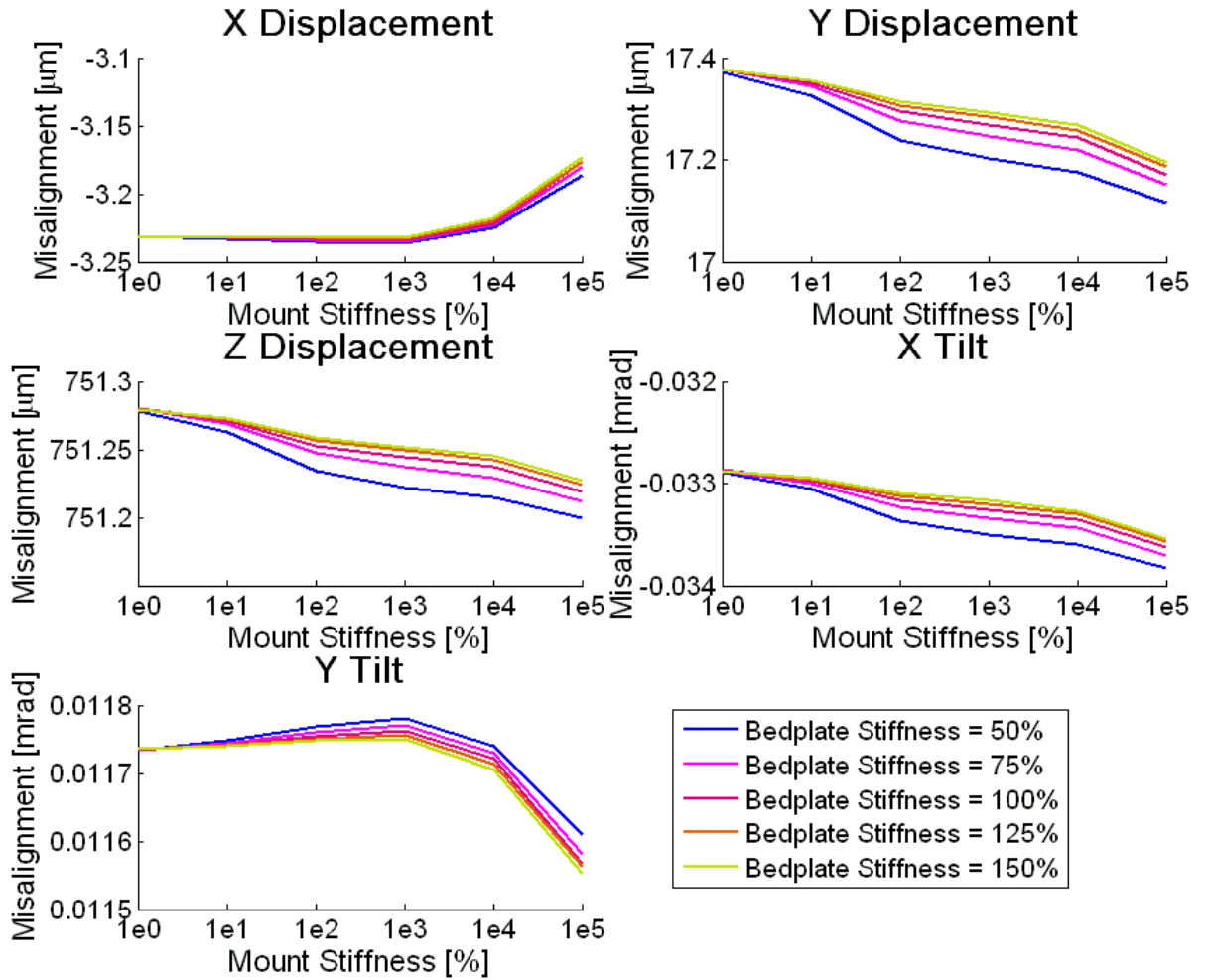


Figure 5.157 - Generator DE Misalignments of Medium Speed Drivetrain

Misalignments of the generator DE (Drive End) bearing show that in all 6 DOFs there is very little change as mount and bedplate stiffness changes. Figure 5.158 reveals how insensitive damage of the generator DE is to mount stiffness variation. By changing drivetrain design to medium speed, the high sensitivity to loading of the high speed drivetrain bearings appears to have mitigated.

Damage Sensitivity

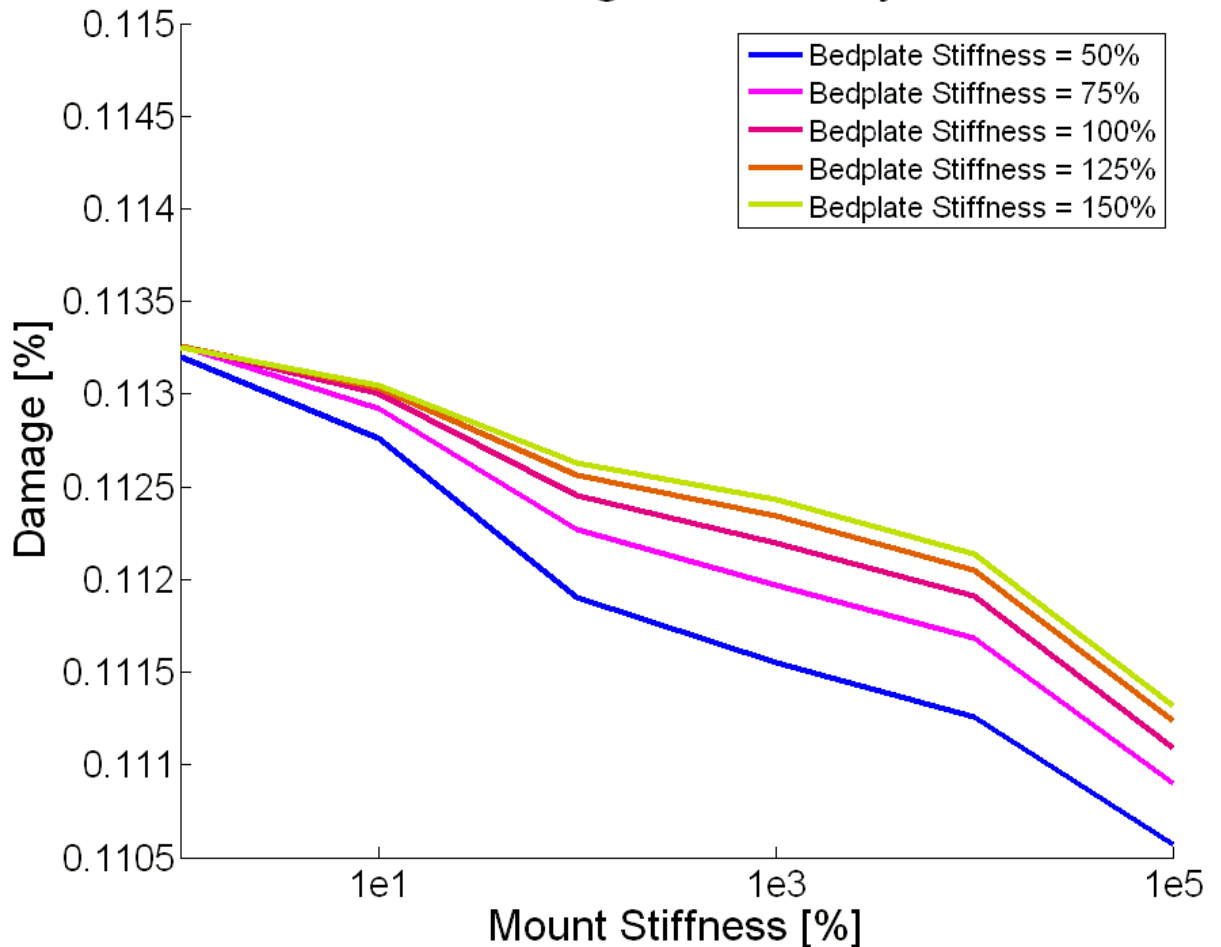


Figure 5.158 - Generator DE damage with Varying Mount Stiffness

Damage to generator DE bearings for each drivetrain is compared in Figure 5.159 displaying effects that the two drivetrain designs have on bearing damage. Blue lines show damage accrued on the generator DE bearing of the high speed drivetrain with varying mount stiffness on the x axis and bedplate stiffness with lighter lines corresponding to higher stiffness. Red lines show the generator DE bearing in the medium speed drivetrain. The high speed drivetrain bearing is sensitive to the flexibility in the structure showing high variation in damage accumulated; the medium speed bearing on the other hand is extremely insensitive to drivetrain flexibility since all lines are tightly packed with little change in damage whilst varying mount stiffness.

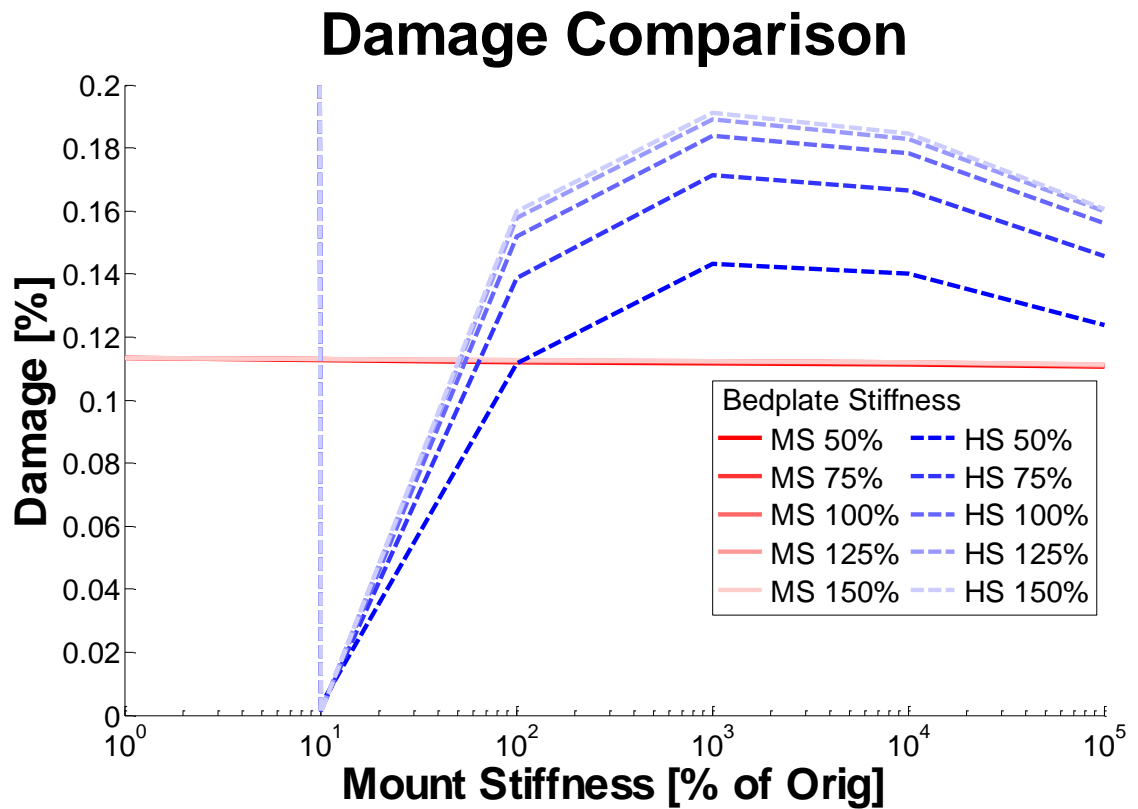


Figure 5.159 - Generator DE Bearing High Speed (HS) and Medium Speed (MS) Drivetrain Comparison.
Bedplate Stiffness described in Legend

By attaching the generator to the back of the gearbox and cantilevering the drivetrain on the mounts, the generator in the medium speed design is unable to move independently with respect to the gearbox. Parallel misalignments will therefore not be as severe, reducing loading on the bearings. Despite inclusion of a flexible coupling in the high speed design, when the rest of the structure is more compliant the flexible coupling is unable to completely remove the misalignment introduced. Results also suggests that increasing mount stiffness may improve loading on bearings, but by increasing stiffness, tolerances in manufacturing, installation and operation become smaller which may lead to poor load sharing between bearings resulting in overloading of certain bearings.

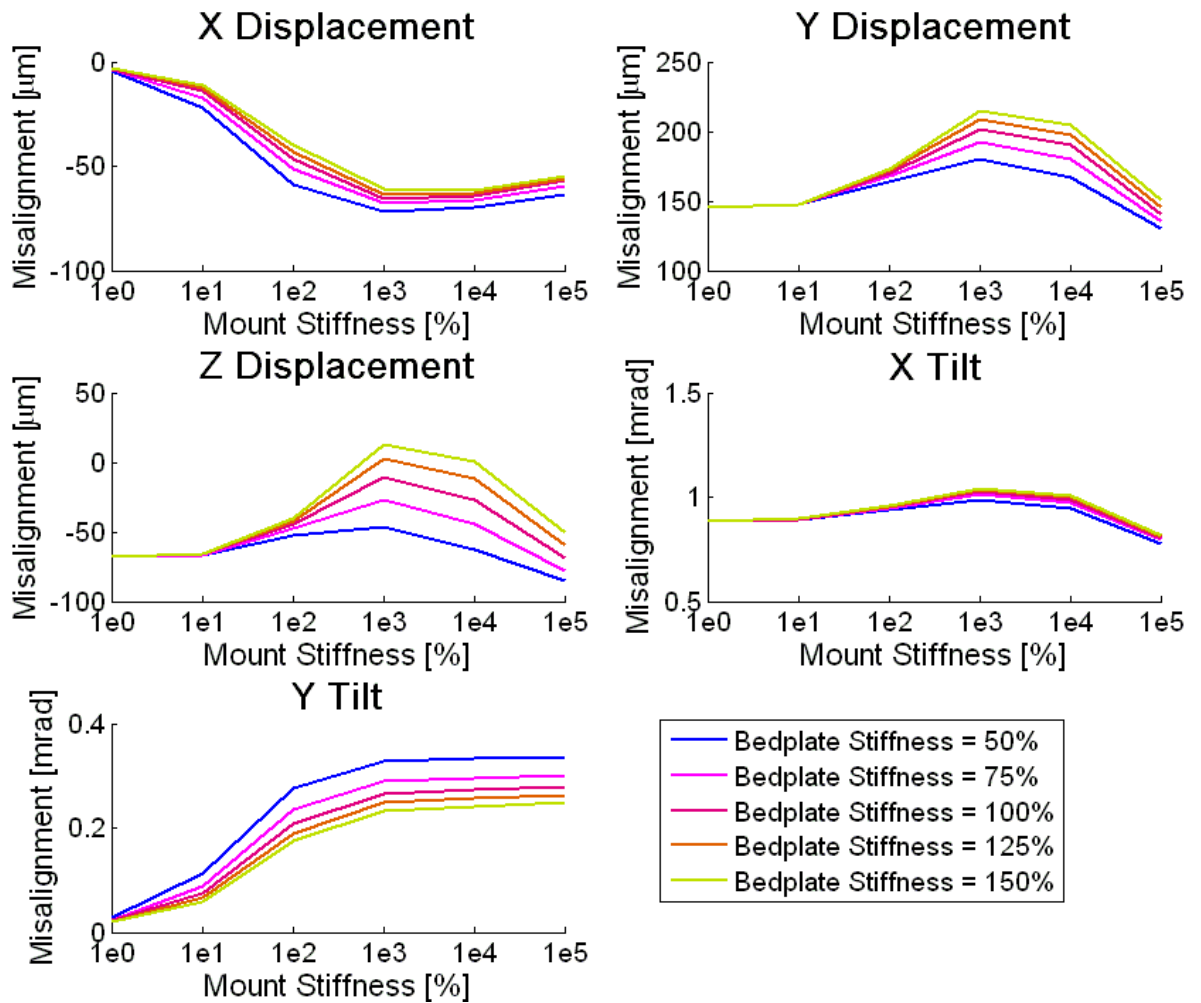


Figure 5.160 - Upwind Stage 1 Carrier Bearing Misalignments for Medium Speed Design

Misalignments, on the upwind stage 1 carrier bearing in Figure 5.160, vary substantially as mount stiffness and bedplate stiffness is changed. A large separation occurs on the Y and Z displacement at the mount stiffness resulting in peak damage. The Y displacement has a substantial increase in misalignment magnitude as bedplate stiffness is increased; the stiffest bedplate again causes the greatest misalignment between inner and outer raceways. Damage of the upwind stage 1 carrier bearing shows how the bedplate stiffness and mount stiffness are affected. While generator bearings are insensitive to either mount stiffness or bedplate stiffness the upwind stage 1 carrier bearing is sensitive to both these parameters. Lines in Figure 5.160’s translation graphs are tight together when mount stiffness is below 100%; above 100%, misalignments spread showing stiffness of both bedplate and mounts are important. Damage to these bearings in Figure 5.161 shows similar

findings to Figure 5.156 where the peak in predicted damage is between 1000% and 10000% of original mount stiffness.

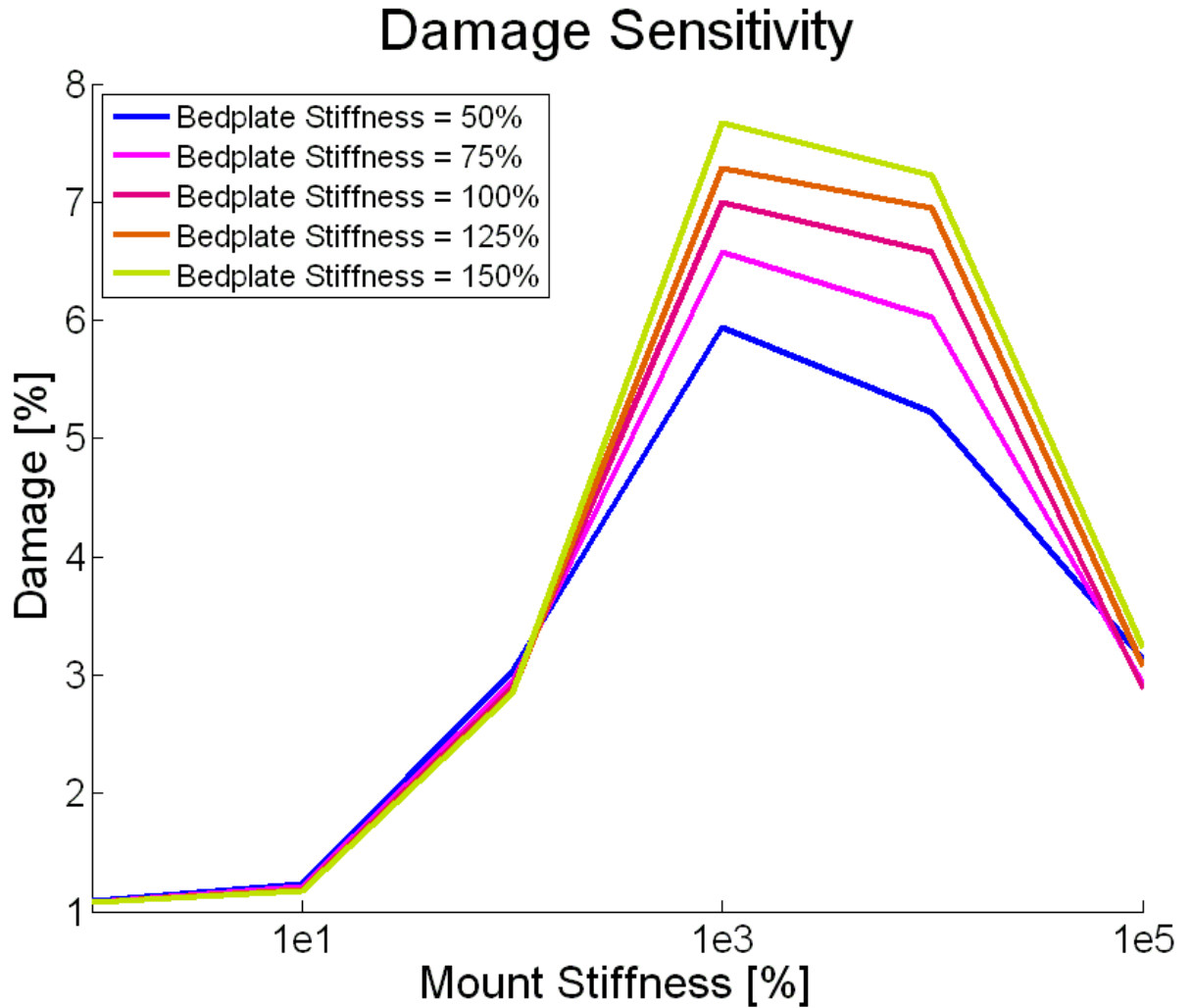


Figure 5.161 - Damage Sensitivity to Mount and Bedplate Stiffness for Upwind Stage 1 Carrier Bearing

5.3. Medium Speed Drivetrain Loads

Two major components in the drivetrain affecting the responses of the wind turbine's dynamics are changed. Gearbox ratio and generator rotor inertia will cause substantial variation to natural frequencies of the drivetrain and subsequently its response to transient loading conditions.

Models of 2MW wind turbines are created in GH Bladed, one with a medium speed drivetrain and one with high speed drivetrain. The high speed drivetrain model is the

same used in Chapter 3 and the medium speed drivetrain has certain parameters altered. A diagram of drivetrain parameters remaining constant is shown in Figure 5.162 with key parameters altered shown in Table 5.9. Values for gearbox ratio and generator inertia are taken from expected designs for each of these drivetrains. Although gearbox inertia will change between a high speed gearbox and a medium speed gearbox, calculation of gearbox inertia can be complex and design dependant therefore since the gearbox inertia is small compared to the generator inertia, it remains constant for this investigation.

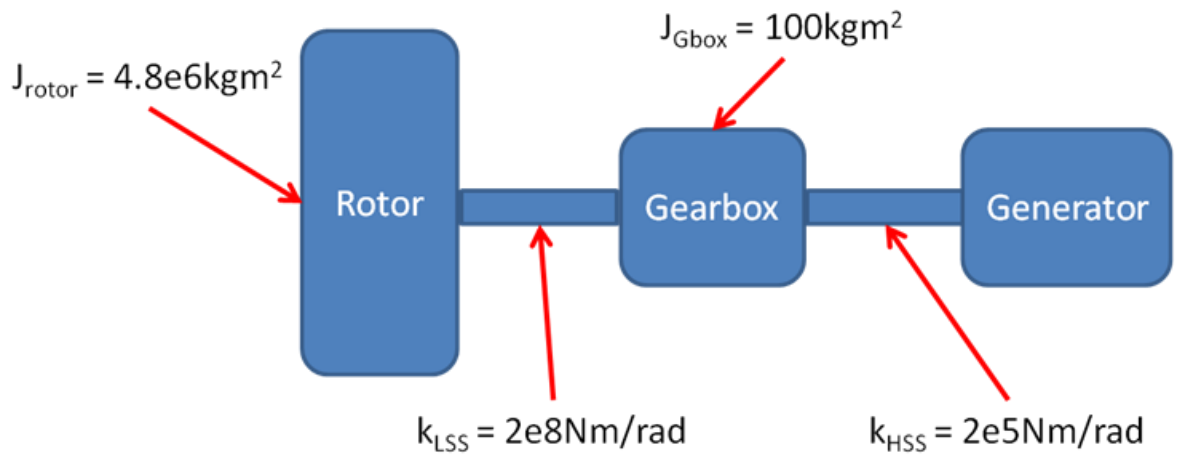


Figure 5.162 - Drivetrain Parameters

Table 5.9 - High Speed and Medium Speed Parameters

	High Speed	Medium Speed
Gearbox Ratio	84.15	26
Generator Inertia	80kgm ²	560kgm ²

To ensure turbines are the same rating, the controller was modified so that generated power is approximately the same for a given applied wind speed. Since the high speed gearbox steps up rotational speed approximately 3.25 times that of the medium speed gearbox, generator reaction torque is 3.25 times greater in order to achieve the same electrical power output. The controller therefore demands 3.25 times higher torque than the high speed controller. Figures 5.163 and 5.164 show electrical power and generator torque steady power curves for both drivetrain types.

Electrical Power Steady Power Curve

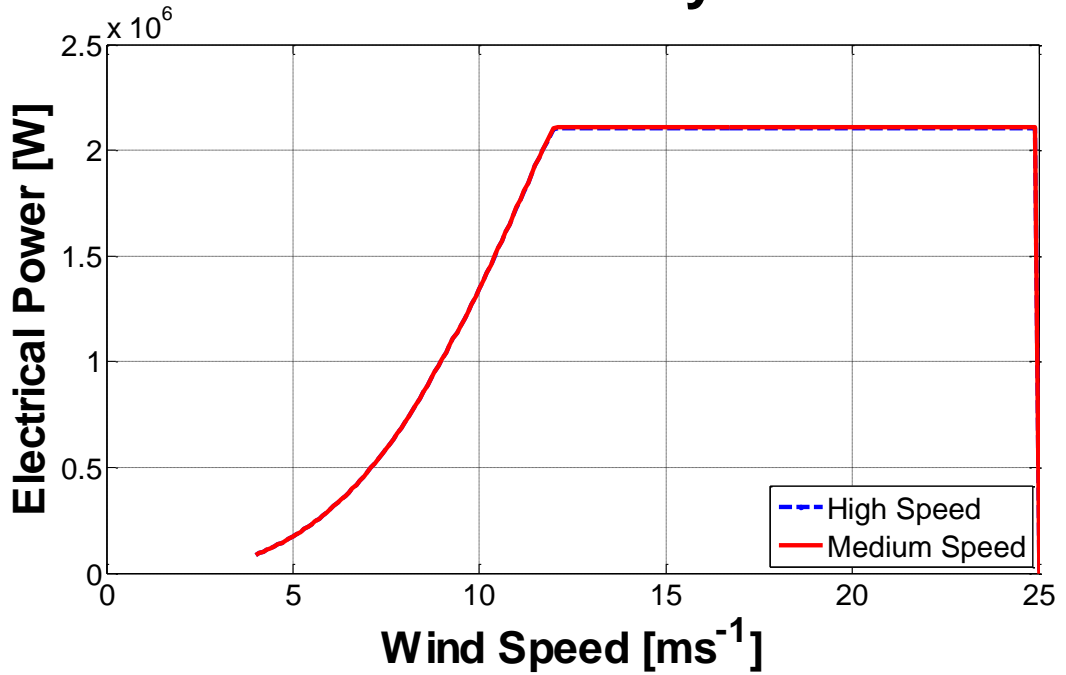


Figure 5.163 - MS and HS Electrical Power Comparison

Generator Torque Steady Power Curve

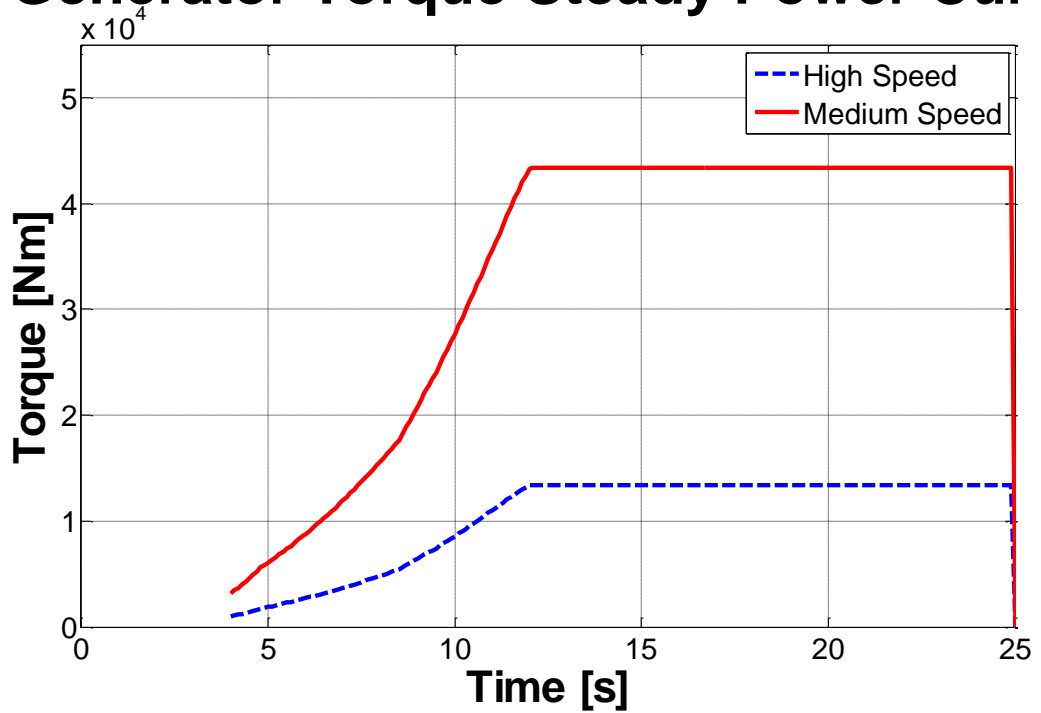


Figure 5.164 - MS and HS Generator Torque Comparison

5.3.1. Response to Transient Events

Despite the medium speed design having a larger generator, the inertia of the whole drivetrain actually decreases due to the reduction in the gearbox ratio. The total inertia of the system is given by $J_{total} = J_{rotor} + J_{gearbox} + GR^2 J_{generator}$ highlighting that gearbox inertia has an effect on the rotating inertia of the system. Table 5.10 shows the medium speed drivetrain has a smaller inertia and therefore is expected to be more responsive to input loads.

Table 5.10 - Drivetrain Inertia

	High Speed	Medium Speed
Drivetrain Inertia	5.367e6kgm ²	5.179e6kgm ²

Both wind turbine models are subjected to a simulated grid loss emergency stop to find the response of this highly transient, potentially damaging, event. The grid loss event is performed at a wind speed of 12ms⁻¹ with the grid loss event occurring at 30 seconds. Responses from both types of drivetrain are shown in Figure 5.165.

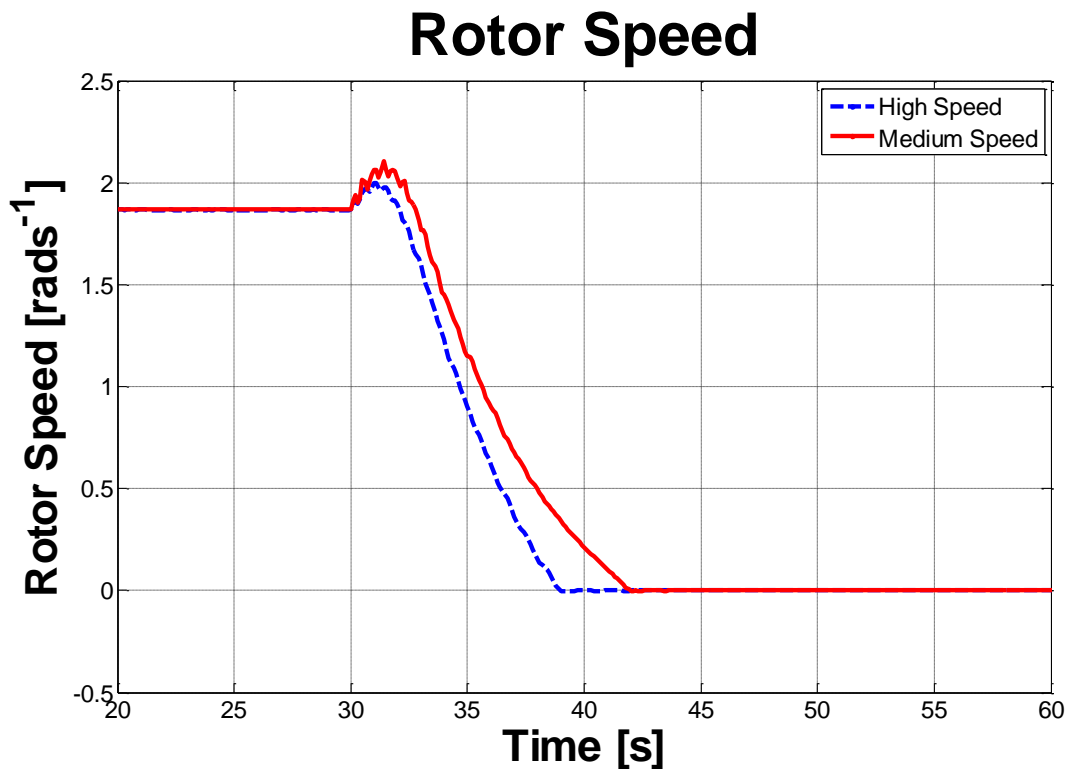


Figure 5.165 - Emergency Stop of Both Drivetrain Types at Wind Speed of 12ms⁻¹

Unexpectedly, the medium speed drivetrain takes longer to reach rest than the high speed drivetrain. Since the medium speed drivetrain has a smaller inertia and braking effort from the rotor is the same, the medium speed is expected to reach rest first. Figure 5.165 shows this is not the case. After the grid loss event, the medium speed drivetrain responds faster, accelerating to a greater peak rotational speed, as expected for a drivetrain of lower inertia. The rotor then decelerates faster with the medium speed but the high speed drivetrain reaches rest quicker due to the initial acceleration. The mechanical brake, assumed to be equal in both cases, provides most of the braking torque in the latter stages of the stop as the aerodynamic brake become increasingly ineffective as the rotor slows. The high speed drivetrain is able to come to rest quicker than the medium speed drivetrain since the brake torque is stepped up through the gearbox meaning the mechanical brake appears 3.25 times greater on the high speed drivetrain. This higher brake torque brings the drivetrain to rest faster.

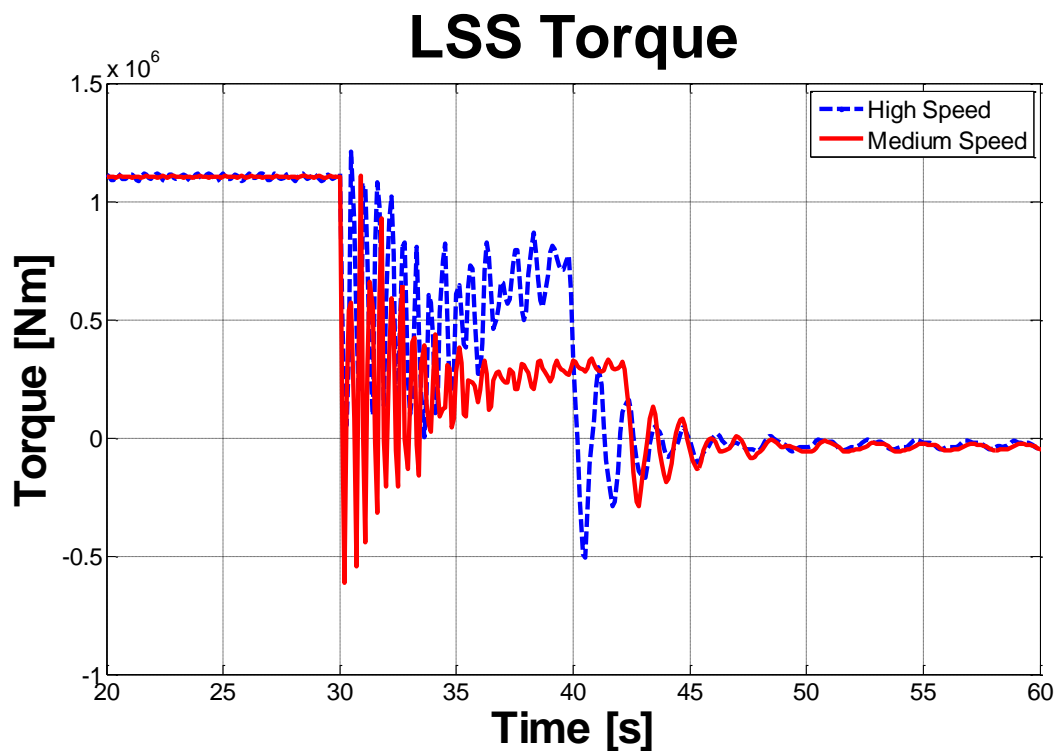


Figure 5.166 - LSS Torque during Emergency Stop at Wind Speed of 12ms^{-1}

Figure 5.166 shows differences in the LSS torque response between the drivetrains. A change of response frequency is observed and mean torque during braking phase

when the rotor is decelerating also changes. Effects of lowering the mean torque are that the magnitude and number of oscillations of the reversals experienced are much more severe. The medium speed drivetrain exhibits a greater initial drop in LSS torque resulting in large negative torques transmitted through the gearbox. Not only are these large magnitude negative torques transmitted through the gearbox, LSS torque also has numerous reversals that are likely to damage gears. The mechanical brake and gearbox ratio are responsible for the shift in mean torque during the first phase of the emergency stop. The advantage of applying the brake immediately after the grid loss event is that the LSS torque is shifted upwards reducing time and occurrence of reverse loading, minimising backlash. Effect of the mechanical brake on the LSS torque can be best explained just before the rotor has come to rest. At this point the rotor provides almost no braking torque, therefore the mechanical brake is the sole component applying torque to the drivetrain. Effects of the mechanical brake are stepped up through the gearbox therefore if both drivetrain have the same brake then the high speed drivetrain will have a greater effect on the drivetrain. Once the turbine has come to rest, the natural frequency afterwards does not change. The mechanical brake cuts the high and low speed side off from each other, effectively constraining the gearbox inertia meaning the LSS side is therefore the same for both high and medium speed drivetrains. Using Fourier transforms, the observed frequencies in the LSS torque can be extracted, viewed in Figure 5.167.

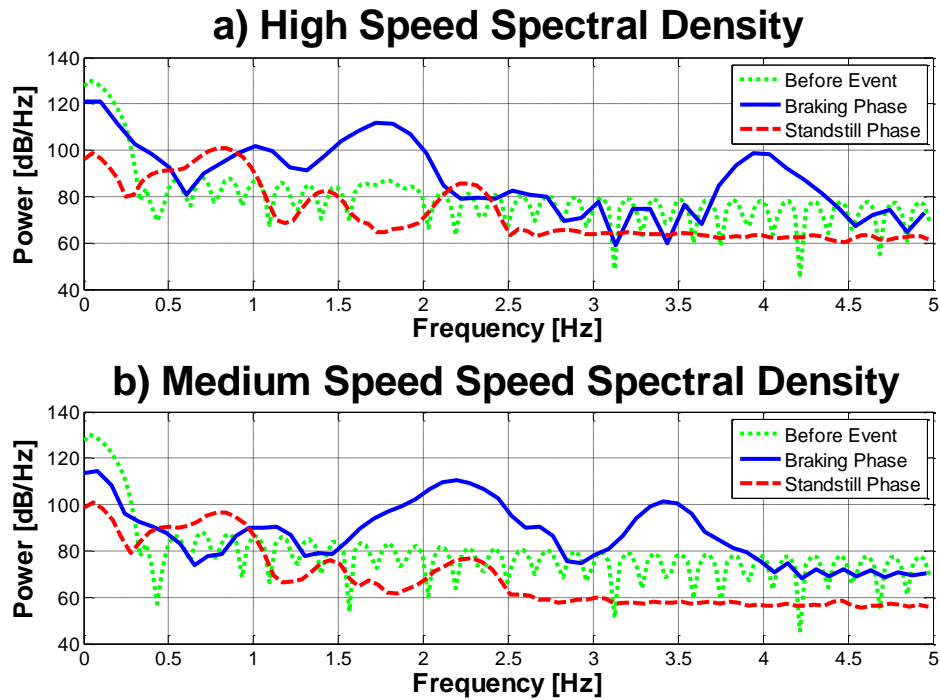


Figure 5.167 - Spectral Response of High Speed and Medium Speed Drivetrains during Emergency Stops

Peaks on the high speed drivetrain spectrum are at 0.78Hz, 1.78Hz and 3.96Hz and the medium speed drivetrain's peaks are observed at 0.80Hz, 2.16Hz and 3.43Hz. A smaller total inertia in the medium speed drivetrain means the first peak is shifted to a higher frequency while the second peak is shifted to a smaller frequency responding to the increase in generator inertia. The higher frequency peak does not appear in the standstill phase as the generator inertia has been cut off from the low speed side by the mechanical brake.

Figure 5.168 shows the reaction torque of the HSS brake for both drivetrains. When the rotor comes to rest, the mechanical brake on the medium speed shaft has to exert more force to keep the rotor stationary since the torque is stepped up 2 stages instead of 3 stages on the high speed drivetrain. This highlights the importance of analysing the size of the brake for its effect on the drivetrain.

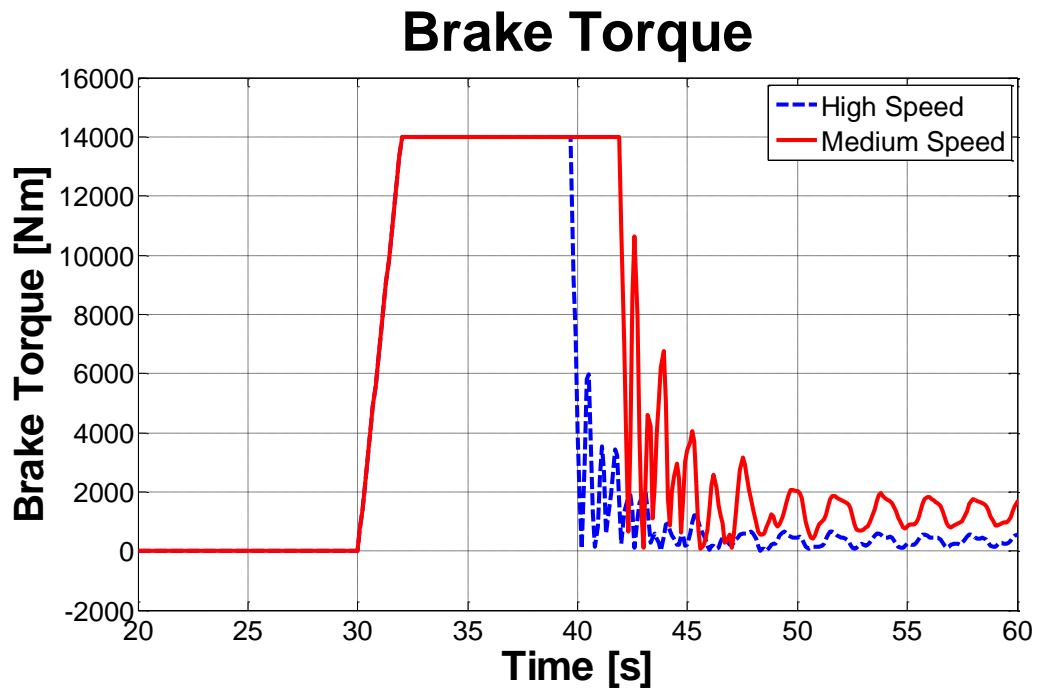


Figure 5.168 - Brake Reaction Torque during Emergency Stop

5.3.2. Resizing Medium Speed Brake

A larger brake was used in the medium speed drivetrain with a maximum braking torque 3.25 times greater than the previous models. Figures 5.169 and 5.170 show comparisons between the existing medium speed drivetrain and a medium speed drivetrain with a larger brake used. The large brake has more of an effect on the smaller inertia drivetrain, coupled with the aerodynamic braking the turbine is slowed faster. Even with the larger brake the medium speed drivetrain still has a large drop in the LSS torque immediately after the grid loss event. The initial trough occurs 0.2 seconds after the grid loss event before the brake is fully applied, therefore the drop is a result of the dynamics of the system since both medium speed drivetrains drop to a similar LSS torque. If a faster brake was applied the maximum torque would be far higher as predicted in the brake application time study in Chapter 3.

Rotor Speed

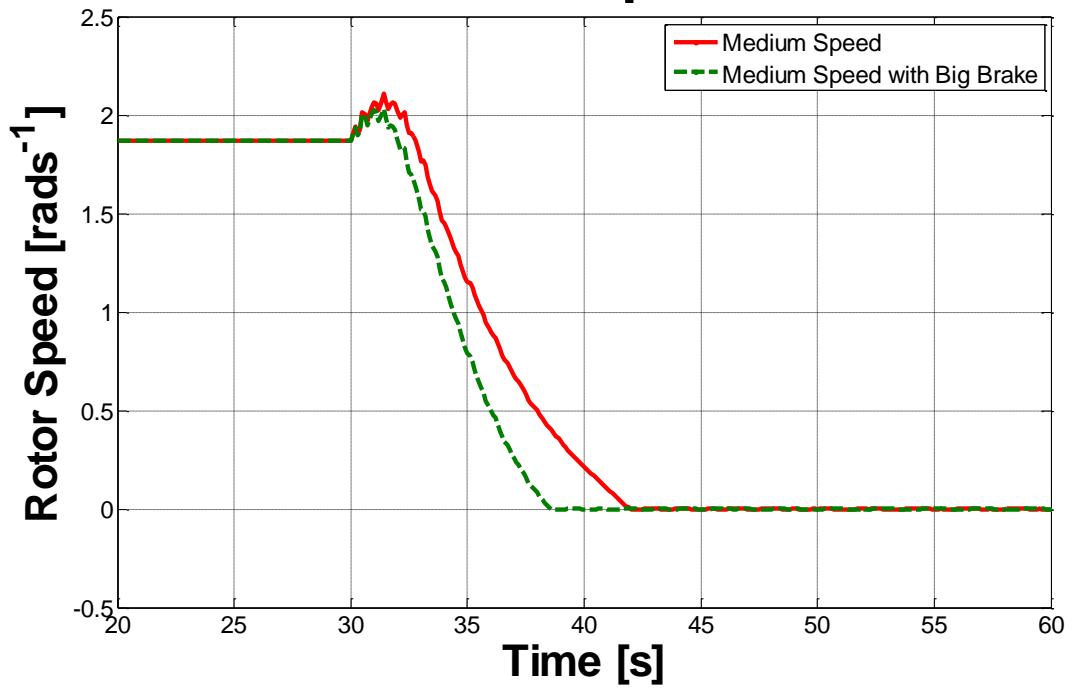


Figure 5.169 – Rotor Speed with Medium Speed having increased Brake Capacity

LSS Torque

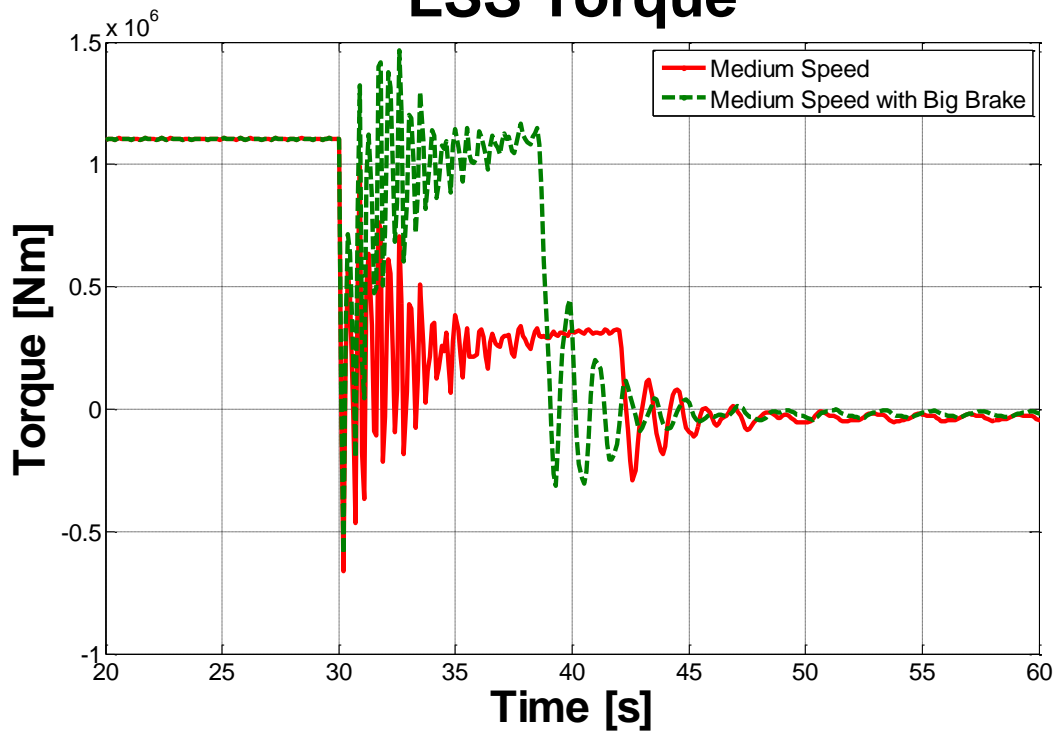


Figure 5.170 - LSS Torque with Medium Speed having increased Brake Capacity

5.3.3. Wind Turbine Response to Turbulent Wind

To highlight the differences in response of each turbine, a turbulent wind was input to the wind turbine models with high speed and medium speed drivetrains. The 3 dimensional turbulent wind files were generated in GH Bladed and covered the entirety of the rotor having an average wind speed of 13ms^{-1} . Information on how these are created can be found in [5.3-5.4].

Figures 5.171 and 5.172 show the turbulent wind loading input to wind turbines models. The turbulent wind field generated in Figure 5.171 has a turbulence intensity of 12.8%. Figure 5.172 shows the turbulent wind file input to the medium speed drivetrain has far more variation than the high speed drivetrain confirming the medium speed is more responsive than the high speed drivetrain.

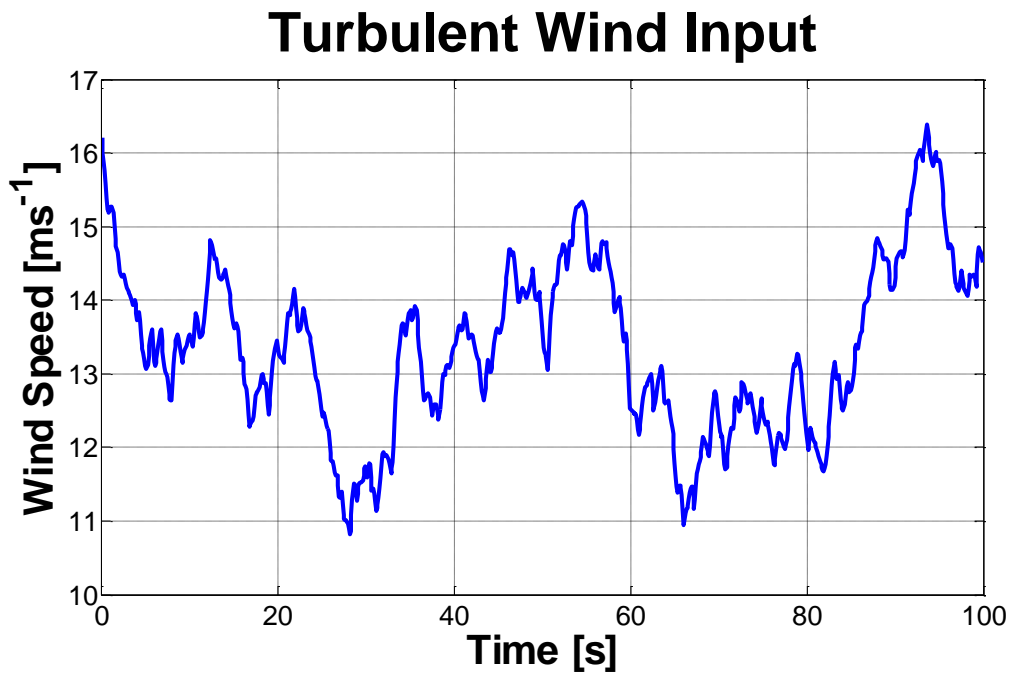


Figure 5.171 - Applied Wind Speed

Rotor Speed Response to Turbulence

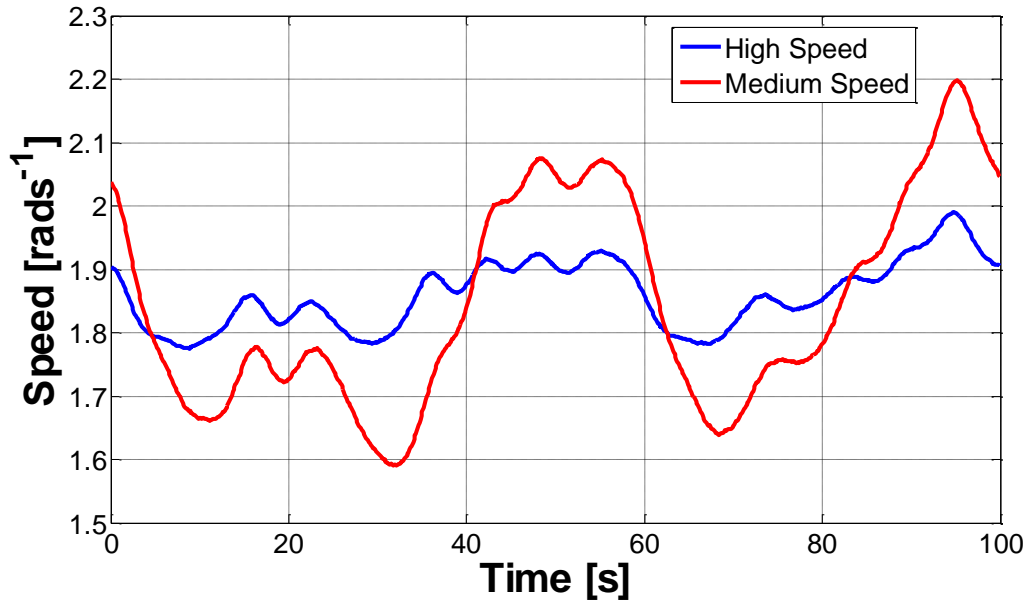


Figure 5.172 - Rotor Speed Response to Turbulent Wind

5.4. Transient Drivetrain Structural Response

Natural frequencies for the system are given in Table 5.11 and the mode shapes are displayed in Figures 5.173 to 5.178.

Table 5.11 - Medium Speed Drivetrain Natural Frequency

Mode	Frequency (Hz)
1.	3.0388
2.	8.1482
3.	16.088
4.	23.937
5.	28.564
6.	29.016

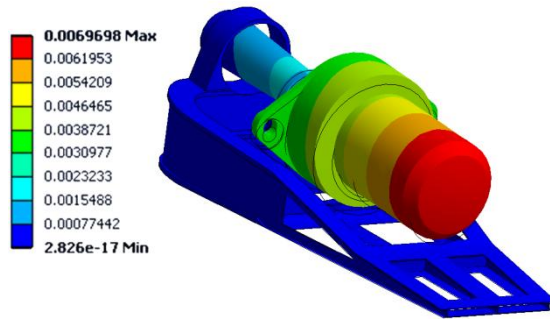


Figure 5.173 - Medium Speed Drivetrain Mode 1 – Gearbox and Generator Bending (3.0388Hz)

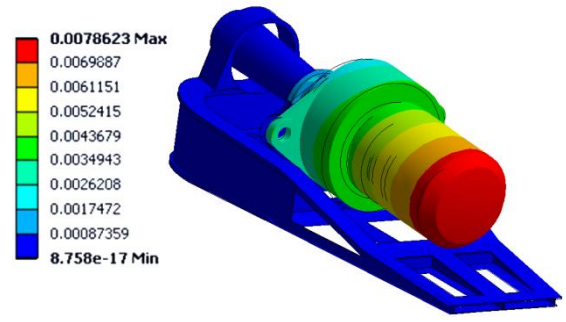


Figure 5.174 - Medium Speed Drivetrain Mode 2 – Gearbox and Generator Bending (8.1482Hz)

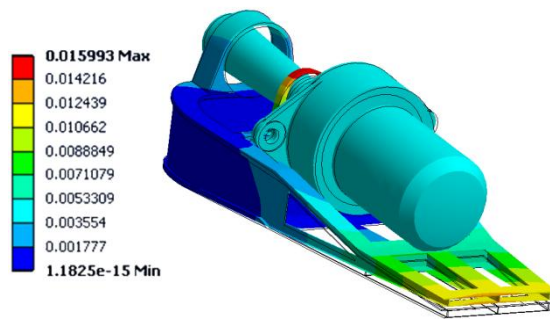


Figure 5.175 - Medium Speed Drivetrain Mode 3 – Bedplate Bending (16.088Hz)

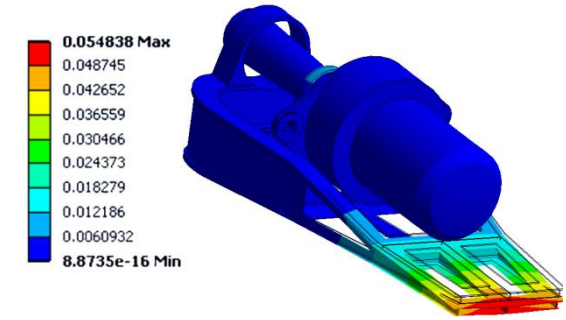


Figure 5.176 - Medium Speed Drivetrain Mode 4 – Bedplate Bending (23.937Hz)

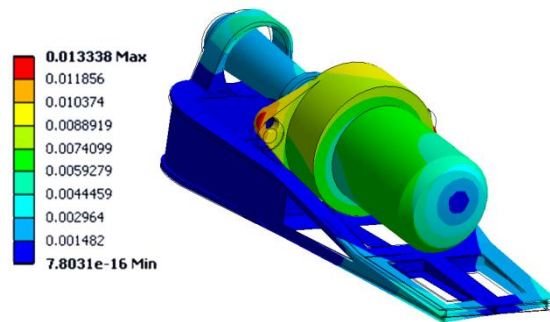


Figure 5.177 - Medium Speed Drivetrain Mode 5 – Drivetrain Torsional (28.564Hz)

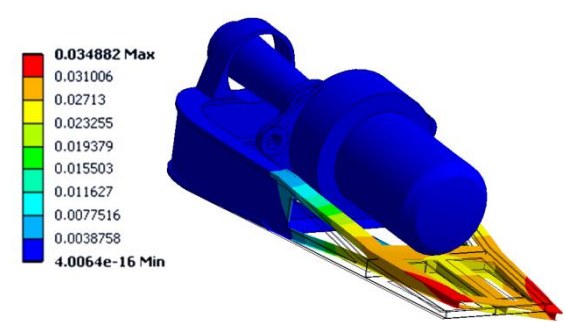


Figure 5.178 - Medium speed Drivetrain Mode 6 – Bedplate Torsional (29.016Hz)

Colours show relative deflections of mode shape with black lines displaying the original position of the edges.

Natural frequencies of the medium speed drivetrain structure are higher than for the high speed drivetrain which is unexpected. Changing design from the high speed drivetrain where the weight is spread across the bedplate to the medium speed case where the weight is cantilevered on the gearbox mounts, the natural frequency was expected to decrease. Model results show the inverse occurs as the compact medium speed design means the drivetrain becomes stiffer with flexible elements such as the flexible coupling and fabricated section of the bedplate not affecting mount displacements. In the high speed drivetrain, flexibility of the bedplate coupled with the components weight spread over the bedplate lowers the natural frequency in comparison with the medium speed design.

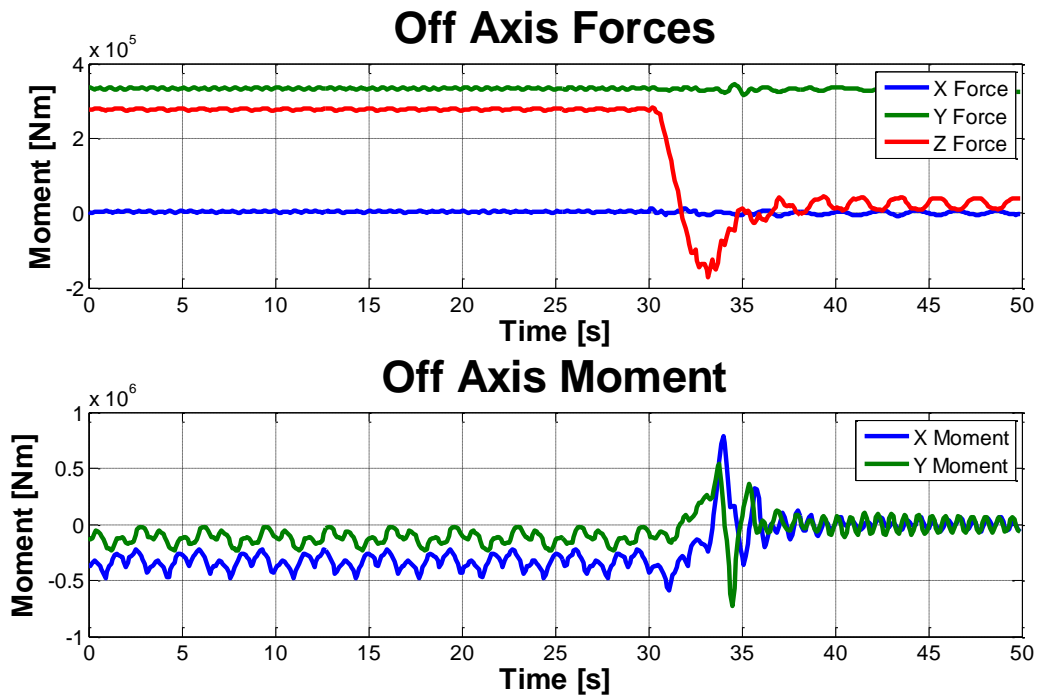


Figure 5.179 - Medium Speed Drivetrain Off Axis Applied Loads

Responses of gearbox mounts to emergency stop input torques are plotted in Figures 5.180 to 5.183. In both gearbox mounts there is substantially more movement predicted in the transient analysis. A large magnitude oscillation is observed at 34 seconds corresponding to a large off axis moment in the input loads when the tower oscillation reaches the first peak after the grid loss event. This has a large effect on loading of mounts in the medium speed drivetrain where the high speed drivetrain is

not as substantially affected by this loading. The pseudo-transient and transient models both move in the same direction immediately after the grid loss event occurs though as stated there is obviously a great deal more movement predicted by the transient analysis. Main bearings in Figures 5.182 and 5.183 show that both models predict similar outputs for the main bearings though slightly more oscillatory content in the transient analysis is observed. In all comparisons there is a constant error between the two analyses suggesting static loads react slightly differently becoming worst the further from the grounding point. This suggests the bedplate responds differently in each of the cases.

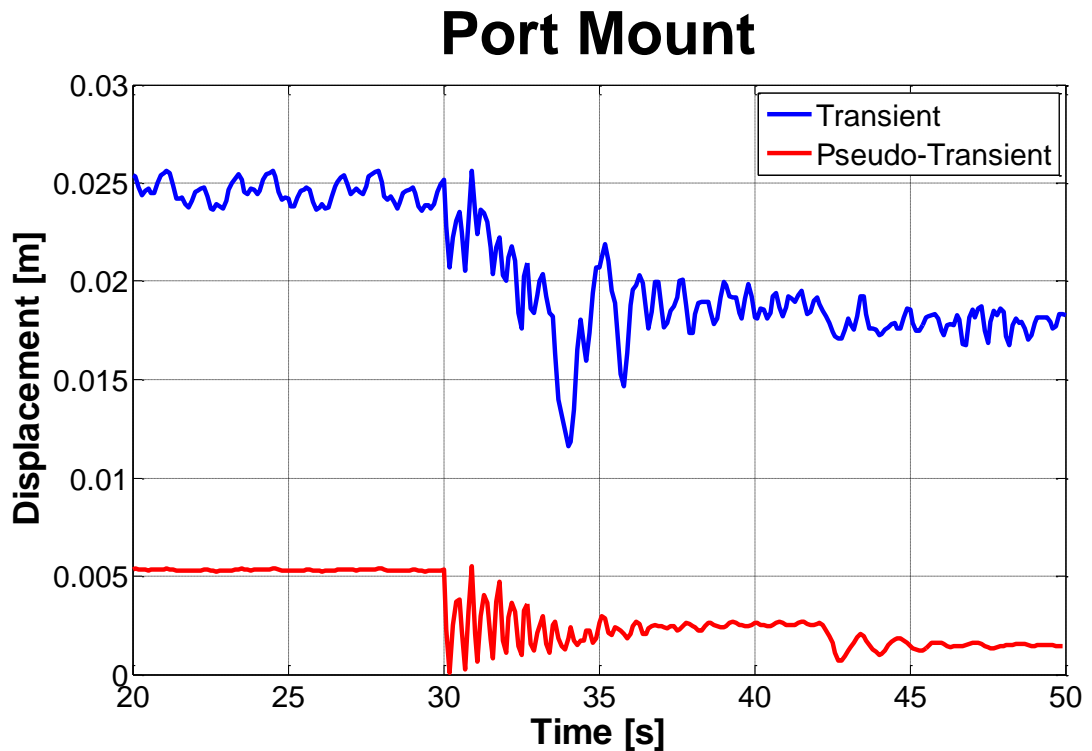


Figure 5.180 - Medium Speed Drivetrain Port Mount Response to Emergency Stop

Starboard Mount

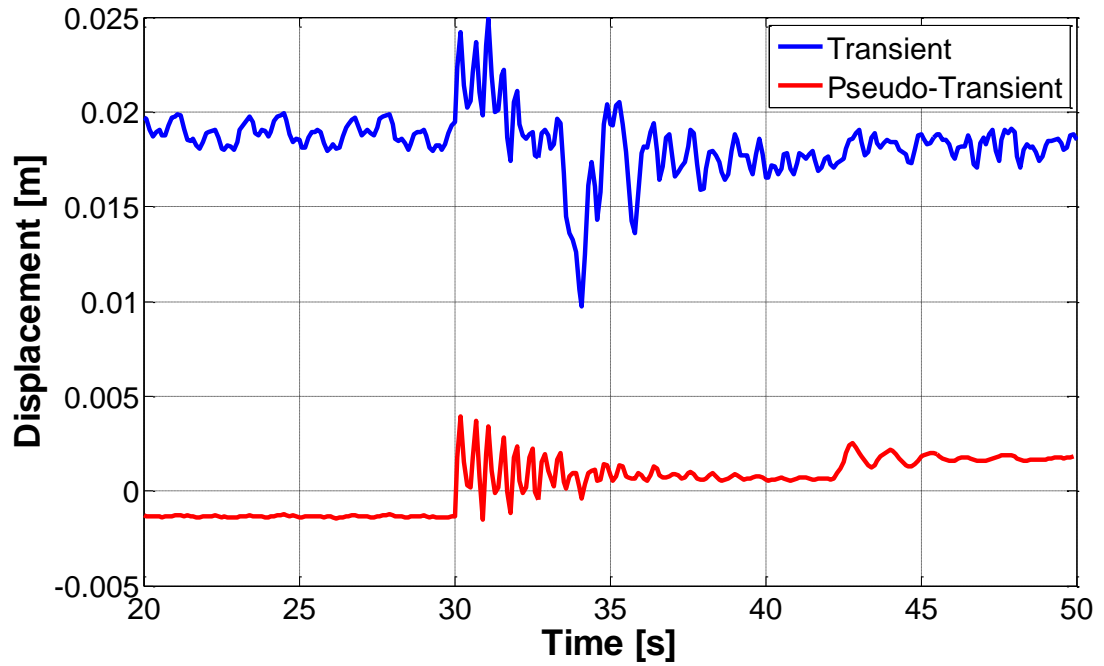


Figure 5.181 - Medium Speed Drivetrain Starboard Mount Response to Emergency Stop

Main Bearing

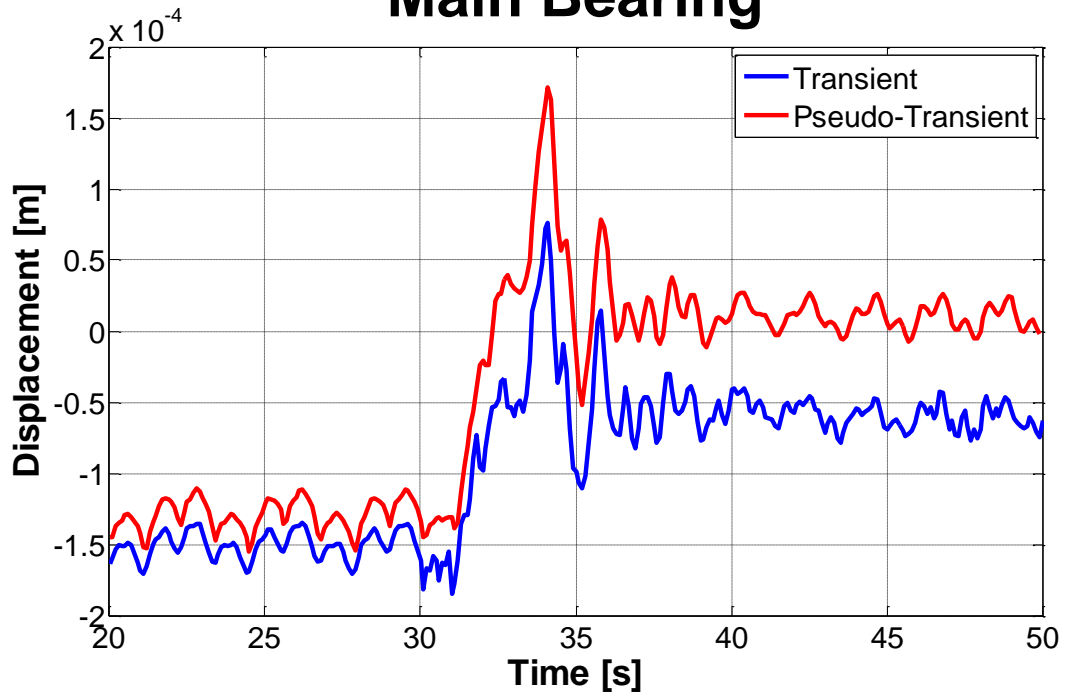


Figure 5.182 - Medium Speed Drivetrain Main Bearing Response to Emergency Stop

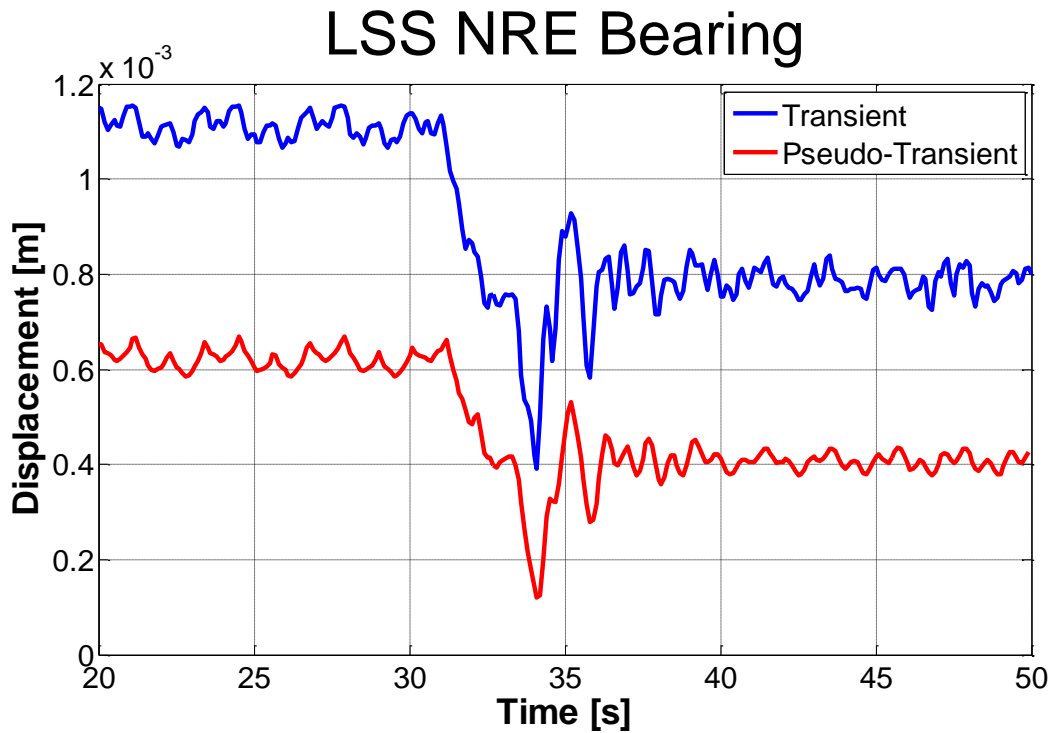


Figure 5.183 - Medium Speed Drivetrain NRE Main Bearing Response to Emergency Stop

Large deflections at 34 seconds in Figures 5.180, 5.181, 5.182, and 5.183 are caused by off axis loading on the rotor from movement of the tower during the emergency stop. When the blades start pitching in response to the grid loss event there is a huge loss of axial thrust (Z Force in Figure 5.179a) causing a surge forward of the nacelle shown in Figures 5.184 and 5.185. The trough, signifying the further point forward, is at 34 seconds coinciding with the large loading oscillation seen at the mounts also accompanied with a surge in nod angle.

Nacelle Translations

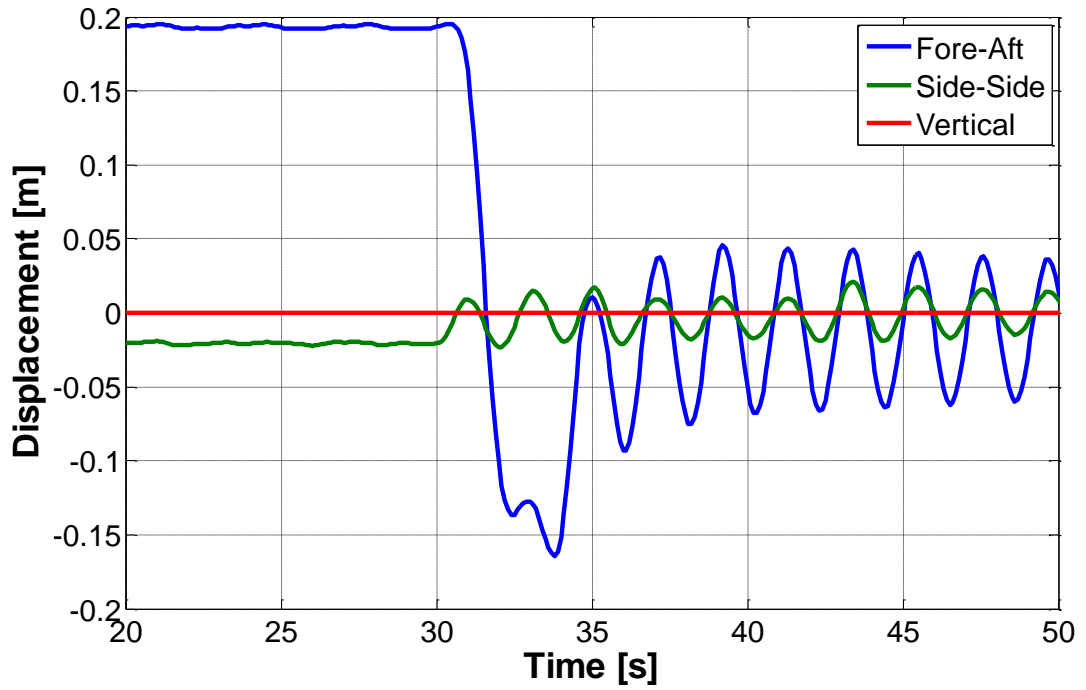


Figure 5.184 - Medium Speed Nacelle Translations during Emergency Stop

Nacelle Rotations

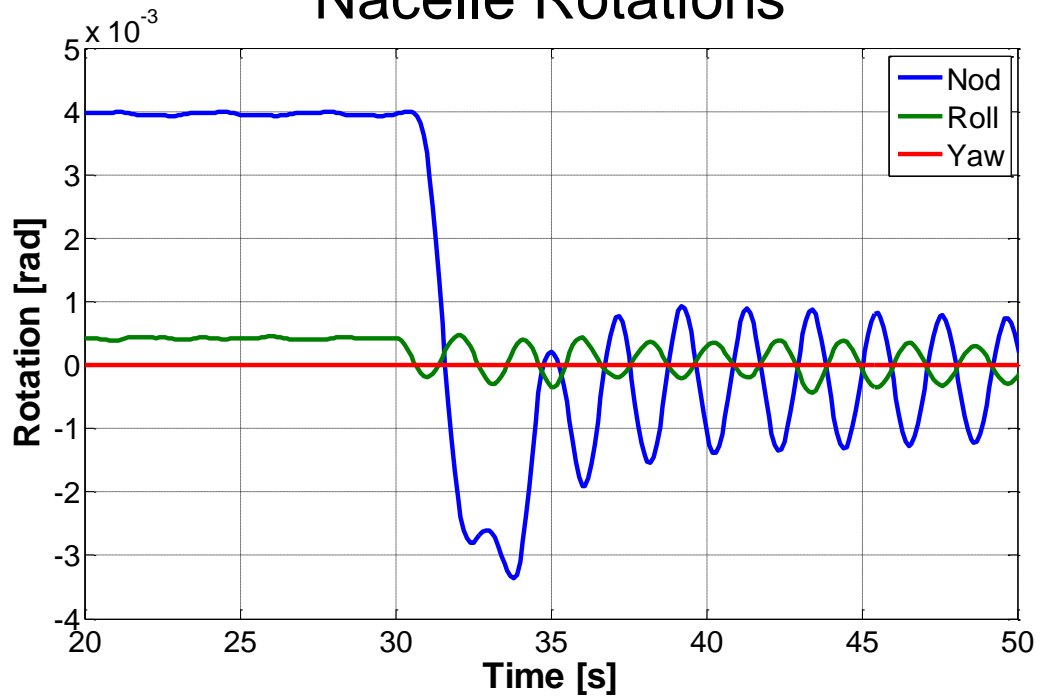


Figure 5.185 - Medium Speed Nacelle Rotations during Emergency Stop

Spectral responses of the port and starboard gearbox mounts can be analysed to discover what frequencies are being transmitted through the structure, displayed in Figures 5.186 and 5.187. In both spectral plots, the input loads are prominent with peaks just above 2Hz from the input loading. Peaks at 3Hz from the structure are not seen though the modes shapes suggest that these modes may not be apparent at the mounts. Since applied loading on the medium speed drivetrain is in-line no offset loading occurs and parallel misalignments are not introduced into the system.

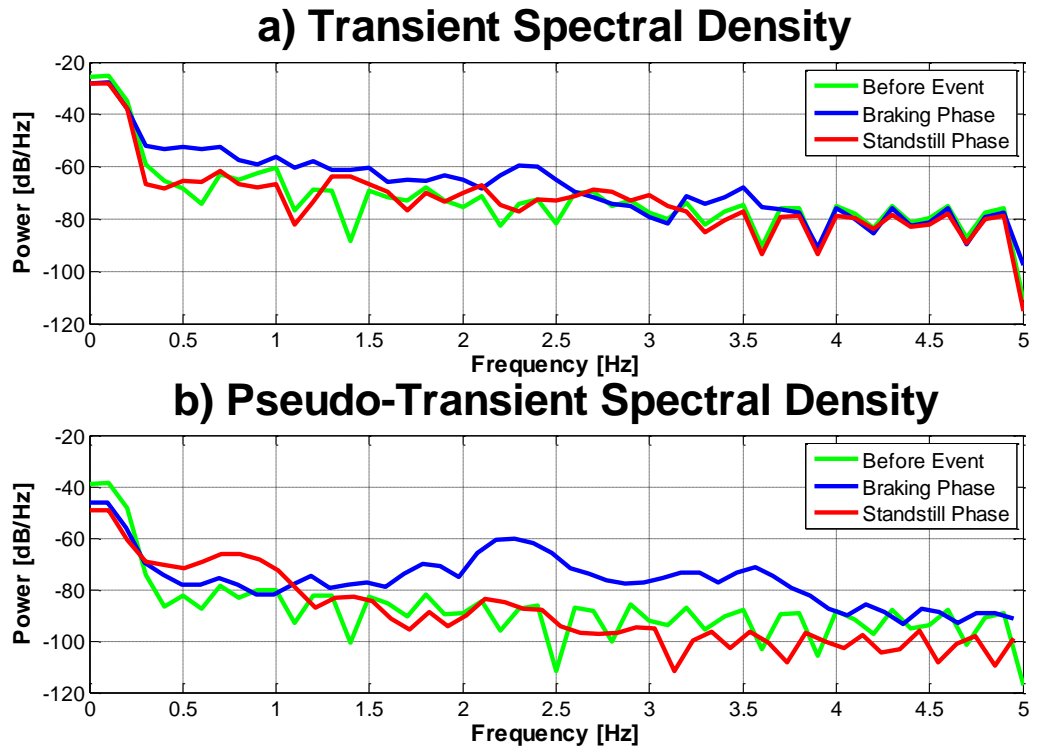


Figure 5.186 - Port Mount Spectral Response

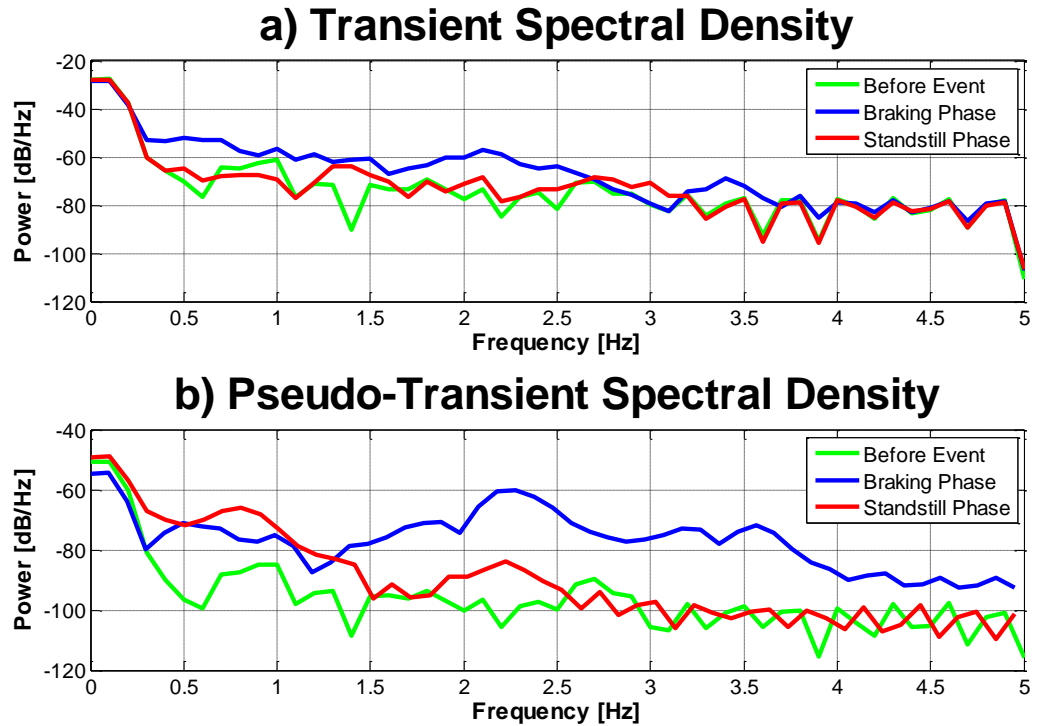


Figure 5.187 - Starboard Mount Spectral Response

5.5. Summary

Medium Speed drivetrains are certainly a viable option when compared to high speed and direct drive drivetrains since they have a predicted lower CoE as a result of the trade off between the two, using the best characteristics of each design type whilst minimising drawbacks.

The cantilevered design isolates internal drivetrain bearings from the rest of the structure removing the bearing load sensitivity of the high speed drivetrain. Stage 1 carrier bearings are affected by changes in mount and bedplate stiffness since weight from the cantilevered drivetrain is resisted by these bearings. Structural stiffness of the drivetrain is therefore important in loading on these bearings. With improved load prediction, stage 1 carrier bearings can be adequately sized during the design phase. Ensure that all bearings can adequately withstand the loading is important for proving the medium speed design has improved reliability.

Chapter 5 – Medium Speed Drivetrains

Despite increased mass in the nacelle, the medium speed drivetrain was found to have lower total inertia due to gearbox ratio effects. Less inertia causes the medium speed drivetrain to react faster meaning transient events such as grid loss emergency stops may experience higher torque if not controlled. Faster acting control measures are required to regain control of the wind turbine quickly to minimise torque experienced. The natural frequency of the medium speed drivetrain increases since the flexible fabricated structure is not attached to the drivetrain and higher response frequencies are therefore observed during transient events. The mechanical brake plays an important role in slowing the wind turbine by applying frictional torque to the HSS allowing the turbine to come to rest. The mechanical brake also shifts LSS torque positively so the gearbox is loaded in the same direction minimising the effects of reverse loading during grid loss emergency stop conditions. With the gearbox stepping up brake torque, the gearbox ratio has important effects on the braking of the rotor; therefore the mechanical brake on the high speed drivetrain exerts more torque on the rotor than for the medium speed drivetrain. A larger brake on the medium speed drivetrain is required to shift LSS torque so that backlash in the gearbox is not such a great problem.

Cantilevering the drivetrain removes the main cause of misalignments between gearbox and generator mitigating damaging effects on high speed bearings. This can prevent problems seen in traditional drivetrain designs with high speed bearings.

Several design challenges exist for the drivetrain including ensuring the generator bearings are adequately sized for the loading. Flexibility of the drivetrain needs to be stiff enough in order for there not to be movement between gearbox and generator.

Chapter 5 References

- [5.1] Romax Technology, 2013, *The Butterfly Drivetrain*. Available:
<http://www.romaxtech.com/products/butterfly-drivetrain-platform.aspx>
- [5.2] S. Schmidt, *et al.*, "Comparison of Existing Medium-speed Drive Train Concepts with a Differential Gearbox Approach," in *EWEA*, Copenhagen, Denmark, 2012.

Chapter 5 – Medium Speed Drivetrains

- [5.3] E. A. Bossanyi, "GH Bladed User Manual," Garrad Hassan2007.
- [5.4] E. A. Bossanyi, "GH Bladed Theory Manual," Garrad Hassan2007.

6.

Summary

6.1. Summary of Project

In this chapter the main findings from each section are summarised. Outcomes will be presented along with impacts it could have on wind turbine and drivetrain design.

6.1.1. Chapter 1

Reliability of components in the wind turbine and in particular the drivetrain is examined in this chapter. Findings show the gearbox and generator contribute the most amount of overall downtime to the wind turbine. In addition new in-depth reliability data of gearbox subcomponent failures highlight high speed bearings as the most failure prone component, previously not found in the literature.

6.1.2. Chapter 2

Models of the gearbox are expanded out to include the whole drivetrain identifying flexibility of certain components having major impacts on misalignments of high speed drivetrain bearings that were previously unknown. The flexible coupling has already been shown to be extremely important in the sensitivity of loading on the high speed bearings but flexibility of the bedplate and gearbox mounts have also now been shown to be important in determining loading on the bearings. Low damage was experienced when mount flexibility approached rigidity but in practice this is not an option as poor load sharing between bedplate connections will occur resulting in overloading of individual bearings. A very important outcome of this modelling is the internal bearings in the gearbox are unaffected by the flexibility of the drivetrain therefore only the high speed bearings are affected by movement of the drivetrain structure.

6.1.3. Chapter 3

Loading of the wind turbine was examined during normal operation and transient events in GH Bladed. Sensitivity of loading to wind speed, pitch rate of the blades, mechanical brake application speed and maximum brake torque was examined with, as expected, higher pitch rates resulting in greater decelerations causing a greater drop in LSS torque during the braking phase of the emergency stop. Sensitivity of loads on the LSS is dependent on the application of the mechanical brake: maximum load and application time shifts the LSS torque substantially.

Wind speed variation gives a surprising outcome: peak rotor speed and LSS torque is achieved at the wind speed where rated power is reached, 12ms^{-1} . At greater wind speeds, blades are already pitched, therefore when the grid loss event occurs the blades can reach a pitch angle to brake earlier so the rotor does not accelerate up to the peak speeds seen at 12ms^{-1} wind speed.

6.1.4. Chapter 4

Static models have been used to analyse loads bearings experience in the drivetrain, though this may not adequately represent conditions they are subjected to during highly transient events.

Comparisons to the NREL test data with a pseudo-transient model show the model picked up most of the deflections though these were a direct response from the input torque. The test rig also showed additional motion that the modelling did not capture.

Comparison between the pseudo-transient and fully transient models as the wind turbine is performing a grid loss emergency stop showed some noticeable differences. When highly transient loading containing the rotational drivetrain natural frequencies was applied, the dominant structural response of the transient model was at the natural frequency of the drivetrain structure, most noticeable when the rotor reaches rest. When bearing stresses are calculated, the transient model predicts stresses higher than the pseudo-transient model which therefore increases predicted damage on components. The major issue this chapter raises is that some of the most serious loads may not be captured with models used currently consequently vastly lower bearing lifetime is experienced than predicted.

Conditions for skidding can be predicted using the transient modelling and particular transient events can be identified as problematic. Results did not conclusively show skidding may occur during the grid loss emergency stop though a higher fidelity model may prove this.

6.1.5. Chapter 5

Medium speed drivetrains are explored as an alternative design to the traditional three stage high speed drivetrain with the aim of minimising the cost of energy of the

wind turbine. The medium speed drivetrain has been shown to have smaller total drivetrain inertia despite having a larger mass. The first natural frequency of the drivetrain increases since inertia of the system decreases but the second drivetrain frequency decreases as inertia of the generator increased.

Changing the layout of the drivetrain from the traditional high speed design, where components are individually attached to the bedplate, to the cantilevered design has removed the sensitivity of problematic high speed bearings so that most drivetrain bearings are isolated from structural loads. The medium speed design is certainly a viable alternative which has removed the major cause for failure in the high speed drivetrain and likely to reduce the cost of energy for wind turbines.

6.2. Recommendations for Future Work

This work has shown that current modelling techniques may not fully capture loading on bearings within the drivetrain of the wind turbine. This opens up lots of new analysis that can be done on drivetrains.

Immediate next steps would involve improvements and expansion of the model to provide a more comprehensive structural model. The nonlinear response of the flexible coupling model is important if the model is to fully capture how the structure responds to the applied loading. A more realistic nonlinear model would give insight into whether the applied loading causes operating conditions out with current expected loading during these transient events subjecting high speed bearing loads to greater loads than anticipated.

The present model also does not take into account the structural twisting of the bedplate caused by the connection to the tower. Modelling this connection can give an idea of how the motion of the tower top can cause deflections of the drivetrain which under highly transient conditions, such as the emergency stop, is likely to be significant.

Testing of these models using measured data is crucial for verifying and validating results. Without the validation there is little confidence that models produce meaningful results. A mix between testing in a wind turbine and on a test rig can be

complimentary in identifying specific areas of interest. In particular, measurements of the deflections of generator mounts and bearings during transient events will be especially useful.

Future work beyond the above suggestions can continue looking at effects of how transient events affect loads created by the structure. Many operational and fault situations may cause highly transient responses to occur with improve representation giving a more realistic response. Turbulent wind conditions may cause strong off axis loading on the turbine that can cause highly transient conditions. With these situations analysed, design of the drivetrain can be improved with an aim of mitigating damaging effects from transient loading.

More accurate modelling of loading on the turbine will allow better predictions of how extreme loads are created. This may take the form of more advanced aerodynamic models coupled with dynamic responses of the rest of the wind turbine. Increased fidelity of the drivetrain model such as modelling of internal components of the gearbox maybe better represent power transfer through the drivetrain. Improved generator models would give better understanding of loading through the drivetrain especially for medium speed designs.

Multibody software is another modelling technique to model internal gearbox components. Coupled with a finite element model of the drivetrain structure this could provide a better insight to load creation in the drivetrain during transient events.

Better fatigue and damage models are required to predict lifetime of bearings. Improved low cycle fatigue models would benefit modelling of transient event where the loading is only for a relatively short period of time but could be extremely damaging. Damage models, where the order of loading has an impact on subsequent lifetime, could be useful where cases when a wind turbine experiences an extreme load at the beginning of its lifetime and experiences increased wear afterwards not predicted by current models. This certainly could be the case for extreme loading events where one of extreme loading can cause permanent deformations to the drivetrain increasing further damage to components.

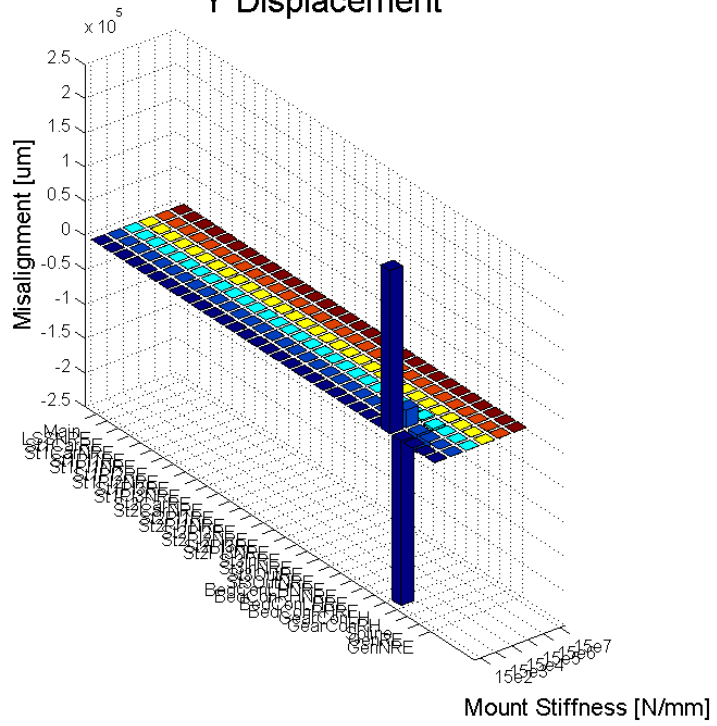
Chapter 6 - Summary

Skidding model improvements will greatly benefit fatigue calculations. Research into the onset of skidding on bearings during accelerations in transient events may give insight into how some bearings prematurely fail this way.

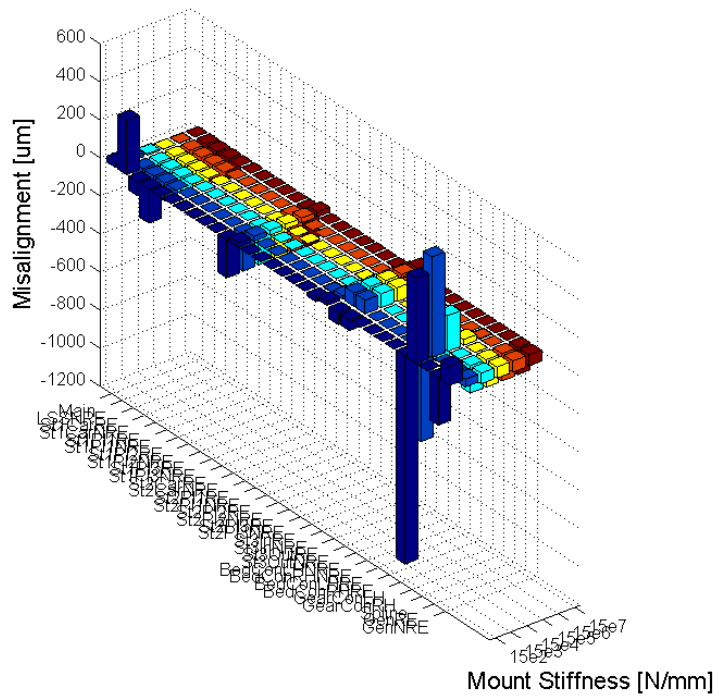
More detailed work into models of the medium speed drivetrain is required to prove the design although initial studies are promising. More detailed work to choosing adequate bearings is required. Testing of the medium speed drivetrain will be the main verification for bearing loading and reliability analysis.

Appendices

Y Displacement

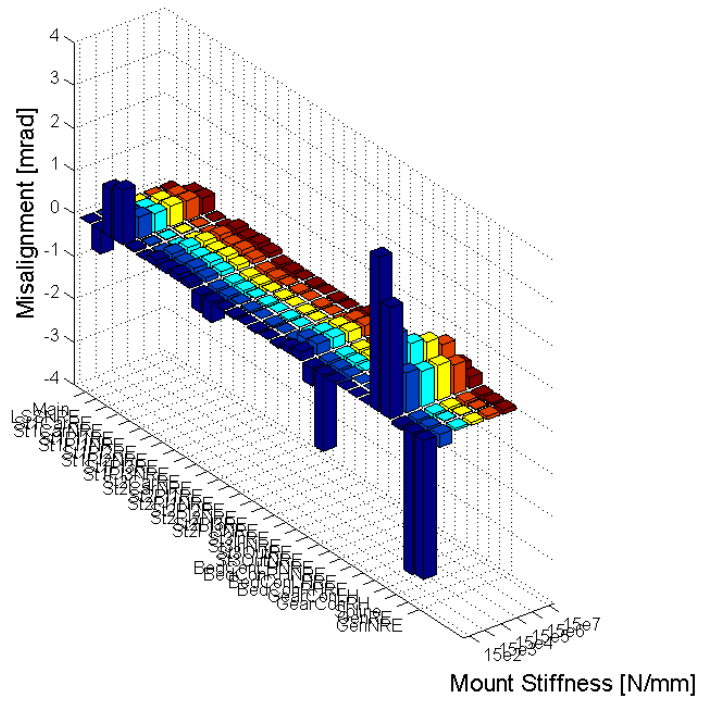


Z Displacement

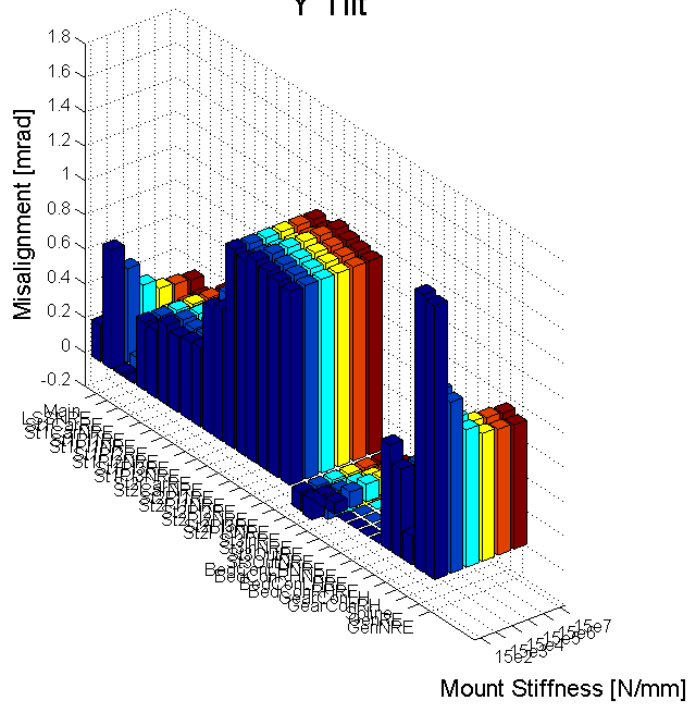


Appendices

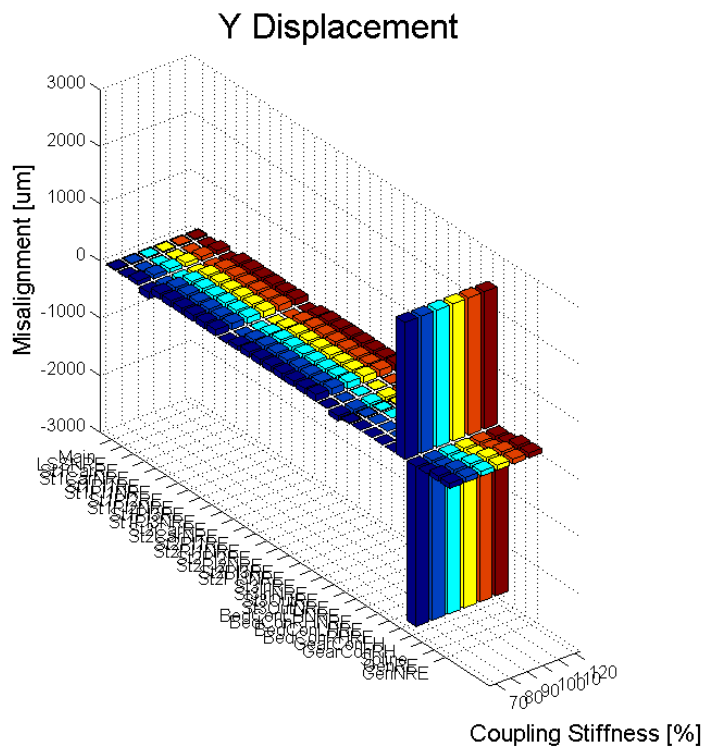
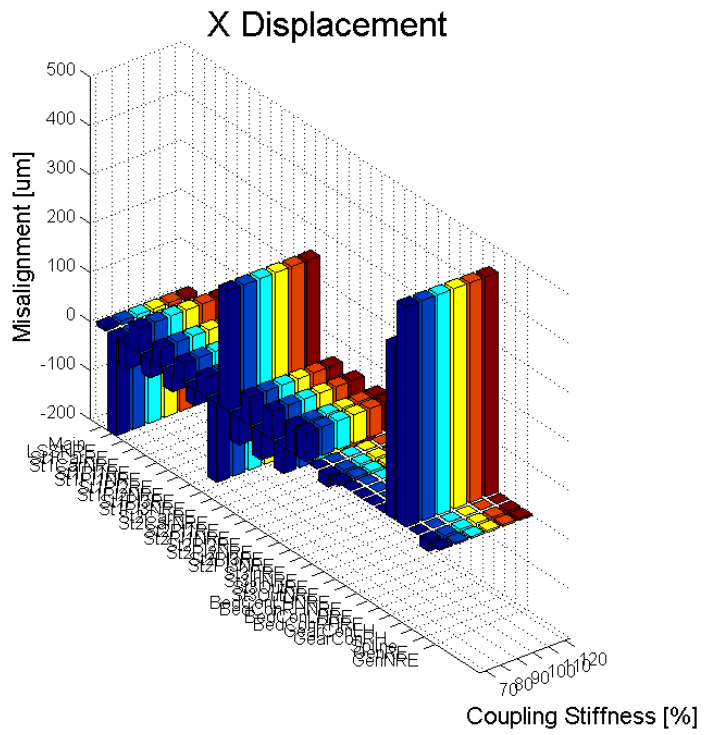
X Tilt



Y Tilt

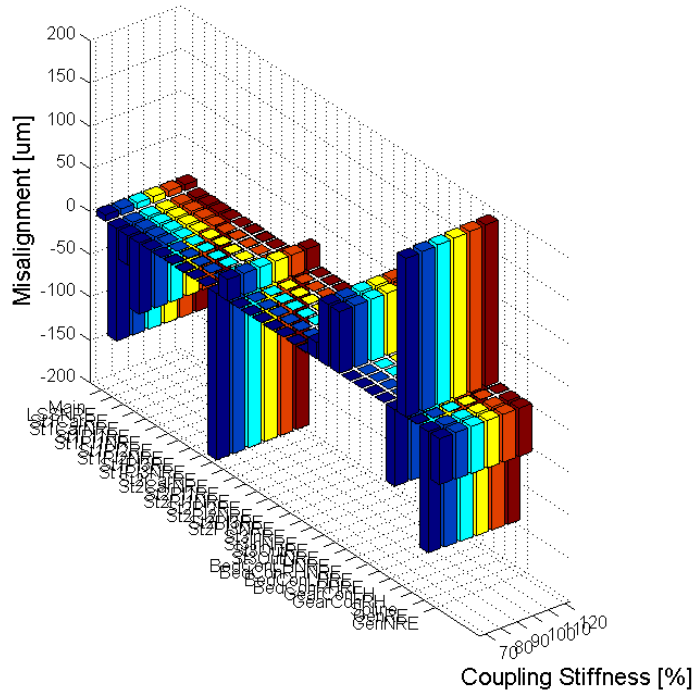


Coupling Stiffness Sensitivity

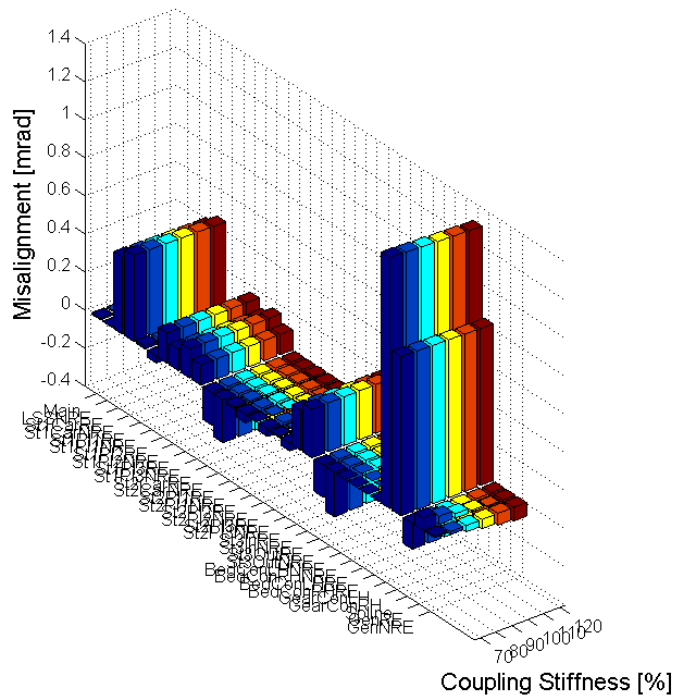


Appendices

Z Displacement

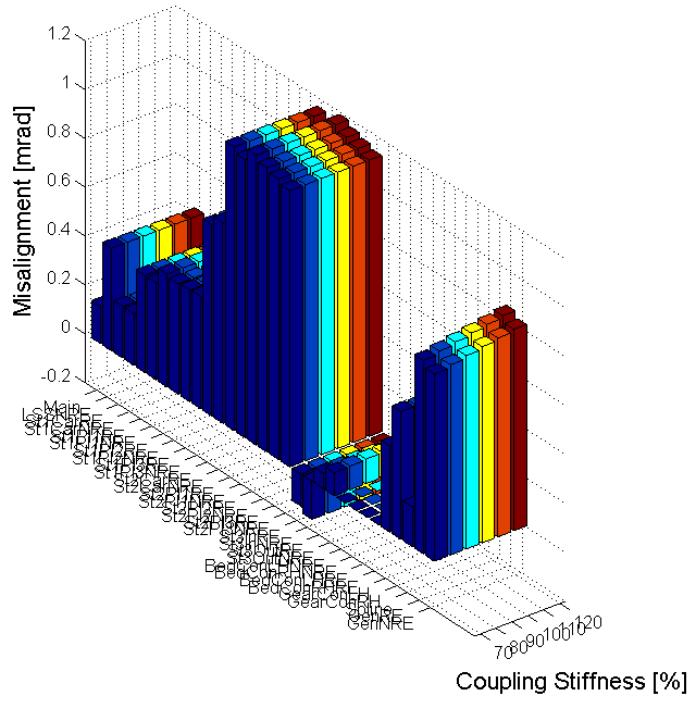


X Tilt



Appendices

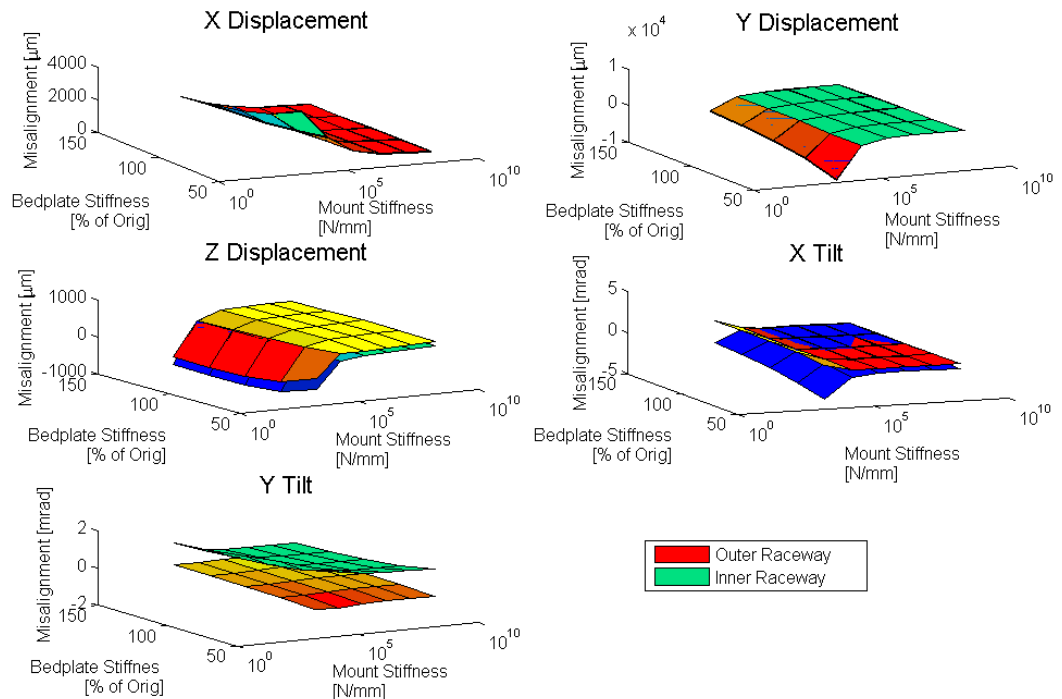
Y Tilt



8. Appendix B

Appendix B shows the absolute misalignments of the inner and out raceways of the high speed bearing for the sensitivity analysis in Chapter 2. Since damage and relative misalignments arise from the difference between the two raceways displacement it is difficult to perform sanity checks to test if the model is producing believable results. Surface plots showing bedplate stiffness, absolute misalignment and mount stiffness or coupling stiffness is plotted. As the stiffness of the components reduces more displacement is observed.

Bearing



Flexible Coupling Stiffness

